

Gran Sasso Science Institute

Ph.D. Programme in

Mathematics in Natural, Social and Life Sciences

data

Statistical Mechanics of Self-Propelled Systems

Ph.D. Candidate

Lorenzo Caprini

Advisors

Prof. Angelo Vulpiani

Università di Roma La Sapienza

Prof. Umberto Marini Bettolo Marconi

Università di Camerino

Gran Sasso Science Institute

Ph.D. Programme in

Mathematics in Natural, Social and Life Sciences

data

Statistical Mechanics of Self-Propelled Systems

Ph.D. Candidate
Lorenzo Caprini

Advisors

Prof. Angelo Vulpiani

University of Rome “La Sapienza”

Prof. Umberto Marini Bettolo Marconi

University of Camerino

Thesis Jury Members

Prof. Roberto Di Leonardo, *University of Rome “La Sapienza”*.

Dr. Luca Angelani, *ISC-CNR, Institute for Complex Systems*.

Prof. Carlo Massimo Casciola, *University of Rome “La Sapienza”*.

Dr. Claudio Maggi, *NANOTEC-CNR, Institute of Nanotechnology*.

Dr. Giacomo Gradenigo, *Gran Sasso Science Institute (GSSI)*.

Thesis Referees

Prof. Roberto Di Leonardo, *University of Rome “La Sapienza”*

Dr. Luca Angelani, *ISC-CNR, Institute for Complex Systems*

Abstract

This thesis aims to unveil the statistical properties of self-propelled microswimmers, a non-equilibrium system in the variegated field of active matter. We shall employ stochastic and hydrodynamics approaches to explain the non-equilibrium behavior of self-propelled entities.

We begin by studying suspensions of dilute active particles also in the presence of chirality. The dynamics in the presence of confinement traps is numerically and theoretically investigated employing effective equilibrium theories or effective equations for the moments of the distribution. As far as, the energetics properties of self-propelled particles are unveiled employing stochastic thermodynamic approaches. Besides, the experimental phenomenology of the accumulation near the walls is reviewed and original contributions to its theoretical understanding are developed, employing suitable hydrodynamic approaches and detecting their transport properties.

Collective fascinating phenomena displayed by self-propelled entities are reviewed and numerically investigated, featuring new long-range orders in the velocity orientations which were not unveiled, up to now. In particular, the non-equilibrium aggregation phases of Active Matter reveal intriguing new features in the presence of an effective alignment interaction induced by the interplay between self-propulsion and excluded volume effects. Even the dilute phase shows the formation of bond (but unstable) pairs, while for denser suspensions of particles a continuous transition with aligned or vortex-like domains coexists with clustering and motility induced phase separation. The usual scenario of equilibrium aggregation phases is strongly modified even at the denser regimes, where the occurrence of empty moving regions or traveling crystals does not have a passive Brownian counterpart.

Acknowledgements

First and foremost, I wish to thank my advisors Umberto Marini Bettolo Marconi and Angelo Vulpiani, for their guidance, advices and the time they devoted to my research during these three years. They suggested me the problems appearing in this manuscript and I am deeply indebted to both of them for the better understanding of Statistical Physics I have achieved at the end of this path. I could not have imagined better advisors for my Ph.D. studies. I am grateful to Andrea Puglisi for giving me the opportunity to work under his supervision; his precious support and knowledge have been crucial to carry out this research. My sincere thanks go also to Fabio Cecconi for the enormous amount of his time devoted to physical discussions, for his constant advices and for teaching me how to tackle research problems. I consider both Andrea and Fabio other two effective advisors. I thank also Massimo Cencini, Giacomo Gradenigo, Massimo Falcioni and Alessandro Sarracino. Besides my advisors, it is a pleasure, as well as a duty, to express my gratitude to Pierangelo Marcati for giving me the possibility to start working in a challenging environment at Gran Sasso Science Institute and, in particular, Paolo Antonelli and Serena Cenatiempo for their availability and the fruitful discussions during the early stages of my research.

I am extremely thankful to my Ph.D. mates Alessandro, Antonio, Cristina, Fabio, Francesco, Luca, Roberta, Roberto, Thoa, Xuan, with whom I shared this Ph.D. and my colleagues from Rome Marco, Francesco and Andrea. In particular, I thank Alessandro and Marco for their patience, support and constant help to face any kind of difficulties. I am also deeply grateful to my hometown friends Giulio K, Aldo, Roberto, Lorenza, Benny, Diva, Belli, Ioio, Giulio, Manga, Giorgio, Sheek, Simone and Giulia for being always present during these years and for the nice moments shared together.

I cannot conclude without expressing my sincere thanks to my parents Mario and Dilia for the constant help and support all along my academic career. Last but not least, a special thank to my love Alice for having always been by my side at every stage of this path.

Contents

Introduction	xi
1 How to model self-propelled Active Matter?	1
1.1 Experimental evidence of active matter	2
1.2 Stochastic models for self-propelled particles	5
1.2.1 Active Brownian Particles model	6
1.2.2 Active Ornstein-Uhlenbeck particles model	7
1.2.3 The chiral motion	9
1.2.4 What is missed by ABP and AOUP models	10
1.3 Unconfined self-propelled particles	11
1.3.1 Unconfined chiral active motion	13
1.4 Calculation of the mean square displacement for self-propelled particles	14
1.4.1 The effect of the chirality on the mean square displacement	15
1.5 Discussion	16
I Self-propelled particles under confinement	19
2 Dynamics of a self-propelled particle in external potentials	21
2.1 A self-propelled particle in a confining potential	22
2.2 Another perspective: the dynamics of the microswimmer velocity	24
2.2.1 Velocity of the ABP dynamics	25
2.2.2 Role of the thermal bath	26
2.2.3 The Unified Colored Noise Approximation	27
2.3 Self-propelled particles in harmonic traps	29
2.3.1 AOUP dynamics	29
2.3.2 ABP dynamics	31
2.3.3 A comparison between the two models in the harmonic case	33
2.4 Non-harmonic confining potentials	34
2.5 AOUP dynamics in one dimension	36
2.5.1 UCNA solution for one-dimensional systems	38

2.5.2	Non-harmonic convex potentials	39
2.6	The double-well potential	41
2.6.1	Regions with local negative temperature	43
2.6.2	Analysis of the Negative Temperature Region	46
2.7	Discussion	51
Appendices		53
2.A	Derivation of Eq.(2.7)	53
2.B	Unified Colored Noise Approximation	54
2.C	Derivation of Eqs.(2.23) and (2.24)	55
3	Accumulation near the walls	57
3.1	A self-propelled particle in a container	59
3.1.1	AOUP dynamics: reduction to a one-dimensional system	60
3.2	The accumulation near the walls	62
3.2.1	Effect of the thermal noise: the screening length	64
3.3	Theoretical treatment: predicting the wall-accumulation	65
3.3.1	Density profile in the wall region	65
3.3.2	Central region	67
3.3.3	Forces on the confining walls	73
3.4	Role of the chirality: accumulation in the bulk region	78
3.4.1	Parabolic channel	80
3.4.2	The slit	81
3.4.3	Momentum profile in the potential-free region $ x < L$	85
3.5	Active transport process along an open-wedge channel	88
3.5.1	The open wedge-geometry	88
3.5.2	Distribution along channel axis	94
3.5.3	Escape process of active particles from the wedge	96
3.6	Discussion and perspectives	102
Appendices		104
3.A	Stationary distribution for the harmonic oscillator in the (\mathbf{x}, \mathbf{v}) variables	104
3.B	How to rationalize the non-Gaussian closure	104
3.C	Exact distribution in the parabolic channel	105
3.D	Transport properties of Brownian particles in open-wedge chan- nels	106
4	Energetics of active matter: a prototype of far from equilib- rium system	111
4.1	Path Integral approach: the probability of a trajectory	113
4.1.1	Time-reversal trajectory	115
4.1.2	Entropy Production and Dissipation	116
4.2	Over-damped dynamics	117
4.2.1	Example I: passive Brownian particles	118

4.2.2	Example II: Self-propelled particles without thermal noise	119
4.2.3	Example III: Self-propelled particles in a suspension at fixed temperature	121
4.3	Energetics and local properties of the entropy production for the AOUP model	124
4.3.1	The stochastic first thermodynamics law	124
4.3.2	The stochastic second thermodynamics law: the generalized Clausius inequality	125
4.3.3	Local properties of the heat and the entropy production	127
4.4	Linear Response Theory	129
4.4.1	Linear Response Theory for self-propelled particles: the generalized fluctuation-dissipation relations	130
4.4.2	Perturbative expansion of $\mathbf{R}(\mathbf{t})$	131
4.4.3	Caveat: calculation of the response function in the (x, \tilde{v}) representation	132
4.4.4	Response function of the UCNA dynamics	134
4.4.5	Numerical study of the response function	135
4.4.6	The harmonic potential: exact results	138
4.5	Conclusions	139
Appendices		142
4.A	Computation of \mathbf{T}^{-1}	142
4.B	Equivalence between Fokker-Planck and path-integral approaches in the computation of the entropy production	143
4.C	Entropy production in the limit of zero thermal noise	144
4.D	Computations of correlations functions and response for the harmonic potential	145
II An overlook of collective phenomena		147
5 High densities active matter		149
5.1	Interacting systems of self-propelled particles	151
5.1.1	The coarse-grained velocity of the particle	153
5.2	Self-propulsive systems at high densities	154
5.2.1	Phase diagram: effective temperature and density non-homogenities	155
5.3	Self-propulsion induced velocity alignment at high densities	158
5.3.1	Spatial correlation of the velocity orientation	159
5.4	Theoretical explanation: effective Vicsek-like interactions	162
5.4.1	A further approximation: predicting the shape of R	164
5.4.2	Distribution functions of the velocity modulus	166
5.5	Confined interacting particles: activity induced freezing	168
5.5.1	Phase diagram: self-propulsion induced freezing	170

5.5.2	Study of the pair correlation function	173
5.6	Conclusion	175
Appendices		177
5.A	The pair correlation function	177
5.A.1	Details about the $\mathbf{g}(\mathbf{r})$ computations for confined systems	178
5.B	Derivation of Eq.(5.5)	179
5.C	Effective equations in the cluster: derivation of Eq.(5.13) and Eq.(5.15)	179
5.D	Forces contributions in the aligned and vortex domains	181
6	Motility Induced Phase Separation	183
6.1	Experimental evidence of clustering	186
6.2	Minimal microscopic models for MIPS	188
6.2.1	Qualitative picture: cluster formation and dilute phase	190
6.3	Effective equilibrium theories for MIPS	192
6.3.1	Binodal decomposition: effective equilibrium approach	194
6.3.2	Cahn-Hilliard equation	196
6.4	MIPS in the large persistence regime	197
6.4.1	Pair correlation function for self-propelled particles displaying MIPS	199
6.4.2	The single-particle velocity distribution	201
6.5	Alignment velocity order and phase separation	203
6.5.1	Effective Vicsek interactions inside the cluster	206
6.6	The dilute phase: unstable pairs outside the cluster	207
6.7	Conclusion	210
Appendices		213
6.A	From the Smoluchowski equation to the coarse-grained theory for Active Brownian Particles	213
Bibliography		219

Introduction

The development of stochastic processes has its roots in the pioneering works of A. Einstein [1, 2] and P. Langevin [3] to explain the erratic motion of small pollen grain particles immersed in water solution, a phenomenology nowadays known as Brownian motion. Its experimental discovery is attributed to the botanist Robert Brown in 1827 [4], even if irregular motions have been reported even earlier, in 1784, by Jan Ingen-Housz [5] through coal dust particles immersed in a fluid. Nevertheless, Brown excludes the possibility to deal with living entities after repeating the experiments with granular and glassy materials, postulating the purely physical nature of the phenomenon. The origin of the perpetual motion due to the molecules of the surrounding liquid has been formulated by C. Wiener [6], who, in particular, was familiar with Maxwells kinetic theory, but a theoretical explanation waited the year 1905, with Einstein's pioneering works, in terms of probability distributions, and Smoluchowski's work [7]. After a few years, P. Langevin formulated the first stochastic equation, recovering Einstein's result and opening a new research area: the mathematical theory of continuous-time stochastic processes. The consequences of their works were revolutionary, being not only related to the explanation of the movement of pollen grains itself but, mostly, to the theoretical formulation and the first experimental validation of the atomistic hypothesis. In particular, in 1911, the experiment of J. Perrin [8] gave the first estimate of Avogadro's number with a measure of the diffusion coefficient.

There are no doubts that Brownian motion (and stochastic processes themselves) has had a key role in thermodynamics and statistical physics, but it also gave (and is still giving) an interdisciplinary contribution to several areas of science, from biology to ecology as well as in finance. Equilibrium and non-equilibrium stochastic models represent one of the most powerful tools to reproduce and predict the experimental behavior of several specimens ranging from animals at macroscopic scales - birds fishes and insects, for instance - and microorganisms at mesoscopic scales - protozoa, spermatozoa, bacteria, and cells. These specimens are intrinsically different from Brownian particles: the evident stochasticity of their motion does not derive from the surrounding molecules but is induced by internal mechanisms - for instance, flagella and chemical reactions - which converts the energy from the environment into direct motion.

The first experiments on living microorganisms were performed by Przymbram in the second decade of the 20th century [9, 10]. Przymbram studied protozoa in water solution, finding a mean square displacement growing linearly in time with diffusion coefficient larger with respect to Einstein’s prediction. His work is the first experimental evidence of “active Brownian motion”. After his work, Fürth introduces the notion of persistent random walk to describe the behavior of biological microorganisms, basing his conclusion on his experimental work [11]. He independently obtains the result of Ornstein [12], who considered underdamped Brownian motion in thermal equilibrium with the environment. Starting from the pioneering works of Przymbram, random walks and, in general, stochastic processes became the leading instrument to model biological and ecological systems [13]. In particular, we mention the contribution of Howard C. Berg, about the behavior of Bacterial colonies [14, 15], such as E.Coli [16]. The modelizations of non-equilibrium systems having their origin in biological sciences have never stopped and several models, at different coarse-grained levels of description, have been implemented even nowadays [17, 18, 19, 20, 21]. Indeed, the improvement of experimental techniques has opened several research opportunities. The motion of biological entities at different length scales could be directly tracked in such a way that models could be easily tested. Even, artificial microswimmers have been recently assembled in labs [20], one one hand, to reproduce biological behaviors, on the other hand, to design new materials with intriguing properties which could be relevant for several engineering applications.

Even if, recently, intense interdisciplinary research, involving biology, statistical physics, and engineering science, has been developed, there is still a lack of theoretical understanding. Models are usually developed in the framework of non-equilibrium stochastic processes for which the absence of a unified theory is well-known. From another perspective, these models are the perfect platform to investigate the properties of systems far from equilibrium. The application of well-known tools of equilibrium Statistical Mechanics and, somehow, their failures is the first step in this direction. This thesis aims to provide a small contribution to this subject, applying several topics both in the framework of Statistical Physics and Liquid theory. From one hand, we study the hindered properties of a single microswimmer confined in external traps or boxes with different geometries, unveiling their energetics and transport properties and, finally, shedding light on the intriguing collective phenomena featured experimentally by these systems, such as clustering and phase separation.

The thesis is divided into two parts where original results are presented, after a brief introductory chapter. In particular, it is structured as follows:

- **Chapter 1** introduces some experimental specimens of self-propelled particles and reviews some simple stochastic models to describe their

behavior. In particular, the “Active Brownian particles” and the “Active Ornstein-Uhlenbeck particles” models are introduced and discussed at the level of single-particle trajectories and mean square displacements, even in the presence of chiralities.

- **Part I** is devoted to the phenomenological and analytical study of non-interacting self-propelled particles. In particular:
 - **Chapter 2** describes the behavior of active microswimmers in the presence of an external confining trap. The non-equilibrium phenomenology arising from the interplay between self-propulsion and external force is elucidated for different shapes of the potential. In particular, the accumulation far from the minimum of the trap is reported and explained employing theoretical arguments. We also study the escape from a double-well potential establishing the existence of negative temperature regions.
 - In **Chapter 3**, we introduce a well-known phenomenon of self-propelled particles, the so-called “accumulation near the walls”. After describing the leading phenomenology, we focus on the effect of solvents and chiralities, developing analytical predictions based on hydrodynamic approaches. Finally, we study the escape properties from a wedge-channel evaluating the role of the self-propulsion on the entropic forces taking place in the well-known Brownian scenario.
 - **Chapter 4** is devoted to the energetics of active particles in the framework of stochastic thermodynamics. Applying path-integral techniques, we calculate the heat-rate and the entropy production, solving a recent debate. We, also, apply the linear response theory discussing the validity of the generalized Fluctuation Dissipation relations for different confining potentials.
- **Part II** is dedicated to collective phenomena common to several systems of active particles. In particular:
 - **Chapter 5** is devoted to the study of the aggregation phases of self-propelled systems at high densities. Traveling crystals and anomalous non-homogeneous states with liquid structures are founded in the large persistence regime as also an additional long-range order in the alignment of the velocities. The analogy with any equilibrium phases, in the framework of liquid theory, is broken.
 - In **Chapter 6**, we review the so-called “Motility Induced Phase Separation”, both experimentally and theoretically, first describing the existing theories. We discover the existence of a new long-range order which involves the velocity alignment, occurring in concomitance with the phase separation. Besides, cluster

dynamics is explored for far from equilibrium regimes, revealing other intriguing novelties which call for experimental verifications.

Finally, a discussion and some conclusions are reported, illustrating future intriguing perspectives of the original studies performed in this thesis.

Chapter 1

How to model self-propelled Active Matter?

With the term “Active Matter” we usually refer to a broad interdisciplinary field at the frontiers of Physics, Biology, and Engineering with applications in several areas of science, from health care to material science. It includes living or “dead” entities from macroscopic to nanoscopic scale featuring fascinating phenomena, from the flocking of birds to the self-organization of motile bacteria [17, 19, 20, 21, 22]. What is the common feature of these systems? Usually, they convert stored energy from the environment - using different and, often, complicated mechanisms - into mechanical motion [19, 20, 23].

Obtaining a deep comprehension of these natural samples is a great deal and constitutes a first step towards understanding life [24], for instance. Recently, the lack of a unified theory capable to predict the leading features of these systems has motivated a large number of studies in the framework of both Statistical Physics and Fluid Mechanics. In general, active matter offers the perfect platform to investigate the non-equilibrium world, which is far from a deep theoretical comprehension, providing several stimuli for the development of new Physics.

In the variegated active matter world, several classifications have been proposed. Systems which conserve the momentum are considered part of the so-called “wet” active matter, while systems which dissipate their momentum in the environment form the “dry” active matter [19]. The study performed along with this thesis is restricted to models belonging to the latter class. Nowadays, the word “self-propelled particles” denotes a large amount of living and non-living entities and forms a small subclass in the complex world of Active Matter systems, which has received growing attention in the last years. Their common feature is the presence of a propulsive mechanism which produces a persistent Brownian motion [18, 20, 25]. These particles are the “building blocks” of new materials, exhibiting a plethora of intriguing and fascinating behaviors, absent in ordinary equilibrium particles and, even, in driven non-equilibrium matter.

Recently, several models have been proposed to explain the complex phenomenology of self-propelled microswimmers, from single-trajectories towards the comprehension of several complex collective phenomena. Propelled particles can be described at two different levels: (i) a fine-grained level fully taking into account the self-propulsion mechanism, the degrees of freedom of microswimmers, such as moving internal elements, and the solvent hydrodynamics [26]. (ii) a coarse-grained level where the motion of microswimmers is modeled by using a stochastic equation of motion and the self-propulsion is represented in terms of effective forces and torques. The approach of (ii) has a long history, which goes back to Langevin's pioneering work [3] and, thus, to the first continuum-time stochastic differential equation to describe the motion of a pollen-grain in a solvent. The great success of his approach is due to its simplicity and opened the door of a new mathematical area. Instead, the numerical and theoretical complexity of (i) establishes natural computational limits which, for instance, prevent the possibility of studying a large number of particles, and, for instance, make difficult the evaluation of collective phenomena. In what follows, we adopt the second level of description which allows a straightforward application of the tools of Statistical Mechanics and computer simulations, both for a single and a large collection of active particles.

In the spirit of (ii), the distinguishing feature of self-propelled particles is the tendency to run along some straight paths before changing direction, a phenomenology completely new with respect to the scenario of ordinary passive colloids, described by ordinary Brownian motions. The mechanism leading to such a new phenomenology is considered as an effective force term, namely the self-propulsion force, arising from physical or chemical processes depending on the microswimmer. Anyway, self-propulsions display the following properties: (a) they are typically noisy and their orientations are random, (b) active forces acting on different self-propelled particles are mutually independent and (c) the directions of driving persist over time scales of the order of the microseconds.

The chapter is structured as follows: in Sec.1.1, we describe some experimental specimens of self-propels particles, while in Sec.1.2 we introduce the stochastic models employed along with this thesis, i.e. the Active Brownian Particles and the Active Ornstein-Uhlenbeck Particles models also in the presence of the chirality. Sec.1.3 review the phenomenology of unconfined self-propelled particles. Particular attention is devoted to mean square displacements, in Sec.1.4. A discussion is reported in the final Section, where a schematic comparison between the two models is reported.

1.1 Experimental evidence of active matter

We report several experimental samples of active matter to provide some examples of the real systems on which the numerical and theoretical study of

the next Chapter is focused. For the sake of simplicity, we divide microswimmers into two different macro-classes, only depending on their origin. Biology involves a large variety of living microswimmers which self-propel (often with rather complicated mechanisms), but, recently, artificial microswimmers characterized by persistent trajectories have been designed. We report only a few examples, focusing particularly on artificial microswimmers which are the experimental samples nearer to the models employed in this thesis.

Biological microswimmers span a large range of length scales, featuring many levels of complex mechanisms to produce self-propelled motion [23].

- a i) Several species of bacteria propel with flagella, i.e. helical filaments, rotated by a “motor” which usually is formed by several proteins. *Escherichia Coli* [16], *Salmonella Typhimurium*, *Rhizobium lupini*, or *Proteus mirabilis*, to name just a few, are typical examples of rod-shaped bacteria with size $\sim 1\mu\text{m}$. They propel using multiple flagella pointing in all directions. Instead, *Vibrio alginolyticus* [27] posses just one flagellum and represents perhaps the simplest microswimmer. At larger length scale, protozoa (typically $\sim 10\mu\text{m}$) [28] and spermatozoa ($\sim 50\mu\text{m}$) [29] are other microorganisms propelling by a snake-like wiggling of its flagellum [30] to reach the egg. In this case, other mechanisms take place to complicate the scenario such as chemotaxis. Other and more complex organisms are single-celled green algae, such as *Chlamydomonas reinhardtii* ($\sim 10\mu\text{m}$), with light-sensing eyes [31]. It is worthy to mention the ciliates, i.e. microorganisms characterized by motile cilia on their surface [32], for instance, *Paramecia* and *Opalina* are groups of unicellular ciliate protozoa ($50\text{-}350\mu\text{m}$). Another interesting green alga is known as *Volvox*. It is formed by up to 50 000 cells, similar to *Chlamydomonas*, enclosed in a sphere with numerous flagella on its surface [33]. Its eye-spot facilitates the motion towards the light. Alternatively, some bacteria move gliding on a substrate, such as *Myxococcus Xanthus* [34], which, acquire identical nematic orientation after collisions.
- a ii) By contrast, other active matter systems involve more complex entities. For instance, cells, cellular cytoskeleton, and, even, living tissues are driven far from equilibrium by nanoscale molecular motors, based on protein machines that convert chemical energy into direct motion [35, 36]. Usually, in these cases, the driving force is obtained by the hydrolysis of adenosine triphosphate (ATP), which produces a release of energy. Even larger scale motions of eukaryotic chromosomes in the nucleus display an active-like motion, produced by motor mechanisms driven by DNA-binding enzymes [37].

Understanding and controlling the behavior of such biological microswimmers could offer interesting applications in several areas of science [20]. For instance, bacteria have been used to implement motors: asymmetric wheels

in a bacterial bath spontaneously start to rotate [38, 39], a mechanism which can be even powered by light [40]. Besides, since some species can move in response to environmental signals - for instance, genetically engineered bacteria can be controlled using light sources - Di Leonardo et. al. have used digital light projectors to control bacteria in such a way that they arrange in complex and reconfigurable patterns [41]. Additionally, self-propelled bacteria are capable to transport colloidal cargoes onto target sites or to segregate passive heavy colloidal particles [42]. In general, modeling and controlling the growth of bacterial colonies is a very challenging problem for medical and histological applications. Additionally, we remark that much control on the motion of spermatozoa - for instance, near surfaces or corners [43] - could be particularly useful to increase the efficiency of artificial inseminations.

The idea behind the existing mechanisms leading to artificial self propulsive forces is connected to a symmetry breaking (in its shape, material, or chemical functionalization) responsible for any phoretic motion [20]. In the cases reported below, inertial effects are negligible. On this basis, we will always assume the overdamped regime in the models employed along with this thesis. In this framework, we can distinguish between two main classes of microswimmers depending on the properties of their propulsive mechanisms:

- b i) microswimmers propelled by local conversions of energy. The generation of a local gradient - for instance with thermal or chemical origins - generates a phoretic motion. First examples occur employing gold-platinum and gold-nickel micro-rods immersed in solutions of hydrogen peroxide [44, 45]. Self-propulsions can be also generated by dielectric particles immersed in the same solution. These are colloids partially coated (usually for one half) with layers of catalytic materials, such as platinum, palladium or hematite. They are often known as “Janus particles” [46]. They decompose hydrogen peroxide into H_2O and O_2 , creating local gradients of concentrations leading to self-diffusiophoresis [47]. It is remarkable to note that, when the hematite is used as the catalyst, the hydrogen peroxide is decomposed by tuning light (so as an external mechanism), producing much control on the experimental device [48]. Propulsion is also induced by self-thermophoretic motion produced by laser power (first time observed with half-coated gold colloids) [49, 50]. Local heatings are also produced in binary liquid mixture close to the critical temperature [51].
- b ii) Microswimmers driven by external electric, magnetic or acoustic fields. Its application induces forces and torques on the swimmer body, resulting in its reorientations and/or geometrical deformations. Vertical alternating magnetic forces to magnetic micro-particles at a liquid-air interface leads to magnetic filaments of particles [52]. Instead, the use of rotating magnetic field leads to rotating self-propelled chiral objects [53] or to semi-flexible rods [54]. Alternatively, excitations of ultra-sound waves induce propulsion, levitation and, even,

alignment in metallic micro-rods. Their persistent motion (due to self-acoustophoretic mechanisms) depends on the asymmetry of their shapes. Other self-propelled systems are reactive water droplets [55], for instance, immersed in oily surfactant medium [56].

Interesting applications in several areas of science turn around the design of these artificial systems. transport, sensing, and manipulation are their basic features which provide high potentiality to these systems, for instance in the design of material with new interesting properties. Besides, the control of their motion is a challenge possibility to design smart devices for drug delivery [57] with intriguing health care applications [58, 59, 60].

1.2 Stochastic models for self-propelled particles

The possibility of tracking the self-propulsive motion of many microswimmers led to the introduction of several phenomenological models to reproduce the single-particle trajectory, accounting both for its persistence at short time and its effective diffusivity at large times. In this framework, an important model to be mentioned is the so-called *Run & Tumble* model (R&T). R&T has been introduced to describe the dynamics of the bacterium *E.Coli* in solution [61, 62]. The Self-propulsion motion is performed by a sequence of “runs” - periods of almost straight-line motion at constant speed - punctuated by sudden and rapid randomizations in direction, or “tumbles”, occurring stochastically with a typical rate. The simplicity of the stochastic rule of R&T allow us to solve explicitly such a model in the one, two and four-dimensional cases [63, 64], while no-explicit solutions are known in three dimensions. Moreover, the discrete feature of such a model hinders the use of many tools in the framework of Statistical Mechanics and stochastic processes and even the numerical implementation of interacting dynamics is rather complex.

To master these problems, other models have been developed in the framework of “continuous-time” stochastic processes to explain the phenomenology of self-propelled microswimmers. This approach is particularly useful to attempt a description of “active particles”, in terms of macroscopic concepts, such as pressure, surface tension, effective temperature to such systems or to explore Statistical Mechanics tools, such as the entropy production, the linear response theory, and generalized Fluctuations-Dissipations relations, for instance.

At variance with the well-known Brownian motion, the self-propulsion is modeled as an effective force evolving with a complex stochastic rule instead of being simply a memory-less Wiener process [65]. At this coarse-grained level, many details of the self-propulsion are neglected and considered to be irrelevant for the dynamics of such microswimmers.

Particles are assumed to be point-like, or, in other words, we consider just an equation for their center of mass, assuming that the deformations in the microswimmer shapes are negligible. Such a hypothesis does not hold for a large class of microswimmers, typically motile cells, even if, in some cases, such a difference does not consistently alter the observed phenomenology. Supported by experimental evidence, the inertial effects can be neglected since most of the self-propelled particles move in solution, aquatic habitats or more complex environments with a large damping [20]. Therefore, we can model the dynamics with a stochastic overdamped equation for the spatial-coordinate, \mathbf{x}_i :

$$\gamma\dot{\mathbf{x}}_i = \mathbf{F}_i + \gamma\sqrt{2D_t}\boldsymbol{\eta}_i + \mathbf{f}_i^a, \quad (1.1)$$

where $\mathbf{F}_i = -\nabla_i V$ is the total force exerted on the particle i , due to the general potential, V , modeling confining mechanisms or inter-particles interactions, for instance. The term $\gamma\sqrt{2D_t}\boldsymbol{\eta}_i$ represents the thermal force induced by the particles of solvent, being $\boldsymbol{\eta} = (\eta_x, \eta_y)$ a two-dimensional noise vector with uncorrelated components, unitary variances and zero averages. The constants γ and D_t are the drag and the diffusion coefficients due to thermal bath at temperature T , which satisfies Einstein's relation $T = \gamma D_t$. As usual for passive colloids, we assume that an active particle does not modify the properties of the environment and cannot produce temperature gradients in the surrounding fluid, for instance. As already anticipated, the last term, \mathbf{f}_i^a , models the self-propulsion force of each microswimmer. Recently, different models of such biological or chemical agents have been developed in the framework of stochastic processes. We mention the Active Brownian particles (ABP) model and the Active Ornstein-Uhlenbeck particles (AOUP) model as two typical examples employed along with the rest of this thesis.

1.2.1 Active Brownian Particles model

The ABP model was originally introduced to describe the motion of artificial microswimmers [47, 66] and explain their ability to explore the environment more efficiently than passive colloids. In the ABP dynamics, the active force is determined by a stochastic vector of fixed modulus, U_0 , and random direction, \mathbf{n}_i , which reads $\mathbf{f}_i^a = \gamma U_0 \mathbf{n}_i$. Thus, U_0 represents the modulus of the constant swimming velocity induced by \mathbf{f}_i^a , while \mathbf{n}_i is a unit vector determining its orientation which embodies the stochastic nature of the self-propulsion. To be specific, its dynamics reads:

$$\dot{\mathbf{n}}_i = \sqrt{2D_r}\boldsymbol{\xi}_i \times \mathbf{n}_i. \quad (1.2)$$

The constant D_r is the rotational diffusion coefficient, while $\boldsymbol{\xi}_i$ is a white noise vector whose uncorrelated components have zero averages and unit variances. Eq.(1.2) conserves the unitary modulus of \mathbf{n}_i determining a random diffusion of its direction whose typical time scales as $\sim 1/D_r$. In two

dimensions, assuming that \mathbf{n}_i belongs to the plain xy , the noise vector $\boldsymbol{\xi}_i$ is directed along the z axis. As a consequence, in this simple case, Eq.(1.2) assumes a simple formulation in polar coordinates. Indeed, the unit vector has components $\mathbf{n} = (\cos \theta, \sin \theta)$ and the angle, θ_i , evolves as a Wiener process:

$$\dot{\theta}_i = \sqrt{2D_r}\xi_i, \quad (1.3)$$

where ξ_i is a white noise with zero average and unitary variance. In this case, a simple diffusion determines the evolution of the polar angle, while in three dimensions the multiplicative nature of Eq.(1.2) emerges also in spherical coordinates. The form of the autocorrelation function, $\langle \mathbf{n}_i(t) \cdot \mathbf{n}_j(0) \rangle$, of the orientational d -dimensional vector \mathbf{n}_i is well-known in the theory of rotational diffusion of polar molecules [67]. For generic dimensions d , averaging over the angular distribution at time t , we simply obtain the steady-state expression:

$$\langle \mathbf{n}_i(t) \cdot \mathbf{n}_j(0) \rangle = \delta_{ij} e^{-tD_r(d-1)}. \quad (1.4)$$

as anticipated, $D_r(d-1)$ is the inverse of the correlation time of the two-time activity-activity correlation function, whose amplitude is $\gamma^2 U_0^2$. Therefore, the smaller is D_r the longer the activity orientation persists in a given direction and $1/D_r(d-1)$ roughly determines the time after which the active force rotates of a significant angle. Such a formula is ill-defined for a one-dimensional system, being the ABP model meaningless in this case.

The ABP model has been successfully used to describe artificial self-propelled microswimmers, such as Janus particles among the others. Anyway, the connection with the R&T model has been evaluated by M.E. Cates and J. Tailleur [68]. Choosing appropriately the parameters of the dynamics, the two models feature some connections allowing us to extend the use of ABP to describe the behavior of several bacterial species. Nevertheless, the R&T model cannot be mapped exactly in the ABP one, but the second can be considered as its continuous (and smooth) approximation. Anyway, despite hydrodynamic interactions or other effects cannot be neglected for several microswimmers, the ABP description remains the more powerful and simpler model to describe the leading phenomenology - at least at a coarse-grained level - featured by the huge class of self-propelled microswimmers.

1.2.2 Active Ornstein-Uhlenbeck particles model

The Active Ornstein-Uhlenbeck particles (AOUP) model has been originally introduced as a simplification of ABP to make progress in its theoretical analysis [69], maintaining the phenomenology of the self-propelled particles. Recently, AOUP has been also used to model passive mesoscopic objects, such as rigid bodies or flexible/semi-flexible polymers, immersed in a suspension of active particles, typically bacteria [70, 71, 72] in diluted regimes. In this interpretation of the model, \mathbf{f}^a does not represent an internal mechanism

but rather the effect of persistent collisions due to the active microswimmers, which are supposed to be smaller than the passive object. This approach is a generalization of the standard procedure to model a passive colloid in a passive solution. In this equilibrium case, the solvent behaves as white noise. Even if a formal derivation from the microscopic dynamics is known only for few (and very simple) cases, such a coarse-grained procedure reproduces the phenomenology of colloids in solution with high accuracy. A similar scenario happens for baths of diluted bacteria, whose difference resides in the persistent motion of the particles' bath [72].

At variance with ABP, in the AOUP model, \mathbf{f}_i^a is a noise vector with exponential memory [73, 74, 75]. Usually, its components evolve as independent Ornstein-Uhlenbeck processes:

$$\tau \dot{\mathbf{f}}_i^a = -\mathbf{f}_i^a + \gamma \sqrt{2D_a} \mathbf{w}_i \quad (1.5)$$

where τ is the correlation time of each component, D_a the effective diffusion constant induced by the active force and \mathbf{w}_i is a white noise vector with unitary variances and zero averages, whose components are uncorrelated. The variance of the active force, D_a/τ , is particularly significant in this model, roughly determining the average value assumed by $|\mathbf{f}_a|$.

The connection line between AOUP and ABP has been already explored in [76, 77, 78] and naturally emerges evaluating the two-time activity-activity correlation function, $\langle \mathbf{f}_i^a(t) \mathbf{f}_j^a(0) \rangle$, which, in dimension d , displays the exponential shape for each component of the Ornstein-Uhlenbeck process:

$$\langle \mathbf{f}_i^a(t) \cdot \mathbf{f}_j^a(0) \rangle = d \delta_{ij} \delta_{\alpha\beta} \frac{\gamma^2 D_a}{\tau} e^{-t/\tau}. \quad (1.6)$$

Eqs(1.4) and (1.6) for ABP and AOUP, respectively, display the same time functional form, an exponential. Thus, we can establish a mapping between the parameters of the two models comparing the correlations functions of the two active forces, i.e. setting the parameters in the proper way:

$$D_r = \frac{1}{\tau(d-1)} \quad (1.7)$$

$$U_0^2 = \frac{D_a}{\tau} d \quad (1.8)$$

We remark that Eq.(1.7) is meaningless in the one-dimensional case, reflecting the fact that even the ABP dynamics is ill-defined for $d = 1$ at variance with the AOUP model.

Despite the analogies observed in Eqs.(1.4) and (1.6), some natural differences between ABP and AOUP active forces occur. ABP active force has only $(d - 1)$ degrees of freedom, being its strength fixed, while the AOUP dynamics independently evolves both the modulus and the angular components of the active force, providing a fluctuating strength in the propulsion mechanism [78]. Besides, higher-order correlations of the active force can

be trivially expressed in terms of the second-order one in the AOUP case, because of the Gaussianity of the process. This is no longer true in the ABP case where the higher-order correlations are non-Gaussian and, in general, more complicated. For these reasons, we can consider AOUP as the Gaussian-like approximation of the ABP model.

Nevertheless, we anticipate that the phenomenology of self-propelled systems, namely the accumulation near the walls and the motility induced phase separation, for instance, is reproduced by both models. We will review these topics in the next Chapters. Thus, AOUP can also be considered as another independent model for self-propelled particles, even simpler than ABP, or also a model for passive bodies in active baths.

1.2.3 The chiral motion

Several microswimmers display circle swimming in two dimensions and helical swimming in three dimensions. In nature, spiral-like trajectories are detected for *E. coli* bacteria [79] and spermatozoa in bulk suspensions [80] while circle-like motion occurs near a planar surface [81]. Additionally, FtsZ proteins on membranes perform clockwise treadmilling [82]. Similar trajectories are accounted by artificial microswimmers, such as L-shaped particles [83, 84], where the left-right symmetry is broken by the particle's shape. In other cases, the application of a magnetic field produces similar effects. This phenomenon is currently known as chirality [20].

Van Teffelen et al. [85] have extended the standard ABP model to account for the chiral motion of micro-swimmers by adding a new ingredient: they imposed a constant angular drift of amplitude Ω to the dynamics of the angle $\theta_i(t)$ to represent an effective constant torque uniformly applied to the particles. The resulting chiral ABP model is described by Eq.(1.1) for the particle position, while Eq.(1.3) for the orientational dynamics is replaced by the following stochastic equation:

$$\dot{\theta}_i = \Omega + \sqrt{2D_r}\xi_i. \quad (1.9)$$

The generalization of Eq.(1.9) is rather obvious in three dimensions. The torque turns the standard exponential form of the autocorrelation function of the orientation vector into a damped oscillatory behavior

$$\langle \mathbf{n}_i(t) \cdot \mathbf{n}_j(0) \rangle = \delta_{ij} e^{-tD_r} \cos \Omega t, \quad (1.10)$$

where $t > 0$. Notice that when $|\Omega t| > \pi/2$ the force autocorrelation function becomes negative, an observation which will be relevant in Chapter 3.

A series of interesting studies of the chiral ABP have been conducted by various authors [86, 87, 88] and they mainly rely on numerical simulations and/or the analysis of the low noise, quasi-deterministic behavior of the equations of motion. Hereafter, motivated by the success of the active

Ornstein-Uhlenbeck model in reproducing and predicting the main behaviors of non-chiral microswimmers [76, 77], we consider its chiral extension [89]. Moreover, the AOUP is considered to be a valid alternative tool to investigate the properties of active particles because of the feature which makes it analytically more treatable than the ABP, namely the property that the fluctuations of the self-propulsion force are Gaussian. We introduce the chiral version of the AOUP model by assuming the same governing Eq.(1.5) for \mathbf{x}_i , but replacing the dynamics of the active force with:

$$\tau \dot{\mathbf{f}}_i^a = -\mathbf{f}_i^a + \Omega \tau \hat{\mathbf{z}} \times \mathbf{f}_i^a + \gamma \sqrt{2D_a} \mathbf{w}_i \quad (1.11)$$

With respect to Eq.(1.5), each component of \mathbf{f}_a is subject to a tangential drift at a fixed frequency Ω around an axis orthogonal to the plane of motion, i.e. $\hat{\mathbf{z}}$. It is very simple to show that, in the case of freely moving particles, the two-time correlation functions of the chiral versions of the AOUP coincides with the functional form of Eq.(1.10) and explicitly reads:

$$\langle \mathbf{f}_i^a(t) \cdot \mathbf{f}_j^a(0) \rangle = \frac{\gamma^2 D_a}{\tau} \delta_{ij} e^{-t/\tau} \cos \Omega t. \quad (1.12)$$

Assuming again the same mapping of Eq.(1.7) and (1.8), we get a connection between the chiral version of ABP and AOUP. Since previous studies [69, 90] have shown that AOUP and ABP share many important aspects of their nonequilibrium behavior, it is not too unlikely to assume that this holds even in the presence of chirality.

1.2.4 What is missed by ABP and AOUP models

The previous models are based on several approximations which restrict their general applicability to make quantitative predictions to some microswimmers, specifically artificial ones such as Janus particles. The coarse-grained description provided by ABP or AOUP neglects the specific origin of the self-propulsions - chemical, mechanical and so on - and focuses only on the leading effects produced on the particle dynamics. Even though active forces have variegated origins, usually they guarantee quite persistent trajectories for small times in most of the cases.

Inertial effects are usually negligible for most of the microswimmers [20] living in aqueous habitats, such as bacteria, spermatozoa, protozoa, and other cellular organisms, or Janus particles. Recently, several authors have focused on the interplay between self-propulsion and inertia, discovering that the leading non-equilibrium phenomenology - such as clustering and wall accumulation - of self-propelled particles is reduced until to its complete suppression when the active force relaxes faster than the velocity.

Another important effect is played by hydrodynamic interactions, which can affect the phenomenology of microswimmers [91, 92, 93]. Several microswimmers self-propel by moving the surrounding fluid and, thus, they

are usually classified into three different families depending on their action on the fluid: pushers, pullers, and neutral [94, 20]. Pushers are those microswimmers which produce flow fields in the fluid pushed out along the propulsion axis and dragged in from the sides. Instead, pullers are those where the fluid is pulled inwards towards the swimmer along the propulsion axis and ejected to the fluid sides. Finally, neutral microswimmers do not produce asymmetries in the surrounding fluid. We remark that, in all these cases, fluid flows are typically characterized by low Reynolds numbers [95]. The simple dynamics adopted in such a thesis neglects hydrodynamic effects. In other words, we can suppose to deal with neutral microswimmers.

As a third feature, we are supposing that the shape of the particle remains unchanged, dealing with rigid spherical bodies for which we can study the position of the center of mass. This approximation does not hold for cells or elongated and deformable specimens such as active emulsion and filaments. The interplay between self-propulsion and deformability could lead to interesting phenomena such as rectification or swelling [96, 97] even for the simpler polymers models.

We outline that our description does not involve any kind of explicit alignment interactions, i.e. forces coupling the orientations of the microswimmers, creating a net polarization. This is the main difference between ABP (or AOUP) and Vicksek-like models often employed to reproduce the behavior of flocks of birds, schools of fishes and swarms of insects. In Chapters 5 and 6, we show some kind of flocking phenomena through non-alignment ABP (or AOUP) dynamics, changing the widespread idea that explicit alignment forces are needed to account for such collective behaviors.

1.3 Unconfined self-propelled particles

The simple stochastic models introduced in Sec.1.2 can explain the behavior of a single microswimmer in its habitat, as an ordinary Brownian motion describes the dynamics of a passive colloid in solution. In the absence of any confinement or driving forces, Eq.(1.1) and (1.3) for the ABP dynamics assumes a very simple form which we rewrite, for completeness, in two dimensions:

$$\gamma\dot{\mathbf{x}} = \gamma U_0 \mathbf{n} + \gamma \sqrt{2D_t} \boldsymbol{\eta} \quad (1.13)$$

$$\dot{\theta} = \sqrt{2D_r} \xi, \quad (1.14)$$

where, for the sake of simplicity, we have dropped the index of the particle. In the same way, the unconfined AOUP dynamics, Eq.(1.1) and Eq.(1.5), reads:

$$\gamma\dot{\mathbf{x}} = \mathbf{f}^a + \gamma \sqrt{2D_t} \boldsymbol{\eta} \quad (1.15)$$

$$\tau\dot{\mathbf{f}}^a = -\mathbf{f}^a + \gamma \sqrt{2D_a} \mathbf{w}. \quad (1.16)$$

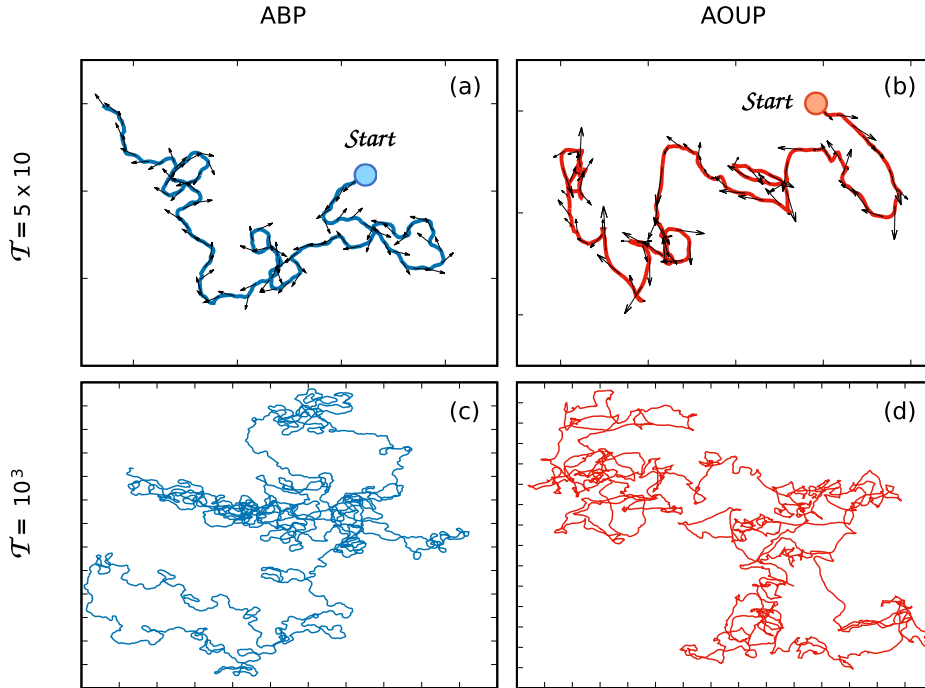


Figure 1.1: Single-particle trajectories for ABP and AOUP self-propulsion, in panels (a), (c) and (b), (d), respectively. Panels (a) and (b) are stopped at the final time $\mathcal{T} = 5 \times 10$, while panels (c) and (d) at $\mathcal{T} = 10^3$. All the panels are obtained setting $\tau = 1 = 1/D_r$ and $D_a/\tau = v_0^2/2 = 1$. The black arrows in panels (a) and (b) are the self-propulsion vectors.

In the absence of interactions and in the limit of zero thermal noise, the active force coincides with the microswimmer velocity, $\dot{\mathbf{x}}$, for both models. In the ABP case, $\dot{\mathbf{x}}$ is distributed as follows: its modulus is fixed to the value γU_0 , while its polar angle is uniformly distributed between 0 and 2π . Instead, in the AOUP model $\dot{\mathbf{x}}$ follows the Gaussian distribution of \mathbf{f}^a . In this last case, the overdamped Eq.(1.15) has the same form of an underdamped potential-free passive dynamics in contact with a fictitious thermal bath with amplitude $\sim D_a/\tau^2$ and constant Stokes force $\propto -\dot{x}/\tau$. The only difference from the underdamped passive counterpart is embodied in the thermal noise term acting directly on the dynamics of the position.

Let us start to discuss the case $D_t = 0$. In Fig.1.1, we plot different single particle trajectories following the ABP and the AOUP dynamics for panels (a), (c) and (b), (d), respectively. In particular, panels (a) and (b) show trajectories obtained for a time $\mathcal{T} = \tau = 1/D_r$, while panels (c) and (d) display longer trajectories stopped at $\mathcal{T} = 10\tau = 10/D_r$. The two models are in good qualitative agreement, showing indistinguishable trajectories [25]. Being τ the correlation time of the active force, a single particle displays, in both cases, a ballistic motion for $\mathcal{T} \lesssim \tau$ and a diffusive behavior for $\mathcal{T} \gg \tau$, a regime which is indistinguishable from a Brownian particle with effective diffusion coefficient $D_t + D_a$. We remark that τ is the only time-scale of the

dynamics so that we can switch from a regime to another by simply changing the time-window of the simulation. Equivalently, the only length-scale is the persistence length, $\sqrt{\tau D_a}$, which determines the average distance traveled by a particle, before that its direction is consistently changed.

For $D_t > 0$ an additional source of thermal noise occurs in the dynamics in such a way that two competing time- (or space-) scales determine the motion. The regime $\sqrt{\gamma D_t} \gtrsim \sqrt{D_a/\tau}$ is not very interesting since the persistence of the motion is erased by the fluctuations of the thermal noise. In this case, the particle displays a simple passive Brownian dynamics, independently of the time window observed. Instead, for $\sqrt{\gamma D_t} \lesssim \sqrt{D_a/\tau}$, the system alternates diffusive and ballistic behaviors. In the further Chapters, we always restrict to the latter case or neglect the contribution of the thermal bath, motivated by experimental evidence.

We remark that these stochastic models are in fair agreement with experimental realizations of independent self-propelled particles, mostly in the framework of artificial microswimmers [47].

1.3.1 Unconfined chiral active motion

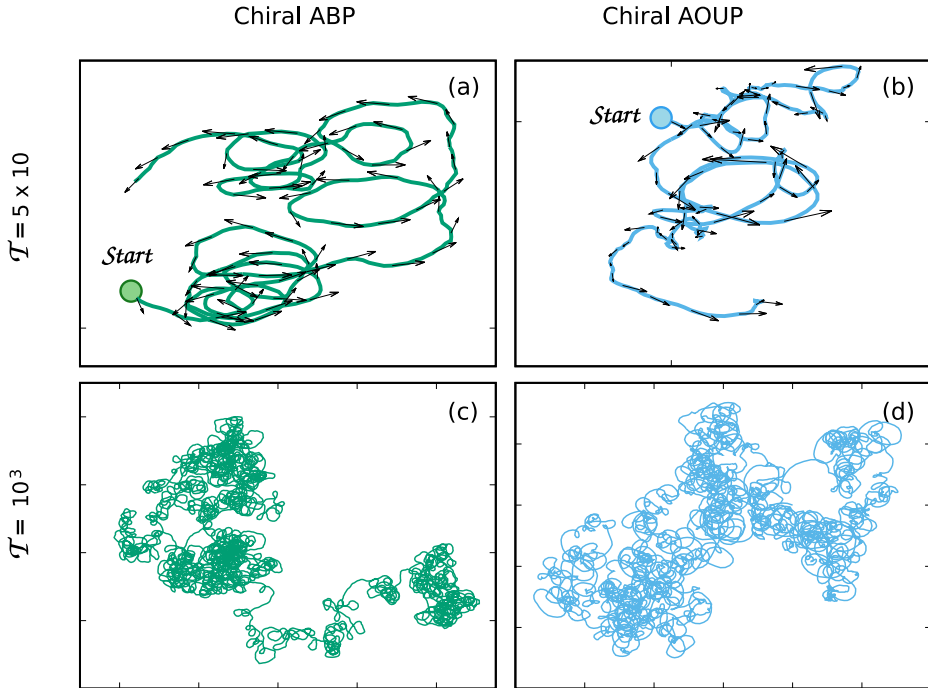


Figure 1.2: Single-particle trajectories for chiral ABP and chiral AOUP self-propulsion, in panels (a), (c) and (b), (d), respectively. Panels (a) and (b) are stopped at the final time $\mathcal{T} = 5 \times 10$, while panels (c) and (d) at $\mathcal{T} = 10^3$. All the panels are obtained setting $\tau = 1 = 1/D_r$ and $D_a/\tau = v_0^2/2 = 1$ and $\Omega = 3$. The black arrows in panels (a) and (b) are the self-propulsion vectors.

In the force-free case, $\mathbf{F} = 0$, the addition of the chirality in the self-propulsion evolution does not alter significantly the statistical properties of the particle velocity both for AOUP and ABP dynamics. In the former case, this is still a Gaussian - with unchanged variance compared to AOUP -, while, in the latter case, the modulus of \dot{x} is not changed by the chirality - it remains fixed to U_0 in the athermal case and is fluctuates around it in the presence of a temperature - but the polar angle is peaked around Ω . Nevertheless, the single-particle trajectory is deeply influenced by $\Omega > 0$ as shown in panels (a)-(d) of Fig.1.2, in both modelizations. Now, the addition of the chirality introduces another time-scale, i.e. $1/\Omega$. As already mentioned in Sec.1.2, the regime $1/\Omega \gtrsim \tau = 1/D_r$ is not so interesting since the chirality does not play a relevant role. In what follows, we always restrict to the opposite regime $1/\Omega \lesssim \tau$.

In both models, each microswimmer performs noisy-circle trajectories in two dimensions, as shown in panels (a) and (b) obtained for $\mathcal{T} = \tau = 1/D_r$, while a diffusive behavior is recovered for $\mathcal{T} = 10\tau$, as in the case $\Omega = 0$, as shown in panels (c) and (d). The typical radius of the circular trajectory deeply depends on Ω : as larger is the value of Ω as smaller is the radius.

1.4 Calculation of the mean square displacement for self-propelled particles

To rationalize the qualitative description obtaining by tracking the single particle trajectory, it is usual to study the Mean Square Displacement (MSD) of the system, i.e. a measure of the deviation of the particle position with respect to a reference position over time. It is measured to determine if a particle is spreading solely due to diffusion, or if an advective force is also contributing. MSD can be simply obtained by means of the well-known Green-Kubo formula [65]:

$$\text{MSD}(t) \equiv \langle (x_\alpha(t) - x_\alpha(0))^2 \rangle = \int_0^t ds \langle \dot{x}_\alpha(s) \dot{x}_\alpha(0) \rangle. \quad (1.17)$$

Such a relation shows that the calculation of the MSD(t) is only recast to the time integral of a correlation function.

Using the explicit expression of the dynamics - Eqs.(1.13) and (1.15) for ABP and AOUP active forces, respectively - the computation of the MSD comes directly from Eq.(1.17) and coincides for both models. Indeed, as shown in Sec.1.2, the two time activity-activity correlation function of ABP and AOUP active forces has the same functional form, a time exponential. Integrating over the time, we get:

$$\langle (x_\alpha(t) - x_\alpha(0))^2 \rangle = 2D_t t + 2D_a \left(t + \tau (e^{-t/\tau} - 1) \right). \quad (1.18)$$

The equivalent expression for the ABP active force can be obtained by using the relations (1.7) and (1.8) between the parameters[66, 98, 99]. Eq.(1.18) is

given by the sum of two terms: i) a thermal noise contribution, $2D_t t$, i.e. the ordinary diffusion due to the solvent where the microswimmer is immersed, and ii) a term solely induced by the presence of the active force, which is $\propto D_a$. Expanding Eq.(1.18) for time $t \ll \tau$, we obtain:

$$\langle (x_\alpha(t) - x_\alpha(0))^2 \rangle \approx 2D_t t + \frac{D_a}{\tau} t^2, \quad (1.19)$$

neglecting terms of order $\sim t^3$. Eq.(1.19) implies the existence of a first diffusive time-regime, for very small time, solely controlled by the amplitude of the thermal noise. A ballistic regime due to the active force manifests for intermediate values of t , becoming more evident in the limit $D_t \rightarrow 0$. Such a regime is determined by the value of D_a/τ (which is U_0^2 in the ABP case).

Instead, evaluating Eq.(1.18) for $t \gg \tau$, we can isolate the leading contributions surviving for very large times:

$$\langle (x_\alpha(t) - x_\alpha(0))^2 \rangle \approx 2(D_t + D_a)t. \quad (1.20)$$

For long times the system behaves diffusively, with a diffusion coefficient $\sim D_t + D_a$ depending both on the thermal noise and on the active force. Anyway, for several microswimmers the thermal diffusion can be neglected, being $D_t \ll D_a = U_0^2 D_r / 2$. Not so surprisingly, more a trajectory is persistent more the effective diffusion increases and, in the same way, larger is the typical particles speed larger is the long time MSD.

Basing on these considerations, several authors have identified the constant $\gamma D_a \propto \gamma U_0^2 / D_r$ as the effective temperature of self-propelled particles. Despite this assumption is reasonable in the case of potential-free microswimmers, it is quite questionable when interactions or external trap affects the dynamics, even in the simpler case of harmonic potentials. This point will be explored in the next Chapters.

1.4.1 The effect of the chirality on the mean square displacement

We, now, consider how the presence of the torque, Ω , in the dynamics of \mathbf{f}_i^a modifies the diffusive properties of self-propelled particles. Using the dynamics - Eq.(1.9) or (1.11) for the chiral versions of ABP and AOUP, respectively - in Eq.(1.17), we find the MSD(t) of a chiral active particle[85]:

$$\begin{aligned} \langle (x_\alpha(t) - x_\alpha(0))^2 \rangle &= 2D_t t + 2 \int_0^t dt_1 \int_0^{t_1} dt_2 \langle u_\alpha(t_1) u_\alpha(t_2) \rangle \\ &= 2D_t t + 2D_\Omega \left(t + \frac{(1 - \Omega^2 \tau^2) \tau}{1 + \Omega^2 \tau^2} (e^{-t/\tau} \cos(\Omega t) - 1) \right. \\ &\quad \left. - \frac{2\Omega \tau^2}{1 + \Omega^2 \tau^2} e^{-t/\tau} \sin(\Omega t) \right), \end{aligned} \quad (1.21)$$

where the factor D_Ω , which represents the effective diffusion due to the chiral self-propulsion, reads:

$$D_\Omega = \frac{D_a}{1 + \Omega^2 \tau^2} > D_a. \quad (1.22)$$

In analogy with the non-chiral case, Eq.(1.21) is the MSD both for chiral ABP and AOUP models since their two-time active force correlations coincide. Expanding Eq.(1.21) for times $t \ll \tau$ and neglecting orders $\sim t^3$, we find:

$$\langle (x_\alpha(t) - x_\alpha(0))^2 \rangle \approx 2D_t t + \frac{D_a}{\tau} t^2, \quad (1.23)$$

which coincides with Eq.(1.19), meaning that the chirality does not affect the small time-regime of the MSD. Anyway, starting from order $\sim t^3$ the chirality determines a complex transient regime, giving a contribution even for $t \rightarrow \infty$. Indeed, evaluating Eq.(1.21) for $t \gg \tau$, we obtain a pure diffusive behavior :

$$\langle (x_\alpha(t) - x_\alpha(0))^2 \rangle \approx 2(D_t + D_\Omega) t, \quad (1.24)$$

One sees that the long-time diffusion coefficient, due to the active force, is decreased by a factor $(1 + \Omega^2 \tau^2)^{-1}$ with respect to the non-chiral case [66], given by Eq.(1.20). This effect is consistent with the occurrence of the cycloid trajectories performed by the chiral self-propelled particles, which even intuitively hinder the diffusion.

1.5 Discussion

The ABP dynamics is yet considered the more realistic and simple model to approximate the behavior of self-propelled particles, in particular of artificial microswimmers. Indeed, these models are consistent with their experiments, at least at the level of single trajectories. On the contrary, the AOUP is less diffused and several authors are skeptical about its applicability to the self-propelled systems and its connection with ABP. In the previous Sections, we have reviewed the features of the single-particle trajectories in the potential-free case, showing the qualitative and quantitative analogies between ABP and AOUP active forces, even in the presence of an additional chirality. In the following Chapters, we describe the leading phenomenology which characterizes and defines the self-propelled particles, showing analogies and differences between the two models. We anticipate that the AOUP dynamics is, in general, consistent with the ABP one except for a few specific cases. Besides, its simplicity allows us to introduce analytical and theoretical procedures which are not so easy to adapt to ABP dynamics and, so, offers a real opportunity to make analytical predictions and develop a theory towards a general comprehension of self-propelled systems.

The practical consequences of the small differences between ABP and AOUP have not been completely elucidated, in the literature. Below, we briefly summarize their phenomenologies, going beyond the unconfined level:

- The dynamics in the presence of a confining potential shows strong similarities between the two models, except for the harmonic trap, where the linearity of the external force restores the equilibrium in the AOUP but not in the ABP. This case has to be intended as the exception. In both cases, particles accumulate far from the minimum of the potential, displaying strong non-gaussianity. This aspect and the explicit comparison between the two dynamics will be investigated in Chapter 2.
- The accumulation in the proximity of obstacles or simply walls is fairly reproduced by ABP and AOUP, from which equivalent hydrodynamic approaches could be developed, for instance. From this point of view, differences are quite negligible mostly in the hard-wall limit. This matter will be studied in Chapter 3.
- Both models undergo the motility induced phase separation, showing the occurrence of spontaneous stable clusters, even in the absence of explicit attractive interactions. This topic will be studied in Chapter 6. Nevertheless, very few studies are known for AOUP and the quantitative comparison between the two dynamics is currently absent in the literature.

Part I

Self-propelled particles under confinement

Chapter 2

Dynamics of a self-propelled particle in external potentials

This chapter is devoted to the study of self-propelled particles under confinement. Such a problem has been largely studied for a passive suspension of Brownian particles, both in the overdamped and in the underdamped regimes. In the passive case, the system is in equilibrium with the thermal bath, the detailed balance holds and the dynamics can be solved exactly [65] for a general external potential. We are able to compute the steady-state probability distribution function of the system, which displays a Maxwell-Boltzmann shape [100]. Particles accumulate, roughly, around the minimum of the potential with positional fluctuations determined by the interplay between the temperature value and the strength of the confinement force.

Such a scenario is altered by the presence of the self-propulsion which leads the system far from equilibrium, producing steady-state currents which invalidate the detailed balance condition [101, 102]. As a consequence, the exact steady-state probability distribution function is unknown for a general potential, except for a few special cases. Therefore, in this Chapter, we focus on the complex phenomenology arising from the interplay between the self-propulsion and external forces due to a potential [103, 104]. We focus on some prototype case, namely single-well and bistable potentials, leaving the treatment of soft-walls, i.e. truncated forces, to Chapter 3.

The study of active matter systems, such as swimming bacteria and molecular motors in geometrically confined environments, plays an important role in understanding many cellular and biological processes. Besides, even self-propelled microswimmers rarely move in unbounded media [20] and, thus, understanding their dynamics in confined environments is realistic and interesting for applications. Finally, a confining trap is a useful tool to study the mechanical pressure of active particles or the non-equilibrium features of their dynamics [105, 106, 107, 108]

Self-propelled particles can be experimentally confined in many ways: suspensions of artificial microswimmers, Janus colloidal particles for instance, can be trapped by thermophoretic [109], acoustic [110] or optical

devices, such as optical tweezers [111]. For instance, acoustic fields can be generated by piezoelectric transducers usually at frequencies in the megahertz. Analogous mechanisms allow us to trap some bacteria. In particular, these fields induce the levitation of self-propelled particles and provides secondary lateral forces to capture them at nodal planes, as in the case of *E. Coli* [112]. In particular, as an interesting application, strong traps have been employed to manipulate structures and place objects at specific locations. Also, acoustic traps have enabled the label-free monitoring for bio-assay, viability assays and bead-based chemical synthesis, the 3D contact-less positioning of small cell populations and the detection of bacteria in blood samples.

The simplest shape of such trapping potentials is the harmonic or the isotropic parabolic one, from which we start our investigation involving both theoretical and numerical studies. Anyway, experimentally complex nonlinear potentials can be realized by combining many of such devices. This justifies experimentally our further study aimed to exploit the effects of non-linearity and, even, non-convexity on the single-particle dynamics.

The chapter is structured as follows: in Sec.2.2, we review the change of variable, originally introduced in the framework of the AOUP model, which allows us to describe the system in terms of the particle's position and its coarse-grained velocity. In particular, such a method is generalized to a system of ABP particles. In Sec. 2.3, we study the harmonic confinement for both AOUP and ABP dynamics, stressing analogies and differences among them, while in Sec.2.4 non-harmonic potentials are considered. We show the so-called "accumulation far from the minimum of the potential", developing analytical approximations in the framework of the AOUP dynamics. Besides, particular attention is provided to the escape dynamics in a double-well potential, on which we focus in Sec.2.5, where interesting connections with negative mobility regions are established [104].

2.1 A self-propelled particle in a confining potential

Let us consider a suspension of independent active particles in the presence of an external force, \mathbf{F} . In this Chapter, we restrict to the case of forces due to an external potential, U . Nevertheless, many concepts could be easily generalized to the case of time-dependent driving forces or also to suspensions of interacting particles. In particular, the latter will be the main topic of Chapters 5 and 6. Having assumed an over-damped dynamics, \mathbf{F} affects directly the equation of motion of the position of the microswimmer, in such a way that its dynamics reads:

$$\gamma \dot{\mathbf{x}} = \mathbf{F} + \mathbf{f}^a + \gamma \sqrt{2D_t} \boldsymbol{\eta}. \quad (2.1)$$

We have assumed the same notation of Chapter 1, dropping the particle index in Eq.(1.1). We recall that $\mathbf{F} = -\nabla U$, γ is the constant drag coefficient and

D_t is the diffusion coefficient due to the solvent. We recall that $\boldsymbol{\eta}$ is a white noise vector whose components are uncorrelated with zero averages and unit variances. For the sake of simplicity, we restrict to the two-dimensional system, even if, in many cases, the generalization to three dimensions is straightforward. The active force follows the ABP or the AOUP dynamics, which we rewrite for completeness. In the first case, $\mathbf{f}^a = \gamma U_0 \mathbf{n}$, where \mathbf{n} is a unitary versor of components $(\cos \theta, \sin \theta)$ and U_0 the strength of the self-propulsion. In addition θ evolves in time as a Wiener process:

$$\dot{\theta} = \sqrt{2D_r} \xi, \quad (2.2)$$

being D_r the rotational diffusion coefficient. Alternatively, \mathbf{f}^a can evolve through two independent Ornstein-Uhlenbeck processes, one for each component:

$$\tau \dot{\mathbf{f}}^a = -\mathbf{f}^a + \gamma \sqrt{2D_a} \mathbf{w} \quad (2.3)$$

where τ is the correlation time of the process, D_a the effective diffusion coefficient induced by \mathbf{f}^a and \mathbf{w} a vector of independent white noises.

In Chapter 1, we have shown that the single-particle trajectory displays strong analogies for both models, which are roughly explained by their two-time activity-activity correlation functions and by their mean square displacements which have the same functional form. Such a scenario could be, in principle, modified by the presence of an external force and large differences could occur between the AOUP and the ABP models. We anticipate that such a possible discrepancy plays only a marginal role and that, even in this case, the leading phenomenology shown by the ABP model is qualitatively the same as the AOUP one.

The presence of an external force introduces an additional characteristic time to be compared with the persistence time τ (or equivalently $1/D_r$) which rules the dynamics of the active force. Such a characteristic time depends on the specific external force considered and, in particular, in the case of a force due to potentials is given by $\gamma/\nabla^2 U(l)$, being l the typical length scale associated to the potential which will be always set to one along with the present thesis. To understand how the active force gives a relevant contribution, let us set $D_t = 0$, for the sake of simplicity. In this simplified case, we call ν the leading parameter which establishes the features of the dynamics, $\nu = \tau \nabla^2 U(l)/\gamma$ ($\tau = 1/D_r$), namely the ratio between the correlation time of the active force and the time due to the potential. When $\nu \ll 1$ - corresponding to a small value of τ or a large value of D_r - the active force is the faster degree of freedom. Therefore, using the adiabatic elimination, we can approximate Eq.(2.3) by means of a Brownian motion, in such a way that $\mathbf{f}^a \approx \gamma \sqrt{2D_a} \mathbf{w}$ for the AOUP model. Such a procedure is less clear in the ABP case, where roughly we have again $\mathbf{f}^a \approx \gamma U_0 \sqrt{1/D_r} \mathbf{w}$. In both these cases, the active force plays only the role of additional white noise, inducing an effective temperature of amplitude γD_a (or $\gamma \nu^2/D_r$), which is nothing but the constant ruling the potential-free

diffusion due to the self-propulsion. This condition corresponds to a near-equilibrium regime, where the self-propelled microswimmer behaves as an overdamped Brownian particle in the presence of some effective temperature, higher than the one due to the solvent. Such a scenario is theoretically clear in the context of equilibrium-like dynamics and does not show the peculiarities of an active suspension of particles. Instead for $\nu \gtrsim 1$ - where τ is large or D_r is small - the situation dramatically changes and both degrees of freedom play an important role [77]. Non-equilibrium features appear and a numerical study of Eq.(2.1) is needed to understand the physics of self-propelled microswimmers due to the interplay between external and active forces.

2.2 Another perspective: the dynamics of the microswimmer velocity

Despite the original version of the ABP and the AOUP models are very simple to be studied numerically, the apparent differences in the form of their dynamics hinder the connection between them. To convince the reader about this issue, it could be very useful to introduce a change of variables aimed to shed light on the physical meaning of the self-propelled dynamics and establish a strong and undisputable bridge between the two modelizations. Even if Eq.(2.1) describes an over-damped dynamics, where the real velocity has been already relaxed, could be useful to find an effective equation for the coarse-grained velocity of the microswimmer, namely $\mathbf{v} = \dot{\mathbf{x}}$. Such a variable, which quantifies the time variation of the particle position in the overdamped regime, coincides with the active force for a potential-free system. Instead, in the presence of an external force the evolution of \mathbf{v} will be different with respect to the one of \mathbf{f}^a .

First attention to this perspective emerged in [113, 101] for the AOUP model neglecting the role of the thermal bath, i.e. setting $D_t = 0$. Then, later studies have been focused on the main consequences due to external potentials for the dynamics of \mathbf{v} [77, 104]. In particular, taking the time derivative of Eq.(2.1), using Eq.(2.3) and, finally, replacing \mathbf{f}_a with \mathbf{v} by means of Eq.(2.1), gives rise to an equation of motion for the variables \mathbf{x} and \mathbf{v} :

$$\dot{\mathbf{x}} = \mathbf{v} \tag{2.4}$$

$$\tau \dot{\mathbf{v}} = -\mathbf{\Gamma} \cdot \mathbf{v} + \frac{\nabla U}{\gamma} + \sqrt{2D_a} \boldsymbol{\xi}, \tag{2.5}$$

where $\mathbf{\Gamma}$ is a d -dimensional matrix depending on the derivatives of the potential, which in components (Greek indices) reads:

$$\Gamma_{\alpha\beta} = \delta_{\alpha\beta} + \frac{\tau}{\gamma} \nabla_\alpha \nabla_\beta U. \tag{2.6}$$

We point out that the mathematical mapping from Eqs.(2.1) and (2.3) to Eqs.(2.4) and (2.5) is nothing but a unitary change of variables - with Jacobian equal one - and, thus, does not involve any approximations. The original over-damped dynamics of each particle is equivalent to the under-damped dynamics of a passive particle immersed into a fictitious thermal bath with an effective diffusion coefficient given by the parameters of the active force. In addition, also the external force ∇U is rescaled by τ . The non-equilibrium feature of such a dynamics is fully contained in the space-dependent, d -dimensional friction matrix, $\mathbf{\Gamma}$, which naturally produces a violation of the Fluctuation Dissipation Relation holding for equilibrium systems. The dynamics of one particle is coupled to all the degrees of freedom through $\mathbf{\Gamma}$, which provides a coupling among the different components of the dynamics of a single particle.

We point out that in the case $\nu \ll 1$, the $\mathbf{\Gamma}$ matrix reduces to an almost spatially homogeneous matrix and the system reaches a Gibbs steady state $\sim \exp(H/T_{eff})$ with $H = \gamma\tau|\mathbf{v}|^2/2 + U(x)$ and $T_{eff} = \gamma D_a$. Thus, γD_a can be identified as the effective temperature of the system [114, 115]. Such a result is fully equivalent with the limit $\nu \ll 1$ obtained in Eqs.(2.1) and Eq.(2.3). Instead, such a scenario is broken in the opposite regime, $\nu \gtrsim 1$, where the elements of $\mathbf{\Gamma}$ strongly depends on the microswimmer position by means of U . In this case, for a general potential, we expect a non-trivial correlation between \mathbf{v} and \mathbf{x} , responsible for the departure from the equilibrium of the system. The whole probability distribution is not-known and, in particular, there are no reasons to identify γD_a with the effective temperature of the system.

2.2.1 Velocity of the ABP dynamics

We extend to the ABP dynamics the change of variables used to obtain Eqs.(2.4) and (2.5) in the framework of the AOUP model. Even in this case, we perform an exact mapping to obtain an equation of motion of the microswimmer velocity, $\dot{\mathbf{x}} \equiv \mathbf{v}$, whose derivation is reported in Appendix 2.A being an original result. In particular, the strategy adopted resembles the previous one for the AOUP model but takes into account the multiplicative nature of the ABP dynamics: assuming the Stratanovich rule for the time derivative, we can eliminate the variable \mathbf{n} in favor of $\mathbf{v} = \dot{\mathbf{x}}$ in the equation of motion. In particular, in the limit $D_t = 0$, we get:

$$\dot{\mathbf{v}}_i = -D_r \mathbf{\Gamma} \cdot \mathbf{v} + \frac{1}{\gamma D_r} \mathbf{F} + U_0 \sqrt{2D_r} \boldsymbol{\xi} \times \frac{(\gamma \mathbf{v} + \mathbf{F})}{U_0}, \quad (2.7)$$

where $\boldsymbol{\xi}$ is the stochastic vector with components $(0, 0, \xi)$ and both \mathbf{v} and \mathbf{x} belong to the xy plane. Besides, the matrix $\mathbf{\Gamma}$ has the following structure:

$$\Gamma^{\alpha\beta} = \delta_{\alpha\beta} + \frac{1}{D_r \gamma} \nabla_\alpha \nabla_\beta \Psi, \quad (2.8)$$

where Greek indices refer to the spatial vector components. Eq.(2.7) is the equation of motion of an underdamped particle under the action of a space-dependent Stokes force and a multiplicative noise both in the velocity and in the position. In the noise term, the second factor of the cross product is nothing but $\hat{\mathbf{n}}$ [see Eq.(2.1) setting $D_t = 0$] meaning that if the active force points towards x , then v_x evolves deterministically, since all the stochastic source due to the activity is concentrated in the evolution of v_y . In other words, the noise vector points every time in the orthogonal direction with respect to $\hat{\mathbf{n}}$. Nevertheless, the variance of the noise scales as $U_0^2 D_r$, being \mathbf{n} a vector with unitary modulus, as in the AOUP model. For such reasons, we remark that Eq.(2.7) shows interesting similarities with the equation of motion obtained for the AOUP dynamics, being very similar to Eq.(2.5) assuming the relations between the model parameters obtained in Chapter 1, i.e. $D_r = 1/\tau$ and $U_0^2 = 2D_a/\tau$. The only difference occurs in the noise term, which in the AOUP model is simply given by $U_0\sqrt{2D_r}\mathbf{w}$, where \mathbf{w} is a white noise vector whose components are independent, while in Eq.(2.7) a multiplicative noise with only one degree of freedom takes place in the dynamics. As already discussed in Chapter 1, ABP and AOUP cannot be mathematically equivalent. Nevertheless, the \mathbf{v} dynamics differs only for vanishing terms - the noise - in the small persistence regime.

2.2.2 Role of the thermal bath

The derivation of Eq.(2.5) or Eq.(2.7) requires the condition $D_t = 0$. If $D_t > 0$, we face up to a mathematical problem since the white noise is not differentiable. Nevertheless, could be interesting to understand how an additional thermal noise, due to the solvent, affects the dynamics of \mathbf{v} , i.e. in which way the change of variables can be generalized to the case $D_t > 0$, both for AOUP and ABP dynamics. This question has been fixed first time in [116] in the AOUP case. Let us consider at first the AOUP model. To avoid any mathematical difficulties, we define the new variable $\mathbf{v} = \dot{\mathbf{x}} - \sqrt{2D_t}\boldsymbol{\xi}$ instead of simply $\mathbf{v} = \dot{\mathbf{x}}$. By means of this trick, we can derive Eq.(2.1) expressed in terms of \mathbf{v} and, after simple algebraic manipulations, the contribution of the thermal bath appears in the dynamics of \mathbf{v} :

$$\dot{\mathbf{x}} = \mathbf{v} + \sqrt{2D_t}\boldsymbol{\xi} \quad (2.9)$$

$$\dot{\mathbf{v}} = -\frac{1}{\tau}\left[\boldsymbol{\Gamma} \cdot \mathbf{v} + \frac{\nabla U}{\gamma} - \sqrt{2D_a}\boldsymbol{\eta}\right] - \frac{\sqrt{2D_t}}{\gamma}\nabla(\nabla U \cdot \boldsymbol{\xi}) . \quad (2.10)$$

As in the case $D_t = 0$, the AOUP dynamics with $D_t > 0$ has been mapped onto the underdamped dynamics of a fictitious Brownian particle of position \mathbf{x} and velocity \mathbf{v} evolving with a space-dependent Stokes force. The new ingredient with respect to the case $D_t = 0$ shows up as two new sources of white noise acting additively on \mathbf{x} and multiplicatively on \mathbf{v} . The latter feature requires the Stratonovich interpretation of the stochastic differential

equation [117]. We remark that such an extra noisy contribution is given by the same vector for both the dynamics of \mathbf{x} and \mathbf{v} . In other words, the diffusive matrix in the space $\mathbf{x} \times \mathbf{v}$ has off diagonal components. Besides, the two contributions have opposite signs: for instance, if a fluctuation of the noise increases $\dot{\mathbf{x}}$ then the same fluctuation decreases $\dot{\mathbf{v}}$.

The same trick can be used with the ABP dynamics in the case $D_t > 0$ to derive an equation of motion for \mathbf{v} , generalizing Eq.(2.7) in the presence of a thermal bath. In particular, the dynamics turns into:

$$\dot{\mathbf{x}} = \mathbf{v} + \sqrt{2D_t}\boldsymbol{\xi} \quad (2.11)$$

$$\dot{\mathbf{v}}_i = -D_r\boldsymbol{\Gamma} \cdot \mathbf{v} + \frac{D_r}{\gamma}\mathbf{F} + U_0\sqrt{2D_r}\boldsymbol{\xi} \times \frac{(\gamma\mathbf{v} + \mathbf{F})}{U_0}. \quad (2.12)$$

As in the AOUP case, Eq.(2.12) has the same terms as Eq.(2.7) and the only difference stems from an additional noise whose amplitude is ruled by D_t . Such a term has the same form of the last addend in Eq.(3.7) for the AOUP model. Therefore, the presence of an additional thermal noise does not produce differences between the AOUP and ABP models.

2.2.3 The Unified Colored Noise Approximation

Eq.(2.5) presents numerous advantages with respect to Eq.(2.1) because of the evident connections with the equation of motion of a passive particle. For instance, leads to the possibility of finding a smart approximation for the marginal probability distribution function of the system, $p(\mathbf{x})$, i.e. the density. Such an approximation, known as Unified Colored Noise Approximation (UCNA), has been originally introduced by Hanngi et. al. in the context of electric fields with a correlated noise [117, 118] but the methodology has been adapted to interacting active particles systems in [75, 74]. We remark that UCNA regards exclusively the AOUP dynamics with $D_t = 0$ since an ABP counterpart for such a result is not known.

The UCNA-dynamics can be obtained by dropping the inertial term in Eq.(2.5), $\dot{\mathbf{v}} \approx 0$, or by performing the adiabatic elimination of the faster degree of freedom in the Smoluchowski equation associated to Eq.(2.5). Following one of this two procedures we get:

$$\dot{\mathbf{x}} = \boldsymbol{\Gamma}^{-1} \cdot \left[-\frac{\nabla\Psi}{\gamma} + \sqrt{2D_a}\boldsymbol{\eta} \right]. \quad (2.13)$$

where $\boldsymbol{\Gamma}^{-1}$ is the inverse of the $\boldsymbol{\Gamma}$ matrix, which involves the spatial derivatives of U . Because of the presence of a multiplicative noise for a general potential U , Eq.(2.13) has to be interpreted in the Stratanovich sense. We remark that the possibility of obtaining Eq.(2.13) is connected with the existence of $\boldsymbol{\Gamma}^{-1}$, which depends on the specific choice of U . In particular, in the limit of $\nu \lesssim 1$ - roughly when τ is small enough - the inverse of $\boldsymbol{\Gamma}$ exists for any choice of U . Instead, in the long persistent regime, $\nu \gtrsim 1$, we

need to assume the convexity of U to give consistence on the definition of $\mathbf{\Gamma}^{-1}$, avoiding that one or more eigevalues of $\mathbf{\Gamma}$ could be zero. Restricting to this case, we can derive and solve the Fokker Planck equation associated to Eq.(2.13) in the limit of vanishing current, obtaining

$$p_u(\mathbf{x}) \propto e^{-H_u(\mathbf{x})/\gamma D_a}, \quad (2.14)$$

$$H_u = U + \frac{\tau}{2\gamma} \sum_{\alpha} (\nabla_{\alpha} U)^2 - D_a \gamma \log |\det \mathbf{\Gamma}|. \quad (2.15)$$

The derivation of Eq.(2.14) is reviewed in Appendix 2.B and involves algebraic manipulations only. UCNA consists in an effective equilibrium approach which predicts the spatial distribution of the particles in terms of an effective potential, which involves the derivatives of U . In particular, the dynamics is ruled by an the effective Hamiltonian given by Eq.(2.15) which depends both on $\nabla_{\alpha} U$ and $\nabla_{\alpha} \nabla_{\beta} U$, by means of the determinant of $\mathbf{\Gamma}$. We remark that the shape of U could induce a change of sign in H_u for large τ/γ , at least for some positions. In this case, the approximation does not hold and further theoretical methods are needed.

The possibility of neglecting $\dot{\mathbf{v}}$ in Eq.(2.5), i.e. taking the overdamped limit, is equivalent to assume the Gaussianity of the conditional probability distribution, $p(\mathbf{v}|\mathbf{x})$, with a kinetic "effective temperature" which satisfies the Einstein relation. In practice, we can build an approximate solution of the Smoluchowski equation associated to Eq.(2.5) by simply assuming that integrating out \mathbf{v} we get $p_u(\mathbf{x})$. The approximate probability distribution reads:

$$p(\mathbf{x}, \mathbf{v}) = p(\mathbf{v}|\mathbf{x})p(\mathbf{x}) \approx p_u(\mathbf{v}|\mathbf{x})p_u(\mathbf{x}) \propto \exp\left(-\frac{\tau}{\gamma} \frac{\mathbf{v} \cdot \mathbf{\Gamma} \cdot \mathbf{v}}{2D_a}\right) p_u(\mathbf{x}), \quad (2.16)$$

where \propto means unless of the normalization of the exponential function which involves the determinant of $\mathbf{\Gamma}$. Eq.(2.16) shows that the different components of the velocity are not independent for a general potential U , and a non-trivial correlation matrix appears. We point out that Eq.(2.16) is not the exact solution of the Smoluchowski equation, but can be just considered as a useful approximation, whose validity will be the object of the next Sections. Without any difficulties, Eqs. (2.14) and (2.16) can be generalized to the case of interacting particles replacing U with a pair-wise repulsive potential. Again, the convexity of the interactions is needed, and, thus, Lennard Jones potential cannot be described in this way. Nevertheless, despite the apparent simplicity of the expression(2.16), it involves many-body interactions, which cannot be easily evaluated. In particular, $\mathbf{\Gamma}$ becomes a $d \times N$ matrix coupling the whole set of velocities, where N is the number of particles. This, the determinant of $\mathbf{\Gamma}$ cannot be easily calculated. For this reason, up to now, the UCNA approximation was not particularly useful to make quantitative predictions to improve the understanding of collective phenomena such as the motility induced phase separation, for instance.

Even though the UCNA is derived under the assumption of vanishing currents and thus restores the detailed balance principle, at least in some regimes it can be useful to explain many interesting aspects of the phenomenology of self-propelled particles, which will be evaluated in the next Sections. In particular, UCNA successfully predicts some important features of active particles, such as the clustering near an obstacle, the tendency of the particles to aggregate and the mobility reduction as the density increases. We will discuss this interesting point in the next Section, checking such approximations for different choices of the potential.

2.3 Self-propelled particles in harmonic traps

In this Section, we study a suspension of non-interacting self-propelled particles in two dimensions confined by means of a harmonic potential, $U(x) = k|\mathbf{x}|^2/2$, centered at the origin of the reference frame, for the sake of simplicity. The constant k represents the strength of the linear force which pushes the particle towards the minimum of the potential. The harmonic trap plays an important role in the literature of stochastic processes: it is the only case where we can find an explicit solution of the propagator - the time-dependent solution of the Fokker-Planck equation - in the well-known passive Brownian case [65]. Adapting Eq.(2.1) to the specific potential of this Section, the dynamics reads:

$$\gamma\dot{\mathbf{x}} = -k\mathbf{x} + \gamma\sqrt{2D_t}\boldsymbol{\eta} + \mathbf{f}^a, \quad (2.17)$$

where the active force, \mathbf{f}^a , evolves with Eq.(2.2) or Eq.(2.3) for the ABP or the AOUP self-propulsions, respectively.

Even if hydrodynamic or simply steric interactions between microswimmers may induce intriguing phenomena - such as the formation of a self-assembled fluid pump [91, 119] or clusters rotating around the trap center [120], respectively - we restrict to the simpler case where these effects are negligible. These assumptions are valid in real systems, mostly in the framework of artificial microswimmers [20].

2.3.1 AOUP dynamics

In the AOUP case, the dynamics - Eq.(2.17) and Eq.(2.3) - is a system of coupled linear stochastic differential equations. In the case $T = \gamma D_t > 0$, both variables are subjected to independent thermal noises, but the drift matrix is not diagonal at variance with the well-known passive case. This observation suggests that non-trivial correlation will occur between \mathbf{f}^a and \mathbf{x} . Nevertheless, the steady-state solution of Eq.(2.17) and Eq.(2.3) can be easily obtained [78] solving the corresponding Fokker-Planck equation for the probability distribution function, $f(\mathbf{x}, \mathbf{f}^a, t)$, which, for the sake of

completeness, we report below:

$$\frac{\partial}{\partial t} f = \nabla_{\mathbf{x}} \cdot \left(\frac{k}{\gamma} \mathbf{x} - \frac{\mathbf{f}^a}{\gamma} \right) f + \frac{T}{\gamma} \nabla_{\mathbf{x}}^2 f + \frac{1}{\tau} \nabla_{\mathbf{f}^a} \cdot \mathbf{f}^a f + \gamma^2 \frac{D_a}{\tau^2} \nabla_{\mathbf{f}^a}^2 f, \quad (2.18)$$

being the vectors $\nabla_{\mathbf{x}} = (\partial_x, \partial_y)$ and $\nabla_{\mathbf{f}^a} = (\partial_{f_x}, \partial_{f_y})$ and $\nabla_{\mathbf{f}^a}^2$ the Laplacian operator with respect to the components of \mathbf{f}^a . The linearity of the process in both variables, \mathbf{x} and \mathbf{f}^a , leads to an explicit solution of Eq.(2.18) in the stationary state, which reads:

$$f(\mathbf{x}, \mathbf{f}^a) = \mathcal{C} \exp \left(-\frac{k}{2} \frac{|\mathbf{x}|^2}{D_a} \frac{D_a \Gamma}{\gamma D_a + \Gamma T} \right) \times \exp \left(-\frac{\tau \Gamma}{2 D_a \gamma} \left| \mathbf{f}^a - \Gamma \frac{\gamma D_a}{\gamma D_a + T} k \mathbf{x} \right|^2 \right), \quad (2.19)$$

being \mathcal{C} a normalization constant, while $\Gamma = 1 + k\tau/\gamma$ is only a numerical factor which grows with τ . In this special case, the matrix $\mathbf{\Gamma}$ in Eq.(2.10) is proportional to the identity matrix, \mathcal{I} , through the constant Γ which appears in the distribution. The result is a multivariate Gaussian distribution with non-zero correlations between each component of \mathbf{x} and \mathbf{f}^a . In other words, a non-zero first moment of the spatial distribution appears, in such a way that $\langle \mathbf{x} \rangle \propto \mathbf{f}^a$, meaning that particles prefer to spend their life far from the minimum of the potential in a position determined by \mathbf{f}^a . Since the active force is a Ornstein-Uhlenbeck process, \mathbf{f}^a can explore large values depending on its variance, D_a/τ , even if the most probable value remains $\mathbf{f}^a = 0$. Instead, its persistence time, τ , rules how long the particle remains fixed in the position determined by the value of \mathbf{f}^a . We remark that the x -component of \mathbf{x} and \mathbf{f}^a are independent of their y -component since both the external force and the active dynamics are linear. We observe that in the equilibrium limit, $\tau \rightarrow 0$, Eq.(2.19) approaches to the Boltzmann distribution of the form $\exp(-|\mathbf{x}|^2/T_{eff})$, where the effective temperature T_{eff} is given by the sum of the diffusive contributions due to the active force and the thermal bath.

From Eq.(2.19), we can easily derive the space density, $p(\mathbf{x})$, by integrating out the active force degree of freedom. Following this scheme, we obtain a Gaussian distribution centered at $\mathbf{x} = 0$, which explicitly reads:

$$p(\mathbf{x}) = \mathcal{N} e^{-\frac{k(x^2+y^2)}{2\gamma} \frac{\Gamma}{D_a + \Gamma D_t}}, \quad (2.20)$$

being \mathcal{N} the normalization. Such a result is not so surprising: even if a particle roughly spends a time $\sim \tau$ with $\langle x \rangle \propto \mathbf{f}^a \neq 0$, the most probable value of \mathbf{f}^a is zero. We observe that in this case, the external harmonic potential affects the distribution modifying its variance or, in other words, its effective temperature [73]:

$$T_e = k \langle x^2 \rangle = k \langle y^2 \rangle = D_a \gamma \left(\frac{D_t}{D_a} + \frac{1}{1 + k\tau/\gamma} \right), \quad (2.21)$$

being $\langle x \rangle = \langle y \rangle = 0$. We remark that T_e is given by the sum of two contributions: the first one is due to the thermal bath and corresponds to the equilibrium temperature in the absence of active forces. Instead, the second one arises from the self-propulsion and contains explicitly a non-trivial dependence both on τ and k . Assuming that $D_t \ll D_a$ and the long persistent regime $\tau k/\gamma \gg 1$, we get:

$$T_e \approx \frac{D_a \gamma^2}{\tau k}. \quad (2.22)$$

Such a temperature is proportional to the variance of \mathbf{f}^a and to $1/k$. Noticing that $D_a \gamma$ is the effective temperature associated with a potential-free suspension of particles, we conclude that even in this simple case the effective temperature is potential-dependent [77].

2.3.2 ABP dynamics

In the case of the ABP active force, the solution of the Fokker-Planck equation associated to the system (2.17) and (2.2) is not known even in the simple case of a harmonic potential [78, 121, 122, 123, 124]. Indeed, even if the external force is linear, the dynamics of the self-propulsion involves a multiplicative noise in Cartesian components. Therefore, the distribution cannot be simply a multivariate Gaussian as in the AOUP dynamics and the numerical study of Eqs.(2.17) and (2.2) is needed.

In Fig. 2.1(a), we show the radial density, $\rho(r) = 2\pi r p(\mathbf{x})$, associated to Eq. (2.17) with the self-propulsion evolving by means of the ABP dynamics. As already mentioned, we can distinguish between i) the small persistence regime with $\nu = D_r \gamma/k \gtrsim 1$ and ii) the large persistence one $\nu = D_r \gamma/k \lesssim 1$. In the first case, the active force plays the role of effective temperature and the marginal probability distribution, $p(\mathbf{x})$, has a Gaussian shape in analogy with AOUP and passive particles. This is illustrated in the inset of Fig.2.1 (a), where the comparison between data and the Gaussian prediction are reported. In this regime, the growth of D_r decreasing only the effective temperature, $\gamma U_0^2/2D_r + T$, determining the variance of the distribution which still remains Gaussian. It is straightforward to check that in this regime of large D_r or small τ the variances of ABP and AOUP coincide - see Eq (2.21). ii) For $D_r \lesssim k/\gamma$, particles arrange on a circular crown: the region near the minimum of the harmonic trap becomes empty. The decrease of D_r enhances the accumulation of particles in the proximity of the typical radius $r^* \approx \gamma U_0/k$, as shown in Fig. 2.1(a). We outline that r^* corresponds to the radius at which the self-propulsion and the confining harmonic force balance each other. When T is small enough with respect to $\gamma U_0^2/D_r$, the distribution shows strongly non-gaussianity [78]. Its shape resembles a δ -Dirac function centered at $r - r^*$, at least in the limit $D_r \rightarrow 0$. At $T = 0$, the distribution $\rho(r)$ displays an asymmetric shape. The explanation easily comes from the following observation: particles cannot explore regions at $r > r^*$ because the modulus of the self-propulsion is fixed at U_0 . This

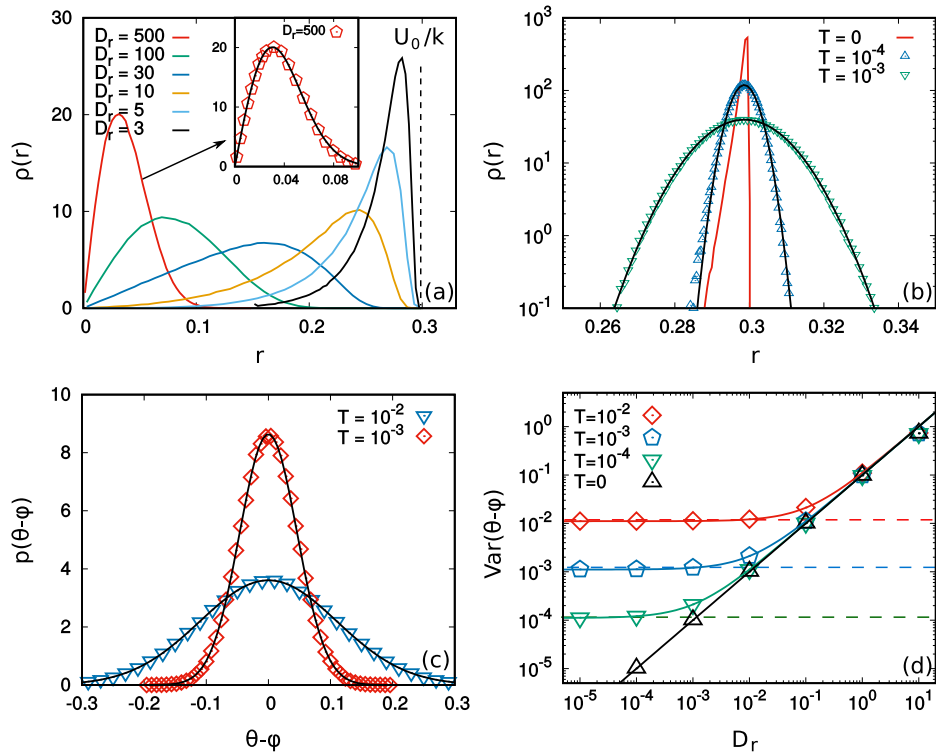


Figure 2.1: A single ABP particle in a harmonic trap. Panel (a): radial probability density $\rho(r)$ for different values of D_r . The inset shows a comparison between the Gaussian approximation with some effective temperature, Eq.(2.21), and numerical data for $D_r = 500$. Panel (b): $\rho(r)$ for $D_r = 0.3$ for three values of T : colored symbols from numerical simulations, black lines from Eq.(2.23). The red line is for $T = 0$. Panel (c): angular probability distribution functions, $g(\theta - \phi)$, for two different values of T (colored points) compared with Eq.(2.24) (black lines). Panel (d): Variances of $g(\theta - \phi)$ vs D_r for different values of T . Points are obtained by simulations while continuum lines correspond to the variances predicted by the distribution (2.23). The dashed lines indicate the limiting variances obtained for $D_r \rightarrow 0$. Other parameters: $k = 10$ and $U_0 = 3$.

effect could be produced only by thermal fluctuations, as we will see below. Besides, when $D_r \lesssim k/\gamma$ the orientational angles, θ , of the particles could be approximated by $\phi = \arctan(y/x)$, i.e. their angular coordinate with respect to the minimum of the potential. In particular, the angular probability distribution, $g(\theta - \phi)$, is a Gaussian which becomes narrow as D_r decreases [78]. In Fig.2.1(d) we study the variances of $g(\theta - \phi)$ in function of D_r , showing the occurrence of a linear scaling (black data). We remark that the angle θ evolves in time as a Wiener process and so the angular coordinate of the particle, due to Eq. (1.3). Each particle fluctuates around the angular coordinate $\phi \sim \theta_0$ until a time $\sim 1/D_r$, after which the value of θ could be consistently changed.

In Fig. 2.1 (b), (c) and (d), we illustrate the effect of the temperature T [78]. On one hand, thermal fluctuations lead the system to explore the space region $r > r^*$, symmetrizing the shape of $\rho(r)$. In this regime, $p(\mathbf{x})$ is well-approximated by a Gaussian centered at $|\mathbf{x}| = r^*$, and assumes the form:

$$\rho(r) \approx \mathcal{N}r \exp\left(-\frac{k}{2T}(r - r^*)^2\right). \quad (2.23)$$

This prediction is confirmed in Fig. 2.1(b). On the other hand, T does not change the Gaussian shape of $g(\theta - \phi)$ but its value affects the variance of the distribution. The variance does not depend on T when D_r is large enough, as we can see in Fig.2.1d). The decrease of D_r induces a deviation from the linear behavior until a T -dependent plateau is reached. In particular, the distribution $g(\theta - \phi)$ is approximated by a Gaussian of argument $\phi - \theta$:

$$g(\theta - \phi) \approx \mathcal{N} \exp\left(\frac{r^*}{2} \frac{\gamma U_0}{T + \gamma D_r (r^*)^2} (\phi - \theta)^2\right). \quad (2.24)$$

The variance of this distribution is in fair agreement with numerical results, as emerged in panel (d) of Fig.2.1. Eqs. (2.23) and (2.24) are derived in Appendix 2.C, where a suitable approximating solution of the Fokker-Planck equation in radial coordinates is calculated [78].

2.3.3 A comparison between the two models in the harmonic case

We conclude noting that in the presence of a harmonic potential, AOUP and ABP gives the same Gaussian result in the regime of small τ or equivalently large D_r , where an equilibrium picture in terms of an effective temperature roughly works. Instead, in the long persistence (and more interesting) regime large differences in the marginal distribution of $p(\mathbf{x})$ occurs, being a Gaussian centered in zero in the first case and approximatively a Gaussian centered at $r^* > 0$ in the second one. Therefore, in the ABP dynamics particles accumulate far from the minimum of the potential, while in the AOUP a Boltzmann distribution with some effective temperature is always recovered. Nevertheless, the single-particle dynamics reveals strong analogies: when a large value of $|\mathbf{f}^a|$ is extracted from its Gaussian distribution, then for a time $\sim \tau$ the accumulation far from the minimum of the potential appears.

In the AOUP case, the fluctuations of the particle position are roughly ruled by the variance given by Eq.(2.21) which scales as $\sim \gamma^2 D_a / \tau k + T$, in the regime of large τ . In this case, we can find a particle at $r > r^*$ with a finite probability, which is controlled by the strength of the active force in the regime of negligible T . A large value of D_a / τ not only increases the values of $\langle |\mathbf{f}^a| \rangle$ but also the probability of finding a particle far away from its most probable value. On the other hand, in the ABP case, fluctuations of the positions are mostly ruled by T , while $\gamma U_0 / k$ only determines the

maximal values of the radius of the ring where particles accumulate, without increasing the positional fluctuations. Only the fluctuation induced by T could lead a particle to explore radial distances, with respect to the center of its cluster, larger than $\gamma U_0/k$.

Anyway, even in the large persistence regime, the variance of the distribution scales in both case as the strength of the self-propulsion, being proportional to D_a/τ and U_0^2 for the AOUP and ABP dynamics, respectively.

2.4 Non-harmonic confining potentials

In this Section, we study a system of non-interacting particles in the presence of a non-harmonic single-well confining potential, which we assume to be convex, for the sake of simplicity. In particular, we focus our numerical study on power-potentials of the form $U(\mathbf{x}) \propto |\mathbf{x}|^{2n}/2n$, being n a positive number. We remark that the theoretical analysis performed in this Section are not restricted to such a choice of U , but is valid for every convex single-well potential. In Section 2.3, the harmonic shape of U has revealed some differences between AOUP and ABP models in the form the steady-state density. In this Section, we will show that such a discrepancy only arises from the linearity of the harmonic force, which represents a pathological case, and that for a more general confining potential the differences are marginal.

For the sake of simplicity, we neglect the thermal noise assuming that $D_t \ll D_a$. This assumption simplifies any theoretical treatment and is valid for several experimental systems. Thus, the dynamics of the active particle position reads:

$$\gamma \dot{\hat{\mathbf{x}}} = -k |\mathbf{x}|^{2n-1} \hat{\mathbf{x}} + \mathbf{f}^a \quad (2.25)$$

where $\hat{\mathbf{x}}$ is a unitary versor and k the strength of the non-linear confining force. As usual, the dynamics of \mathbf{f}^a is ruled by Eq.(2.3) and Eq.(2.2) for the AOUP and the ABP dynamics, respectively. The equilibrium-like regime for $\nu \lesssim 1$ is consistent with a Brownian-like picture and does not reveal any surprises: particles accumulate around the minimum of the potential, exploring an effective average volume determined just by the interplay between the external potential and the active force which acts roughly as a thermal bath. Indeed, the system has effective temperature γD_a , and no far-from-equilibrium physics is involved both for AOUP and ABP dynamics, which are fully consistent, as expected. In the non-equilibrium regime, namely $\nu \gtrsim 1$, the area close to the potential minimum empties and the system shows strong delocalization in favor of an annular region at an average distance r^* from the origin [77]. Such a phenomenology, which we call ‘‘accumulation far from the minimum of the potential’’ is common to both modelizations and only irrelevant differences could emerge. At large values of ν , r^* appears to saturate and a further increase of ν just produces

a dynamical effect, leading to a slowdown of the particles in the circular crown. This phenomenology reproduces the experimental result obtained in [110] for Janus particles inside an acoustic trap with negligible interactions. We remark that, at variance with the harmonic potential case, such a phenomenology is common both to the ABP and the AOUP dynamics. Therefore, the linear interaction has to be considered as a special case, an exception in the class of the single-well confining potential. Instead, in the non-linear case, ABP and AOUP models are fully consistent, showing the accumulation far from the minimum of the potential in the shape of the density.

In order to make analytical progress and to improve the physical understanding of the self-propelled dynamics in the presence of a convex but anharmonic potential, it is useful to consider the transformed dynamics, adapting Eq.(2.5) to the particular choice of the potential of this Section:

$$\dot{\mathbf{x}} = \mathbf{v} \quad (2.26a)$$

$$\dot{\mathbf{v}} = -\frac{1}{\tau}\mathbf{\Gamma} \cdot \mathbf{v} - \frac{k}{\gamma\tau}|\mathbf{x}|^{2n-1}\hat{\mathbf{x}} + \mathbf{k}, \quad (2.26b)$$

where we use Greek indices for indicating the d components of the particle coordinates and \mathbf{k} represents the noise term of Eq.(2.5) or Eq.(2.7) for the AOUP or ABP dynamics, respectively. The representation of the dynamics given by Eqs.(2.26) sheds light on the delocalization phenomenon observed above, which could be quite obscure looking only at the original dynamics (2.25). The radial delocalization phenomenon can be physically understood as follows: the effective damping coefficient, $\Gamma(\mathbf{x})/\tau$, is small near the minimum of the potential well and increases as \mathbf{x} departs from it. Indeed, for the potential considered in this Section we obtain:

$$\Gamma_{\alpha\beta} = \delta_{\alpha\beta} + \frac{\tau}{\gamma} [(2n-1)|\mathbf{x}|^{2n-2}\hat{x}_\alpha\hat{x}_\beta + \delta_{\alpha\beta}|\mathbf{x}|^{2n-2}]. \quad (2.27)$$

Therefore, particles with $|\mathbf{x}| \approx 0$ can attain large velocities, being their damping very small, and leave the region in a small time. Instead, particles with $|\mathbf{x}|$ large reduce their “effective speed”, \mathbf{v} , since the effective damping is large as the microswimmer is far from the minimum of the potential. As a limiting case, microswimmers at infinity are completely blocked. Anyway, this situation is prevented because of the confining force which pushes the microswimmer towards the origin. The complex interplay between these two effects is responsible of the particles accumulation on a circular crown with a typical radius $r^* > 0$. The peculiarity of the case $n = 1$ emerges since, in this case, the elements of $\mathbf{\Gamma}$ are constant with respect to \mathbf{x} . Therefore, we can always define an effective temperature as the ratio between the amplitude of the noise and the constant effective drag coefficient, whose elements are given by the constant elements of $\mathbf{\Gamma}$. In this case, the fluctuation-dissipation relations hold even if the effective temperature is affected by the shape of

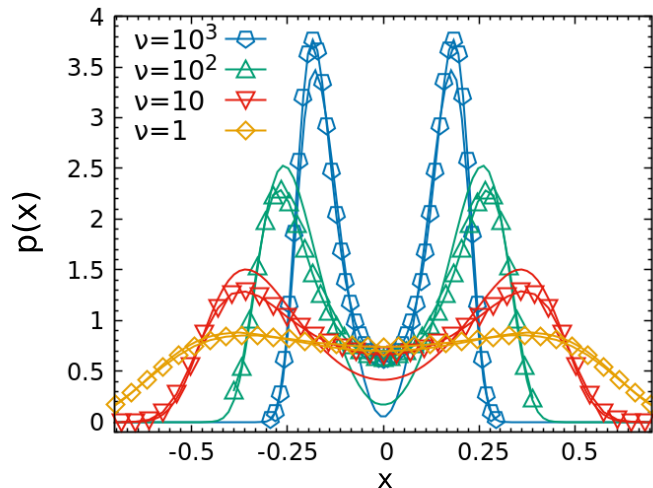


Figure 2.2: $p(x)$ computed from data (line+dot) and p_u (line), for different values of ν . The probabilities are calculated from a narrow section of the plane passing for the minimum of the potential placed at the origin of the reference frame. Parameters: $D_a = 1$, $k = 10/4$, $n = 2$.

U . Anyway, in the AOUP harmonic case, the simple form of the noise gives rise to the dynamics of an underdamped equilibrium particle, while, in the ABP harmonic case, the multiplicative nature of the noise is responsible for the non-Boltzmann phenomenology analyzed in the previous Section. For this reason, we restrict to the case $n \geq 2$ in what follows.

Besides, we check the validity of the unified colored noise approximation (UCNA) comparing the prediction given by Eq.(2.16) with the numerical probability distribution function obtained for a section of the annular region, namely the x -component [77]. In Fig. 2.3 (a), we show the comparison between the numerical probability density in space, $p(x)$, and $p_u(x)$, i.e. the density prediction of the UCNA approximation, given by Eq.(2.14). Remarkably, the effective potential H_u takes the shape of a double-well which fairly reproduces the numerical simulations. The comparison is optimal when $\tau \ll 1$, and gives fair quantitative information for the location of the density maxima also when $\tau \gg 1$. In particular, p_u correctly predicts the accumulation in some regions, depending on τ , but it underrates the probability of finding a particle in the bottom of the well, for large τ . This discrepancy is not surprising since UCNA is derived under the assumption of vanishing currents and thus restores the Detailed Balance principle, while in such a non-linear case currents cannot be zero.

2.5 AOUP dynamics in one dimension

An advantage of the AOUP model lies in the possibility of studying a one-dimensional suspension of particles, which is, instead, ill-defined following

the ABP dynamics. Such a choice is particularly useful in order to understand some basic features of self-propelled particles such as the non-trivial correlation between position and velocity, the breaking of the detailed balance and the occurrence of a non-Boltzmann distribution [101, 102, 113, 77]. The dimensional reduction is also convenient with the aim of studying a classical problem in the framework of stochastic processes: the escape from a double-well potential, also known as Kramers problem, which will be the object of the last subsection of this chapter.

For the sake of completeness, we rewrite the dynamics in one dimension. In particular, Eqs.(2.1) and (2.3) assumes the simple form:

$$\gamma \dot{x} = F(x) + f^a + \gamma \sqrt{2D_t} \xi \quad (2.28a)$$

$$\tau \dot{f}^a = -f^a + \gamma \sqrt{2D_a} \eta. \quad (2.28b)$$

We fix the ratio D_a/τ , in order to keep constant the average modulus of the self-propulsion velocity of a single particle $\sqrt{\langle (f^a)^2 \rangle} \propto \sqrt{D_a/\tau}$. Besides, we consider the limit of strong self-propulsion and consequently we neglect the contribution due to thermal fluctuations, represented by the last term of Eq. (2.28a). Such a choice is supported by experimental studies performed by bacterial colonies, where D_a can be much larger than D_t . For instance, the coefficient D_a of typical living bacteria in pure water is about $\sim 100 \mu\text{m}^2/\text{s}$, while the diffusion coefficient of dead bacteria is approximately $\approx 0.3 \mu\text{m}^2/\text{s}$. In many cases, the diffusion due to the thermal agitation of the solvent is estimated to be at least ten times smaller than the one due to the self-propulsion [125]. $F(x) = -U'(x)$ represents the deterministic force due to the external potential, U , and the prime denotes the spatial derivative. In addition, we restrict our study to the case $\nu \geq O(1)$, to study a far from equilibrium regime.

In the one-dimensional case, the transformed dynamics, Eq.(2.4) and (2.5), are particularly useful and explicitly reads:

$$\dot{x} = v \quad (2.29)$$

$$\dot{v} = -\frac{\Gamma(x)}{\tau} v + \frac{F(x)}{\tau\gamma} + \frac{\sqrt{2D_a}}{\tau} \eta. \quad (2.30)$$

where we have considered the case $D_t = 0$. The simultaneous action of deterministic and active forces produces a space-dependent frictional force $-\gamma v \Gamma(x)/\tau$ [74]. The coefficient Γ is given by

$$\Gamma(x) = 1 + \frac{\tau}{\gamma} U''(x), \quad (2.31)$$

where the double prime denotes the second spatial derivative. The statistical properties of the system are described by the probability distribution $p(x, v, t)$ which obeys the following Kramers-Fokker-Planck equation:

$$\frac{\partial p}{\partial t} + v \frac{\partial p}{\partial x} + \frac{F(x)}{\tau\gamma} \frac{\partial p}{\partial v} = \frac{\partial}{\partial v} \left(\frac{D_a}{\tau} \frac{\partial}{\partial v} + \Gamma(x)v \right) \frac{p}{\tau} \quad (2.32)$$

In spite of the restriction to one-dimension, the dynamics described by the stochastic equations (2.29) and (2.30) (or equivalently by Eq. (3.9)) are not easy to solve even in the steady state. Up to now, the only known analytical result in the presence of the general potential $U(x)$ has been obtained looking for a solution in the basis of Hermite polynomials, performing an expansion in power of $\sqrt{\tau}$. Thus, such a result applies only when $\nu \ll 1$ [101, 102] being a near-equilibrium solution. Such an expansion cannot capture the main phenomenology of self-propelled particles occurring for $\nu \gg 1$, a regime where analytical predictions are not known.

2.5.1 UCNA solution for one-dimensional systems

Adapting Eq.(2.16) to a one-dimensional system, we get the one-dimensional version of the UCNA approximation in the (x, v) space [113], which approximate the steady state solution of Eq. (3.9). This procedure reads the simple form:

$$p(x, v) \approx \rho_{ucna}(x) \sqrt{\frac{\tau\gamma}{2\pi\theta(x)}} \exp\left(-\frac{\tau\gamma v^2}{2\theta(x)}\right) \quad (2.33)$$

where we have

$$\rho_{ucna}(x) \propto \exp\left(-\frac{H(x)}{D_a\gamma}\right). \quad (2.34)$$

The function $H(x)$ is the effective configurational Hamiltonian, given by:

$$H(x) = U(x) + \frac{\tau}{\gamma} U'(x)^2 - \gamma D_a \ln\left(1 + \frac{\tau}{\gamma} U''(x)\right). \quad (2.35)$$

In Eq.(2.33) we have introduced the the local kinetic temperature [102]

$$\theta(x) = \frac{D_a\gamma}{1 + \frac{\tau}{\gamma} U''(x)}, \quad (2.36)$$

which coincides with the ratio between the amplitude of the effective thermal noise due to the active force, D_a/τ^2 , and the space-dependent damping Γ/τ of Eq.(2.30). Thus, $\theta(x)$ depends on the space through the potential, breaking the details balance condition and producing irreversible currents coupling positions and velocities. Hereafter, the symbol $\langle v^n(x) \rangle$ will indicate the conditional average of the observable v^n , obtained at fixed x , formally $\langle v^n|x \rangle$. We observe that the local variance of the velocity distribution $\langle v^2(x) \rangle$ is approximated by the following formula, according to the UCNA approximation:

$$\langle v^2(x) \rangle \approx \frac{\theta(x)}{\tau\gamma} = \frac{\frac{D_a}{\tau}}{1 + \frac{\tau}{\gamma} U''(x)}. \quad (2.37)$$

We remark that $\theta(x)$ is determined by the shape of the potential, by means of its second derivative, meaning that is constant respect to x only for linear and quadratic potentials [102].

For $\nu \gtrsim 1$ (or equivalently $\tau \gg 1$), there are no reasons to consider the UCNA distribution as a good approximation of $p(x, v)$, except for quadratic potentials for which it is even exact. Anyway, we anticipate that for general potentials the UCNA solution can locally reproduce or not the whole probability distribution depending on the space region considered. This fact allows us to classify the space as follows: regions where approximation (2.33) works, which we name "equilibrium-like regions" (ER), and the remaining "non-equilibrium regions" (NER) where the approximation breaks down [77]. Since UCNA is an equilibrium-like approximation, obtained assuming a sort of local detailed balance principle, we guess that in the ER particles are almost in local equilibrium at variance with the NER where particles are far from this condition. We will turn on this matter in Sec.4.3 of Chapter4 where we study the heat-rate of the system in the framework of stochastic thermodynamics for several potentials to check this intuition.

2.5.2 Non-harmonic convex potentials

To fix the ideas, we consider the same shape of the potential already used in Sec.2.4 adapted to the one-dimensional case: $U \propto x^{2n}$, with $n > 1$. Now, the system displays two symmetric accumulation regions at $x \approx \pm r_m$ in such a way that the density profile displays a bimodal distribution. The system behaves as if an effective double-well potential controlled the dynamics, whose shape is approximatively predicted by means of the effective Hamiltonian (2.35) of the UCNA solution. In panel (b) of Fig.2.3, we observe that the positions of the two peaks of $p(x)$ correspond to the two minima of the conditional average of the single-particle energy:

$$\langle e(x) \rangle = \gamma\tau \langle v^2(x) \rangle_x + U(x), \quad (2.38)$$

written as the sum of the local kinetic energy and the potential energy, separately reported in panel (b) of Fig.2.3. The possibility of reducing the accumulation problem to an energy minimization even for far equilibrium particles is quite suggestive [77] and constitutes an interesting research line for future works.

In panel (a) of Fig. 2.3, we numerically compare the temperature $\theta(x)$, predicted by the UCNA approximation with the second moment of the distribution, $\gamma\tau \langle v^2 \rangle_x$, for different values of τ ranging from 10^{-4} to 10. Around the minimum of the potential, a clear discrepancy manifests which becomes more pronounced as τ increases. In particular, in that space region $\theta(x) \gtrsim \gamma\tau \langle v^2 \rangle_x$. Moving far from the origin of the reference frame, towards $\pm r_m$, both observables decrease roughly approaching to the same value, $\gamma\tau \langle v^2 \rangle_x \sim \theta(x)$. We observe that in these accumulation regions, i.e. where density assumes the higher values, the system is very cold with respect to the central region [77]. This fact is in agreement with our interpretation of the phenomenon in term of a space-dependent Stokes force taking place in the dynamics. The local validity of Eq.(2.37) suggests that the Detailed

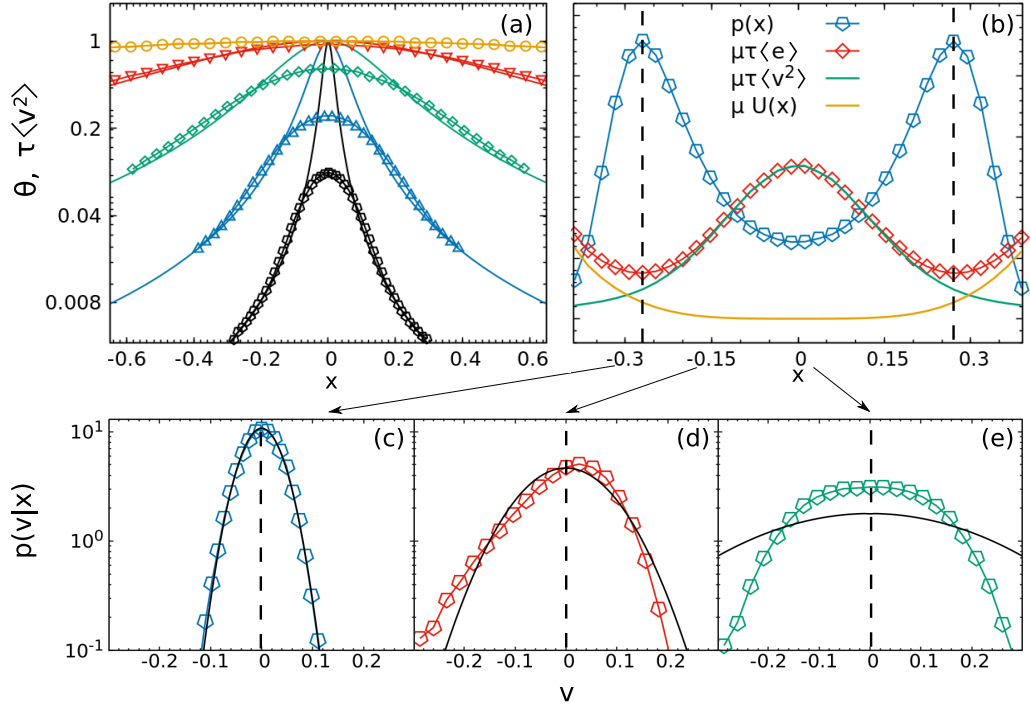


Figure 2.3: Panel (a): comparison between $\theta(x)$, calculated from Eq.(2.37), and $\tau\langle v^2 \rangle_x$ computed from numerical simulations for different values of $\tau = 10^{-3}$ (yellow), 10^{-2} (red), 10^{-1} (green), 1 (blue), 10 (black). Panel (b) is obtained with $\tau = 10$. We plot $p(x)$ (blue points), the energy $\langle e \rangle_x = \tau\langle v^2 \rangle_x + U(x)$ (red points), $\langle v^2 \rangle_x$ (green line) and $U(x)$ (orange line). Two vertical black lines are drawn at $x = x_m$, corresponding to the most probable position. Panels (c)-(d) display the conditional probability distribution, $p(v|x)$, for three different positions, $x = -0.3, -0.15, 0$, from left to right. The black line in each graph are the equilibrium prediction obtained by Eq.(2.33). Parameters: $D_a = 1$, $\tau = 10$, $k = 10/4$, $n = 2$.

Balance is locally satisfied in the two symmetric accumulation regions even if globally it is not. Indeed, the UCNA approximation is derived assuming zero currents. Thus, the two accumulation regions are identified as the ER, where particles are almost in equilibrium with the thermal bath, while the central region corresponds to the NER, i.e. the region strongly far from equilibrium, responsible for the global violation of the detailed balance principle. In order to confirm our intuition, we plot $p(v|x)$, for three different values of x in panels (c), (d) and (e) of Fig. 2.3 which refer to the same configuration reported in the panel (b) of the same figure. Panel (c) shows the $p(v|x)$ for a typical position within the ER, where the Gaussian prediction (2.33) at temperature $\theta(x)$ is fairly confirmed, as revealed by the comparison with the black curve. Instead, Panels (d) and (e) are obtained for two positions in the NER and show that $p(v|x)$ becomes an asymmetric function with a skewed tail going towards the origin [77]. The symmetrization is again reached in

$x = 0$, where the non-Gaussianity is still clear.

Such conclusions are not restricted to the particular choice of the external force employed in this study. We remark that the only requirement to obtain such a phenomenology lies in the convexity of the confining potential.

2.6 The double-well potential

As discussed in Sec.2.2.3, UCNA can be applied under some conditions on the external potential, such as the positivity of its Hessian. For a one-dimensional system, this is equivalent to require to deal with a convex potential, i.e. with positive second derivative. Indeed, when this condition is not fulfilled, the UCNA distribution is not normalizable since $\theta(x)$ becomes negative in some regions for τ large enough. The break down of UCNA opens the problem to estimate the space density in these cases, for which no approximations are known. In this Section, we study Eqs.(2.29)-(2.30) with a non-convex potential, $U(x)$, to understand what happens in the space regions where θ is negative. To evaluate non-equilibrium phenomena we consider the large persistence regime. The present study follows [104] where the AOUP dynamics has been employed. We, also, mention two later studies: the first employs the AOUP dynamics [126] and the second uses a path-integral approach in the framework of ABP dynamics [127] aimed to predict the escape time in the presence of additional thermal noise.

Here, for the sake of simplicity, we focus on a double-well shape with two symmetric minima and a maximum placed at the origin of the reference frame. In continuity with the well-studied literature of passive Brownian particles, we choose the following potential:

$$U(x) = b\frac{x^4}{4} - a\frac{x^2}{2}, \quad (2.39)$$

where a and b are the two constants determining the height of the barrier and the positions of its minima. The escape problem in a bistable potential has received large attention in the passive Brownian literature [128], being very important in physics and also chemical applications, such as chemical reactions. The stationary escape rate has been successfully predicted by Kramers [129], at least in the high friction or low-temperature regime, where the spatial diffusion dominates the motion.

In the passive case, the escape mechanism from a well to the other is clear: the particle crosses the barrier with a mean time given by Kramers formula [130]. The analog problem has been recently studied for active particles following the AOUP dynamics. In particular, the authors of [131] proposed to generalize the Kramers formula. This approach works only in the near-equilibrium regime ($\nu \ll 1$) and is somehow related to the validity of the UCNA approximation. Indeed, the authors found an escape rate in terms of an effective potential which resembles the one of Eq.(2.35).

In contrast with [131], we consider a far from equilibrium regime with $\nu \gtrsim 1$, for which a Kramers' approximation does not work due to the presence of very large currents. From Eq. (3.9), we expect that the space-dependent matrix $\Gamma(x)$ plays an important role in the dynamics for $\nu \gtrsim 1$ which coexists with the phenomenology determined by the two stable minima of the potential. Indeed, a non-convex shape of U (for instance, (2.39)), leads the factor $\Gamma(x)$, defined in Eq. (2.31), to become negative around the maxima of U when $U''(x) < -\gamma/\tau$. In this case, $\Gamma(x)$ cannot be considered a friction anymore but produces an acceleration. In other words, $\Gamma(x)$ is not a damping force but its inverse can be simply interpreted as negative mobility. Besides, the negative sign of $\theta(x)$ around the maximum of U is quite suggestive and seems to be related to the existence of local negative temperatures. This allows us to dub Negative Temperatures Regions (NTR), the space where $\Gamma(x) < 0$. These observations will have interesting physical consequences on the dynamics.

We call τ_c the critical value of τ , such that the constant $\Gamma(x)$ is globally positive for $\tau \leq \tau_c$, which depends on the properties of the potential only:

$$\tau_c = -\min_x \left(\frac{\gamma}{U''(x)} \right). \quad (2.40)$$

For the specific potential choice (2.39), we simply obtain $\tau_c = \frac{\gamma}{b}$, and a sort of bifurcation depending on τ occurs: i) when $\tau < \tau_c$, the value of $\theta(x)$ is positive for all positions. ii) when $\tau \geq \tau_c$, the effective temperature becomes locally negative in the regions near the maximum of U . The size of such a region can be determined by the solutions of Eq. (2.40), replacing τ_c with a fixed value of τ and reads

$$|x_N| = U''^{-1}\left(-\frac{\gamma}{\tau}\right), \quad (2.41)$$

where $\pm x_N$ are the points such that $\Gamma(\pm x_N) = 0$ and U''^{-1} is the inverse function of the second derivative of the potential. The increase of τ enlarges the size of the NTR, until x_N reaches a saturation value, which is given by

$$\lim_{\tau \rightarrow \infty} |x_N| = \lim_{\tau \rightarrow \infty} \sqrt{\frac{b}{3a} \left(1 - \frac{\gamma}{\tau b}\right)} = \sqrt{\frac{b}{3a}}, \quad (2.42)$$

for the potential (2.39). We observe that for $\tau \rightarrow \infty$ the value of x_N is given by the points such that $U''(x) = 0$, i.e. the binodal line.

To justify the nomenclature NTR, we mention that even in equilibrium statistical mechanics negative temperatures are not forbidden. In particular, some Hamiltonian models, such as systems of heavy rotators immersed in a bath of light rotators [114, 132], shows absolute negative temperatures. The probability distribution has the well-known Maxwell-Boltzmann shape with a negative coefficient. In these cases, the occurrence of NT is a consequence of the functional form of the kinetic energy, chosen as a periodic function

of the momenta instead of the usual quadratic form. This feature does not prevent the derivation of a Langevin equation for the momenta of the heavy particles, the slow variables of the dynamics. The authors of [133] show that the only difference from the well-known Brownian case lies in the form of the Stokes force, due to the modification of the kinetic energy. In particular, such a force changes sign as occurs locally for a system of self-propelled particles in a double-well potential.

2.6.1 Regions with local negative temperature

Hereafter, we perform a numerical study of Eqs.(2.29) and (2.30) to unveil the active escaping mechanism from a double-well potential. In the top panel of Fig. 2.4, the space density, $\rho(x)$, is reported. The shape of $\rho(x)$ seems to resemble the spatial distribution of a passive Brownian suspension of particles: $\rho(x)$ displays two symmetric peaks. The main difference lies in the positions of such peaks, which are shifted with respect to the positions of the potential minima. We estimate these shifts balancing the self-propulsion, f^a , and the deterministic force, $F(x)$, approximating the former by the average value of its modulus $\sim \pm\gamma\sqrt{D_a/\tau}$, where the minus and the plus sign have to be chosen for particles in the right and the left well, respectively. We remark that such an approximation of f^a works only in the large persistence regime for large values of ν . Instead, where the persistence is small ($\nu \ll 1$), f^a does not contribute to the balance of the forces, behaving like white noise, and the peaks are placed at the minima of U . Using the potential shape (2.39) in the force balance argument, we get the new positions of the peaks as the real solution of:

$$-ax^3 + bx = \gamma\sqrt{\frac{D_a}{\tau}}[\theta(-x) - \theta(x)], \quad (2.43)$$

being $\theta(x)$ the Heaviside step function. To get the correct shifts we need to take the negative root for $x < 0$ and the positive one for > 0 . With this choice, we roughly reproduce the positions of the leading peaks of $\rho(x)$. As predicted by Eq. (2.43), we observe that the distance between the two peaks increases with D_a/τ , i.e. when the average value of the active force modulus enlarges.

The frequency of the jumps from a well to the other is controlled by D_a/τ , since this ratio is proportional to the average value of the modulus of the self-propulsion: decreasing the ratio D_a/τ with respect to the height of the barrier the jumps becomes rarer events. To observe frequent jumps, we need to impose that $\gamma\sqrt{D_a/\tau}$, in such a way that the mean amplitude of the self-propulsion, exceeds the maximum of $F(x)$.

The peculiarities of an active system do not emerge from the study of the density, whose differences from a passive Brownian suspension of particles are not so surprising. Instead, the study of the conditional probability distribution of the velocity, $p(v|x)$, reveals an interesting phenomenology which

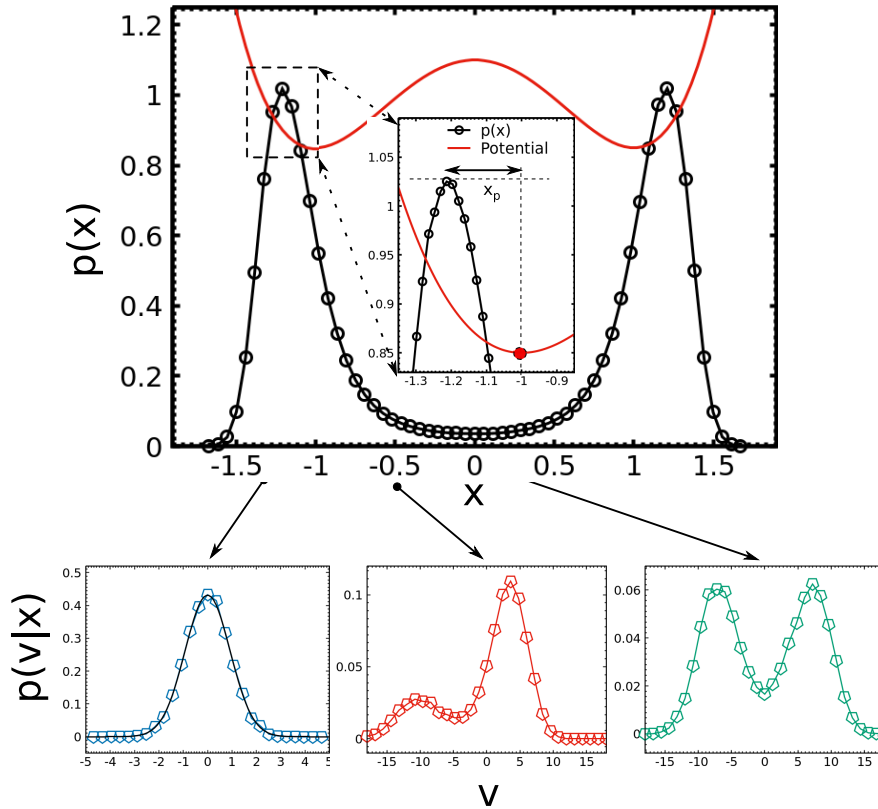


Figure 2.4: Upper panel: The marginal distribution $\rho(x)$ (black data) obtained from the numerical data and the double well potential (the red curve, rescaled for presentation reasons) for the parameter choice $a = b = 10$ and. In the inset, we zoom the distribution near its left maximum. The variance of the self-propulsion force is $D_a/\tau = 10^2$ and $\tau = 10$. Notice that the positions of the peaks of the density $\rho(x)$ are slightly shifted with respect to the minima of the double well potential (2.39) and correspond fairly well to the roots of (2.43). Lower panel: we display the conditional velocity distribution, $p(v|x)$, for three different positions, $x = -1.2, -0.5, 0$. from the left to the right, respectively. In the vicinity of the two peaks of $\rho(x)$ at $x = \pm 1.2$ the distribution is unimodal $p(v|x)$. At $x = \pm 0.5$ a lateral shoulder appears as a clear indication of the onset of bimodality in the velocity distribution. Finally, at the symmetric point $x = 0$ the bimodality of $p(v|x)$ is fully developed and the particles form two distinguishable populations: one of particles propagating towards the right and the other towards the left.

has not a Brownian counterpart. In the bottom panels of Fig. 2.4, we plot $p(v|x)$ for three different typical positions, x : at the peak of $\rho(x)$ (bottom left panel), at the origin where the potential is maximum (bottom right panel) and at the intermediate point between them (bottom middle panel). In the bottom left panel of Fig. 2.4, $p(v|x)$ displays a single peak and reveals a fair agreement with the distribution predicted by Eq. (2.33) (see the comparison between data and black line). In this case, the local kinetic temperature is

well-approximated by $\theta(x)$, given by (2.37), a signal that the UCNA approximation works. Interestingly, the ER exists also for non-convex potentials and, again, they coincide with the accumulation regions where the density is higher. Moving towards the origin of the reference frame, a strong discrepancy between the form of $p(x, v)$ and the UCNA prediction clearly occurs, as illustrated in panels (d) and (e) of Fig.2.4. These zones correspond to the NER which coincide with a region near the maximum of U . We also observe that the NTR defined above is strictly contained in the NER. These regions reveal an intriguing scenario since $p(v|x)$ becomes a bimodal distribution: in the bottom middle panel of Fig. 2.4, the main peak of $p(v|x)$ is shifted towards a positive value of v instead of being placed at $v = 0$. Besides, a second lower peak placed at $v \approx 5$ emerges. increasing the value of x up to the maximum of the potential, the second peak of $p(v|x)$ moves towards lower values of v while the leading one shifts to smaller v . In addition, the relative height of the former peak increases, until the symmetry $x \rightarrow -x$ is restored in the origin. In this point, the two peaks have the same weight and are placed at the same distance as shown in the bottom right panel of Fig. 2.4. Such a bimodality of the functional form of the velocity probability distribution displays strong analogies with systems displaying absolute negative temperature.

In Fig. 2.5, we report two snapshot configurations in the plane (x, v) obtained with a large number of independent particles. Left and right panels are realized with two different values of $\tau = 1, 10$, respectively. The ration D_a/τ is kept fixed at the value 10^2 to deal with a self-propulsion with the same strengths. Both snapshots confirm the previous observations shedding

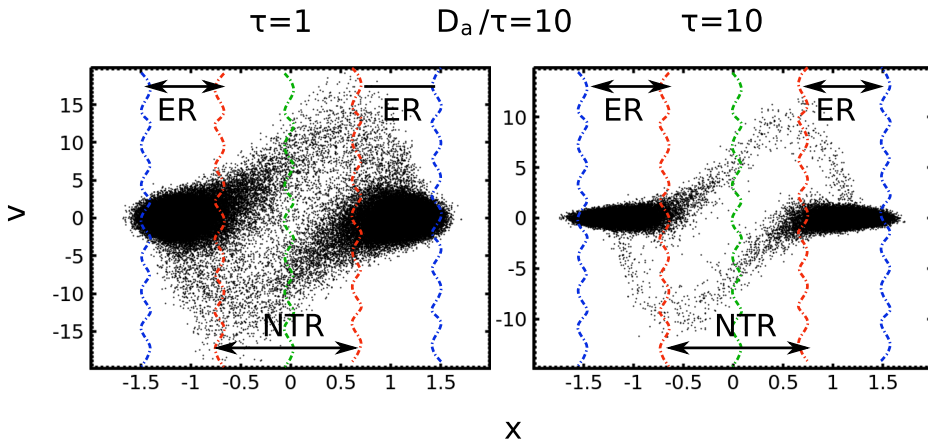


Figure 2.5: We show the snapshots representing the phase-points in the (x, v) -plane for two different choices of the persistence time τ : left panel $\tau = 1$ and right panel $\tau = 10$. The remaining parameters are $D_a/\tau = 10^2$ and $a = b = 10$. Each point represents the state of one system at a given instant. We simulated a collection of $N = 10^3$ particles. The vertical dashed curves are only a guide to the eye.

light on the phenomenology already emerged from the study of $p(v|x)$: each particle spends most of its life in the ER and rarely visits the NER to overcome the potential barrier. Anyway, the escape displays large differences from the well-known passive dynamics. When the particle enters in the NTR (so inside the NER), it accelerates towards the opposite well because of the effective negative mobility ($1/\Gamma(x) < 0$). So, the particle rapidly crosses the NTR reaching the opposite well, where $\Gamma(x)$ assumes positive values, the motion becomes damped again and the local distribution of the velocity turns to be a Gaussian. In particular, in both panels particles form two symmetric lanes in the middle region, one in the upper half-plane and the other in lower half-plane consistently with the bimodality of the distribution shown in panels (d) and (e) of Fig.2.4. The increase of τ produces thinner lanes as clearly emerged by the comparison between the left and right panel of Fig.2.5, and, also, induces a stronger selection mechanism of the escaping particles: in other words, the fraction of particles able to overcome the potential barrier decreases.

To provide an explicit confirmation of the proposed escaping mechanism, we report the values of $x(t)$ (bottom panels of Fig.2.6) and $v(t)$ (top panels of Fig.2.6) for a single particle trajectory. Left panels are obtained setting $\tau = 1$ while the right panels are realized with $\tau = 10$. In both cases, when the escape events occur, the velocity of the particle increases exponentially. Such a scenario has not a Brownian counterpart and is peculiar of active dynamics. At the crossing barrier time, $v(t)$ displays a pronounced spike, with height larger than the values obtainable through equilibrium-like fluctuations, predicted by the UCNA distribution. In the inset of Fig. 2.6 we enlarge a velocity peak in correspondence of an escape event. Its clean shape means that the trajectory is almost deterministic and not particularly influenced by the random force taking place in the dynamics.

Summarizing, we have found the existence of ER and NER, even for non-convex potentials. When an escape event occurs, the particle leaves the ER crossing rapidly the NTR where its velocity grows exponentially until to reach almost deterministically the opposite well, where the velocity is again depressed by the strong Stokes force of the ER. This feed-back mechanism explains why the average velocity does not increase indefinitely.

2.6.2 Analysis of the Negative Temperature Region

A self-propelled particle spends most of its life in the regions near the two minima of the potential, where the $U(x)$ is convex. In these regions, the UCNA prediction works also in the far equilibrium regime, as revealed by the numerical study of the probability distribution functions performed in the previous Section. Nevertheless, this approximation does not work uniformly in space as emerged by the form of $p(v|x)$ far from the minima of the potential. In the present Section, we develop theoretical tools alternative to the UCNA prediction to explain the rich phenomenology presented above in

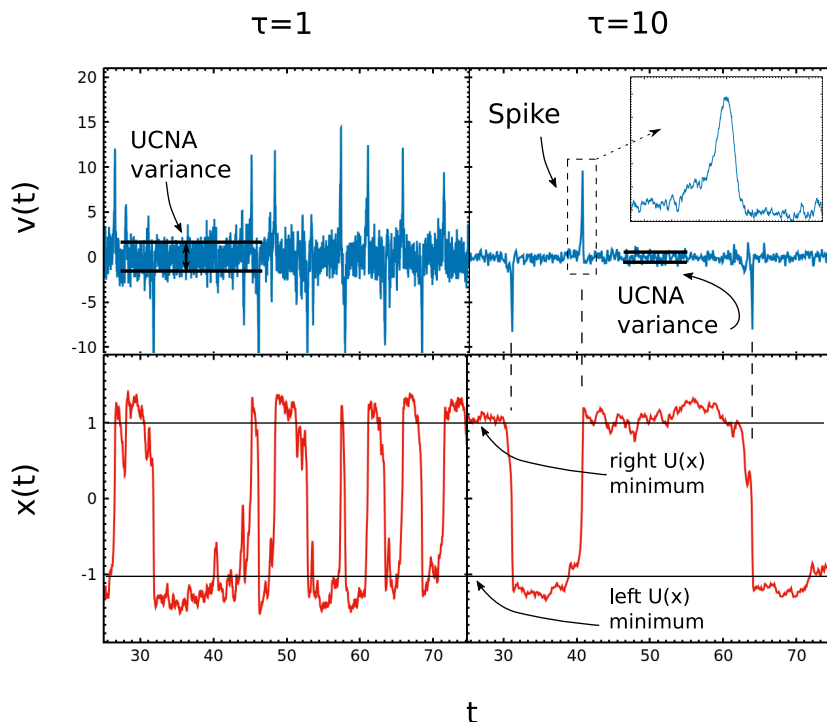


Figure 2.6: In the upper left and right panel we show the evolution of the position, $x(t)$ for $\tau = 1$ and $\tau = 10$, respectively. In the lower panels, we display the corresponding velocities. The values of the remaining parameters are: $D_a/\tau = 10^2$ and $a = b = 10$.

the negative temperature region $(-x_N, x_N)$, i.e. where $\Gamma(x) < 0$.

We propose a description of this unstable region based on the study of the slow variables taking place in the dynamics, which are at least the conditional average velocity, $\langle v(x) \rangle$, and the conditional velocity variance, $\langle v^2(x) \rangle$, thus, both obtained at fixed x . The idea is to find the effective equations which rule the dynamics of such observables. The function $\langle v(x) \rangle$ vanishes for every position in the steady-state, even if the phase-space snapshots of Fig.?? have revealed that we can separate the dynamics in two symmetric lanes. This suggests studying separately the population of particles going from the right well to the left one from those moving in the opposite direction.

To distinguish between the two populations we define $p_+(x, v)$ and $p_-(x, v)$ as the unnormalized probability distribution function of the particles whose dynamics starts from the left and the right well, respectively. In particular, p_{\pm} is computed counting the particles in the two lanes as shown in Fig. 2.5 and normalizing them by means of the total number of particles. We observe that the sum over the two populations reads the whole distribution:

$$p(x, v) = p_+(x, v) + p_-(x, v). \quad (2.44)$$

We note that in the left ER, $p_+(x) \rightarrow p_U(x)$ and $p_- \rightarrow 0$, and viceversa in the right ER. In the present Section, we will investigate the form of p_{\pm}

within the NTR region. Also, we introduce the first conditional velocity moment with respect to $p_{\pm}(x, v)$ as:

$$\langle v(x) \rangle_{\pm} = \frac{\int p_{\pm}(x, v) v dv}{\int p_{\pm}(x, v) dv}. \quad (2.45)$$

Taking the average with respect to $p_{\pm}(x, v) / \int dv p_{\pm}(x, v)$ in the v -dynamics given by Eq. (2.30), we get

$$\frac{d}{dt} \langle v(x) \rangle_{\pm} = -\frac{1}{\tau} \left(1 + \frac{\tau}{\gamma} U''(x) \right) \langle v(x) \rangle_{\pm} - \frac{U'(x)}{\gamma\tau}. \quad (2.46)$$

The top-right panel of Fig. 2.6 suggests that $\langle v(x) \rangle_{\pm}$ in the NTR increases (or decreases) exponentially in time before collapsing to zero again. In what follows, we restrict to the regime $\gamma\tau \gg 1$, which allows us to neglect the last term in the right-hand side of the Eq. (2.46). We outline that this condition guarantees that we are considering the most interesting regime which is strongly far from equilibrium. In the integration of Eq.(2.46) we take into account that $\langle v(x) \rangle_{\pm}$ depends both on x and t in such a way that the operator d/dt corresponds to the total derivative:

$$d/dt = \partial_t + v\partial_x \approx \partial_t + \langle v(x) \rangle_{\pm} \partial_x. \quad (2.47)$$

Performing the integration of Eq. (2.46), we get:

$$\langle v(x) \rangle_{\pm} = \langle v(x_0) \rangle_{\pm} - \frac{U'(x)}{\gamma} + \frac{U'(x_0)}{\gamma} + O\left(\frac{1}{\tau}\right) \quad (2.48)$$

where x_0 is the lower limit of the integration given by $-x_N$ and x_N if the particle starts from the left and right well, respectively. We point out that Eq.(2.48) states the conservation of the average active force, because of the relation

$$\langle f_a(x_{\pm}) \rangle = \gamma \langle v(x) \rangle_{\pm} + U'(x) = \pm const, \quad (2.49)$$

for $x \in (-x_N, x_N)$. The particles able to enter in the NTR are those with self-propulsion f_a large enough to reach the point x_0 . Due to the large value of τ the self-propulsion remains almost constant during all the escape event.

Now, let us focus on the dynamics of $\langle v^2(x) \rangle_{\pm}$. Multiplying Eq. (2.30) by v , applying the rules of Ito calculus [65] we have:

$$v dv = -\frac{\Gamma(x)}{\tau} v^2 dt + v \frac{\sqrt{2D_a}}{\tau} dw - v \frac{U'(x)}{\tau\gamma} dt \quad (2.50)$$

being dw the Wiener process associated with the white noise, η . Integrating out the velocity v using the average, $\langle \cdot \rangle_{\pm}$, we obtain the equation which rules the time evolution of $\langle v^2(x) \rangle_{\pm}$:

$$\frac{d}{dt} \langle v^2(x) \rangle_{\pm} = \langle v(x) \rangle_{\pm} \frac{d \langle v^2(x) \rangle_{\pm}}{dx} = -2 \frac{\Gamma(x)}{\tau} \langle v^2(x) \rangle_{\pm} - 2 \langle v(x) \rangle_{\pm} \frac{U'(x)}{\tau\gamma} + 2 \frac{D_a}{\tau^2} \quad (2.51)$$

being d/dt the total derivative. We remark that this equation is in agreement with the second moment of the UCNA distribution. Indeed, in the case of zero currents, i.e. for $\langle v(x) \rangle_{\pm} = 0$, and positive temperature Eq.(2.51) turns to be

$$\langle v^2(x) \rangle_{\pm} = \frac{D_a}{\tau \Gamma(x)},$$

which coincides with Eq. (2.37). Instead, in the case of non-vanishing currents, Eq. (2.51) is a first order differential equation for $\langle v^2(x) \rangle_{\pm}$ which depends on the first order momentum, $\langle v(x) \rangle_{\pm}$. The solution of Eq. (2.51) reads:

$$\langle v^2(x) \rangle_{\pm} = \langle v^2(x_0) \rangle_{\pm} e^{-\int_{x_0}^x dx' g(x')} + e^{-\int_{x_0}^x dx' g(x')} \int_{x_0}^x dx' T(x') e^{\int_{x_0}^{x'} dx'' g(x'')} \quad (2.52)$$

being $g(x) = 2 \frac{\Gamma(x)}{\tau \langle v(x) \rangle_{\pm}}$, $T(x) = \frac{2D_a}{\tau^2 \langle v(x) \rangle_{\pm}}$. We outline that the term $\frac{U'(x)}{\tau \gamma} = O(1/\tau)$ and, thus, has been neglected. Therefore, in the limit of $\tau \gg 1$ we find:

$$\int dx g(x) = \int dx \frac{2\Gamma(x)}{\tau \langle v(x) \rangle_{\pm}} \approx -2 \ln \langle v(x) \rangle_{\pm} + O(1/\tau), \quad (2.53)$$

in such a way that we obtain an ordinary differential equation whose solution reads:

$$\langle v^2(x) \rangle_{\pm} \approx \langle v^2(x_0) \rangle_{\pm} \left(\frac{\langle v(x) \rangle_{\pm}}{\langle v(x_0) \rangle_{\pm}} \right)^2 + (\langle v(x) \rangle_{\pm})^2 \int_{x_0}^x dx' \frac{2D_a}{\tau^2 (\langle v(x') \rangle_{\pm})^3}. \quad (2.54)$$

In the end, since the last the last term in the right-hand side of Eq. (2.54) is order $O(D_a/\tau^2)$, we can neglect it so that the variances $\Delta_{\pm}(x) \equiv \langle (v - \langle v(x) \rangle_{\pm})^2 \rangle_{\pm}$ can be approximated as:

$$\Delta_{\pm}(x) \approx (\langle v(x) \rangle_{\pm})^2 \frac{\Delta_{\pm}(x_0)}{(\langle v(x_0) \rangle_{\pm})^2}. \quad (2.55)$$

Eq. (2.55) states an approximate relation between $\Delta_{\pm}(x)$ and $\langle v(x) \rangle_{\pm}$, holding in the large persistence regime. To complete the analysis we observe that the velocity variance at x_0 is given by $\Delta_{\pm}(x_0) \approx D_a/(\tau \Gamma(x_0)) \sim D_a/(\tau^2 U''(x_0))$. This explains why the lanes of Fig. 2.5 becomes thinner as τ increases, even keeping fixed the ratio D_a/τ .

Now, we can approximate the whole distribution $p(x, v)$ in the central region by means of the above results. $p(x, v)$ can be approximated by the sum of two Gaussians with average values $\langle v(x) \rangle_{\pm}$ and variances $\Delta_{\pm}(x)$,

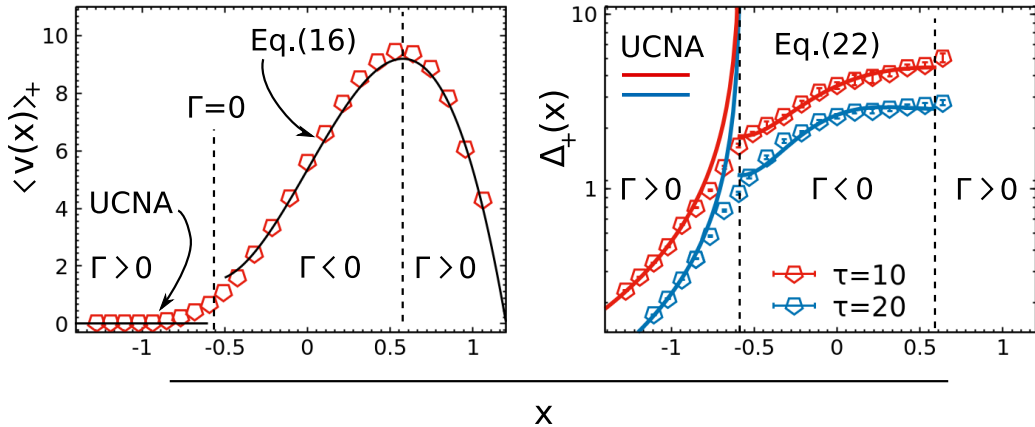


Figure 2.7: Left Panel: $\langle v(x) \rangle_+$ computed from data (red points) and from the theoretical prediction (black line) of Eq. (2.48) with the initial value, $\langle v(x_0) \rangle_+ = 1.5$, obtained from the numerical data values in correspondence of $\tau = 10$. Right Panel: Variance $\Delta_+(x)$ computed from data (points) and from the theoretical prediction, respectively: in the left sector ($\Gamma > 0$) the continuous lines represent the UCNA theoretical value for $\tau = 10$ and 20. In the central region ($\Gamma < 0$) the continuous lines represent the prediction of Eq. (2.55). The remaining parameters are $D_a/\tau = 10^2$, $a = b = 10$.

which represents the left and right population, respectively:

$$\begin{aligned}
 p(x, v) \approx \mathcal{N} \left(\rho_+(x) \sqrt{\frac{1}{2\pi\Delta_+(x)}} \exp \left(-\frac{(v - \langle v(x) \rangle_+)^2}{2\Delta_+(x)} \right) \right. \\
 \left. + \rho_-(x) \sqrt{\frac{1}{2\pi\Delta_-(x)}} \exp \left(-\frac{(v - \langle v(x) \rangle_-)^2}{2\Delta_-(x)} \right) \right)
 \end{aligned}
 \tag{2.56}$$

where \mathcal{N} is the normalization of the whole distribution. The functional form reported in (2.56) reproduces the shape of $p(x, v)$ observed in the bottom panels of Fig. 2.4 and in particular the bimodal shape of the velocity distribution in the NTR.

In Fig. 2.7 we test the theoretical predictions for the conditional moments $\langle v(x) \rangle_{\pm}$ and $\langle v^2(x) \rangle_{\pm}$ with numerical data, revealing a fair agreement which confirms our theory in both cases. In particular, in the left panel we study $\langle v(x) \rangle_+$ finding that Eq.(2.48) fits data in the NTR region, while does not hold in the ER where $\Gamma > 0$ and $\langle v(x) \rangle_{\pm} \approx 0$. Indeed, these conditions break the hypothesis under which Eq.(2.48) has been derived. Instead, in the ER, the observable $\langle v(x) \rangle_+$ is well-described by the UCNA prediction.

The right panel of Fig. (2.7) shows the variance of the left population, namely $\Delta(x)_+ = \langle v^2(x) \rangle_+ - [\langle v(x) \rangle_+]^2$. This observable grows monotonically with x both in the ER and in NTR. As we expect, the UCNA prediction is in fair agreement with data in the ER where $\Gamma(x) > 0$. Moving from the left towards $-x_N$, i.e. the point where $\Gamma = 0$, the UCNA prediction diverges

in disagreement with the numerical evaluation $\Delta(x)_+$. Anyway, from the point $-x_N$ we can test our theoretical prediction. Eq. (2.55) reveals a good agreement with the numerical findings, confirming our theory also in this case.

Selection mechanism and super-fast particles

The phenomenology which emerges by our study suggests a useful application: we can use a non-convex potential to select particles depending on their velocities. Indeed, when the particles enter in the negative temperature region the profile of their average velocity follows the prediction (2.48) almost deterministically, reaching even very larger values. In this way, instead of guiding a particle in the other well we can design a device which takes out the particles, for instance in the proximity of the maximum of the potential. In this way, we obtain a powerful selection mechanism for the velocity. Its efficiency increases with the growth of the persistence time if the strength of the self-propulsion is fixed. Employing this “theoretical device” we can emit self-propelled particles with very large velocities, $|v_s|$, which are even some order of magnitude larger than the typical velocity experienced by potential-free particles. This effect can also be amplified by suitably choosing the non-convex potential, for instance, in such a way that $\Gamma(x)$ assumes smaller negative values.

2.7 Discussion

In this chapter, we have studied diluted suspensions of self-propelled particles confined by external potentials, comparing AOUP and ABP active forces. We have established a connection between these two models generalizing a change of variables originally developed in the framework of AOUP to the ABP model. In both cases, the dynamics of the particle velocity is controlled by the same space-dependent friction matrix which involves the spatial derivatives of the confining potential. The only difference is fully contained in the noise vector, whose amplitude is constant in the AOUP case and v -dependent in the ABP one. Interestingly, we discover the existence of space regions with different features: equilibrium regions, where the whole distribution has a Boltzmann-like shape with space-dependent effective temperature, and non-equilibrium regions, where an intriguing and, somehow, unexpected phenomenology takes place: interestingly, particles spend most of their life in the equilibrium-like regions [77]. We do not argue about the generality of such observation, which requires to be tested also in other stochastic systems.

Specifically, in the single-well case, the interplay between self-propulsion and external trap shows that active particles in two dimensions accumulate far from the potential minimum [78]. A circle of space around the poten-

tial minima is left empty at variance with a passive Brownian suspension of particles. Thus, pronounced differences from a Maxwell-Boltzmann shape appears in the whole probability distribution function [77, 101]. The system behaves as if an effective bistable potential controls the dynamics, a feature captured by the UCNA equilibrium approach [77]. We point out that such a study is in qualitative agreement with the experimental phenomenology of Takatori et. al [110] for a suspension of diluted Janus particles experimentally confined by acoustic traps. Unveiling the effect of pure repulsive interactions on such a system will be one of the last subject of Chapter5.

Our theory predicts a very rich and intriguing phenomenology, depending on the curvature of the potential. A negative curvature induces the occurrence of regions with “negative friction” where any equilibrium-like approaches do not hold. This is the case of a double-well potential studied in the last Section of the Chapter. The non-equilibrium regions, placed around the maximum of the potential, induce negative mobilities in the dynamics of the particle [104]. In these regions, the distribution of the velocities displays a bimodal shape, typical for systems with negative temperatures [114, 132, 133]. Once a particle starts to cross the barrier its velocity grows exponentially until the particle reaches the other well. Going beyond any equilibrium-like approach, we develop effective equations for the first two moments of the distribution which show fair agreement with the results of the simulations. The phenomenology of such a simple stochastic model is surprisingly in agreement with a recent experiment performed with cancerous (MDA-MB-231) and a non-cancerous (MCF10A) cells [134]. Authors developed two-state micropatterns, consisting of two adhesive sites connected by a thin constriction, in which migrating cells perform repeated stochastic transitions. The thin constriction induces an effective potential barrier in the dynamics of the cells, which overcome it by means of irreversible deformations. Authors measured experimentally the velocities of the cells discovering the same phenomenology discussed in Sec.2.6.

It is worth to mention that the negative mobility regions are more severe in two and three dimensions [135] for passive suspension of particles, while they naturally occurs near a concave surface [136]. In this case, the mobility is a tensor and its tangential components may become negative. An intriguing point to be adress in future works could be the adaptations of the methods developed in this Chapter to the multidimensional case. Moreover, generalizing the present study to a suspension of interacting self-propelled particles will be another fascinating platform for future studies. Indeed, unveiling how the interactions affect the escape processes is a very interesting question: we wonder if the escape rate is increased or decreased by the well-known collective phenomena taking place in the dynamics of interacting self-propelled particles, such as clustering or motility induced phase separation, which will be investigated in Chapter6.

Appendices

2.A Derivation of Eq.(2.7)

To derive Eq.(2.7) in the case $D_t = 0$, it is convenient consider the active force dynamics in cartesian components, in such a way that Eq.(2.2) is replaced by:

$$\dot{\mathbf{n}} = \sqrt{2D_r}\boldsymbol{\xi} \times \mathbf{n}, \quad (2.57)$$

being $\boldsymbol{\xi}$ a three dimensional vector with components $(0, 0, \xi)$, while \mathbf{n} belongs to the plain xy . Taking the variation of the ABP version of Eq.(2.1) and defining $\mathbf{v}dt = d\mathbf{x}$, we get:

$$d\mathbf{v} = -\frac{1}{\gamma} (\mathbf{v} \cdot \nabla) \nabla U dt + U_0 d\mathbf{n}. \quad (2.58)$$

The variation of \mathbf{n} reads:

$$d\mathbf{n} = \sqrt{2D_r} d\boldsymbol{\xi} \times \mathbf{n} - D_r \mathbf{n} dt, \quad (2.59)$$

where the last term appears because of the switching from Stratanovich to Ito differentiation rule. In order to derive Eq.(5.39), we write Eq.(2.57) in a more compact form:

$$\dot{\mathbf{n}} = \sqrt{2D_r} \mathbf{B}(\mathbf{n}) \cdot \mathbf{w} \quad (2.60)$$

where \mathbf{w} is a vector on the plain xy whose components are both ξ . The matrix \mathbf{B} of elements b_{jk} reads:

$$\mathbf{B} = \begin{bmatrix} b_{xx} & b_{xy} \\ b_{yx} & b_{yy} \end{bmatrix} = \begin{bmatrix} 0 & n_y \\ -n_x & 0 \end{bmatrix}$$

To switch from Stratanovich to Ito rule, we need to add the following drift term:

$$\alpha_i(\mathbf{v}) = \sum_j \sum_k b^{kj} \frac{\partial}{\partial v_k} b^{ij}, \quad (2.61)$$

where the indices i, j and k runs over every space components of the dynamics, namely x and y for a dimensional system. Taking into account such a thing the only terms which survive are:

$$\alpha_x - a_x = D_r b^{xy} \frac{\partial}{\partial v_x} b^{xy} = D_r v_y \frac{\partial}{\partial v_x} v_y \quad (2.62)$$

$$= D_r v_y \frac{\partial}{\partial v_x} \sqrt{v_0^2 - v_x^2} \text{sign}(v_y) = -D_r v_x$$

$$\alpha_y - a_y = D_r b^{yx} \frac{\partial}{\partial v_y} b^{yx} = D_r v_x \frac{\partial}{\partial v_y} v_x \quad (2.63)$$

$$= D_r v_x \frac{\partial}{\partial v_y} \sqrt{v_0^2 - v_y^2} \text{sign}(v_x) = -D_r v_y$$

where the function $\text{sign}(\cdot)$ takes the sign of its argument. This concludes the derivation of Eq.(5.39). Putting Eq.(5.39) into Eq.(5.38) and replacing \mathbf{n} with \mathbf{v} , using that:

$$\gamma U_0 \mathbf{n} = \gamma \mathbf{v} + \nabla U \quad (2.64)$$

we get:

$$d\mathbf{v} = -\frac{1}{\gamma} (\mathbf{v} \cdot \nabla) \cdot \nabla U dt - D_r \mathbf{v} dt - \frac{D_r}{\gamma} \nabla U dt + U_0 \sqrt{2D_r} d\boldsymbol{\xi} \times \mathbf{n}.$$

Finally, putting together the first two addends of the right-hand side, using the definition of the matrix $\boldsymbol{\Gamma}$, we obtain the final result after replacing again \mathbf{n} with \mathbf{v} by means of Eq.(2.64).

An alternative derivation, which leads to the same result, could be obtained working directly on the rotational angle, representing the active force in polar coordinate. In this case, the Stratonovich rule needs to be considered in the variation of $\cos \theta$ and $\sin \theta$.

2.B Unified Colored Noise Approximation

In this Appendix, we report the derivation of the Unified Colored Noise approximation (UCNA) following [74, 113], but we adapt the computations to the case of a particle in the presence of a confining potential, U . As a first step we take the over-damped limit, $\dot{v}_\alpha \approx 0$, in Eq.(2.5). This procedure leads to a relation between $\mathbf{v} = \dot{\mathbf{x}}$ and \mathbf{x} . Replacing \mathbf{v} with such a relation we get the UCNA dynamics, which in components reads:

$$\dot{x}_\alpha = v_\alpha = \Gamma_{\alpha\beta}^{-1} \left[-\frac{\partial_\beta U}{\gamma} + \sqrt{2D_a \eta_\beta} \right]. \quad (2.65)$$

Here, the indices α and β run over the space components of the particle, x and y in two dimensions. Eq.(2.65) involves a multiplicative noise and does not satisfy the fluctuation-dissipation theorem. The associated Fokker-Planck equation associated to Eq.(2.65) - using the Stratonovich integration -, for the density $p_u(\mathbf{x}, t)$, reads:

$$\partial_t p = -\partial_\alpha J_\alpha, \quad J_{i\alpha} = -\Gamma_{\alpha\beta}^{-1} \left[\partial_\beta U p + D_a \partial_\beta (\Gamma_{\alpha\beta}^{-1} p) \right], \quad (2.66)$$

where we have adopted Einstein's convention for repeated indices. Looking for a stationary solution of Eq. (2.66) under the condition of vanishing current we find the following equation:

$$-p \frac{\partial_\alpha U}{D_a \gamma} - p \partial_\beta \Gamma_{\beta\alpha}^{-1} = \Gamma_{\beta\alpha} [\partial_\beta p]. \quad (2.67)$$

After some algebra we obtain:

$$-p \frac{\tau}{D_a \gamma} \Gamma_{\alpha\beta} \partial_\beta U + p \Gamma_{\beta\delta}^{-1} \partial_\beta \Gamma_{\delta\alpha} = \partial_\alpha p \quad (2.68)$$

Moreover, by using the identity, $\partial_\beta \Gamma_{\alpha\gamma} = \partial_\gamma \Gamma_{\alpha\beta}$ - since Γ involves only the second derivatives of U - and the Jacobi's formula:

$$\frac{1}{\det \Gamma} \partial_y \det \Gamma = \text{Tr} (\Gamma^{-1} \partial_y \Gamma) \quad (2.69)$$

we obtain:

$$\Gamma_{\alpha\beta}^{-1} \partial_\alpha \Gamma_{\beta\delta} = \frac{1}{\det \Gamma} \partial_\delta \det \Gamma \quad (2.70)$$

Using this result in Eq.(2.68):

$$- D_a \gamma (\partial_\alpha p - p \partial_\alpha \log \det \Gamma) = p \Gamma_{\alpha\beta} \partial_\beta U \quad (2.71)$$

Solving this set of partial first-order differential Equations, we find the UCNA probability distribution:

$$p \propto \exp \left(- \frac{\mathcal{H}}{D_a \gamma} \right), \quad (2.72)$$

$$\mathcal{H} = U + \frac{\tau}{2\gamma} \sum_\beta (\partial_\beta U)^2 - D_a \gamma \log \det \Gamma,$$

which concludes the derivation.

2.C Derivation of Eqs.(2.23) and (2.24)

To derive Eqs.(2.23) and (2.24), it is convenient to switch from the differential stochastic equation (1.1) in the presence of the ABP active force, to the associated Fokker Planck equation for the probability distribution, $\mathcal{P}(\mathbf{x}, \theta)$, which reads:

$$\frac{\partial}{\partial t} \mathcal{P} = \nabla \cdot (\nabla U - U_0 \mathbf{n}) \mathcal{P} + T \nabla^2 \mathcal{P} + D_r \frac{\partial^2}{\partial \theta^2} \mathcal{P}, \quad (2.73)$$

where we have assumed that $\gamma = 1$, for the sake of simplicity. The external potential, U , is a harmonic trap of the form:

$$U(x, y) = \frac{k}{2} (x^2 + y^2).$$

Because of the radial symmetry of U , it is quite natural to switch from cartesian to polar coordinates $(x, y, \theta) \rightarrow (r, \phi, \theta)$, being $r = \sqrt{x^2 + y^2}$ and $\phi = \arctan(y/x)$, in such a way that the Fokker-Planck equation for the probability distribution function $\tilde{\mathcal{P}}(r, \phi, \theta)$ becomes:

$$\begin{aligned} \frac{\partial}{\partial t} \tilde{\mathcal{P}} = & \frac{\partial}{\partial r} \left[kr \tilde{\mathcal{P}} - \frac{T}{r} \tilde{\mathcal{P}} + T \frac{\partial}{\partial r} \tilde{\mathcal{P}} - U_0 \tilde{\mathcal{P}} \cos(\theta - \phi) \right] \\ & + \left[\frac{T}{r^2} \frac{\partial^2}{\partial \phi^2} \tilde{\mathcal{P}} + \frac{U_0}{r} \tilde{\mathcal{P}} - \frac{U_0}{r} \sin(\theta - \phi) \frac{\partial}{\partial \phi} \tilde{\mathcal{P}} \right] + D_r \frac{\partial^2}{\partial \theta^2} \tilde{\mathcal{P}}. \end{aligned} \quad (2.74)$$

Finding an exact solution of such a partial differential equation is not so easy. Our analytical approach consists of finding an approximate solution based on the identification of different relaxation regime between the radial and the angular component. It is straightforward to identify the leading angular variable with the angular difference $\phi - \theta$. Assuming that $\theta \sim \phi$, we can approximate $\sin(\phi - \theta) \approx \phi - \theta$ and $\cos(\phi - \theta) \approx 1$, neglecting at least the order $(\theta - \phi)^2$. Assuming that the first and second square brackets separately approach to zero, we can find an approximate solution of Eq.(2.74). This means to assume that the radial coordinate has a relaxation time different with respect to $\phi - \theta$. The first square bracket leads to the Gaussian shape of $\tilde{\mathcal{P}}$ centered at U_0/k , whose variance is ruled by T/k and is independent of U_0 and D_r :

$$\tilde{\mathcal{P}}(r, \theta_0, \phi) \approx g(\theta_0, \phi) r \exp\left(\frac{1}{T} \left[-k \frac{r^2}{2} + U_0 r\right]\right), \quad (2.75)$$

where $g(\theta_0, \phi)$ is an unknown function to be determined. We remark that the factor r takes into account the role of the Jacobian and disappear coming back to the cartesian components. In the regime of this approximation, the role of the activity is only recast into a constant radial force of strength U_0 and works only if the radial coordinate is the faster degree of freedom. Assuming that the angle difference $\phi - \theta$ relaxes faster than θ itself, meaning that $1/D_r \gg r_m U_0/T$ (the time which rules the variation of θ has to be larger than the associated to variation of ϕ) but slower than r , we can approximate $r \approx r_m$ in the second square brackets of Eq.(2.74), in such a way that $\tilde{\mathcal{P}}$ reads:

$$\tilde{\mathcal{P}}(r, \theta_0, \phi) \approx p(r) \exp\left(\frac{U_0}{T} r_m \left[\theta_0 \phi - \frac{\phi^2}{2}\right]\right), \quad (2.76)$$

which a Gaussian centered at the fixed value of θ_0 , whose variance is proportional to $T/(U_0 r)$. Combining both the results we get an approximate solution of the Fokker-Planck equation. Finally, in the slow time regime a Brownian motion rules the change in $\theta_0 \rightarrow \theta_t$:

$$\frac{\partial}{\partial t} \tilde{\mathcal{P}} = D_r \frac{\partial^2}{\partial \theta^2} \tilde{\mathcal{P}} \quad (2.77)$$

$$\tilde{\mathcal{P}}(t=0) \propto r \exp\left(\frac{1}{T} \left[-k \frac{r^2}{2} + U_0 r\right]\right) \exp\left(\frac{U_0}{T} r_m \left[\theta_0 \phi - \frac{\phi^2}{2}\right]\right). \quad (2.78)$$

Chapter 3

Accumulation near the walls

In microbiology and biological applications typical specimens of active microswimmers, such as cells, living tissues but also spermatozoa, protozoa or bacterias, often move and live in confined geometries. Indeed, living bodies harbor bacterial colonies which are normally localized in the skin, in external mucosae or gastrointestinal tracts [137]. It is also well-known that mammalian spermatozoa swim in closed confinement of the winded Fallopian tube, where interactions with boundaries play a very important role. In general, the dynamics across channels is also relevant for Phytoplankton, photosynthetic microorganisms living in aquatic habitats. Typical examples of such microorganisms are *Heterosigma akashiwo* and *Amphidinium carterae*, which propel through flagella, behaving as pushers. Instead, *Dunaliella tertiolecta* and *Chlamydomonas reinhardtii* behaves as pullers and the last one, in particular, represents a model organism for cell motility [138].

The recent developments of microfluidic allow researchers to design experiments to track the trajectories of many of these microswimmers confined in simple geometries [139]. For instance, the behavior of the bacterium *C. resensus* [140] near the surfaces has been studied, as also the trajectories of the well-known *E. Coli* [141, 142]. In this framework, even spermatozoa have been experimentally analyzed [143, 43]. In addition, the trajectories near obstacles of artificial microswimmers, such as Janus particles, have been monitored in the different regimes of rotational diffusion and self-propulsion velocity [144]. The few cases described above are typical examples of the active microswimmers which show a similar phenomenology when they are confined in simple geometries. All of them reveal a typical behavior in front of walls or obstacles: they accumulate in the proximity of a rigid boundary which prevents the motion in a given space direction. Active particles spend more time attached to the wall than in the bulk, a property which introduces pronounced density gradients in the system. In some cases, the effect of the walls extends even in the bulk, i.e. far from the boundaries, displaying a long-range influence which has not a Brownian counterpart. This feature is opposite to the behavior of passive colloids, modeled as equilibrium Brownian particles without any form of persistence, whose density

is just homogeneously distributed in the bulk regions of the channel [65, 100]. We remark that the accumulation near the walls is common to a broad class of systems and could be considered as one of the leading phenomenological observations which characterize self-propelled microswimmers.

In Chapter 1, ABP and AOUP models have been introduced and successfully used to describe the motion of unconfined self-propelled particles. Both these stochastic dynamics qualitatively reproduce the accumulation near walls. In particular, the aggregation with an external object, in the absence of any explicit attraction, occurs even when active particles are not subject to mutual interactions [145] and is only related to the interplay between self-propulsion and wall repulsion [75, 116]. Recently it has been shown that the properties of a given microswimmer - considering, for instance, hydrodynamic interactions and thus distinguishing between puller and pushers - does not change the phenomenology and affect the description only from a quantitative point of view [146], reducing or increasing the accumulation. Similarly, both the shape of the microswimmers and the explicit presence of alignment interactions between particles are not so qualitatively relevant.

Building a thermodynamic theory, based on minimal stochastic models, which predicts and explains the accumulation, is a great deal and is of fundamental relevance both from a theoretical point of view both for engineering and biological applications. Recently, channels with asymmetric shapes have been built to induce spermatozoa to move in some directions. Due to their tendency to accumulate near walls, the channel behaves as a guide in some regimes inducing an average motion towards a target. As an important application, the efficiency of artificial inseminations could increase taking into account such a mechanism [43]. Active particles have been also used to design motors based on the accumulation near obstacles. Asymmetric gear wheels into a suspension of self-propelled particles give rise to a very interesting phenomenon: particles accumulate on their surfaces and a spontaneous rotation of the gears is induced [147]. In particular, Di Leonardo et coworkers have designed a 3D micromotor, based on bacteria, whose power can be controlled by light [40]. Shedding light on the accumulations of self-propelled particles could induce important challenges in the motor-realization, for instance, with the result of maximizing its efficiency.

The present Chapter is structured as follows. In Section 3.1, we introduce a general simplified dynamics to account for the interplay between self-propulsion and hard-walls or in general repulsive obstacles, modeling the boundaries as soft-potentials and accounting for the self-propulsion through ABP or AOUP dynamics. In particular, we focus on the latter which allows us to consider directly a one-dimensional dynamics reducing the complexity of the problem. In Sec. 3.2, we review the phenomenology of the accumulation near boundaries, focusing also on the role of the additional thermal noise due to the environment [116]. The theoretical methods derived in [116] are presented in Sec. 3.3, based on a hydrodynamic approach and rea-

sonable approximations. In this Section, the effective forces exerted by the active particles on the walls, i.e. the mechanical pressure, are briefly discussed. In Sec. 3.4, the role of the chirality is analyzed: we discover a new phenomenology called “bulk accumulation” [89] arising from the interplay between boundaries, self-propulsion, and chirality, with the additional presence of surface currents. We develop a theoretical method, starting from the hydrodynamics approach of Sec. 3.3, to approximate the complex profile of the density. Finally, we focus on first passage properties in the presence of an open-wedge geometry in Sec.3.5, presenting the recent results of [148]. We present a final discussion, focused on future perspectives, in the conclusive Section.

3.1 A self-propelled particle in a container

In this Section, we introduce the model to describe a suspension of independent self-propelled particles in a container. To confine the system, we reproduce the repulsion due to the walls by truncated soft potentials in such a way that the stiffness of the walls and the width of the channel can be varied independently. In particular, we restrict to pure-repulsive potentials, preventing the escaping across the container and excluding any attracting layers or surface tensions. Despite such a simple choice some results could be easily adapted to account for such additional effects. Assuming that walls exert forces, \mathbf{F}_w , along the normal direction to their surfaces (which are just lines for a two-dimensional system), the resulting model for a self-propelled particle, at position \mathbf{x} , is described by the following stochastic equation:

$$\gamma \dot{\mathbf{x}} = \mathbf{F}_w + \gamma \sqrt{2D_t} \boldsymbol{\xi} + \mathbf{f}^a, \quad (3.1)$$

where \mathbf{f}^a follows the ABP or the AOUP dynamics, given by Eq.(1.2) or Eq.(1.5), respectively. In practice, Eq.(3.1) coincides with Eq.(2.1) except for the specific choice of the external force, which takes into account the shape of the walls.

In two dimensions, we need to fix the geometry of the container and recent studies [149] have revealed that such a choice could determine very interesting and peculiar behaviors, which are only partially discussed in the present thesis. Even in the simpler cases, as the semi-infinite channel, a theoretical explanation in terms of probability density is unknown and only few approximations exist to estimate the density profile in the whole space. Thus, we fix the geometry as simpler as possible, choosing a semi-infinite channel along the y direction, realized with two parallel walls at distance $2L$. Each of them exerts a piece-wise force, \mathbf{F}_w , constant with respect to y , which reads

$$\mathbf{F}_w = U'(x + L)\theta(-x - L)\hat{\mathbf{x}} - U'(x - L)\theta(x - L)\hat{\mathbf{x}}, \quad (3.2)$$

where θ is the Heaviside step-distribution selecting the region $(-\infty, -L]$ and $[L, \infty)$ for the first and second addend of Eq.(3.45), respectively. U is the potential representing the wall and the prime stems for the derivative with respect to the argument of U . The coordinate x represents the component of \mathbf{x} which is normal to the surface of the wall. In what follows we choose $U(x)$ to be a continuous function of its argument, approaching to zero at its edges. This setup provides a realistic description of a straight capillary since the potential regions and the bulk-like region can be distinguished. Indeed, the space between the walls extending from $x = -L$ to $x = L$ forms a force-free region, while the remaining parts of the space can be identified as the wall regions. In the numerical simulations, in order to model an infinite vertical channel, we assume periodic boundary conditions along the y -direction.

Eq.(3.1) in the semi-infinte channel geometry has been numerically studied by several authors, employing both the ABP [150, 151, 152, 153] and the AOUP dynamics [75, 116, 154]. Both models reproduce the experimental phenomenon of the accumulation at the walls and are qualitatively in agreement even if a quantitative comparison between them has not yet been realized. Anyway, despite the simplicity of the dynamics, the theoretical understanding in terms of density functions cannot be easily found at variance with the well-known Brownian case. Indeed, an exact solution of the Fokker Planck equation associated with Eq.(3.1) (independently of the choice of ABP or AOUP models) is currently unknown. In the following Sections, we will develop reasonable approximations to shed light on the comprehension of such non-equilibrium phenomenology.

We consider a different geometry only in the final Section, where active particles will be constrained in an open-wedge channel. In general, if the profile of the wall is described by the function $w(x)$, then a repulsive force along the direction $\hat{\mathbf{n}} = (w'(x), -1)/\sqrt{1 + w'(x)^2}$, normal with respect to the profile of the boundary, will take place in the dynamics. Assuming that the shape of the wall is determined by the potential $U(s)$, being s the coordinate along the direction $\hat{\mathbf{n}}$, the force exerted on a particle will be simply:

$$\mathbf{F}_w = -U'(w(x) - y)\hat{\mathbf{n}}, \quad (3.3)$$

assuming that no-torque take place in the dynamics. With this choice, the form of the force determines specular-like reflection when particles “collide” with the walls.

3.1.1 AOUP dynamics: reduction to a one-dimensional system

The advantage of studying the AOUP dynamics lies in the possibility of reducing the dimensions of the system, considering the one-dimensional version of Eq.(3.1). Using the ABP active force such a simplification cannot be obtained and, thus, the AOUP plays an important role to improve the theoretical comprehension of the accumulation near rigid obstacles.

In the AOUP dynamics, just the normal component to the surface of the wall, namely the x direction, plays a role, being completely independent of the y degree of freedom. Thus, the active force and the microswimmer position, $f^a = \gamma u$ and x , respectively, will represent scalar functions in the current Section. The force due to the wall turns to be $U'(x)$, where the prime stems for the spatial derivative. The dynamics is governed by the following equations:

$$\gamma \dot{x} = -U'(x) + \gamma u + \gamma \sqrt{2D_t} \xi, \quad (3.4)$$

$$\tau \dot{u} = -u + \sqrt{2D_a} \eta, \quad (3.5)$$

where ξ and η are two independent white noises with unit variance and zero average. D_t and γ refer to the interactions with the solvent while D_a and τ are the parameter of the self-propulsion. The change of variable derived in Sec.2.2 for the case $D_t > 0$ (and obtained first time in [116] in this case), can be simply adapted to the one-dimensional case. In this simple case, the dynamics of x and v read

$$\dot{x} = v + \sqrt{2D_t} \xi \quad (3.6)$$

$$\dot{v} = -\frac{1}{\tau} \left[v + \frac{U'(x)}{\gamma} - \sqrt{2D_a} \eta \right] - \frac{U''(x)}{\gamma} v - \frac{\sqrt{2D_t}}{\gamma} U''(x) \xi. \quad (3.7)$$

Thus the original AOUP dynamics, given by Eqs. (3.4)-Eq. (3.5), has been mapped onto the underdamped dynamics of a fictitious Brownian particle of position x and velocity v evolving with a space-dependent Stokes force and experiencing a delta-correlated thermal noise which acts additively on the x and multiplicatively on the v [116]. As usual, we use the Stratonovich interpretation of the stochastic differential equation [117], required by the presence of the multiplicative noise term. This change of variables will be particularly useful in this Section since allows to derive the hydrodynamic equations of the model.

We restrict our study to the case where the confining walls are represented by repulsive truncated harmonic potentials chosen for mathematical convenience. We confine the system in the region $\approx (0, 2L)$ setting

$$U(x) = \theta(-x)k \frac{x^2}{2} + \theta(x - 2L)k \frac{(x - 2L)^2}{2}, \quad (3.8)$$

where θ is the Heaviside function which selects the regions $(-\infty, 0)$ and $(2L, \infty)$. The harmonic force is proportional to k , which models the penetrability of the wall. Such a shape could describe an elastic membrane of stiffness k allowing the particles to explore thin regions at $x \leq 0$ and $x \geq 2L$, being the strength and the range of the force both finite. The central region, within $(0, 2L)$, is force-free region. We point out that the use of a sharp interface model, obtained by assuming no-flux boundary conditions ref. [155], is well justified only if the penetrability of the wall is small with respect to the spatial resolution of the experimental device.

The stationary Fokker-Planck equation (FPE) [100] for the probability distribution, $f(x, v)$, associated to the dynamics provides an equivalent description of the system (3.6)-(3.7), which will be useful for the theoretical methods of Sec. 3.3. Substituting $U'(x) = k[x\theta(-x) + (x - 2L)\theta(x - 2L)]$ and $U''(x) = k[\theta(-x) + \theta(x - 2L)]$, we obtain

$$\begin{aligned}
& v \frac{\partial f(x, v)}{\partial x} - D_t \frac{\partial^2}{\partial x^2} f(x, v) \\
& - \frac{1}{\tau} \frac{\partial}{\partial v} \left(\frac{D_a}{\tau} \frac{\partial}{\partial v} + \left(1 + (\theta(-x) + \theta(x - 2L)) \frac{\tau k}{\gamma} \right) v \right) f(x, v) = \\
& \left(\theta(-x) \frac{kx}{\tau\gamma} + \theta(x - 2L) \frac{k(x - 2L)}{\tau\gamma} \right) \frac{\partial f(x, v)}{\partial v} \\
& + (\theta(-x) + \theta(x - 2L)) \frac{D_t}{\gamma} k \left(\frac{k}{\gamma} \frac{\partial^2}{\partial v^2} f(x, v) - 2 \frac{\partial^2}{\partial v \partial x} f(x, v) \right),
\end{aligned} \tag{3.9}$$

where γ/k is the typical time induced by the potential on the x -process. Even if the harmonic case is well-known and solvable considering the AOUP dynamics, we point out that, in this case, we are dealing with discontinuous forces, which introduce non-linear effects at least near the edges.

3.2 The accumulation near the walls

We start the numerical study in the absence of thermal noise, a condition roughly holding for several biological microswimmers, with the aim of showing the basic features of the so-called accumulation near the walls. In Fig. 3.1 we show the steady state density of the system, $\rho(x)$, for particles evolving with Eqs.(3.4) and (3.7) in the case $D_t = 0$. We discuss just the left wall, for the sake of simplicity: particles accumulate in a thin region close to the wall position, at $x = 0$, showing a density profile which is extremely peaked and continuously approaches to the density value of the bulk which is smaller than the height of the main peak [75]. The continuity of $\rho(x)$ is not reproduced by some equilibrium-like approaches, such as the UCNA one, which predicts a finite jump at the edge of the walls, at $x = 0$ and $x = 2L$ [136] in this geometry.

Such a phenomenology does not have a Brownian counterpart: in fact, a Brownian suspension of particles in the same geometry would be uniformly distributed in the bulk of the box between 0 and $2L$, while the distribution in the wall-regions would follow the Boltzmann weight $\propto \exp(-U(x)/T)$, where T is the temperature. In this way, the distribution would be strongly depleted within these regions. We remark that this limit can be explored for $\tau \rightarrow 0$, where a self-propelled suspension of particles can be approximated by a Brownian one at temperature $T = (D_a + D_t)\gamma$.

In the two panels of Fig. 3.1 we show simulations with different parameters of the active force, to unveil the different effects of τ and D_a/τ . In

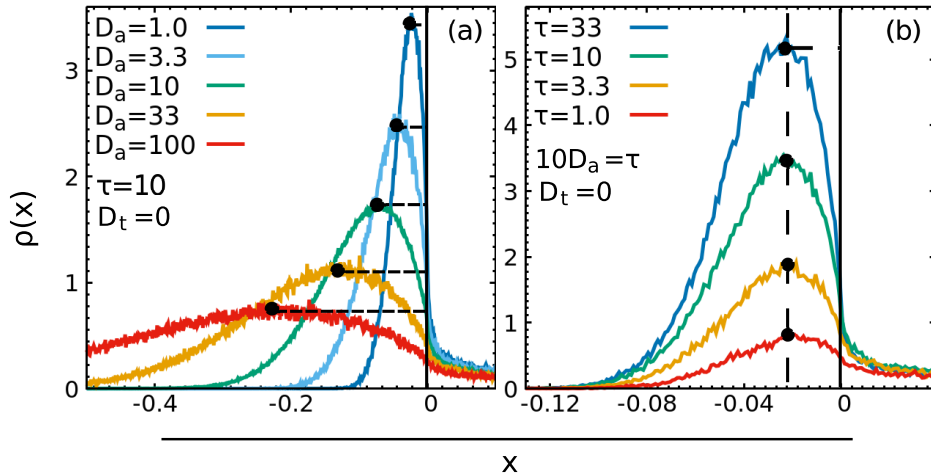


Figure 3.1: Density profiles, $\rho(x)$, for a system with $D_t = 0$, $k = 10$ and symmetric harmonic walls placed at a distance $2L = 8$ at $x = 0$ and $x = 8$. In these panels, for presentation purpose, we only show $n_0(x)$ in the proximity of the left wall. Left panel: each line corresponds to a system with $\tau = 10$ fixed and different values of D_a in an interval between 1 and 100, (and so varying the active power D_a/τ). Notice that the peak broadens and shifts towards more negative values of the x -coordinate with increasing active power. Right panel: Simulation results with $D_t = 0$ and different values of τ , keeping constant the ratio D_a/τ .

the left panel of Fig. 3.1 each distribution is obtained setting $\tau = 10$ and D_a between 1 and 100. We observe that the accumulation peak broadens and shifts towards negative values of the x -coordinate as the variance of the active force, D_a/τ , is increased. In the right panel of Fig. 3.1, D_a/τ remains constant and we explore just different values of τ . With this protocol, the position of the peak is unchanged while its height grows as τ increases: indeed, a larger value of τ induces particles to spend a long time in front of the wall, an effect which does not change the dispersion of the peak.

Eq.(3.9) with $D_t = 0$ can be useful to understand the accumulation at the boundary occurring for $\tau > 0$: the Stokes force in Eq.(3.7) is discontinuous, being γv for $x > 0$ and $\gamma\Gamma v$ for $x < 0$, with $\Gamma = 1 + \tau k/\gamma$. Hence, on one hand, the repulsive wall pushes the particles towards the edge $x = 0$, on the other hand particles slow down in the regions $[-\infty, 0]$. The interplay between these two effects induces the accumulation phenomenon observed in the simulations. In agreement with this explanation, the accumulation becomes relevant when the parameter $\nu = \tau k/\gamma$ introduced in Chapter 2 is such that $\nu \gtrsim 1$. This is the condition for which the Stokes force in the bulk is smaller than the Stokes force in the wall-regions.

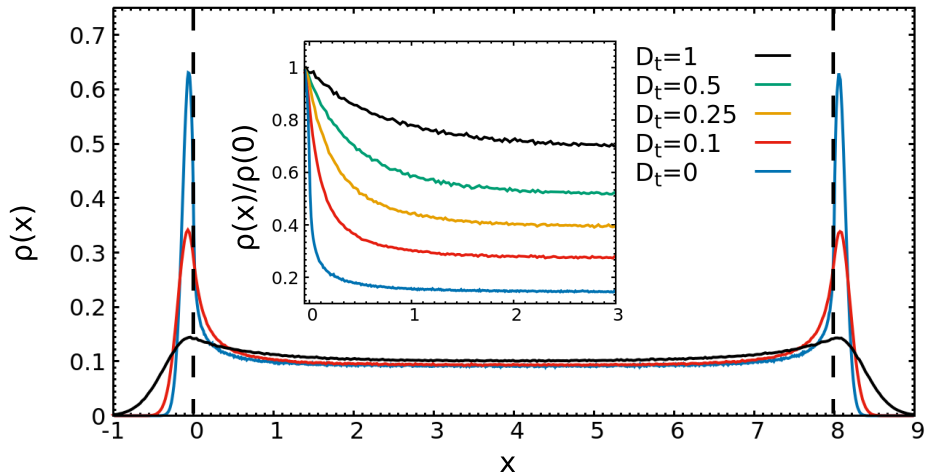


Figure 3.2: Density profile, $\rho(x)$, for a system with symmetric harmonic walls placed at a distance $2L = 8$ at $x = 0$ and $x = 8$. The curves correspond to simulation results for different values of D_t as shown in the legend, while $D_a = 1$, $\tau = 1$ and $k = 10$ are kept fixed. In the inset: rescaled density profiles, $\rho(x)/\rho(0)$.

3.2.1 Effect of the thermal noise: the screening length

We turn to study the full dynamics (3.4) and (3.7) to unveil the effect of $D_t > 0$ on the accumulation in front of the walls, following [116]. In Fig. 3.2, we show the density profile, $\rho(x)$, in the whole box obtained by numerical simulations, confirming that the accumulation near the walls can survive in the presence of the thermal noise due to the environment. To fix the dispersion of the peak due to the active force dynamics, we keep constant the ratio D_a/τ and vary the intensity of the thermal noise D_t , as shown in the legend. The density profile, $\rho(x)$, is continuous for all values of D_t including the value $D_t = 0$ (as already mentioned), displaying two symmetric peaks at the edges of the two walls. Increasing the thermal diffusion, D_t , the accumulation is depleted. In addition, the distribution broadens with respect to the case $D_t = 0$ both in the wall-regions and in the wall-free one, as shown in the inset of Fig. 3.2: the profiles corresponding to the larger values of D_t have slower decay. This scenario resembles the one observed in the ABP dynamics studied in [155, 156]: the presence of thermal noise has two main consequences: a) it reduces the accumulation near the walls and b) it induces a pronounced profile of the density in the force-free region, an exponential decay with screening length, λ , which depends on the ratio $\Delta = D_t/D_a$. We conclude that the accumulation near a repulsive wall is hindered by the presence of an additional thermal noise, even if for $D_t \lesssim D_a$ it survives. Such a non-equilibrium phenomenon disappears only for $D_t \gtrsim D_a$ when the particles behave as passive ones. Anyway, D_t favors the dispersion and induces the formation of a bulk profile promoting the long-range effect of the wall.

3.3 Theoretical treatment: predicting the wall-accumulation

In this Section, we present a theoretical analysis deriving approximate solutions of FPE (3.9) using a velocity-moment expansion. We compare the theoretical predictions with the numerical solutions of Eqs. (3.4)-(3.5). For mathematical convenience we study separately the two wall regions and the central force-free region and look for a solution of the steady state distribution associated with the FPE (3.9) of the form $f(x, v) \propto \theta(-x)f_l(x, v) + \theta(x)\theta(L-x)f_c(x, v) + \theta(x-L)f_r(x, v)$, where f_l and f_r are the distribution functions in the left and right wall regions, respectively, while f_c is the one of the central region. The aim is to develop an approximation for the density of the system, $\rho(x)$, reproducing the numerical results presented above. We analyze separately the wall-regions, in SubSec.3.3.1, and the central region, in SubSec.3.3.2.

3.3.1 Density profile in the wall region

We start by evaluating $\rho(x)$ in the wall regions, focusing on the left one at $x < 0$ without loss of generality. In this Section, we maintain the (x, u) which will be useful to develop our final approximation. Following previous studies, we begin by approximating $p_l(x, u)$ by the steady state, $p_h(x, u)$, obtained from a system of self-propelled particles evolving with the AOUP dynamics and confined in a harmonic potential, $(\frac{kx^2}{2})$, [76]:

$$p_h(x, u) = \mathcal{N} e^{-\left(\frac{kx^2}{2D_a\gamma} \frac{1}{1+\Delta}\right)} e^{-\left(\frac{\tau\Gamma}{2D_a} \left(u - \frac{k}{\gamma} \frac{x}{1+\Delta}\Gamma\right)^2\right)}, \quad (3.10)$$

where \mathcal{N} is a normalization factor and $\Delta = D_t/D_a$. A similar expression for $f_h(x, v)$, in the (x, v) representation, is reported in Appendix3.A. Using Eq. (3.10), we can compute the density as the marginal probability distribution, $\rho(x) = \int du p_h(x, u)$. Such an expression shows poor agreement with the numerical results of Fig. 3.1: The prediction is a Gaussian centered at $x = 0$ while Figs.3.2 and 3.1 show distributions where the main peak is shifted towards negative values of x . We also test the validity of the harmonic approximation (3.10) by comparing the conditional probability distribution function, $p(x|u) = p(x, u)/p(u)$ (where $p(u) = \int dx p(x, u)$), obtained from Eq. (3.10) with the numerical results from simulations. Left panel of Fig. 3.3 shows significant deviations between the two curves which are more pronounced for x near zero. We also display the comparison between the conditional x -variance, $\int dx x^2 p(x|u)$, computed from simulations and the Gaussian prediction (3.10). The latter remains constant, while the first starts to decrease monotonically for some value of u . Thus, the departure from the Gaussian prediction becomes relevant for $u \gtrsim 0$, while it seems to be negligible for $u \lesssim 0$.

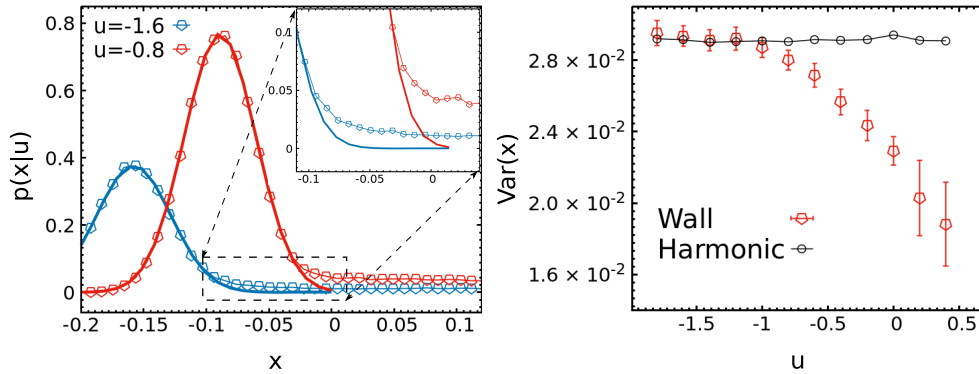


Figure 3.3: Left panel: Comparison between the conditional probability distribution $p(x|u)$ (data) and a fitted Gaussian (solid line), for two different negative values of u . Right panel: We show for different values of u the comparison between the x -variance, $\int dx x^2 p(x|u)$ obtained from numerical simulations (red symbols) and the corresponding variance computed using the harmonic potential formula (3.10). Parameters: $k = 10$, $D_a = \tau = 1$, $D_t = 0$.

We conclude that the Gaussian prediction (3.10) is in good agreement with the numerical results for the conditional probabilities $p(x|u)$ and $p(u|x)$, when $u < 0$ and $x < 0$, respectively, but such a formula is not able to predict the shape of $n_0(x)$ for $x < 0$. These numerical evidences suggest to modify the Gaussian approximation (3.10) changing $p_l(x, u)$ as follows

$$p_l(x, u) \approx p_h(x, u)\theta(-u)\theta(-x). \quad (3.11)$$

In the same way, the distribution of the right wall turns to be $p_r(x, u) \approx p_h(x, u)\theta(u)\theta(x - L)$. The new profile (3.11) can be justified by a kinetic-like argument: interpreting the wall as a very massive body with zero speed and the self-propelled particle as a moving object with persistent velocity γu , a necessary condition for their collision is that u assumes negative values and $x < 0$. Since formula (3.11) contains these two conditions, we, now derive an approximate expression for $\rho(x)$ in the wall region $x \leq 0$ simply integrating with respect to u , obtaining:

$$\rho^{left}(x) = n_w e^{-\left(\frac{kx^2}{2D_a\gamma} \frac{1}{\Gamma + \Delta}\right)} \text{erfc} \left(\sqrt{\frac{\tau\Gamma}{2D_a}} \frac{1}{(1 + \Gamma\Delta)} \frac{k}{\gamma} x \right) \theta(-x), \quad (3.12)$$

where n_w is the density value at $x = 0$ and $x = 2L$. The left panel of Fig. 3.4 reveals a fairly good agreement between simulation data and Eq.(3.12) both for $D_t = 0$ and $D_t > 0$. The argument of the complementary error function in Eq. (3.12) is proportional to the ratio between the wall force $-kx$ and $\gamma\sqrt{D_a}/\tau$, i.e. the typical value assumed by the active force. Such a profile predicts a shift depending on the ratio D_a/τ in the large persistent regime. Instead, if $\tau = 0$ there is no shift being the accumulation phenomenon

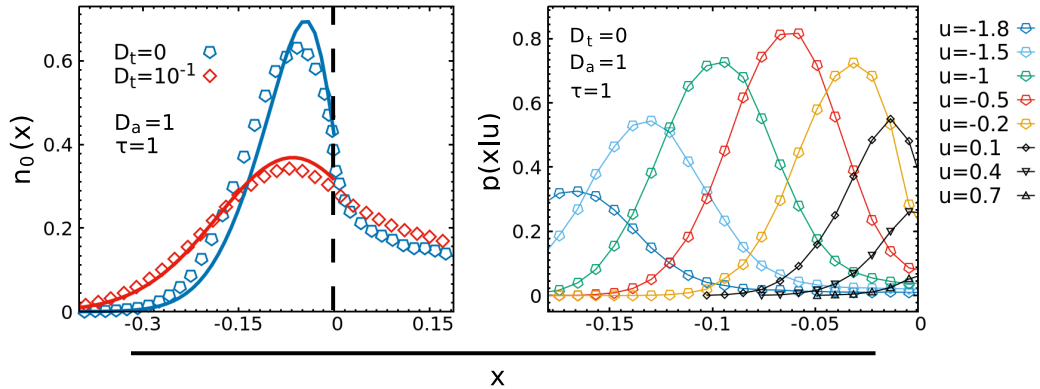


Figure 3.4: Left Panel: Density profile, $n_0(x)$, in the wall region for $D_t = 0, 10^{-1}$, respectively blue and red curve. Circles represent the numerical data and lines the theoretical prediction Eq. (3.12). Right Panel: Conditional probability distribution $p(x|u)$ as a function of x for different values of u as reported in the legend: the colored curves represent the data with $u \leq 0$ and the three black curves the data for $u \geq 0$. Parameters: $D_a = 1$, $\tau = 1$, $k = 10$.

completely suppressed. In this case, the density is depleted in the wall region accordingly to the Maxwell-Boltzmann weight. We analyzed the joint probability distribution $p(x|u)$ at fixed u . In order to check directly the leading approximation in Eq.(3.12), namely $p_l(x, u) = p_h(x, u)\theta(-u)\theta(-x)$, estimating the contribution of the population with $u \geq 0$ which is neglected by our prediction. In the right panel of Fig. 3.4, we show that $p(x, u > 0)$, i.e. the population with positive active force is very small in the region $x \leq 0$ and thus provide only a negligible contribution to the density $\rho(x)$ for $x \leq 0$. This roughly validates the approximation leading to Formula (3.12). In addition, $p(x, u \geq 0)$ decreases much faster than $p(x, u \leq 0)$ as x becomes more negative. Such a scenario resembles the observations of Widder and Titulaer obtained for a related model [157], in the presence of partially absorbing walls with specular reflection. They found that $p(x, u)$ at the boundary (i.e. $x = 0$) was peaked at negative values of u and rapidly decreasing towards zero for positive u . With Eq. (3.12) we generalize the result of [155] to a soft-wall, which is modeled as an external truncated potential. Moreover, we overcome the unphysical results of the UCNA approximation at $D_t = 0$ presented in ref.[136], where the prediction for the density is a discontinuous function of x .

3.3.2 Central region

In the force-free regions, we cannot recover the numerical phenomenology by setting to zero the external potential in Eq. (3.10), nor for $D_t = 0$ nor for $D_t > 0$. With this simple choice we obtain a constant $\rho(x)$ between $(0, 2L)$, while the numerical $\rho(x)$ shows a smooth decay from the value at $x = 0, 2L$

towards the value in the middle of the box, $x = L$. To find an approximation scheme for $\rho(x)$, we develop a hydrodynamic approach for which it is useful to switch to the (x, v) representation of the distribution function. Since in a force-free system $f(x, v)$ is a Maxwell-Boltzmann distribution, we expand $f(x, v)$ in Hermite functions of the velocity, taking into account only a few leading terms. To find an approximate solution of the FPE (3.9) in the central region, we employ the following Hermite expansion:

$$f_c(x, v) = \left(\frac{\tau}{2\pi D_a}\right)^{1/2} \sum_{\nu \geq 0} n_\nu(x) h_\nu(v) \exp\left(-\frac{\tau}{2D_a} v^2\right), \quad (3.13)$$

where the Hermite polynomials are

$$h_\nu(v) = (-1)^\nu \left(\frac{D_a}{\tau}\right)^{\nu/2} \exp\left(\frac{\tau}{2D_a} v^2\right) \frac{d^\nu}{dv^\nu} \exp\left(-\frac{\tau}{2D_a} v^2\right). \quad (3.14)$$

By substituting the above expansion in the FPE (3.9) with $k = 0$ we find recursion relations for the amplitudes n_ν for the steady state:

$$\frac{\partial n_{\nu-2}(x)}{\partial x} + \nu \frac{D_a}{\tau} \frac{\partial n_\nu(x)}{\partial x} = -\frac{\nu-1}{\tau} n_{\nu-1}(x) + D_t \frac{\partial^2}{\partial x^2} n_{\nu-1}(x), \quad (3.15)$$

assuming the condition $n_{-1} = 0$ and defining $\rho(x) \equiv n_0(x) = \int dv f_c(x, v)$. It is convenient to introduce the steady-state average polarization, $m(x)$, as the first moment of the velocity distribution function:

$$m(x) = \int dv v f_c(x, v) = \frac{D_a}{\tau} n_1(x). \quad (3.16)$$

For $D_t = 0$, since $u = v$ in this region, $m(x)$ is proportional to the local average of the self-propulsion. Thus, $m(x)$ vanishes in the absence of external forces because of Eq. (3.4), as shown by Eq. (3.16) and Eq. (3.15) for $\nu = 1$:

$$\frac{\partial m(x)}{\partial x} = D_t \frac{\partial^2}{\partial x^2} n_0(x), \quad (3.17)$$

and assuming a zero current condition. On the contrary, if $D_t > 0$, the absence of external forces does not mean that $m(x) = 0$. Indeed, using again Eq. (3.17) and considering a finite density gradient term $D_t \frac{\partial n_0(x)}{\partial x}$, we can induce a polarization even if the external force is locally zero. In particular, the coupling between diffusion and polar order leads to an effective force between an object immersed into an active suspension, as explicitly evaluated in SubSection 3.3.3.

Eqs. (3.15) are an infinite hierarchy of coupled differential equations for the coefficients n_ν . To capture the phenomenology discussed numerically, we need to develop a suitable truncation procedure coming easily in the Hermite-basis: we set $n_\nu(x) = 0$ for all $\nu \geq n_{max}$, which means to assume

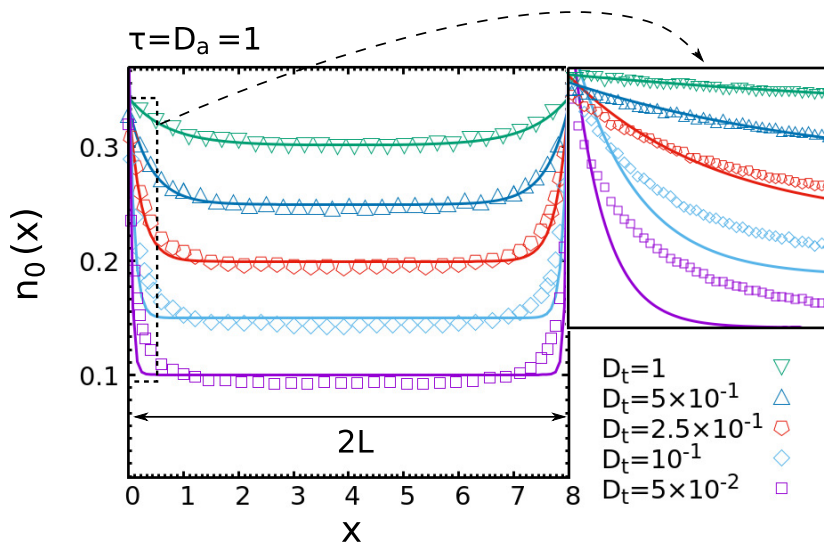


Figure 3.5: System with translational noise for different values of D_t , as shown in the legend: comparison between $n_0(x)$ computed numerically (symbols) and analytically from Eq.(3.21) (solid lines) where λ is the screening length predicted by the Eq. (3.20). Parameters: $D_a = \tau = 1$, $k = 10$. For the sake of clarity we applied to each curve a shift 0.05 with respect to the curve below. In the inset we display a magnification of the region in the proximity of the wall.

corrections around a Gaussian-like approximation. We consider two possibilities: case A, where we set $\nu_{max} = 2$, which gives rise to the screening-approximation. Case B, where we assume $\nu_{max} = 4$. The latter closure is equivalent to develop the hydrodynamic treatment based on the first three moments of the distribution of the velocity [158], assuming that the analog of the heat flux, $n_3(x)$, can be replaced by the spatial gradient of a kinetic temperature, represented by $n_2(x)$. Using Eq. (3.17) to eliminate $n_0(x)$, we write the following equations:

$$\frac{1}{\tau} \left(1 + \frac{D_a}{D_t}\right) m(x) - D_t \frac{\partial^2}{\partial x^2} m(x) + 2 \frac{D_a^2}{\tau^2} \frac{\partial n_2(x)}{\partial x} = 0, \quad (3.18)$$

$$\frac{\tau}{D_a} \frac{\partial m(x)}{\partial x} + \frac{2}{\tau} n_2(x) - D_t \frac{\partial^2}{\partial x^2} n_2(x) + 3 \frac{D_a}{\tau} \frac{\partial n_3(x)}{\partial x} = 0. \quad (3.19)$$

The closure is $n_2(x) = 0$ in case A while it is $n_3(x) = -\frac{\tau}{3} \frac{\partial n_2(x)}{\partial x}$ in case B, in analogy with the phenomenological procedures adopted in hydrodynamic treatments. Both closures lead to exponential solutions for $n_0(x)$ and $m(x)$. For the sake of simplicity, we report just the result for the screening approximation (case A), which has been originally developed in [155] for the ABP model. The combination of two walls leads to a hyperbolic profile of $n_0(x)$

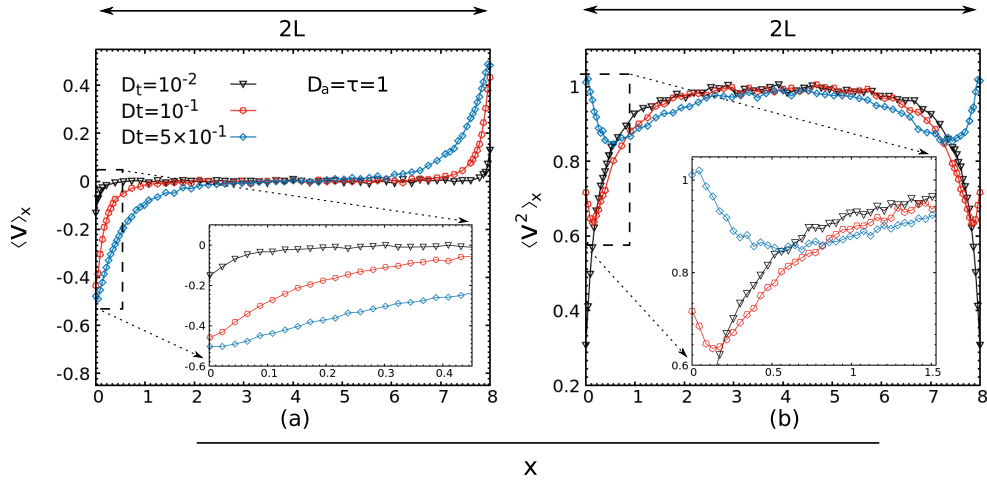


Figure 3.6: Panels (a) and (b) show $\langle v \rangle_x$ and $\langle v^2 \rangle_x$, respectively, for three different values of D_t as shown in the legend. The parameters of the active force are fixed as $\tau = D_a = 1$ while $k = 10$.

and $m(x)$ whose decay lengths are

$$\lambda = \sqrt{\frac{\tau D_t^2}{D_a + D_t}}. \quad (3.20)$$

This typical length increases as D_t grows [155]. Explicitly, $n_0(x)$ reads

$$n_0(x) = (n_w - n_M) \frac{\cosh(\frac{x-L}{\lambda})}{\cosh(\frac{L}{\lambda})} + n_M, \quad (3.21)$$

where $n_w = n_0(0) = n_0(2L)$ and n_M depends on the geometry of the problem while $m(x)$ is given by:

$$m(x) = m_w \frac{\sinh(\frac{x-L}{\lambda})}{\cosh(\frac{L}{\lambda})} = \frac{D_t}{\lambda} (n_w - n_M) \frac{\sinh(\frac{x-L}{\lambda})}{\cosh(\frac{L}{\lambda})} \quad (3.22)$$

being m_w the polarization field at the wall. In Fig.3.5 we compare $n_0(x)$ obtained from simulations with the analytic prediction (3.21), finding a good agreement when D_t is not too small with respect to D_a . In particular, the inset of Fig.3.5 enlarges a thin region near the left wall showing the increase of the decay length as D_t grows both for data and predictions. Indeed, we notice that the polarization field (given by Eq.(3.22)) vanishes if $D_t = 0$ at variance with numerical data.

In Fig. 3.6 (a) and (b) we plot $\langle v \rangle_x$ and $\langle v^2 \rangle_x$, respectively, for different values of D_t . The parameters of the active force are fixed to deal with a large persistence. We observe that $\langle v \rangle_x$ decays monotonically to 0, displaying a negative and a positive profile for the left and the right wall, respectively, in such a way that $\int dx \langle v \rangle_x = 0$. The decay length decreases as D_t becomes

smaller and disappears when $D_t \ll D_a$, in the limit of negligible thermal noise. Instead, $\langle v^2 \rangle_x$ displays a non-monotonic behavior, decreasing in a thin region close to the wall, until to reach a minimum, and then increasing again towards D_a/τ , i.e. the limit value of $\langle v^2 \rangle_x$ (being $D_t \ll D_a$). This effect cannot be explained by the Gaussian closure ($n_2 = 0$) and requires the truncation of the hierarchy (3.15) at a higher level. This analysis is not included in the present thesis.

We point out that the screening length result is consistent with [155], where the authors found the same profile for the ABP model. This fact confirms that the AOUP can be considered as a useful approximation of ABP since AOUP can reproduce the leading phenomenology of the accumulation phenomenon even in the presence of the thermal noise. In addition, the simplicity of the AOUP allows us to reduce the dimensionality of the problem and to shed some light on the hydrodynamic-like approach which can be evaluated in terms of the particle velocity.

Beyond the Gaussian approximation for systems without thermal noise.

In the absence of thermal noise, $\langle v \rangle_x$ vanishes, as expected from the hydrodynamic approach at variance with the case $D_t > 0$. Nevertheless, the higher-order moments reveal a space-dependent profile which cannot be explained by the simpler closure, Eq. (3.21), since the limit $D_t \rightarrow 0$ is singular. To confirm our statement, in Fig. 3.7 (a)-(d) we study the moments of the distribution, from the second to the fifth, for different parameters of the active force. In panels (a) of Fig.3.7 we study the spatial profile of $\langle v^2 \rangle_x$ which grows until reaches the middle of the box. In the bulk, between $(0, 2L)$, we can distinguish two symmetric thin regions close to the walls where $\langle v^2 \rangle_x < D_a/\tau$ and a central region where $\langle v^2 \rangle_x \approx D_a/\tau$. In virtue of the fact that D_a/τ is the value of $\langle v^2 \rangle_x$ for a confinement-free system, the latter is a bulk region. Instead, the former are regions deeply influenced by the presence of the walls. In the case, $D_a = 10$ the saturation does not occur and thus the bulk-region is absent since the persistence length $\sqrt{D_a\tau}$ is comparable with the size of the box, L . The same analysis holds for the third moment, plotted in panel (b) of Fig.3.7. In this case, and in general for all the odd moments, the bulk-value is zero and a clear profile emerges in the regions near the walls.

The hierarchy (3.15) with $D_t = 0$ and $\nu = 2$, predicts that $n_0(x)$ and $n_2(x)$ are related by the following relation

$$\frac{\partial n_0(x)}{\partial x} + 2 \frac{D_a}{\tau} \frac{\partial n_2(x)}{\partial x} = 0,$$

being $n_1(x) = n_0(x)\langle v \rangle_x/(D_a/\tau) = 0$. Therefore, the Gaussian closure $n_2(x) = 0$, which leads to Eq. (3.21), would predict constant profiles for n_0 and for all the moments in the force-free region: in particular, the odd

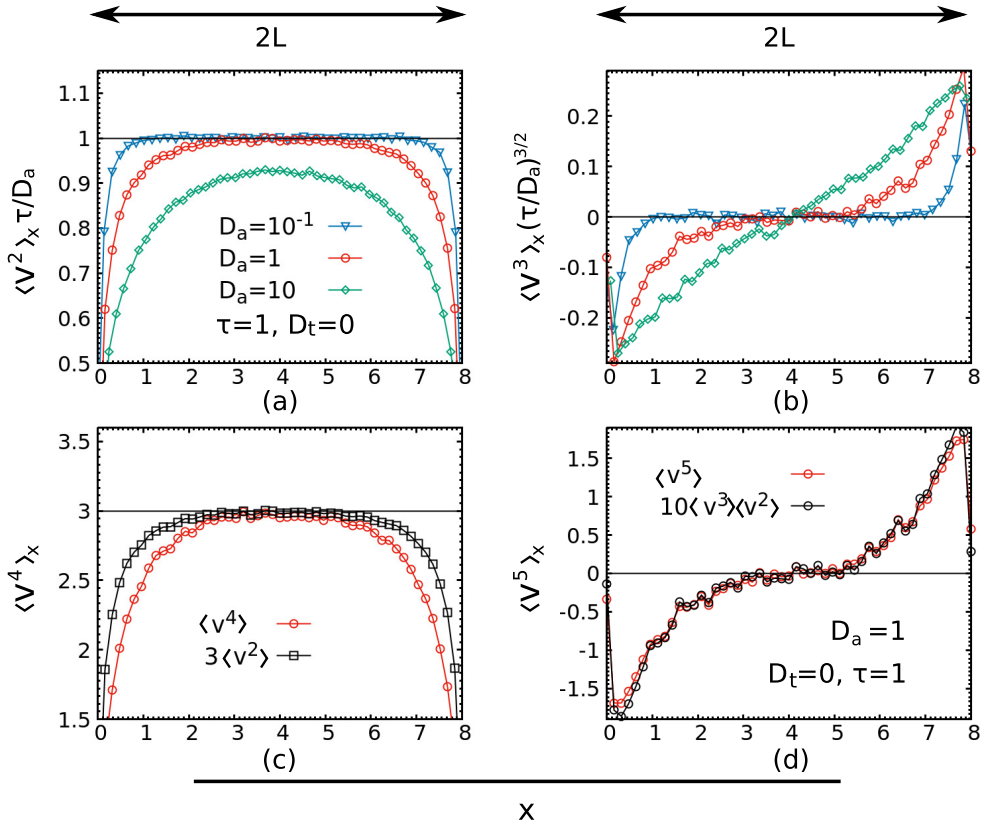


Figure 3.7: Panel (a) and (b): the second and third moment of the velocity $\langle v^2 \rangle_x$ and $\langle v^3 \rangle_x$ as a function of the position x for $D_t = 0$ and different values of $\sqrt{D_a \tau}$, as shown in the legend, and $k = 10$. In panel (c) we display the comparison between $\langle v^4 \rangle_x$ and the Gaussian closure $3 \langle v^2 \rangle_x$ when $\tau = D_a = 1$ and $D_t = 0$: the deviation from the Gaussian prediction $\langle v^3 \rangle_x = 0$ and $\langle v^4 \rangle_x = 3 \langle v^2 \rangle_x \langle v^2 \rangle_x$ is evident. In panel (d) in the case $\tau = D_a = 1$ and $D_t = 0$, we compare the average $\langle v^5 \rangle_x$ with the empirical closure $10 \langle v^2 \rangle_x \langle v^3 \rangle_x$.

moments would be zero. This is not consistent with the numerical data, implying the failure of the Gaussian approximation. In addition, the following relations should hold for a Gaussian distribution of the velocities: $\langle v^{2n+1} \rangle_x = 0$ and $\langle v^{2n} \rangle_x = C_{2n,2} \langle v^2 \rangle_x^n$, where $C_{2n,2}$ is the binomial coefficient. As a further confirmation of the failure of the gaussian closure, in panel (c) of Fig. 3.7, such a relation is numerically compared for the fourth moment and shows evident deviations from the Gaussian prediction.

To capture the observed behavior, we employ a higher-order truncation of Eq.(3.13), considering terms $n_\nu(x)$ with $\nu = 4$ in the Hermite expansion. In this way, one can obtain a solution for $n_0(x)$ with the same form of Eq. (3.21) with a screening length, $\lambda = \sqrt{5D_a \tau}/6$, which is proportional to the persistent length, $\sqrt{D_a \tau}$, and captures the phenomenology of the density even for $D_t = 0$. The details of the calculations are reported in Appendix

3.B. In what follows, we only discuss the approximate factorization of the fifth velocity moment employed to close the hierarchy, which is:

$$\langle v^5 \rangle_x \sim 10 \langle v^2 \rangle_x \langle v^3 \rangle_x. \quad (3.23)$$

The factor 10 counts the number of ways to factorize the average. In addition, in appendix 3.B, we present an argument to support the factorization (3.23). Fig. 3.7(d) plot the numerical comparison between $\langle v^5 \rangle_x$ and $10 \langle v^2 \rangle_x \langle v^3 \rangle_x$, showing the validity of Eq. (3.23) and confirming our methods.

3.3.3 Forces on the confining walls

The derivation of the pressure for an active suspension of active particles has been a controversial matter in the literature [108, 98, 159] with particular attention towards the existence of an equation of state [107]. Nevertheless, since self-propelled particles are far from equilibrium, the only definition of pressure which is physically meaningful is the mechanical one, \mathcal{P}_{wall} , i.e. the force per unit area exerted by the active gas on the wall. By assuming the mechanical balance condition, \mathcal{P}_{wall} is proportional to the force exerted by the wall on the N particles spatially distributed according to $n_0(x)$, which we write for the left-wall for the sake of simplicity:

$$\mathcal{P}_{wall} = -N \int_{-\infty}^0 dx n_0(x) U'(x). \quad (3.24)$$

The upper limit of the integral comes from the shape of the left-wall potential which vanishes for $x > 0$. Using the harmonic shape of $U(x) = k/2x^2$ and the prediction (3.12) we get

$$\mathcal{P}_{wall} = N n_w D_a \gamma \left(\frac{1}{\Gamma} + \Delta \right) s(\Gamma, \Delta), \quad (3.25)$$

where $N n_w$ is the numerical density at $x = 0, 2L$, namely the edges of the walls, while the factor $D_a \gamma (\frac{1}{\Gamma} + \Delta)$ can be identified as the effective temperature of an active particle confined in a harmonic potential [73, 76]. The last factor in Eq. (3.25)

$$s(\Gamma, \Delta) = \frac{1}{1 + \frac{\Gamma-1}{1+\Gamma\Delta} \left[1 + \sqrt{1 + \frac{1+\Gamma\Delta}{\Gamma-1}} \right]} \leq 1, \quad (3.26)$$

takes into account the two main effects of the accumulation phenomenology: i) the shift of the peak of the density towards negative x and ii) its broadening. Eq.(3.25) can be considered as the generalization of the ideal gas formula to an active suspension of particles in the dilute regime. Indeed, $\Gamma = s(\Gamma, \Delta) = 1$ for $\tau = 0$ and, thus, Eq. (3.25) reduces to $N n_w (D_a \gamma + D_t \gamma)$ which is nothing but the pressure exerted against a wall by Brownian particles at effective temperature $D_a \gamma + D_t \gamma$.

The wall boundary conditions

In the pressure formula (3.25), we need to determine the constant n_w , which depends on the interplay between the parameters of the active force and the size of the box. Let us multiply the FPE (3.9) by v and integrate out v . Using the “no particle flux” condition, which we report for completeness

$$\frac{D_a}{\tau}n_1(x) = D_t \frac{\partial}{\partial x}n_0(x), \quad (3.27)$$

we derive the following expression

$$\begin{aligned} \frac{\partial}{\partial x} \left(\left(\frac{D_a}{\tau} + \frac{D_t}{\tau} \right) n_0(x) + 2 \frac{D_a^2}{\tau^2} n_2(x) - D_t^2 \frac{\partial^2}{\partial x^2} n_0(x) - \frac{D_t}{\gamma} U''(x) n_0(x) \right) \\ = - \frac{U'(x)}{\tau\gamma} n_0(x). \end{aligned} \quad (3.28)$$

Integrating Eq. (3.28) with respect to x between $-\infty$ and \bar{x} (with $\bar{x} > 0$), we get

$$\begin{aligned} \tau\gamma \left(\frac{(D_a + D_t)}{\tau} n_0(x) + 2 \frac{D_a^2}{\tau^2} n_2(x) - D_t^2 \frac{\partial^2}{\partial x^2} n_0(x) - \frac{D_t k}{\gamma} \theta(-x) n_0(x) \right)_{-\infty}^{\bar{x}} \\ = \frac{\mathcal{P}_{wall}}{N}, \end{aligned} \quad (3.29)$$

where we have used Eq. (3.24). Such a formula will be very useful in the next subsections, where we adapt the pressure formula to two cases: the semi-infinite system and the slit system.

Semi-infinite system.

Now, we restrict our analysis to the range of applicability of our theory: when D_t is not too small with respect to D_a , excluding so the singular limit $D_t = 0$. We also assume that $\bar{x} \gg \lambda$, meaning that $n_2(\bar{x}) \approx 0$ and so that a bulk-region, where the system behaves as in the force-free case, exists. The left-hand side of Eq. (3.29), using Eq. (3.21), can be compared with the result:

$$\mathcal{P}_{wall} = D_a \gamma \left(1 + \Delta \right) N n_M. \quad (3.30)$$

By means of Eq.(3.25), i.e. of the expression for \mathcal{P}_{wall} , we obtain n_w in terms of n_M and of the other parameters of the model:

$$n_w = n_M \frac{1 + \Delta}{\frac{1}{\bar{r}} + \Delta} \frac{1}{s(\Gamma, \Delta)}. \quad (3.31)$$

We remark that $n_w > n_M$ because, if $\tau > 0$, both factors $\frac{1+\Delta}{\frac{1}{\bar{r}}+\Delta}$ and $\frac{1}{s(\Gamma, \Delta)}$ are larger than 1. Thus, the wall density is higher than the density at middle of the box and there is a positive surface excess. For $\tau = 0$, i.e. in the Brownian limit, we have $n_w = n_M$ for all k .

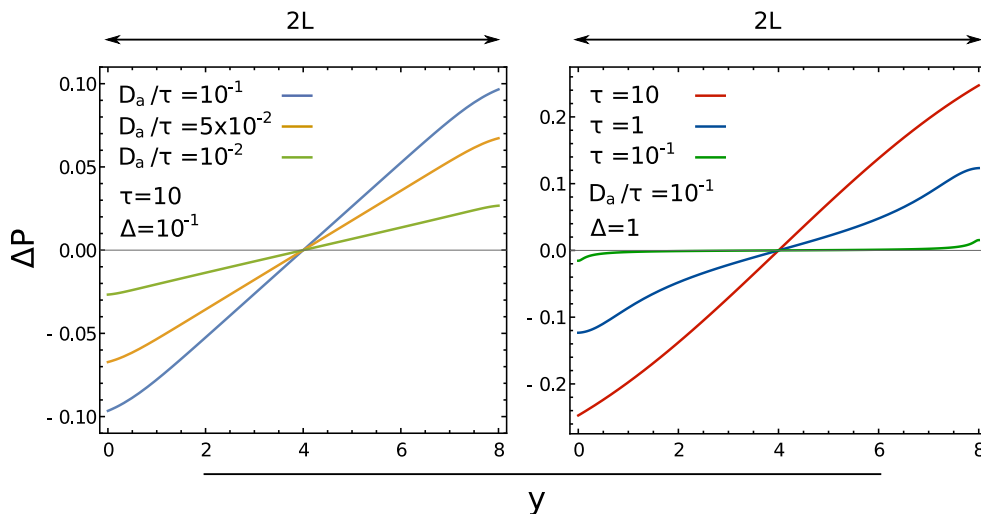


Figure 3.8: Pressure difference between two compartments hosting two active suspensions having the same average numeric density of particles. Panel (a) corresponds to a system where the persistence time is fixed and so the ratio between the active and thermal diffusion coefficient, but the active power is varied. The largest active power corresponds to the largest pressure difference. Panel (b): The active power is fixed, but the persistence time τ is varied. When τ increases the pressure difference increases as the system departs more and more from thermodynamic equilibrium.

In the limit of semi-infinite system, namely $L \rightarrow \infty$, we obtain $n_0(x) = (n_w - n_M)e^{-x/\lambda} + n_M$ and we can identify $\rho = Nn_M$ and $\rho_w = Nn_w$, being ρ and ρ_w the bulk and wall numerical densities, respectively. Using the mechanical equilibrium condition, $\mathcal{P}_{bulk} = \mathcal{P}_{wall}$, the right hand side of (3.30) can be identified with the bulk pressure, \mathcal{P}_{bulk} , of a system uniformly distributed at density ρ , i.e. $\mathcal{P}_{bulk} = D_a\gamma(1 + \Delta)\rho$.

Wall Pressure in a slit system.

Now, we study the pressure in a slit-like geometry. To obtain a prediction for the active pressure, we need to compute $n_0(x)$ in the whole space. To calculate the density at the wall, n_w , we must match the expression (3.12) with (3.21) at each wall and then impose the normalization of the profile in such a way that $n_0(x)$ can be written as:

$$n_0(x) = \theta(-x)n_0^{left}(x) + \theta(-x)\theta(2L-x)n_0^f(x) + \theta(2L-x)n_0^{right}(x), \quad (3.32)$$

where $n_0^{left(right)}(x)$ is the spatial probability density in the left and right wall-regions, given by Eq. (3.12), while $n_0^f(x)$ is the density in the central region, within $[0, 2L]$, given by Eq. (3.21). The normalization of the whole

probability implies the condition:

$$\int_0^{2L} dx n_0^f(x) + 2 \int_{-\infty}^0 n_0^{left}(x) = 1, \quad (3.33)$$

where the factor 2 in the second addend is due to the left-right symmetry of the two walls. Integrating and, then, eliminating the integrals we get:

$$\begin{aligned} \frac{1}{n_w} = & \frac{2}{\sqrt{\pi}} \left(\frac{2\gamma D_a (1 + \Gamma\Delta)}{k\Gamma} \right)^{1/2} \arctan \left(\sqrt{\frac{(1 + \Gamma\Delta)}{\Gamma - 1}} \right) \\ & + 2\lambda \tanh\left(\frac{L}{\lambda}\right) + 2 \frac{\frac{1}{\Gamma} + \Delta}{1 + \Delta} \frac{L - \lambda \tanh\left(\frac{L}{\lambda}\right)}{1 + \frac{\Gamma-1}{1+\Gamma\Delta} \left[1 + \sqrt{1 + \frac{1+\Gamma\Delta}{\Gamma-1}} \right]}. \end{aligned} \quad (3.34)$$

The first addend of the r.h.s. of Eq.(3.34) is due to the softness of the walls and, thus, vanishes in the limit $k \rightarrow \infty$ for all values of the active force parameters. Eq.(3.34) is consistent with the equilibrium limit $\tau \rightarrow 0$ which reads

$$\begin{aligned} \lim_{\tau \rightarrow 0} \mathcal{P}_{wall} &= N n_w D_a \gamma (1 + \Delta) \\ \lim_{\tau \rightarrow 0} \frac{1}{n_w} &= \left(\frac{2\pi D_a \gamma (1 + \Delta)}{k} \right)^{1/2} + 2L \geq 2L. \end{aligned} \quad (3.35)$$

In this case, \mathcal{P}_{wall} corresponds to the pressure of an overdamped passive system with thermal bath at temperature $\gamma(D_a + D_t)$ while the density at the wall is reduced by a factor which depends on k among the other parameters. Taking the hard-wall limit, $k \rightarrow \infty$, we have $n_w = 1/2L$ and $\mathcal{P}_{wall} = \frac{N}{2L} D_a \gamma (1 + \Delta)$, which is the equilibrium equation of state of a colloid at effective temperature $\gamma(D_a + D_t)$, as we expected.

Effective force between plates and Casimir effect

Let us restrict to the hard-wall limit, $k \rightarrow \infty$, in the non-equilibrium case with $\tau > 0$. Eq.(3.34) proves the accumulation at the wall, being $n_w \geq 1/2L$, quantifying its value in terms of the active force parameters. Inserting Eq. (3.34) in Eq. (3.25) we can compute the wall pressure, which we report in the limit $k \rightarrow \infty$ for the sake of simplicity

$$\mathcal{P}_{wall} = D_a \gamma \frac{N}{2L} \frac{(1 + \Delta)}{1 + \frac{\lambda}{L} \tanh\left(\frac{L}{\lambda}\right) \left(\frac{1}{\Delta} + \frac{(1+\Delta)^{3/2}}{\Delta^2} \right)}. \quad (3.36)$$

Our theory can provide a quantitative prediction of another phenomenon occurring in the presence of two parallel plates: even in the case of non-interacting particles, an effective force between the plates is induced. To show this result we compare the pressure of two systems with different sizes, L_1 and L_2 , with $L_1 < L_2$ without loss of generality. The systems are chosen with the same average density $\bar{\rho} = \frac{N_i}{2L_i}$. According to Eq. (3.36), the smaller

system will exert the lower pressure on the wall. Thus, we conclude that two parallel plates immersed in a sea of non-interacting active particles feel an effective attractive force. In particular, if $L_2 \rightarrow \infty$ with fixed $\bar{\rho}$ and with the condition $L_1/\lambda \gg 1$, we obtain

$$\mathcal{P}_{wall}^{(1)} - \mathcal{P}_{wall}^{(2)} \approx -D_a \gamma \bar{\rho} \left(\frac{(1 + \Delta)}{\Delta} + \frac{(1 + \Delta)^{5/2}}{\Delta^2} \right) \frac{\lambda}{L}. \quad (3.37)$$

Therefore, the pressure difference increases linearly with D_a and decreases monotonically with the plate separation, L . Such a result is in agreement with the numerical work of Ni et al. [160] and with theoretical work of Vella et al. [161] which predicts a decay $\propto 1/L$.

This effect emerges also by the following gedanken-experiment: let us consider a box of size $2L$ and insert a hard wall (which we call wall C) at an arbitrary position $y \in (0, 2L)$ creating two compartments. For the sake of simplicity, we choose the wall C equal to the lateral walls of the box. Then, we introduce the active gas within the two compartments in such a way that their average numerical densities are equal. This implies the condition $N_l/y = N_r/(2L - y)$ with $N_l + N_r = N$, being N_l and N_r the numbers of particles in the left and right compartments with sizes $y < 2L$ and $2L - y$, respectively. Our theory predicts that the pressure difference, $\Delta\mathcal{P}$, on the central wall is

$$\Delta\mathcal{P} = D_a \gamma (1 + \Delta) \left[\frac{N_l}{y} \frac{1}{1 + \frac{\lambda}{y} \tanh(\frac{y}{\lambda}) \left(\frac{1}{\Delta} + \frac{(1+\Delta)^{3/2}}{\Delta^2} \right)} - \frac{N_r}{(2L - y)} \frac{1}{1 + \frac{\lambda}{2L-y} \tanh(\frac{2L-y}{\lambda}) \left(\frac{1}{\Delta} + \frac{(1+\Delta)^{3/2}}{\Delta^2} \right)} \right]. \quad (3.38)$$

In the limit $\tau \rightarrow 0$, i.e. for a Brownian system, $\Delta\mathcal{P}$ reads zero for any y , because of the condition $N_l/y = N_r/(2L - y)$. In Fig. 3.8 we plot the pressure difference, given by Eq.(3.38) for difference values of D_a/τ , for a large value of τ (panel (a)), and varying τ but at fixed D_a/τ (panel (b)). Following both these procedure we get a non-vanishing pressure difference as larger as τ (or D_a/τ) increases. In particular, $\Delta\mathcal{P} < 0$ if $y < L$ and $\Delta\mathcal{P} > 0$ if $y > L$. Such a strange phenomenology can be understood by observing that larger is τ at fixed D_a/τ (or D_a/τ at fixed τ) bigger is the fraction of particles accumulating in front of the walls, meaning that more collisions occur per unit time. When the size of one of the two compartments is larger, then more particles are available to accumulate in front of the walls and so a larger pressure is exerted from that side.

For small $2L$ the approximations at the basis of the pressure calculations, i.e. $n_2(x) \approx 0$, do not work. Therefore, we expect that the force does not scale as L^{-1} . A further improvement of Eq.(3.38) could be obtained by considering a higher-order closure, including terms n_3 and n_4 , for instance.

3.4 Role of the chirality: accumulation in the bulk region

As mentioned in Chapter 1, several microswimmers could exhibit spiral or circle trajectories, for instance, when they move or swim in aqueous solutions. A similar phenomenology has been experimentally observed for microswimmers swimming in channels with a Poiseuille flow: in this case, even non-chiral particles behave as if their dynamics were governed by an effective chirality. This is confirmed by experimental studies, realized by Stocker et coworkers [138] using four different species of Phytoplankton, which represent some experimental realizations of the phenomenology which we are going to present and explain.

In the present Section, we consider active chiral particles immersed in a semi-infinite container evaluating the effects of the chirality on the accumulation near boundaries presented both numerically and theoretically in the previous Sections. The position, \mathbf{x} , of the microswimmer evolves with Eq.(3.1) while the dynamics of \mathbf{f}_a is described by the chiral version of the AOUP model which we rewrite for clarity:

$$\tau \dot{\mathbf{f}}^a = -\mathbf{f}^a + \Omega \tau \hat{\mathbf{z}} \times \mathbf{f}^a + \sqrt{2D_a} \mathbf{w}. \quad (3.39)$$

We remark that the present study could be easily adapted to the chiral ABP model. As usual, the choice of the model is dictated by the simpler mathematical structure of the AOUP, which facilitates the theoretical treatments with respect to the ABP. At variance with the non-chiral case, both x and y directions matter and the reduction to a one-dimensional problem is not possible neither for the AOUP dynamics.

Also in the chiral case, it is possible to derive the equation of motion of the microswimmer velocity, $\mathbf{v} = \dot{\mathbf{x}}$, switching from the description in $(\mathbf{x}, \mathbf{f}^a)$ to (\mathbf{x}, \mathbf{v}) variables. Using the same trick of Sec.2.2 of Chapter2, we get in the case $D_t = 0$ [89]:

$$\dot{\mathbf{v}} = -\frac{\nabla U}{\gamma \tau} - \frac{1}{\tau} \Gamma \cdot \mathbf{v} + \frac{\sqrt{2D_a}}{\tau} \boldsymbol{\eta} + \Omega \hat{\mathbf{z}} \times \mathbf{v} + \frac{\Omega}{\gamma} \hat{\mathbf{z}} \times \nabla U, \quad (3.40)$$

where Γ is the same space-dependent friction matrix obtained in Sec.2.2 in the case $\Omega = 0$, whose components are:

$$\Gamma_{\alpha\beta} = \delta_{\alpha\beta} + \frac{\tau}{\gamma} \nabla_\alpha \nabla_\beta U. \quad (3.41)$$

As discussed in Sec.2.2 for the case $\Omega = 0$, Eq.(3.40) represents the dynamics of an underdamped particle in contact with a thermal and under the effect of a space dependence Stokes force depending on the external potential. The novel, due to the presence of chirality, resides in the last two terms both $\propto \Omega$. The first one, the third addend of the right-hand side of Eq.(3.40), has the form of an effective Lorentz force with amplitude Ω , being orthogonal

to \mathbf{v} . This term rotates the particle velocity conserving its modulus and producing circular-like trajectories. Instead, the second one, i.e. the fourth addend of the right-hand side of Eq.(3.40), couples chirality and external potential because it is orthogonal to the external force. Such a description will be particularly useful in what follows. We observe that Eq.(3.40) can be easily generalized to the presence of an additional thermal noise without any complications.

In previous Sections, we have shown that self-propelled particles with $\Omega = 0$ accumulate in the proximity of repulsive walls[150, 162]. Such a non-equilibrium phenomenon becomes more pronounced for large values of the persistence time, τ , and when D_a/τ is larger than the amplitude of the thermal noise, γD_t . Intuitively, when the self-propulsion pushes a particle along the direction normal to the surface of the wall, the particle remains trapped and can escape only when the direction of the active force changes, typically after the average time τ . This mechanism leads the density to be peaked near obstacles, where the particle concentration is larger than the typical bulk value.

We expect that the chirality reduces the particles accumulation at the walls. Indeed, assuming that a particle is trapped for a typical time, t_w , before leaving the wall, we can show that t_w is a decreasing function of $|\Omega|$. This is suggested by the form of the two-time activity-activity correlation function, given by Eq.(1.12) discussed in Sec.1.2.3 of Chapter 1. Indeed, we remind that this correlation is characterized by two time-scales: τ and $1/\Omega$. In absence of chirality, $\Omega = 0$, $t_w \approx \tau$, being τ the typical time after which the inversion of the self-propulsion is possible. Instead, in the case $|\Omega| > 0$ the autocorrelation changes sign for $t_\Omega = \pi/(2\Omega)$, corresponding to the smallest zero of cosine. Thus, we can identify two regimes: i) $t_\Omega \gg \tau$, where the chirality plays a negligible role in the dynamics of the particle, meaning that $t_w \approx \tau$. ii) $t_\Omega \leq \tau$, where the correlation changes direction due to the chiral mechanism, i.e. for times smaller than τ . In this case, $t_w \sim t_\Omega$. Since in the regime i) a particle behaves as a non-chiral one, we restrict to regime ii) in what follows. Following the approach of Lee [145] we can distinguish between two different populations of particles: the bulk and the wall population, with n_b and n_w members, respectively. We call t_b and t_w the residence times associated to them. We observe that there is a continuous exchange of particles between the two groups and the condition $n_w/t_w = n_b/t_b$ holds in the stationary state. We conclude that the wall population decreases as t_w decreases, i.e. when Ω grows.

To understand the effects of the chirality in a confined system, we consider two different set-ups to model a semi-infinite channel. At first, we study an infinite parabolic channel with particles free to move along the y -direction and harmonically confined along x . In this case, due to the linearity of the problem, we can solve the Fokker Planck equation computing the steady-state probability distribution function. We shall show the existence of velocity currents induced by the chirality. Then, we consider the

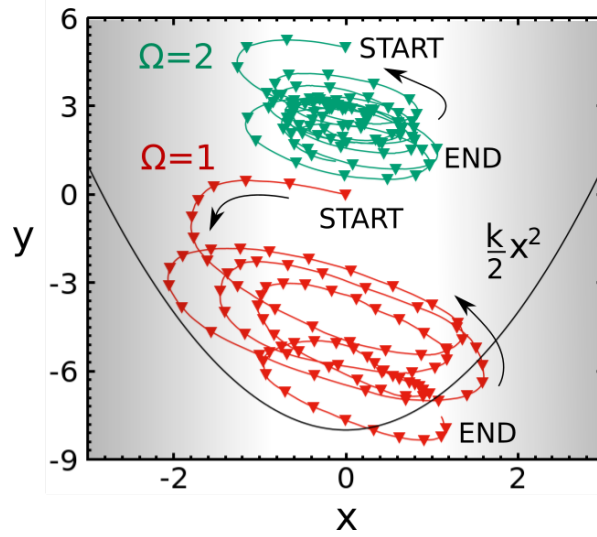


Figure 3.9: Two typical trajectories of active chiral particles confined to a parabolic channel. The particles perform spiral motion. Notice the stronger localisation of the particle near the bottom of the well, with increasing value of the torque Ω as predicted by Eq. (3.44).

slit confinement, already studied in Sec.3.1.1 for a non-chiral system. In this case, the chirality plays the opposite role of the self-propulsion decreasing the accumulation at the walls until to induce a bulk profile with particles accumulating in the middle of the channel.

3.4.1 Parabolic channel

A rough model of a semi-infinite channel can be obtained by considering a quadratic well along the x -direction, $U(\mathbf{x}) = k\frac{x^2}{2}$, with periodic boundary conditions on y . In this case, the linearity of the external force allows us to find the steady-state probability distribution function of the process, in the form of a multivariate Gaussian. The distribution shall contain three diagonal terms proportional to (v_x^2, v_y^2, x^2) and three cross terms of type $(v_x v_y, x v_y, x v_x)$. Indeed, the translational symmetry along the y -direction prevents the presence of terms which depend on y . The six amplitudes in the Gaussian are functions of the parameters of the potential and the active force: $k, \tau, \gamma, \Omega, D_a$. Their exact expressions are reported in appendix 3.C. In what follows, we write the distribution in a more transparent and simple form, expanding the coefficients of the Gaussian in powers of Ω , for the sake of simplicity, obtaining:

$$P(\mathbf{x}, \mathbf{v}) \approx \mathcal{N} \exp \left[-\frac{\tau}{2D_a} \left(\Gamma v_x^2 + v_y^2 + 2\frac{\Gamma-1}{\Gamma} \Omega \tau v_x v_y \right) \right] \exp \left[-\frac{\Gamma-1}{2D_a \tau} \Gamma x^2 \right] \exp \left[\Omega \frac{\tau}{D_a} \frac{\Gamma-1}{\Gamma} v_y x \right]. \quad (3.42)$$

Using whole distribution, reported in appendix 3.C we compute the x -dependent average velocity along the y -direction:

$$\langle v_y \rangle_x = \frac{\Gamma - 1}{\Gamma} \Omega x. \quad (3.43)$$

The above result shows the occurrence of a current parallel to the walls and directed along the downward y -direction for $x < 0$ and upwards for $x > 0$ [89]. The current in the two halves of the channel changes sign, reversing the sign of Ω . In the same way, we can prove that there is no average current, $\langle v_x \rangle_x$, along the x -direction. Integrating the distribution (3.89) over the velocities we obtain the density of the system

$$\rho(x) = \mathcal{N} \exp \left(-\frac{1}{2D_a\tau} \frac{\Gamma - 1}{\Gamma} (\Gamma^2 + \Omega^2\tau^2) x^2 \right). \quad (3.44)$$

The result is a Gaussian centered at $x = 0$ and the chirality affects only the variance of the distribution. Eq.(3.44) shows that the density is more localized near the center with respect to the non-chiral case, $\Omega = 0$, as if the chirality plays the role of an additional effective potential $\frac{\Gamma-1}{\Gamma} \Omega^2 \tau^2 x^2 / 2$, which pushes the particle towards the middle of the channel. Fig. 3.9 shows two typical trajectories of a single in the presence of the same harmonic potential but with different Ω : the increase of the chirality leads to more localized circular trajectories.

3.4.2 The slit

We turn, now, to study a more realistic channel, where the stiffness of the soft-walls and the width of channel are independent. The slit is realized with the same set-up of Sec.3.1.1, i.e. with two parallel repulsive soft-walls, with a harmonic truncated shape:

$$F_w(x) = k(x + L)\Theta(-x - L) - k(x - L)\Theta(x - L), \quad (3.45)$$

where, now, the potential-free region extends from $x = -L$ to $x = L$ and the wall-regions from $-\infty$ to $-L$ and from L to ∞ . Now, we choose k large enough to minimize the penetration inside the wall in such a way that the accumulation peaks are placed at $\sim -L$ and $\sim L$ in the non-chiral case. Along the y -direction we assume periodic boundary conditions to model a semi-infinite channel.

To confirm the qualitative argument described at the beginning of Sec.3.4, we measure the density at the walls, n_w . Such a study is not possible for harmonic confinements because the distinction between bulk and wall region is not clear. Instead, in the slit case n_w can be evaluated by counting the number of particles in the regions $x \geq L$ and $x \leq -L$ for the right and the left wall, respectively. In Fig. 3.10 we show n_w for the as a function of Ω for two different values of τ ($\tau = 1$ and $\tau = 10$) keeping fixed the ratio D_a/τ .

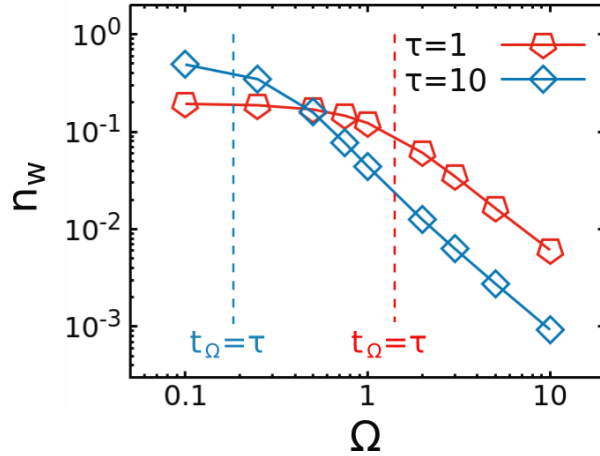


Figure 3.10: Density at the walls n_w versus Ω for two different values of $\tau = 1$ (red pentagons) and 10 (blue diamonds). The parameters are: $D_a = \tau$, $\gamma = 1$, $k = 10$, $L = 8$, and the walls are at positions $x = \pm L$.

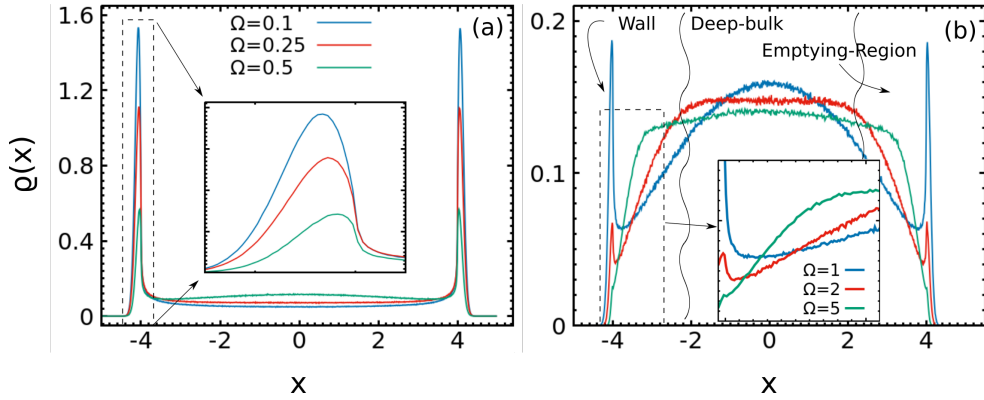


Figure 3.11: Density profile $\rho(x)$ for different values of Ω as shown in the legend: $\Omega = 0.1, 0.25, 0.5$ (Panel (a)), $\Omega = 1, 2, 5$ (Panel (b)). The control parameters are: $D_a = 10$, $\tau = 10$, $\gamma = 1$, $k = 10$ and $L = 4$. In the insets, we report the zoomed profiles in regions delimited by dashed vertical lines.

We find that n_w is roughly constant until the condition $t_\Omega = 2\pi/\Omega \geq t_w \approx \tau$ is satisfied [regime i)], meaning that the chirality does not affect the accumulation near the walls. Instead, when $t_\Omega \leq t_w$ the population at the wall, n_w , decreases as $\sim 1/\Omega$ [regime ii)]. Therefore, in what follows we restrict to the regime ii).

To unveil the effect of the chirality on the accumulation near the wall, In Fig.3.19 we plot the density distribution, $\rho(x)$ for different values of Ω . We choose τ and D_a/τ to deal with a configuration which shows strong accumulation in the non-chiral case In panel (a) of Fig .3.19, we introduce a small chirality, whose effect is to reduce the peaks of $\rho(x)$ in front of the two walls. Increasing Ω the role of the chirality is richer: on one hand, particles accumulate near the wall (less than the case $\Omega = 0$), on the other hand, a

bulk profile occurs. A layer near the walls is left empty and particles prefer to populate the middle of the channel, as shown in panel (b) of Fig.3.19. Further growth of Ω depletes the two symmetric peaks of $\rho(x)$ in favor of bulk region until the wall regions remain empty for very large Ω . In such a strong chiral regime, the situation is inverted with respect to the case $\Omega = 0$: particles leave the wall and the region adjacent to it [89]. We point out that, at variance with active chiral particles confined by harmonic potential, in a slit system we can observe a transition from wall to bulk accumulation. This phenomenon has been observed for different species of Phytoplankton in recent experiments conducted by Stocker and coworkers [138]. In particular, they can measure the density distribution for a section of the channel discovering that particles prefer to leave the boundaries in favor of the middle of the bulk. A similar scenario occurs also for elongated microswimmers confined in a channel, which swim due to the self-propulsion (ABP or AOUP dynamics) in the presence of an additional Poiseuille flow [163]. In this case, the interplay between the elongated shape and the flow induces rotations in the microswimmer dynamics, generating an effective chirality and leading to a similar phenomenology.

The emptying of the wall region in favor of the middle of the channel when $\Omega \neq 0$ can be understood evaluating the effect of the chirality on the particle velocity. Adapting Eq.(3.40) to the slit geometry, the equations of motion for \mathbf{v} take the simple form

$$\dot{v}_x = - \left[1 + (\Gamma - 1) (\Theta(-x - L) + \Theta(x - L)) \right] \frac{v_x}{\tau} - \Omega v_y, \quad (3.46)$$

$$- \Theta(-x - L) \frac{k}{\gamma\tau} (x + L) - \Theta(x - L) \frac{k}{\gamma\tau} (x - L) + \frac{\sqrt{2D_a}}{\tau} \eta_x$$

$$\dot{v}_y = - \frac{v_y}{\tau} + \Omega v_x + \frac{\Omega}{\gamma\tau} [k(x + L)\Theta(-x - L) + k(x - L)\Theta(x - L)] + \frac{\sqrt{2D_a}}{\tau} \eta_y. \quad (3.47)$$

As mentioned before, the chirality behaves as an effective magnetic field of strength Ω , which rotates the direction of the velocity without modifying its modulus, independently of the presence of the external force (second addends of Eqs.(3.46) and (3.47)). Instead, the interplay between chirality and wall-repulsion for $|x| > L$ generates a tangential force along the unbounded direction (third addend of Eq.(3.47)). Such a force, which acts in the wall regions, produces a local net momentum current along y : positive and negative on the right and left boundary, respectively. The two contributions are symmetric in such a way that $\int dx \langle v_y \rangle_x = 0$. Let us sketch the typical steps of the dynamics: when a particle reaches the potential region, its v_x is strongly damped by the Stokes force, $-\Gamma v_x/\tau$, which is larger than the bulk one, being $\Gamma > 1$. As in the case $\Omega = 0$, the particle remains trapped at the wall. The first difference occurs in the dynamics of v_y , which rapidly increases due to the action of the tangential force which is $\propto \Omega$. The growth of the chirality increases the amplitude of such a force, which accelerates the

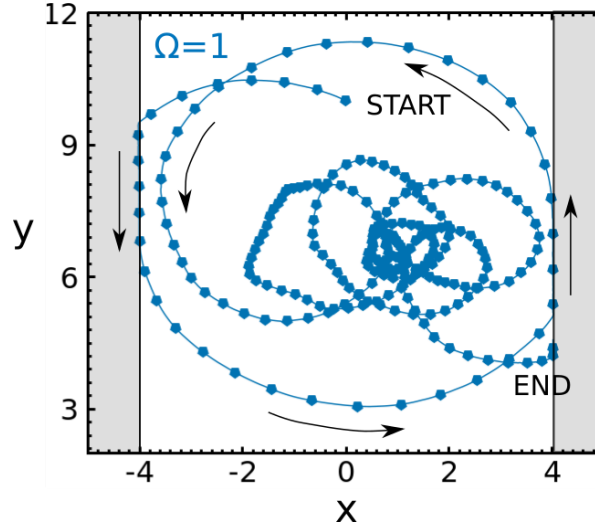


Figure 3.12: A typical trajectory of an active chiral particle confined to a slit-like channel. In the inner region, the particle performs spiral-like motion, while at the walls it slides vertically. Notice that the sliding is downwards at the left wall and upwards at the right wall.

particle, gaining “kinetic energy”. Due to its effect, the particle moves along y for a time t_Ω after which the chirality rotates the velocity transferring the “kinetic energy” accumulated from v_y to v_x , in such a way that v_x points towards the bulk. Thus, the particle leaves the wall with an initial velocity determined by Ω and perform a spiral motion with a very large initial radius in the bulk. Due to the dissipation caused by the bulk Stokes force, the radius of the trajectory shrinks, as shown in Figure 3.12. The bulk dissipation consistently decreases the value of $\langle |v| \rangle$ after a time $\approx \tau$, until to reach the typical value of a confinement-free system $\sim \sqrt{D_a/\tau}$. When a fluctuation of the self-propulsion (which in the bulk corresponds to the velocity) leads a particle to reach again the wall, a new cycle starts. Since the chirality removes the particles from the walls, it is quite evident that its effect is to reduce the accumulation in front of the walls, and, thus, to increase the bulk population. Instead, the formation of an empty layer can be qualitatively explained by the following observation: particles leave the boundaries with a very large v_x so that they visit this layer for a time smaller than the residence time spent in the bulk region.

The physical explanation of the emptying mechanism is based on the existence of momentum surface currents along the y direction. In Fig. 3.13, we study the profile of the average y -component of the velocity $\langle v_y \rangle_x$ as a function of x for two different values of Ω to confirm our thesis. the observable $\langle v_y \rangle_x$ displays a monotonic behavior in agreement with a hyperbolic sine function, as shown in both panels of Fig. 3.13. The profile of $\langle v_y \rangle_x$ extends also in large bulk-layer near the boundaries which depends on the value of Ω . Its relation with the emptying phenomenon clearly emerges in the right

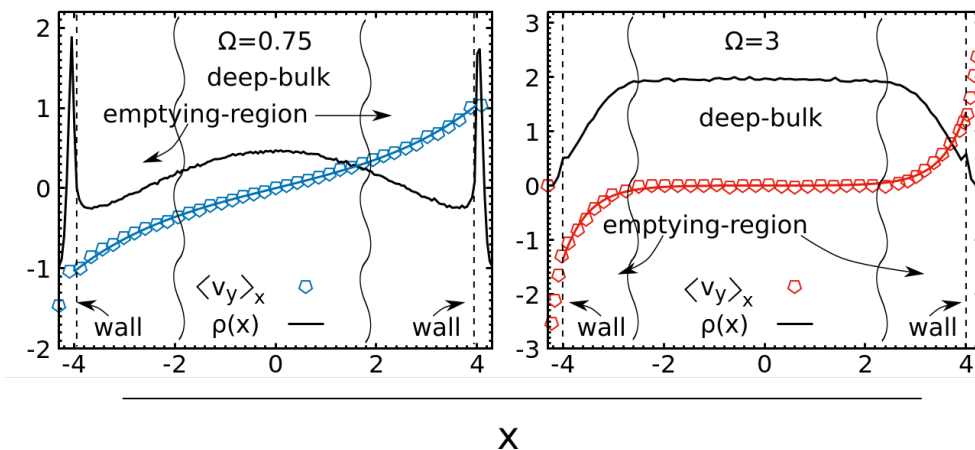


Figure 3.13: Velocity and density profiles for the slit-like channel. Left panel: case $\Omega = 0.75$. Mean vertical velocity $\langle v_y \rangle_x$ as a function of the x -coordinate (blue symbols) and theoretical prediction (blue line) Eq. (3.60). The black line indicates the corresponding density profile $\rho(x)$. Right panel: case $\Omega = 3$. Mean vertical velocity $\langle v_y \rangle_x$ versus x (red symbols) and theoretical prediction (red line) Eq. (3.60). The black line indicates the density profile $\rho(x)$. For both panels the control parameters are: $\tau = 10$, $\gamma = 1$, $D_a = 10$, $L = 4$.

panel: the density in the bulk becomes flat when $\langle v_y \rangle_x$ approaches to zero. The left panel does not disagree with this statement since $\langle v_y \rangle_x = 0$ only in the middle point and, thus, the inner region with constant density does not exist. The momentum surface currents occur also in the harmonic channel, even if in the slit system its consequences are richer due to the discontinuity of the Stokes force acting on the v_x dynamics while the centripetal force $\Omega \hat{\mathbf{z}} \times \mathbf{v}$ is uniform in the whole space.

3.4.3 Momentum profile in the potential-free region $|x| < L$

The y component of the average velocity field has a pronounced bulk profile, as shown in Fig. 3.13. To understand such an effect we consider the Fokker-Planck equation for the probability distribution, $f(\mathbf{x}, \mathbf{v})$, associated to the dynamics (3.46)-(3.47). Following the same approach of Sec.3.3.2, we develop hydrodynamics equations for the potential-free region by projecting the Fokker-Planck equation in the space of the velocity moments. We get the continuity equation by integrating the Fokker-Planck over v_x and v_y :

$$\frac{\partial \rho(\mathbf{x}, t)}{\partial t} + \frac{\partial j_x(\mathbf{x}, t)}{\partial x} + \frac{\partial j_y(\mathbf{x}, t)}{\partial y} = 0 \quad (3.48)$$

having introduced the currents j_x and j_y as

$$j_\alpha(\mathbf{x}, t) = \int dv_x dv_y v_\alpha P(\mathbf{x}, \mathbf{v}, t).$$

being $\alpha = x, y$. The condition $\frac{\partial \rho(\mathbf{x}, t)}{\partial t} = 0$ holds in the stationary state and because of the translational symmetry along y the vector current, \mathbf{j} , can be only a function of x . Thus, $\frac{\partial j_x(x, t)}{\partial x} = 0$ from which follows that $j_x(x) = 0$ from the wall boundary conditions. On the contrary, $j_y(x)$ is a non-vanishing function of x . Let us introduce the pressure tensor \mathcal{P} as:

$$\mathcal{P}_{\alpha\beta}(\mathbf{x}) = \int dv_x dv_y v_\alpha v_\beta P(\mathbf{x}, \mathbf{v}). \quad (3.49)$$

Multiplying the FPE of the potential-free region, $|x| < L$, by v_x and v_y and integrating out the velocities, we get two equations involving the components of \mathcal{P} :

$$-\Omega j_y(x) - \frac{\partial \mathcal{P}_{xx}(x)}{\partial x} = 0, \quad (3.50)$$

$$-\frac{1}{\tau} j_y(x) - \frac{\partial \mathcal{P}_{xy}(x)}{\partial x} = 0. \quad (3.51)$$

Our goal is to determine $j_y(x)$ using Eq. (3.51). We will pursue this task through a simple kinetic argument developed hereafter. Let us introduce the average momentum flux along y per unit length and per unit time, J_y^+ , crossing a segment at $x = x_0$, with $-L < x_0 < L$. To fix the ideas, we consider the region $x < x_0$. Let us divide the space into cells of linear size λ_Ω , which we assume to be the smaller distance below which the mean values of the physical observables do not vary. In addition, we assume that a particle moves at the constant average velocity, $|\bar{v}_x|$, when it passes from one side to the other of the unit vertical segment placed at $x = x_0$. Under these assumptions, J_y^+ assumes the form:

$$J_y^+(x_0) = \frac{1}{4} |\bar{v}_x| j_y(x_0 - \lambda_\Omega). \quad (3.52)$$

In the same way, the momentum flux of the particles on the right is

$$J_y^-(x_0) = -\frac{1}{4} |\bar{v}_x| j_y(x_0 + \lambda_\Omega). \quad (3.53)$$

The factor $1/4$ is related to the different possible directions of the particle velocity, assuming the isotropy of the velocity distribution. As a result, we obtain a net transfer of the y -component of the momentum across the segment $x = x_0$:

$$J_y^+(x_0) - J_y^-(x_0) \approx -\frac{1}{2} \lambda_\Omega |\bar{v}_x| \frac{\partial j_y}{\partial x} \Big|_{x_0}. \quad (3.54)$$

Being $(J_y^+ - J_y^-)$ the rate change of the momentum per unit length, which is equivalent to the shear force per unit length exerted by the particles at $x < x_0$ on the particles at $x > x_0$. This corresponds to the off-diagonal components of \mathcal{P} :

$$\mathcal{P}_{xy} = J_y^+ - J_y^- = -\nu_\Omega \frac{\partial j_y}{\partial x} \quad (3.55)$$

being $\nu_\Omega = \frac{1}{2}\lambda_\Omega|\bar{v}_x|$. Defining J_N as the number of particles per unit time crossing a unit vertical segment, we can apply the same kinetic argument, by replacing $j_y(x)$ by $\rho(x)$. We conclude that a gas of chiral active particles of non-constant density $\rho(x)$ produces a net flux J_N according to the equation:

$$J_N = -\frac{1}{2}\lambda_\Omega|\bar{v}_x|\frac{\partial\rho(x)}{\partial x}\Big|_{x_0}. \quad (3.56)$$

The self-diffusion coefficient, D_Ω , of a suspension of chiral particles is defined by the ratio between $-J_N$ and $-\frac{\partial\rho(x)}{\partial x}$ and reads:

$$D_\Omega = \frac{1}{2}\lambda_\Omega|\bar{v}_x|. \quad (3.57)$$

We may extend a well-known result in the kinetic theory of Brownian gas to a suspension of active chiral particles in the dilute regime: $\nu_\Omega = D_\Omega$. The kinematic shear viscosity and the diffusion coefficient are equal. We can find the value of ν_Ω by the comparison with the exact result for the long-time diffusion coefficient $D_\Omega = \frac{D_a}{1+\Omega^2\tau^2}$, which is given by Eq. (1.21). We obtain:

$$\mathcal{P}_{xy} = -\frac{D_a}{1+\Omega^2\tau^2}\frac{\partial j_y}{\partial x}. \quad (3.58)$$

Finally, substituting this result in Eq. (3.51) we get

$$\frac{\partial^2 j_y}{\partial x^2} = \frac{1+\Omega^2\tau^2}{D_a\tau}j_y \quad (3.59)$$

which can be easily solved

$$j_y(x) = A \sinh\left(\frac{x}{\sqrt{\nu_\Omega\tau}}\right) = A \sinh\left(\frac{\sqrt{1+\Omega^2\tau^2}}{\sqrt{D_a\tau}}x\right), \quad (3.60)$$

obtaining a hyperbolic profile with typical length $\sqrt{D_a\tau}/\sqrt{1+\Omega^2\tau^2}$, while A is a constant to be fixed by the boundary conditions at $x \pm L$. The expression for \mathcal{P}_{xx} is obtained with the help of Eq. (3.50):

$$\mathcal{P}_{xx}(x) = \int_{-L}^x dx' j_y(x') = \mathcal{P}_0 - A\Omega\sqrt{\nu_\Omega\tau} \cosh\left(\frac{x}{\sqrt{\nu_\Omega\tau}}\right). \quad (3.61)$$

\mathcal{P}_0 is a free constant which depends on the boundary conditions. The prediction of Eq. (3.60) is in quantitative agreement with the numerical data [89] upon a rescaling of a factor $\sqrt{2}$ in the characteristic length, i.e. by replacing $\sqrt{\nu_\Omega\tau} \rightarrow \sqrt{2\nu_\Omega\tau}$. Nevertheless, we point out that $j_y(x)$ is proportional to $\langle v_y \rangle_x$ when $\rho(x)$ varies slower than $\langle v_y \rangle_x$. Only in this regime the comparison between the solution $j_y(x)$ of Eq. (3.60) and the profile $\langle v_y \rangle_x$, numerically obtained in Fig. 3.13, makes sense.

3.5 Active transport process along an open-wedge channel

In the previous Sections we have explored the active dynamics in a semi-infinite channel, evaluating qualitatively and quantitatively the so-called wall-accumulation. The influence of geometrical constraints on the dynamics of self-propelled particles is an issue less explored and understood, in spite of its experimental importance. For instance, harbor colonies of bacteria normally localized in the skin, external mucosae, gastrointestinal tracts etc. Crossing narrow constrictions, these bacteria usually invade and often infect the internal tissues of the hosts that instead need to remain sterile [137]. Understanding the leading features of this passage is a problem of great relevance, especially in cases of pathogen infections.

Using the R&T dynamics, first-passage properties have been already studied both with [164] and without [165, 64] thermal noise for a one-dimensional channel. The same problem was numerically studied for a variant of the ABP-model [166] adapted for a one-dimensional system and then in two-dimensional corrugated channels in Refs. [167, 168]. In a similar context, a Fick-Jacobs transport equation [169] accounting for the channel geometry via an entropic effective force [170, 171, 172] has been proposed for weakly active particles [173]. In general, the distribution of the escape events has been addressed by several authors [104, 174, 175, 131] which studied the dynamics in a double-well channel, focusing on the first mean passage time from a well to the other.

In the present Section, we idealize the motion of bacteria using the ABP dynamics and model the channel as a narrow wedge-shaped capillary. At variance with previous works, we investigate how the first-passage process of an ABP through a narrow constriction depends on the parameters of the active force and on the geometry. In this Section, we also focus on the general features of escape processes, comparing the efficiency of “active” transport with the Brownian transport [148] finding an interesting phenomenology induced by the self-propulsion. We remark that for such a phenomenology, ABP and AOUP dynamics are equivalent, giving rise to the same results.

3.5.1 The open wedge-geometry

We consider an assembly of N independent self-propelled particles constrained to move in the two-dimensional truncated-wedge channel shown in Fig.3.14. We choose the active force evolving by means of the ABP dynamics, for the sake of simplicity. In this case (both for ABP and AOUP model), both the dimensions are relevant even for the AOUP case because of the asymmetric shape of the channel. Thus, there are no clear advantages in considering the AOUP model. We also perturb the dynamics with a drift along the axis of the channel, $\epsilon\hat{x}$, which represents a systematic bias

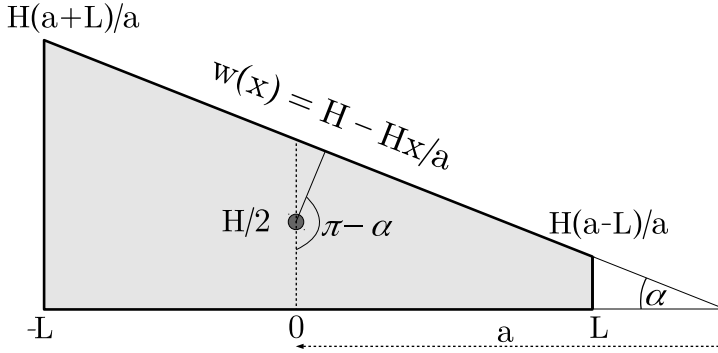


Figure 3.14: Sketch of the truncated wedge used as simulation box $Q = \{|x| \leq L, 0 \leq y \leq w(x)\}$, bounded by the lines $y = H - Hx/a$ and $y = 0$. Absorbing conditions are placed at $x = \pm L$, for which the particles crossing $x = \pm L$ are removed from the system. The black circle, centered in $(0, H/2)$, marks the narrow region where particles are either initially emitted or re-injected after their absorption.

associated to a drag or biological agents acting towards positive x . For completeness, we rewrite the equations of motion for the position, \mathbf{x} , of the microswimmer and for the self-propulsion, \mathbf{f}^a :

$$\gamma \dot{\mathbf{x}} = \mathbf{F}_w(\mathbf{x}) + \epsilon \hat{\mathbf{x}} + \gamma U_0 \hat{\mathbf{e}}(t), \quad (3.62)$$

We neglect the thermal bath to enhance the wall accumulation since for several microswimmers such approximation holds [125]. We point out that the results of the present Section for the ABP dynamics are perfectly consistent with not shown results obtained with AOUP active force.

Particles are constrained in the domain $Q = \{(x, y) : |x| \leq L, 0 \leq y < w(x)\}$, which defines the space which can be explored by each microswimmer. Q is bounded on the bottom at $y = 0$ and on top by the linear profile:

$$w(x) = \frac{H}{a}(a - x), \quad (3.63)$$

where $a > L > 0$ and $H > 0$, as shown in Fig.3.14. Motivated by biological applications (bacteria in a capillary or microswimmers in small tubes), we fix $H \ll L$, restricting our study to narrow channels. In correspondence of the two y -extremes of the domain we place soft reflecting walls, while at $x = \pm L$ we insert two vertical absorbing boundaries. As discussed in Sec.3.1, the force exerted by each wall, \mathbf{F}_w , is normal with respect to its profile, so that the contribution of the bottom boundary is a force in the $\hat{\mathbf{y}} = (0, 1)$ direction which is applied in the stripe $|x| < L$ with $y < 0$. Instead, the contribution of the top wall is a force along the direction $(-H/a, 1)/\sqrt{1 + H^2/a^2}$ which comes into play for $|x| < L$ and $y > w(x)$. The wall repulsion is modeled by a soft-potential $U(s) = V_0/m(\sigma/s)^m$, with $m > 0$, where s is the coordinate along the normal direction to its profile. The constants V_0 and σ defines

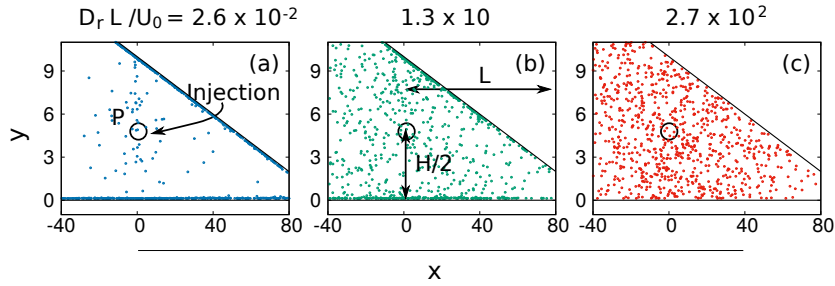


Figure 3.15: Snapshots of particle configurations, upon re-injection at the site $(0, H/2)$, for different values of the parameter $D_r L/U_0$ in the absence of field $\epsilon = 0$. Panels (a), (b) and (c), showing a different degree of particle accumulation to the walls, are obtained with $D_r L/U_0 = 2.6 \times 10^{-2}, 1.3 \times 10, 2.7 \times 10^2$, respectively. Other system parameters are $L = 80$, $a = 100$, $H = 10$, and $U_0 = 3$.

the energy and the length scale of U . In particular, the latter is assumed to be smaller than the geometrical lengths of the wedge-channel, L and H . In practice, \mathbf{F}_w reads:

$$\mathbf{F}_w = -U'(w(x) - y) \mathbf{n} - U'(y) \hat{\mathbf{y}}, \quad (3.64)$$

where the prime represents the derivative with respect to the argument of U . We choose the functional form of U to prevent excessive penetration inside the wall region and thus we assume $\sigma \sim 10^{-2}H$ and $V_0 = 1$, $m = 4$.

To mimic the injection of particles by means of a “micro-pipette”, we place the particles in the middle of the wedge in a small neighborhood of the point $P = (0, H/2)$, as shown in Fig.3.14. Microswimmers leave the channel at $x = \pm L$ because of the absorbing boundaries. The reinjection of particles occurs at the point P , with a protocol which keeps fixed their number, $N = 10^4$. At the re-injection instant, the orientational angles are initialized with a uniform distribution in the interval $[0, 2\pi]$.

The following analysis will be focused on the discussion of the escape properties from an open-wedge channel varying D_r and, later, ϵ , to evaluate the differences with a Brownian suspension of particles. Hereafter, we shall present the results obtained in [148]. We anticipate that the accumulation near the walls will play a fundamental role in the escape process and leads to optimal values of the active force parameters which maximize the transport efficiency.

Case $\epsilon = 0$

Let us start from the bias-free case, $\epsilon = 0$. As founded in Section 3.2, the accumulation is stronger as τ increases and becomes negligible only in the small persistence regime $D_r \gg \gamma$, where the system behaves as a Brownian-like suspension of particles at effective temperature, $T = \gamma U_0^2 / 2D_r$. In what follows, the latter regime will be used to make a comparison with

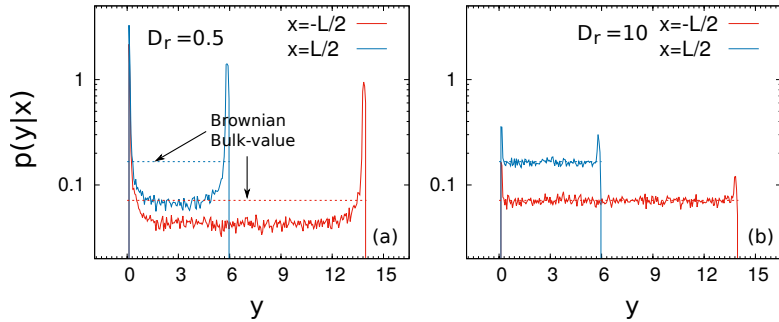


Figure 3.16: Conditional probability distribution functions, $p(y|x)$, evaluated at $x = L/2$ (blue line) and $x = -L/2$ (red line). Panel a) and b) are obtained for $D_r L/U_0 = 1.3 \times 10, 2.7 \times 10^2$, respectively. System parameters are: $L = 80, a = 100, H = 10, \epsilon = 0, U_0 = 3$.

the Brownian counterpart system. A crucial role in the relevance of the accumulation is played by the persistence length, $\lambda_a = U_0/D_r$ ($\sqrt{D_a \tau}$), which states the typical length-scale after which particles change direction. Comparing λ_a with H and L , i.e. the two typical sizes of the wedge-channel, we obtain three different regimes:

- i) the regime $H \ll L \ll \lambda_a$. Particles swim ballistically and the majority of them slides along the two walls, being accumulated in front of them. In this case, the bulk-particles give a non-significant statistical contribution to the computation of any global observables.
- ii) The regime $H \ll \lambda_a \ll L$. Along the axis of the channel (x -direction) the motion is diffusive, while on the transversal direction the motion is characterized by rebounds between the walls. The accumulation phenomenon is reduced with respect to the regime i) even if yet relevant.
- iii) The regime $\lambda_a \ll H$. Since the persistence length is smaller than any geometrical scale, the majority of the particles are in the bulk behaving like Brownian colloids at temperature, $T = \gamma U_0^2/2D_r$. The small fraction of particles stuck at the walls is statistically negligible in the calculation of the observables on which we are interested in this Section

We remark that the description in terms of λ_a is not equivalent to the one in terms of τ . Indeed, D_r/γ simply determines the height of the peak respect to the bulk-value, while λ_a/H (or λ_a/H) provides the fraction of particles stuck in front of the boundaries in relation to the whole population, N . In principle, we could have a large accumulation (high peak of the density), since $D_r \ll \gamma$, but a very small fraction of particles in front of the wall, since $\lambda_a \ll H$, and the majority of them are in the bulk. Since in this Section we are interested in determining the transport properties of the active suspension, such as the escape time, the most important role is played

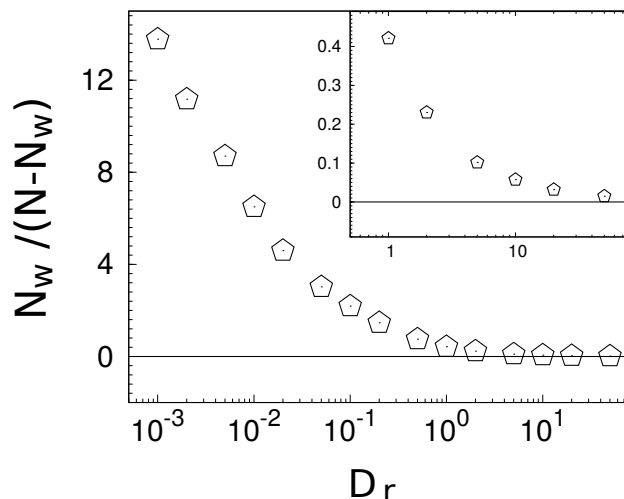


Figure 3.17: Ratio $N_w/(N - N_w)$, between the number of particles accumulating at the walls and the remaining ones in the bulk, as a function of D_r . The inset is a blow-up of the range $D_r > 1$. System parameters are the same as in Fig.3.16.

by the length-scales: we need to understand if the larger contribution to statistics of the observable comes from the wall or from the bulk population.

Fig.3.15 shows three steady-state configurations obtained for different values of $D_r L/U_0$, which is the ratio between the larger size of the channel, L , and the persistence length, U_0/D_r . In particular, panels (a), (b) and (c) refer to the regimes i), ii) and iii), respectively. Thin denser stripes of particles occur in front of the two walls, due to the phenomenon of the accumulation near repulsive boundaries, described in previous Sections. This effect decreases as $D_r L/U_0$ increases, as shown in panels (a) and (b) until to disappear in panel (c). To quantify the degree of accumulation, we plot the conditional probability distribution, $p(y|x)$, on vertical sections of the channel placed at $x = \pm L$. In panels (a) and (b) of Fig.3.16, we report the $p(y|x)$ corresponding to the snapshot (b) and (c) of Fig.3.15, respectively, with the aim of comparing a strong-active with a Brownian-like regime. As we expected, panel (a) shows the occurrence of two pronounced peaks, which interestingly are not symmetric. The bulk profile is smoothly non-uniform and it is clear that the value of the bulk-density is smaller than its Brownian counterpart (shown by dotted lines). Instead, in panel (b) the peaks are strongly depleted and the comparison with the Brownian counterpart shows a fair agreement. As a consequence of a fast transversal homogenization, $p(y|x)$ turns to be a flat function in the bulk in this case. Following Lee, we report a quantitative measure of the accumulation: in Fig.3.17, we plot the ratio between the fraction of particles stuck at the walls, N_w , and the remaining which populate the bulk, $N - N_w$, in function of D_r . $N_w/(N - N_w)$ decreases monotonically with D_r towards the Brownian limit. This indicates that the growth of D_r reduces the accumulation near the walls, as we expect.

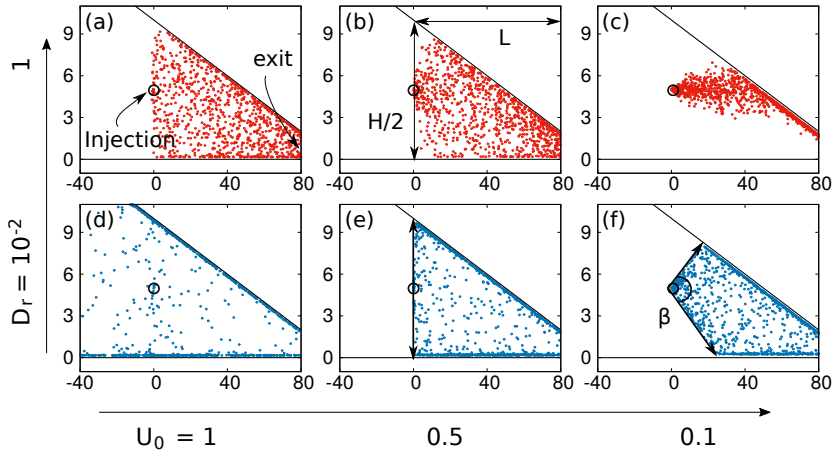


Figure 3.18: Snapshots of particle positions in the presence of a field $\epsilon = 0.5$ at different U_0 and D_r . Panels (a), (b) and (c) refer to values $U_0 = 1.0, 0.5, 0.1$ and the same $D_r = 1.0$, while panels (d), (e) and (f) are obtained with the same set of U_0 but a value $D_r = 0.01$. Black lines represent the walls, and the gray circle centered at $(0, 5)$ is the area where particles are reinjected when they cross the right exit at $x = L = 80$. The remaining parameters are $a = 100$ and $H = 10$.

Case $\epsilon > 0$

We consider the case $\epsilon > 0$, where a constant driving force with amplitude ϵ pushes the particles towards the right exit. Now, U_0 plays a fundamental role, at variance with the case $\epsilon = 0$. Indeed, the ratio $\gamma U_0/\epsilon$ determines if the active force can overcome the external force or not. Keeping fixed $\epsilon = 0.5$, we vary U_0 exploring the regimes $\gamma U_0 \geq \epsilon$ and $\gamma U_0 < \epsilon$, for several values of D_r .

Fig.3.18 displays six snapshots of particle configurations for different D_r and U_0 . Panels (a), (b) and (c) are obtained with $D_r = 1.0$ and $U_0 = 1, 0.5, 0.1$, respectively. The values of the parameters (in particular D_r) allows us to conclude that we are in a Brownian-like case, i.e. in the regime iii). We observe that in this case, The effective fluctuation of active force (which behaves as a thermal bath) are not able to compensate the effect of the bias in such a way that particles cannot escape towards the left exit. In particular, in panels (a) and (b), both with $\epsilon \lesssim \gamma U_0$, particles fill vertically the whole space of the channel, having time to explore the whole section of the channel before reaching an exit. In contrast, when $\epsilon \gtrsim \gamma U_0$, the bias prevails over the diffusion producing a sort of “plume” towards the right, as emerged in panel (c).

Instead, panels (d), (e) and (f) show the persistence case at $D_r = 10^{-2}$. Despite the action of the drift, the particles explore the whole section of the channel in panel (d) when $\gamma U_0/\epsilon$ is large. The decreasing of $\gamma U_0/\epsilon$ leads the bias to prevail in such a way that the particles injected near the point P can

explore only angles β given by

$$|\beta| \leq \tan^{-1} \left(\frac{\epsilon}{U_0} \right) \quad (3.65)$$

as clearly illustrated in panels (e) and (f). The maximal value of $|\beta|$ is estimated by the less favorable case, i.e. when the self-propulsion points towards x . Indeed, we have $\dot{x} = \epsilon, \dot{y} = \pm U_0$ in this case.

3.5.2 Distribution along channel axis

The transport of passive Brownian particles in narrow channels with non-uniform section has been solved employing the Fick-Jacobs (FJ) approximation [169, 170, 172], which consists in reducing a multidimensional dynamics to a one-dimensional one with an effective potential accounting for the channel asymmetry. The FJ approximation can be applied if the homogenization hypothesis works on the transversal direction with respect to the channel axis: the typical relaxation time on x should be larger than the one on y [176, 177, 171]. The possibility of generalizing the FJ approach to a system of self-propelled particles is not clear. when $D_r < \gamma$ we show that the homogenization along y is not fulfilled because of the accumulation at the walls induced by the self-propulsion, even if we can apply the approximation in the opposite regime.

We numerically study the marginal probability distribution, $p_{st}(x)$, in the steady state

$$p_{st}(x) = \frac{1}{w(x)} \int_0^{w(x)} dy P_{st}(x, y) \quad (3.66)$$

obtained from the whole density distribution $P_{st}(x, y)$. In Fig.3.19 we show the $p_{st}(x)$ computed numerically for several values of D_r . In particular, panels (a) and (b) refer to $\epsilon = 0$ and $\epsilon > 0$, respectively. Starting from the case $\epsilon = 0$, we observe that the distribution displays a pronounced asymmetry with respect to $x = 0$ in the small persistence regime. This effect comes from the narrowing of $w(x)$, which induces an “entropic” force, favoring the occupation of the region $x < 0$, where the section of the channel is larger. We note that the asymmetry is maximal in the regime i), which we obtain for large values of D_r . In this Brownian-like case, we can compute analytically the distribution (shown as a dashed black line) using a Fick-Jacobs approach[169, 172, 171]:

$$p_{st}(x) = \begin{cases} A(a-x) \ln \left(\frac{a+L}{a-x} \right) & x \in [-L, 0] \\ B(a-x) \ln \left(\frac{a-x}{a-L} \right) & x \in [0, L] \end{cases} \quad (3.67)$$

where A and B are two coefficients which depend only on the channel geometry. The details of the computations are reported in appendix 3.D. Eq.(3.67)

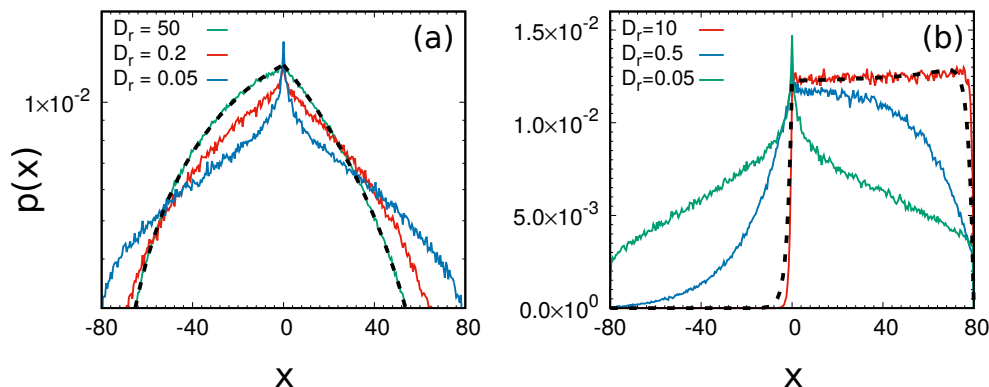


Figure 3.19: Stationary marginal space probability distribution, $p_{\text{st}}(x)$, at different values of D_r . Panel a) refers to $\epsilon = 0$, panel b) to $\epsilon > 0$; dashed lines represent the Brownian predictions: Eq.(3.67) for $\epsilon = 0$ and Eq.(3.68) for $\epsilon > 0$. System parameters are: $L = 80$, $a = 100$, $H = 10$, $U_0 = 3.0$.

is applicable to a system of active particles only in the regime i), or simply till to values around $D_r \approx \gamma = 1$. Indeed, for smaller values of D_r , the persistence of the motion contrasts the entropic force. As a consequence, the distribution becomes more symmetric as D_r is reduced until the asymmetry is completely suppressed. In addition, a narrow peak at $x = 0$ occurs, whose height increases as $1/D_r$ decreases. The latter effect, not present in the Brownian-like regime, is due to the interplay between persistence and re-injection.

In the case $\epsilon > 0$, the “entropic” force is overwhelmed by the bias in such a way that particles populate approximatively only the region $x > 0$ in the large persistence regime. Again in such a Brownian-like scenario, we are able to compute analytically the shape of $p_{\text{st}}(x)$, which reads

$$p_{\text{st}}(x) \propto e^{\varepsilon x} (a - x) \begin{cases} A(\text{Ei}[\varepsilon(a + L)] - \text{Ei}[\varepsilon(a - x)]) & x \in [-L, 0] \\ B(\text{Ei}[\varepsilon(a - x)] - \text{Ei}[\varepsilon(a - L)]) & x \in [0, L]. \end{cases} \quad (3.68)$$

The derivation of such a profile is reported in Appendix 3.D. In Eq.(3.68), ε is defined as $\gamma\epsilon/T$, where $T = \gamma U_0^2/2D_r$ is the effective temperature of the Brownian-like regime, while the function $\text{Ei}[\dots]$ is the Exponential Integral function (cfr. pp. 661–662 of Ref.[178]). The Brownian-like shape of $p_{\text{st}}(x)$ is strongly deformed by the active force when D_r is reduced. At first, the distribution develops a tail for $x < 0$, until for the smaller values of D_r the asymmetric shape is erased: both the entropic and the bias effects are suppressed.

The extension of the Fick-Jacobs approximation to the active case is possible only for small values of the persistent time and activity strength [173]. When it happens, the far-equilibrium feature of active particles do not

emerge and the Brownian theory with an effective temperature agrees with numerical data. On the contrary, when the active force is very persistent and large, our study of particle distributions shows that the main hypothesis underlying the Fick-Jacobs approximation breaks down since the density is not homogeneous in each channel section, as an effect of the accumulation near the walls. Quantifying how the effective entropic barrier is reduced by this mechanism could represent an intriguing next point in understanding biological transport processes. In Sec.3.5.3, we see how the accumulation mechanism of the particles to the walls strongly affects the escape process.

3.5.3 Escape process of active particles from the wedge

Now, we study the escape statistics from the wedge showing the differences between the three regimes introduced in this Section. The time at which a particle leaves the channel, reaching one of the two absorbing boundaries, provides the definition of the left and right first passage times, $\tau_{L,R}$:

$$\tau_L = \min_t \{0 < t \leq T_w \mid x(t) < -L\} \quad (3.69)$$

$$\tau_R = \min_t \{0 < t \leq T_w \mid x(t) > L\}. \quad (3.70)$$

$\tau_{L,R}$ are computed within the simulation time T_w chosen of order $\sim 10^4/D_r$. Such a choice allows all the particle to exit from the wedge at least one time within the interval $[0, T_w]$, in such a way that we can compute numerically the exit-time distributions, $\Psi_{L,R}(\tau)$. At first, we consider the bias-free case, $\epsilon = 0$, and then we extend our study to the driven system, $\epsilon > 0$.

Active escaping time at $\epsilon = 0$

In Fig. 3.20 we report the exit-time distributions, $\Psi(\tau)$, for several values of D_r , in such a way that we explore the three different length regimes. For presentation reasons, we separate the large and the small persistence regime, shown in panels (a) and (b), respectively.

In the regime $\lambda_a \ll H \ll L$ [regime iii)], the larger fraction of particles swim diffusively in the bulk and the accumulation is only a marginal phenomenon. The shape of $\Psi(\tau)$ resembles the distribution of the escape time of Brownian particles, with effective temperature $\gamma U_0^2/2D_r$, since particles in the bulk behave in this way.

In the regime ii), for $H \ll \lambda_a \ll 2L$, a large fraction of particles is stuck to the bottom and up walls. We observe that the vertical component of the velocity of the particles behaves quite “deterministically” producing a bouncing ball effect between the upper and lower boundaries. This effect lasts for an average time $\sim 1/D_r$ [145]. We observe a sort of dimensional reduction which strongly changes the shape of $\Psi(\tau)$ with respect to its Brownian counterpart. In particular, $\Psi(\tau)$ develops pronounced asymmetries, with a fat

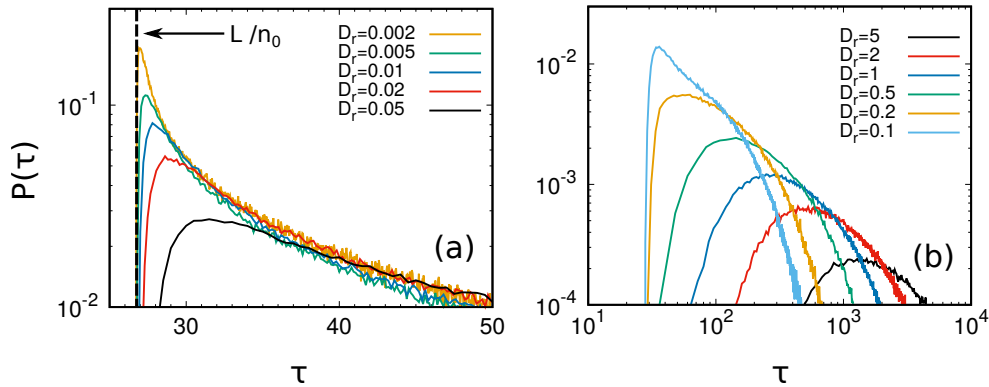


Figure 3.20: Escape time distribution, $\Psi(\tau)$, for $\epsilon = 0$, computed at selected values of D_r in the range $[2 \times 10^3, 5]$, see the legend. Plots have been split in two panels for readability reasons: panel (a) refers to the range $[2 \times 10^{-3}, 5 \times 10^{-2}]$ while panel (b) to the range $[0.1, 5.0]$ Other used parameters are $L = 80$, $a = 100$, $H = 10$, and $U_0 = 3$.

tail for larger times and a rather steep shoulder for shorter times, as emerged both in panels (a) and (b) of Fig.3.20.

In the regime i), when $H \ll L \ll \lambda_a$, the majority of the particles accumulate on the walls. The two boundaries act as trails, which guides the particles to the left or right exit, approximatively in a time $t_d \sim L/U_0$. This means that the escape problem reduces to the combination of two one-dimensional escape processes. As a consequence, $\Psi(\tau)$ becomes peaked near t_d . In this regime, the escape clearly depends on the initial conditions of the orientational angle of the self-propulsion at the injection point, P . In particular, we can divide the particles into two groups: in the group A particles reach the exit (the left or the right one), in a time, $t \sim t_d$, i.e. without changing direction. On the contrary, group B is formed by particles which change direction at least one time before leaving the channel, in such a way that their escape occurs in a time $t \gtrsim t_d$. The components of group A arrive at the exit in the same time t_d , forming the peak of the $\Psi(\tau)$, while group B contribute to the formation of the long tails. In this case, higher and thinner spikes and longer tails are produced when D_r is decreased.

Fig.3.21 displays the right and the left escaping probability, p_R , $p_L = 1 - p_R$, respectively. These weights are measured counting the fraction of exit events from the right and the left in the simulation time. The value of p_R (and equivalently p_L) starts from a plateau for $D_r \rightarrow 0$ and decreases monotonically in function of D_r until to reach a second plateau for $D_r \rightarrow \infty$, i.e. in the Browian regime which is given by:

$$\lim_{D_r \rightarrow \infty} p_R = \frac{\ln(a+L) - \ln a}{\ln(a+L) - \ln(a-L)} = \frac{\ln(1 + \mu \tan \alpha)}{\ln \left(\frac{1 - \mu \tan \alpha}{1 + \mu \tan \alpha} \right)} \quad (3.71)$$

where α is the angle of the wedge, as illustrated in Fig.3.14 and $\mu = L/H$.

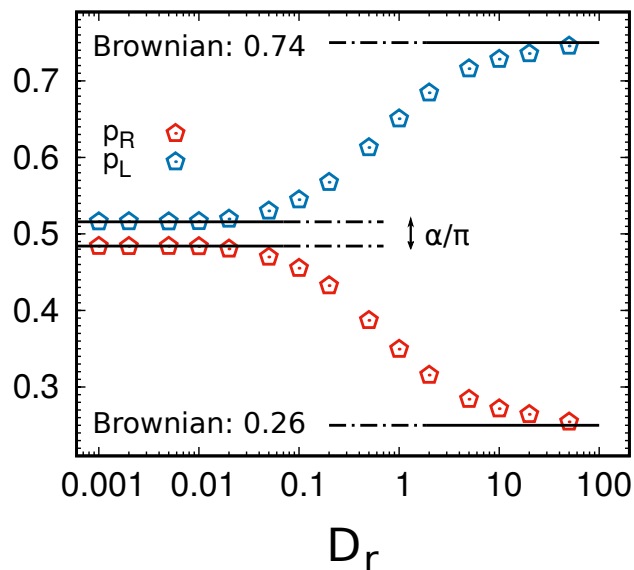


Figure 3.21: Dependence of the left/right escape probabilities, p_L and p_R , on D_r . Black lines indicate the two limiting plateaus: the Brownian prediction from Eq.(3.71), and the infinite- τ prediction given by Eq.(3.72).

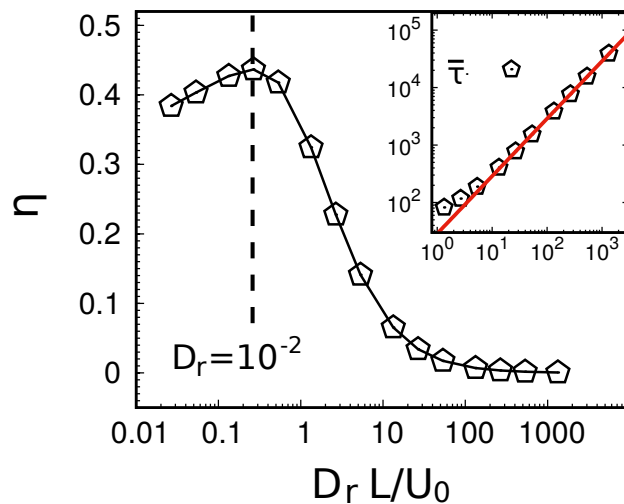


Figure 3.22: Efficiency, defined by Eq.(3.74), as a function of the dimensionless parameter $D_r L/U_0$, in the case of zero drift $\epsilon = 0$. The peak is attained at $D_r \approx 10^{-2}$. The inset shows $\bar{\tau}$ (black data) vs. $D_r L/U_0$ for a comparison with the Brownian result, Eq.(3.75). Parameters: $L = 80$, $a = 100$, $H = 10$, $U_0 = 3$.

In appendix 3.D [see Eq.(3.105)] we report the derivation of the expression (3.71). We point out that in the Brownian-like limit, p_R is independent of the temperature value. In particular, Eq.(3.71) gives the prediction $\lim_{D_r \rightarrow \infty} p_R \simeq 0.2675$ for $a = 100$ and $L = 80$ and $H = 10$, in fair agreement with the values of the simulations. Because of the action of the entropic force produced by the asymmetry of the channel geometry, $p_L > p_R$, mean-

ing that the exit from the larger left side is favored. Such a Brownian-like scenario holds up to $D_r \sim 10$.

A decrease of D_r produces a strong dependence on the D_r in the shape of p_R . This fact indicates that the self-propulsion counteracts the entropic drift, facilitating the exit from the right side, i.e. the narrow side of the wedge. Thus, the accumulation in front of the walls and the consequent dimensionality collapse reduces the entropic barrier. A similar phenomenon was observed in a system of Janus particles confined in a periodic channel which alternates two wedge compartments [179]. For D_r small enough, p_R and p_L saturate to the values p_R^* and p_L^* , respectively, which are roughly given by

$$p_{L,R}^* = \frac{\pi \pm \alpha}{2\pi}. \quad (3.72)$$

The above formula is in fair agreement with data and can be explained by the following argument: in the regime of very large persistence [namely, regime i)] the motion of the particles is quite “ballistic” and so is strongly influenced by the re-injection conditions. In particular, two complementary angular intervals are identified in Fig.3.14: $\mathcal{A}_L = [\pi/2 - \alpha, 3\pi/2]$ and $\mathcal{A}_R = [-\pi/2, \pi/2 - \alpha]$. In the regime i), the self-propelled particles, re-injected at P with orientational angles $\theta \in \mathcal{A}_L$, exit almost surely to the left exit, while the particles such that $\theta \in \mathcal{A}_R$ are bound to exit to the right. Eq.(3.72) plays the same role of Eq.(3.71) in the regime of small D_r . We point out that particles with self-propulsion normal to the wall profiles cannot exit from the channel before time $\propto 1/D_r \gg t_d$. These particles contribute to the formation of the long tail in $\Psi(\tau)$ but are statistically not so relevant.

To quantify the transport efficiency, with the aim of understanding if the random active force favors or not the exit from the channel, we focus on the average exit time from the wedge, $\bar{\tau}$, given by

$$\bar{\tau} = \int_0^\infty d\tau \Psi(\tau) \tau. \quad (3.73)$$

This observable depends on the active force parameters and on the geometry by means of $\Psi(\tau)$. In addition, we introduce the transport efficiency, η , as the ratio between the deterministic time, L/U_0 , needed by a particle at fixed velocity U_0 to reach the exit, and the mean exit time $\bar{\tau}$:

$$\eta = \frac{L}{U_0 \bar{\tau}}. \quad (3.74)$$

Fig.3.22 shows η as a function of the adimensional parameter $D_r L/U_0$. Interestingly, this observable displays a non-monotonous behavior with a maximum at $D_r L/U_0 \approx 0.3$, corresponding to $D_r \simeq 10^{-2}$ with the specific geometry and U_0 of the present study. Tuning the parameters of the active force, the exit from the challenge can be optimized. We explain the increase of the

efficiency of the transport using the dimensional reduction: when boundaries are used as trails, particles perform a one-dimensional motion along the wall. This fact increases the possibility of finding an exit with respect to the Brownian case, where the full channel is explored and an entropic force arises from the restriction of the cross-section.

In the regime of very small $D_r L/U_0$, the observable $1/\bar{\tau}$ decreases. Indeed, particles which collide normally to the wall profile are stuck for a time $1/D_r \gg t_d$ (which diverges for $D_r \rightarrow 0$). This population slows down the exit process. Instead, when $D_r \gtrsim \gamma$ and system behaves as a Brownian-like suspension of particles, $\bar{\tau}$ linearly grows with $D_r L/U_0$, as illustrated in the inset of Fig.3.22. Indeed, the Brownian-like behavior is controlled by its effective temperature $T = \gamma U_0^2/2D_r$ which increases as $D_r L/U_0$ becomes larger. In the inset of Fig.3.22, we compare $\bar{\tau}$ computed numerically with the formula obtained from a Brownian suspension of particles with temperature $T = \gamma U_0^2/2D_r$:

$$\bar{\tau} = \frac{D_r L^2}{2\gamma U_0^2} \left(1 + \frac{a}{2L} \frac{\ln[a^2/(a^2 - L^2)]}{\ln[(a+L)/(a-L)]} \right). \quad (3.75)$$

The derivation of such a prediction is reported in appendix 3.D. The first addend of Eq.(3.75) is the average exit time of a one-dimensional system in a box of length $2L$. instead, the second one reflects the asymmetry of the channel and is related to the entropic force which governs the dynamics. Such a prediction confirms the linear dependence of $\bar{\tau}$ with D_r when regime iii) occurs and it is in fair agreement with data shown in the inset of Fig.3.22.

Active escaping time at $\epsilon > 0$

Now, we study the influence of the constant force $\epsilon \hat{\mathbf{x}}$ on the escape process. In panels (a) and (b) of Fig.3.23, we plot the exit time distributions, $\Psi(\tau)$, for two different values of U_0 exploring several D_r for each case. We use the same geometrical set-up of the case $\epsilon = 0$ and fix $\epsilon = 0.5$. We expect that for large D_r a Brownian-like regime is recovered in analogy with the case $\epsilon = 0$. Therefore, the exit time distribution, $\Psi(\tau)$, has the same shape of the corresponding Brownian distribution with temperature $\gamma U_0^2/2D_r$ [see panel (a) of Fig.3.23 for the larger values of D_r]. In this regime, $\Psi(\tau)$ is peaked around the time, employed by particles at velocity ϵ/γ to reach one of the exits, which is given by $t_m \sim \gamma L/\epsilon$. Reducing D_r or U_0 the leading effect is to enlarge the variance of $\Psi(\tau)$, even if its skewness is enhanced and a long right tail starts to occur.

When D_r is decreased, the peak of $\Psi(\tau)$ shifts to the left until to its minimal possible value $t_m \sim \gamma L/(\gamma U_0 + \epsilon)$, as shown in panel (a) of Fig.3.23. In fact, even the particles which do not change their orientation cannot exit from the wedge before the time $\sim \gamma L/(\gamma U_0 + \epsilon)$. In this large persistence regime, when D_r is decreased, a different phenomenology occurs depending on the ratio $\gamma U_0/\epsilon$. If $\gamma U_0 > \epsilon$, as shown in panel (b) of Fig.3.23 the

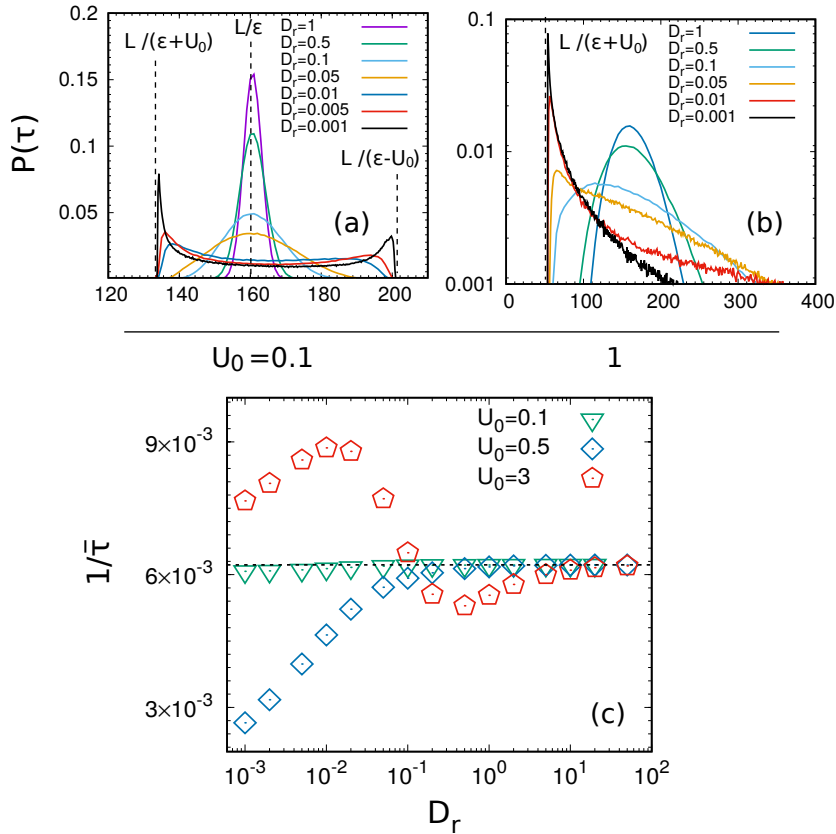


Figure 3.23: Panels a) and b): escape time distributions at different values of D_r and two different values of $U_0 = 0.1, 1$ in the presence of an external bias $\epsilon = 0.5$. Panel (c): dependence of $1/\bar{\tau}$, namely the transport efficiency, on D_r at values $U_0 = 0.1, 0.5, 3$ and $\epsilon = 0.5$. Geometry parameters are $L = 80$, $a = 100$, $H = 10$.

first peak of $\Psi(\tau)$ becomes higher and a long right tail occurs. Instead, if $\gamma U_0 < \epsilon$ a secondary peak in the shape of $\Psi(\tau)$ emerges approximatively at time $\approx \gamma L/(\epsilon - \gamma U_0)$, before that the distribution abruptly drops down [see panel (a) of Fig.3.23]. The occurrence of the secondary peak, whose height is always lower than the first peak, is due to the particles with orientational angles oriented along $-\hat{\mathbf{x}}$, the opposed direction with respect to the bias.

In the case $\epsilon > 0$, the natural definition of the efficiency η comes by replacing $U_0 \rightarrow U_0 + \epsilon$ in Eq.(3.74), i.e. by considering the deterministic velocity to reach the right exit in the presence of the bias. Since $\eta \propto 1/\bar{\tau}$, we report directly $1/\bar{\tau}$ to estimate η . In particular, in panel (c) of Fig.3.23 we plot $1/\bar{\tau}$ in function of D_r for three different values of U_0 . For $\epsilon > \gamma U_0$, the growth of D_r leads $1/\bar{\tau}$ to monotonically increase towards the Brownian plateau. In this regime, the efficiency of the transport is reduced by the presence of the self-propulsion: even if some particles swim towards the right exit with facility, others employ a large time to leave the wedge, because they have an orientation pointing against the direction of the bias. When

U_0 is near ϵ particles could be stuck until their orientation changes, i.e. approximatively after time $\sim 1/D_r$ (blue diamonds shown in panel (c) of Fig.3.23). Instead, if $\gamma U_0 \ll \epsilon$ the bias pushes the particles out of the channel without any appreciable effects of the self-propulsion (gree triangle in panel (c) of Fig.3.23).

When $\epsilon < \gamma U_0$, the scenario becomes very interesting since a non-monotonic behavior versus D_r occurs in the shape of $1/\bar{\tau}$. In particular, the decreasing of D_r leads $1/\bar{\tau}$ to become smaller in a similar fashion of the case $\epsilon > \gamma U_0$. Anyway, in this case, $1/\bar{\tau}$ reaches a minimum and then increases up to a maximum value higher than the Brownian plateau. Then, when D_r becomes very small, $1/\bar{\tau}$ decreases because of the analogue mechanism explained for the case $\epsilon = 0$ [see red data in Fig.3.23 (c)] Thus, in this regime of the parameters, the persistence time can be used to maximize the transport efficiency, reaching values larger than its Brownian counterpart, even in the presence of the external bias. Interestingly, this parameter can also be tuned to obtain a minimization of η , an effect which comes only by the interplay between the self-propulsion and the driving force.

3.6 Discussion and perspectives

In this Chapter, we have reviewed one of the most important phenomena experienced by self-propelled particles: the accumulation near boundaries or obstacles, an effect of great interest recently used to design bacterial motors and to induce the motion of spermatozoa in a given direction. Modeling the channels as soft-potentials, we develop a theory to predict the stationary state in the case of the coarse-grained models adopted in this thesis. We are able to approximate the whole probability distribution in the wall-region and in the bulk of the system, where the interplay between the self-propulsion and the thermal noise due to the environment induces pronounced density gradients. Being able to approximate the full probability distribution of the system, we derive an approximate expression for the pressure proposing an experiment based on movable pistons to test our theory.

A non-uniform density profile also occurs in the presence of a spontaneous chirality taking place in the dynamics. In such a case, steady momentum currents appear and the accumulation along the boundaries of the container is reduced with the increasing of the chirality until particles accumulate in the middle of the channel. This new phenomenology which is opposite with respect to the accumulation near the walls of non-chiral particles, agrees with our theoretical predictions. In addition, a recent experiment obtained for several species of Phytoplankton [138] confirms our phenomenology for which we have provided an explanation. We outline a practical interest related to the chiral systems: on the basis their handedness, chiral self-propelled particles can be selected, a property useful in pharmaceutical or biotechnological applications, where chiral levogyre or dextrogyre is related

to different functionalities [86, 88].

As an interesting application, we have also studied the transport properties along an open-wedge channel. The comparison with the Brownian system counterpart shows that the active force facilitates the escaping from the narrow exit, generating an effect which counteracts the entropic force. The tuning of the parameters, in particular the persistence time, could be used to maximize the transport efficiency with respect to the Brownian counterpart. This application could be particularly useful for artificial microswimmers whose self-propulsion can be modified by external control parameters. We remark that the physical mechanism which improves the exit-efficiency is the accumulation near the walls studied in this Chapter, which leads to a depletion of the inner region. Somehow, the activity is able to operate a sort of dimensional reduction, since makes surface effects prevailing over the bulk properties. Our study suggests that the transport of active particles can be facilitated by designing the surface of the channel in a proper way. This is nothing but a manifestation of the “ratcheting mechanism” observing in self-propelled particles in the presence of asymmetric potentials[179].

Future works will concern the extension of the theory, with or without the chirality, to more complex geometries, with the aim of increasing the accumulation mechanism, an effect which could be useful to maximize the efficiency of the bacterial motors experimentally designed by Di Leonardo and coworkers [40]. Including the interactions among the particles is another important step to extend the theory to more realistic systems, with and without the explicit presence of a chiral dynamics. Since even repulsive interactions could promote clustering or phase separation, which will be the subject of the next Chapter, the transport properties could drastically change. Assessing the effects of such a phenomenology on the mean exit time from the channel will certainly constitute an interesting subject for future investigations.

Appendices

3.A Stationary distribution for the harmonic oscillator in the (x, v) variables

In the presence of a harmonic potential the steady state solution for the probability distribution of the whole system is well-known and has been already studied in Chapter 2 in the (x, f^a) representation. In this appendix, we report its expression in the (x, v) variables

$$f_h(x, v) = \mathcal{N} \exp\left(-\frac{kx^2}{2D_a\gamma} \frac{\Gamma}{1+\Gamma\Delta}\right) \times \exp\left(\frac{(v - \langle v \rangle_x)^2}{2\sigma_v^2}\right), \quad (3.76)$$

with

$$\langle v \rangle_x = -\frac{\Gamma\Delta}{1+\Gamma\Delta} \frac{k}{\gamma} x, \quad \sigma_v^2 = -\frac{D_a}{\tau\Gamma} \left(\frac{1+\Gamma^2\Delta}{1+\Gamma\Delta}\right). \quad (3.77)$$

Eq.(3.76) is a double Gaussian with a velocity distribution centered on $\langle v \rangle \neq 0$, which corresponds to the mean velocity at fixed x . $f_h(x, v)$ has the form of the distribution of a system in local but not global equilibrium, at variance with the case $\Delta = 0$, since the average velocity $\langle v \rangle_x \propto x$ is non-zero except for the point $x = 0$.

3.B How to rationalize the non-Gaussian closure

The screening length (3.20) in Eq.(3.21) vanishes in the limit of zero thermal noise, $D_t \rightarrow 0$, even at fixed $D_a > 0$ and $\tau > 0$. This feature is not physical, as confirmed by our numerical studies. We also remark that the limit $D_t \rightarrow 0$ is singular and breaks the Gaussian assumptions invalidating the approximation (3.21), meaning that we require to go beyond the closure $n_2(x) = 0$ taking into account higher order terms. Here, we will show that adopting this procedure we are able to predict a non-vanishing decay length giving also a derivation for the closure(3.23) Starting from the case $D_t = 0$ and considering the condition $n_1(x) = 0$, the hierarchy (3.15) assumes the form:

$$\frac{\partial n_0(x)}{\partial x} + 2\frac{D_a}{\tau} \frac{\partial n_2(x)}{\partial x} = 0, \quad (3.78)$$

$$3\frac{D_a}{\tau} \frac{\partial n_3(x)}{\partial x} = -\frac{2}{\tau} n_2(x), \quad (3.79)$$

$$\frac{\partial n_2(x)}{\partial x} + 4\frac{D_a}{\tau} \frac{\partial n_4(x)}{\partial x} = -\frac{3}{\tau} n_3(x), \quad (3.80)$$

$$\frac{\partial n_3(x)}{\partial x} + 5\frac{D_a}{\tau} \frac{\partial n_5(x)}{\partial x} = -\frac{4}{\tau} n_4(x). \quad (3.81)$$

Our choice is break the hierarchy using $n_5(x) = 0$ and after eliminating $n_4(x)$ we get

$$\frac{2}{\tau}n_2(x) + 3v_a^2 \frac{\partial n_3(x)}{\partial x} = 0, \quad (3.82)$$

$$\frac{\partial n_2(x)}{\partial x} + \frac{3}{\tau}n_3(x) - v_a^2 \tau \frac{\partial^2 n_3(x)}{\partial x^2} = 0. \quad (3.83)$$

In this way, we have obtained a set of linear differential equations, which we can solve by combining solutions of the form $e^{\pm\mu x}$, with μ determined by a simple algebraic equation. In particular, we obtain $\mu^2 = \frac{6}{5} \frac{1}{D_a \tau}$. Again, the profile of $n_0(x)$ is given by $n_0(x) = A \cosh(\mu x) + C$, where A and C are constant to be determined. The hypothesis (3.23) can be checked using the Hermite expansion (3.13) with $n_1 = 0$ and $v_a^2 = \frac{D_a}{\tau}$, in such a way we get the relations:

$$n_0(x) \langle v^2 \rangle_x = 2v_a^4 n_2(x) + v_a^2 n_0(x), \quad (3.84)$$

$$n_0(x) \langle v^3 \rangle_x = 6v_a^6 n_3(x), \quad (3.85)$$

$$n_0(x) \langle v^4 \rangle_x = 24v_a^8 n_4(x) + 12v_a^6 n_2(x) + 3v_a^4 n_0(x), \quad (3.86)$$

$$n_0(x) \langle v^5 \rangle_x = 60v_a^8 n_3(x) + 120v_a^{10} n_5(x). \quad (3.87)$$

The condition $n_5 = 0$ means that

$$\langle v^5 \rangle_x = 10v_a^2 \langle v^3 \rangle_x. \quad (3.88)$$

Such a relation coincide with Eq.(3.23) only if we can replace $\langle v^2 \rangle_x$ with the constant factor v_a^2 in Eq (3.88). This is possible in the regime of small τ where $\langle v^2 \rangle_x - v_a^2 = 2v_a^4 \frac{n_2(x)}{n_0(x)} \approx 0$.

Instead, (3.23) is consistent with the choice $n_5(x) = \frac{n_3(x)n_2(x)}{n_0(x)}$, even if the substitution of such a relation into Eqs. (3.87) leads to a closed set of non-linear equations which cannot be easily solved.

3.C Exact distribution in the parabolic channel

In this appendix, we report the expression of the whole distribution for an active chiral particle in a parabolic channel, $kx^2/2$. As discussed in the main text, the distribution is a multivariate Gaussian which does not depend on y for symmetric reasons. The distribution, $P(\mathbf{x}, \mathbf{v})$, has the form:

$$P(\mathbf{x}, \mathbf{v}) = \mathcal{N} \exp\left(-\frac{A}{2}x^2\right) \exp\left(-\frac{K_1}{2}v_x^2 - \frac{K_2}{2}v_y^2 - K_3v_xv_y\right) \times \exp(-M_1v_x x - N_2v_y x), \quad (3.89)$$

where N is the normalization and $A, K_1, K_2, K_3, M_1, N_2$ are constants with respect to the variables \mathbf{x} and \mathbf{v} . For the sake of simplicity we introduce the symbol

$$\Delta = \Omega^2 \tau^2 + \Gamma^2,$$

which allows us to express the amplitudes in a more suitable form in terms of the control parameters:

$$\begin{aligned} A &= \frac{k}{D_a \gamma} \frac{\Omega^4 \tau^4 + 2\Omega^2 \tau^2 + 3\Omega^2 \tau^2 (\Gamma - 1) + \Gamma^3}{\Delta}, \\ K_1 &= \frac{\tau}{D_a} \frac{\Omega^2 \tau^2 + \Gamma^3}{\Delta}, \quad K_2 = \frac{\tau}{D_a} \Gamma \frac{\Omega^2 \tau^2 + \Gamma}{\Delta}, \quad K_3 = \frac{\Omega \tau^3}{D_a \gamma} \frac{\Gamma}{\Delta} k, \\ M_1 &= -\Omega^2 \tau^4 \frac{1}{D_a \gamma} \frac{k^2}{\gamma} \frac{1}{\Delta}, \quad N_2 = -\frac{\Omega \tau^2}{D_a \gamma} \frac{\Omega^2 \tau^2 + \Gamma}{\Delta} k. \end{aligned}$$

From the exact distribution derived in this appendix, we can compute the expression of the the y components of the average velocity, which reads

$$\langle v_y \rangle_x = \frac{\Gamma - 1}{\Gamma} \Omega x \quad (3.90)$$

and, in particular, is proportional to $\frac{\Omega \tau}{\gamma} k$.

3.D Transport properties of Brownian particles in open-wedge channels

In this appendix we employ the Fick-Jacobs approach [169] to derive the distribution, $P(x, t)$, along the axis of the wedge-channel employed in our numerical study. This theory can be applied to channels with variable section if the relaxation time towards the stationary state along y (i.e. the transversal direction with respect to the axis of the wedge) are shorter than the time scale associated with the longitudinal motion. In particular for a system of Brownian particles $p(y|x)$ is roughly constant, a condition also known as transversal homogenization. Such a condition cannot hold for self-propelled particles in the large persistence regime, because of the accumulation near the walls largely described in this Chapter. Thus, the approximation developed in this appendix works in the Brownian-like regime [or alternatively in regime iii)].

The condition of elongated channels, $H \ll L$, leads possible a description in terms of a one-dimensional equation for the longitudinal probability distribution, $P(x, t)$:

$$\frac{\partial P}{\partial t} + \frac{\partial J}{\partial x} = k \delta(x) \quad (3.91)$$

$$P(L, t) = P(-L, t) = 0, \quad (3.92)$$

where $\delta(x)$ is the Dirac-delta function. The right hand side of the first equation accounts for the particles re-injection at $x = 0$, while the last two equations implement the absorbing boundary conditions at $x = \pm L$. The constant k states the re-injection rate and will be determined later. The function $J(x, t)$ is the current along x obtained integrating out the y -degree of freedom in the whole Fokker Planck equation and reads:

$$J(x, t) = -\frac{T}{\gamma} e^{\gamma\epsilon x/T} w(x) \frac{\partial}{\partial x} \left[e^{-\gamma\epsilon x/T} \frac{P(x, t)}{w(x)} \right]. \quad (3.93)$$

Eq.(3.93) describes the longitudinal transport along the channel axis for a wedge with section described by the profile $w(x) = H - Hx/a$ with the additional presence of a bias with amplitude ϵ which acts along $\hat{\mathbf{x}}$. For the sake of simplicity, we define

$$D_0 = \frac{T}{\gamma}, \quad \varepsilon = \frac{\gamma\epsilon}{T}. \quad (3.94)$$

In the steady state, reinjection and absorption balance, being the number of particles preserved, in such a way that the following relation holds

$$J(L) - J(-L) = k, \quad (3.95)$$

which states the loss fluxes at the two boundaries are balanced by the re-injection. The steady state distribution, $P(x)$, is determined by the following equation:

$$-D_0 \frac{\partial}{\partial x} \left[w(x) e^{\varepsilon x} \frac{\partial}{\partial x} e^{-\varepsilon x} \frac{P}{w(x)} \right] = k \delta(x). \quad (3.96)$$

The solution of Eq.(3.96) can be obtained as a piece-wise function in the two domains $[-L, 0]$ and $[0, L]$, in such a way that:

$$P(x) = \begin{cases} A Y_1(x), & -L \leq x < 0 \\ B Y_2(x), & 0 \leq x \leq L \end{cases} \quad (3.97)$$

being

$$Y_1(x) = e^{\varepsilon x} w(x) \int_{-L}^x du \frac{e^{-\varepsilon u}}{w(u)} \quad (3.98)$$

and

$$Y_2(x) = e^{\varepsilon x} w(x) \int_x^L du \frac{e^{-\varepsilon u}}{w(u)}. \quad (3.99)$$

Y_1 and Y_2 are the solutions of the homogenous equation obtained setting $k = 0$, which satisfies the boundary conditions $Y_1(-L) = Y_2(L) = 0$. A and B are two coefficients to be determined using the continuity of the solution, i.e. $P(0^+) = P(0^-)$, and from Eq.(3.96): integrating Eq.(3.96)

over the interval $[-\Delta, \Delta]$ and then taking the limit $\Delta \rightarrow 0$ we get the second condition. In this way we obtain:

$$A = \int_0^L dx \frac{e^{-\varepsilon x}}{w(x)}, \quad B = \int_{-L}^0 dx \frac{e^{-\varepsilon x}}{w(x)},$$

and by means of algebraic manipulation we get

$$A = \text{Ei}[\varepsilon a] - \text{Ei}[\varepsilon(a - L)] \quad (3.100)$$

$$B = \text{Ei}[\varepsilon(a + L)] - \text{Ei}[\varepsilon a], \quad (3.101)$$

where $\text{Ei}[\cdot]$ is the Exponential integral function [178]. Using the explicit expression of A and B we obtain the prediction for $P(x)$:

$$P(x) \propto e^{\varepsilon x} (a - x) \begin{cases} A(\text{Ei}[\varepsilon(a + L)] - \text{Ei}[\varepsilon(a - x)]), & \text{when } x \in [-L, 0] \\ B(\text{Ei}[\varepsilon(a - x)] - \text{Ei}[\varepsilon(a - L)]), & \text{when } x \in [0, L]. \end{cases} \quad (3.102)$$

This formula is exact except for the normalization constant to be imposed by assuming that the integral of $P(x)$ in the interval $[-L, L]$ is one and complete the derivation of Eq.(3.68). The formula (3.102) simplifies in the case $\varepsilon = 0$, in absence of any driving force:

$$P(x) = C(a - x) \begin{cases} A \ln \left[\frac{a + L}{a - x} \right], & x \in [-L, 0] \\ B \ln \left[\frac{a - x}{a - L} \right], & x \in [0, L] \end{cases} \quad (3.103)$$

being $A = \ln[(a + L)/a]$, $B = \ln[a/(a - L)]$ and C a normalization constant which reads:

$$C^{-1} = \frac{L}{4} \left[2a \ln \left(\frac{a^2}{a^2 - L^2} \right) + L \ln \left(\frac{a + L}{a - L} \right) \right]. \quad (3.104)$$

The solution (3.103) corresponds to Eq.(3.67) of the main text.

Estimate of p_R and $\bar{\tau}$

Now, we derive Eq.(3.71) for p_R in the Brownian-like limit obtained for $D_r \rightarrow \infty$, corresponding to the right plateau of Fig.3.21. Since $P(\pm L) = 0$, the fluxes at the absorbing boundaries are proportional to the derivatives of P in the points $x = \pm L$, in such a way that $J(\pm L) = -D_0 P'(\pm L)$. Thus, we can obtain p_R as ratio between the fraction of the flux towards the right exit and the total flux:

$$p_R = \frac{J(L)}{J(L) + J(-L)} = \frac{\ln(a + L) - \ln(a)}{\ln(a + L) - \ln(a - L)}. \quad (3.105)$$

corresponding to Eq.(3.71) of the main text.

Let us derive the expression for $\bar{\tau}(x)$ in the Brownian-like limit. In this case it is necessary to estimate the first-arrival time at $\pm L$. For a particle released at x , such an observable is related to the survival probability $S(x, t)$ [65], which is the probability that a particle has not yet left the interval $[-L, L]$ at time t , by definition. In particular, the following relation between $\bar{\tau}(x)$ and $S(x, t)$ holds:

$$\bar{\tau}(x) = \int_0^\infty dt S(x, t). \quad (3.106)$$

It is known that $S(x, t)$ satisfies the backward Fokker-Planck equation [65]:

$$\frac{\partial S}{\partial t} = \frac{D_0}{w(x)} \frac{\partial}{\partial x} \left[w(x) \frac{\partial S}{\partial x} \right] \quad (3.107)$$

with the additional boundary conditions $S(\pm L, t) = 0$. Integrating Eq.(3.107) in the interval $0 \leq t < \infty$ and using that $S(x, \infty) = 0$ and $S(x, 0) = 1$, we can derive the following differential equation for $\bar{\tau}(x)$:

$$\frac{d}{dx} \left[w(x) \frac{d\bar{\tau}}{dx} \right] = -\frac{w(x)}{D_0}. \quad (3.108)$$

To get a solution we have to impose the obvious conditions $\bar{\tau}(\pm L) = 0$, which means that particles emitted at the boundary are instantaneously absorbed. Since we are interested in the average arrival time from the injection point at $x = 0$, we have

$$\bar{\tau}(x = 0) = \frac{L^2}{4D_0} + \frac{aL}{2D_0} \frac{\ln[a^2/(a^2 - L^2)]}{\ln[(a + L)/(a - L)]} \quad (3.109)$$

which is Eq.(3.75) of the main text.

Chapter 4

Energetics of active matter: a prototype of far from equilibrium system

Nowadays, the manipulation of matter at the single molecule level represents a new intriguing frontier for modern Statistical Physics, made possible by the rapid developments of nanotechnologies. The trajectories of single microswimmers at the mesoscale level, such as bacteria and spermatozoa among the others, can be experimentally tracked and the recent increase of resolution extends the observations to biological and man-made objects even at micro and nano-scales. For these reasons, the attention of the physicists has been attracted by systems with a small number of degrees of freedom, far from the thermodynamic limit [180, 181]. At variance with the approach of usual Statistical Mechanics, the fluctuations around the average values of thermodynamic variables cannot be neglected and are responsible for many non-trivial behaviors.

The developments of the so-called “stochastic thermodynamics” introduce new important tools to generalize familiar observables such as exchanged heat, work, entropy and internal energy to very small systems, even formed by a single particle. This approach is based on the probability associated with a trajectory, i.e. a single realization of the dynamics purely determined by the properties of the noise [182, 183]. Averaging over several realizations the theory returns the values of the thermodynamic variables. The path-integral methodology, which, for instance, leads to the computation of the entropy production of the system - estimated as the log-ratio between the probability of the forward and backward trajectories - was originally developed for a system of a passive particle immersed in a thermal bath. Successively, this study has been connected to the currents in the Fokker Planck equation associated to the dynamics, leading to a deeper physical interpretation of this methodology [184]. The concepts of entropy production of the medium, i.e flux of entropy towards the environment, and the total entropy production of the system have been introduced and connected with

the path-integral calculations [185, 186]. In the passive Brownian systems, the entropy production has been identified as the energy dissipated in the thermal bath and is determined by the deterministic forces taking place in the dynamics.

Some years ago, path-integral methods have been generalized to non-Markovian systems, with memory effects both in the Stokes force and in the noise term [187]. This is possible since the method is only based on the estimate of the path-probability from the properties of the stochastic source of the noise. Nevertheless, going beyond the Gaussianity is not an easy issue and only a few useful results are currently available in the literature. Even if the methods can be extended without complications, their connection with thermodynamic variables is not clear. A definition of work and heat rate is not so straightforward and even the extension of the entropy production rate definition is questionable. Nevertheless, this observable remains a powerful tool to understand how far from equilibrium is the system under investigation.

The applicability of path-integral techniques goes beyond the calculation of the entropy production: they can also be used to address several problems common in stochastic processes. For instance, they have been employed to calculate the escape rate from a well of a bistable potential [127] or study the linear response due to a perturbation field [188, 189]. Besides, they have been employed in polymer physics to estimate the end-to-end distance of particles' chains [190]. Elucidating the correct way to use this method is an important issue for modern physics, mostly concerning non-equilibrium systems. In particular, the calculation of the entropy production for systems of self-propelled particles [101, 191], following the AOUP dynamics, gives rise to a theoretical debate, which was solved in [192, 103] and, successively, in [193] from another point of view. One of the main goals of the Chapter is to review this matter, shedding light on the correct way to apply the method and reviewing the computation of the entropy production accounting also for the presence of the solvent [103]. Besides, we propose a reasonable definition of the heat-rate flux to restore the Clausius inequalities for self-propelled particles [102, 194].

The relation between the response due to external fields and the spontaneous fluctuations of the system is one of the most important results of Statistical Physics. In the framework of equilibrium Statistical Mechanics, it connects the correlation functions to macroscopic observables such as compressibilities, specific heats, and susceptibilities. Instead, in non-equilibrium systems, the time-dependent response can be calculated through the time-dependent correlations for the unperturbed system, i.e. without applying any external fields. This general idea has its roots in Einstein's work on Brownian motion and, later, in the Onsager regression hypothesis [195, 196] [see also [197]]. From this idea, the fluctuation-dissipation (FD) theorem, also known as fluctuation-dissipation relations (FDR), has been formulated by Callen and Welton [198] and then expanded by Kubo's theory [199] of

time-dependent correlation functions, holding for Hamiltonian systems near thermodynamic equilibrium. Successively, the FDR has been generalized to a vast class of systems [200], for instance, with chaotic dynamics very interesting in the framework of geophysics and climate [201]. The application of the generalized FDR to non-equilibrium stochastic dynamics has been independently obtained in [202]. In the last 20-25 years, the theoretical understanding of the response goes beyond the linear regime and several relations have been developed to study systems arbitrarily far from equilibrium [203]. In particular, in 1993, the Fluctuation Relation (FR) has been introduced to study the fluctuations of the entropy production rate in a fluid under shear [204], by Evans, Cohen and Morriss, and by Gallavotti and Cohen [182]. Successively, the Crooks [205] and Jarzynski relations [206] have been proposed. The application and the possible “violation” of such relations in active matter systems is a debated topic. For this reason, the second part of the Chapter will be devoted to the study of the linear response theory due to a small perturbation for self-propelled particles and to the application of the generalized fluctuation-dissipation relations in such a system.

The Chapter is structured as follows: in Sec. 4.1, we present the path-integral approach to estimate the probability of the forward and backward paths generalized to systems affected by non-Markovian noises. We derive a general formula for the entropy production and the injected power, generalizing Sekimoto’s result. Some examples are discussed in Section 4.2: i) the passive Brownian particle as a consistency check, ii) the self-propelled particles evolving with the AOUP dynamics and iii) the same system in the presence of the additional thermal noise due to the solvent. In Sec.4.3, we discuss the energetics of AOUP particles, reporting the expression of the heat-rate and deriving a generalized version of the Clausius inequality. Besides, we use the heat-rate to confirm the existence of equilibrium and non-equilibrium regions for confined systems, as already discussed in Chapter 2. Then, in Sec.4.4, we apply the generalized version of the fluctuation-dissipation relations to the same system, to compute the response function due to a small perturbation. Finally, in Sec. 4.5, we summarize the results and present some conclusions.

4.1 Path Integral approach: the probability of a trajectory

Let us start by introducing the path-integral method to estimate the path probability for non-Markovian systems. In what follows, we adopt a different notation, consistent with overdamped systems of self-propelled particles, to outline the generality of the present concepts. The application of such techniques to the active systems will be explicitly presented in the further sections. We consider a general dynamics in terms of the set of state variables, ω , describing our physical system. We express the dynamics as a set

of first-order differential equations, without loss of generality:

$$\dot{\boldsymbol{\omega}} = \mathbf{F}(\boldsymbol{\omega}) + \boldsymbol{\eta}. \quad (4.1)$$

\mathbf{F} is a generic vector force, which can depend on all the variables of the dynamics and contains all the deterministic contributions taking place in the dynamics. Instead, the vector $\boldsymbol{\eta}$ encloses every stochastic source which could be even strongly correlated. The term $\boldsymbol{\eta}$ could arise from a coarse-grained procedure of some degrees of freedom, usually faster than the state variables, $\boldsymbol{\omega}$, which typically evolve on slower scales. To make an example, the set $\boldsymbol{\omega}$ can be identified with the position, \boldsymbol{x} , of a colloid immersed in a bath of very fast and small particles. In this case, the contributions of the small particles to the dynamics of the colloid can be approximated by a white noise, which will be contained in $\boldsymbol{\eta}$. nevertheless, there exist many physical systems where the properties of the noise are more complicated, displaying time or spatial correlations among their different components. For the sake of simplicity, we assume that $\langle \boldsymbol{\eta} \rangle$ vanishes and that the two-time correlation matrix of the noise is given by

$$\nu_{ij}(t-s) = \langle \eta_i(s) \eta_j(t) \rangle.$$

While for a colloid $\nu_{ij}(t-s)$ is a delta-correlated function, in the AOUP model $\nu_{ij}(t-s)$ decays exponentially in time, for instance. In this Section, to exhibit the generality of our result, we consider $\boldsymbol{\nu}(t-s)$ as a general invertible matrix.

In what follows, we denote the time history of a single trajectory between the initial time, t_0 and the final time, \mathcal{T} , by $\underline{\boldsymbol{\omega}} = \{\boldsymbol{\omega}\}_{t_0}^{\mathcal{T}}$. The features of the noise, $\boldsymbol{\eta}$, determines the path-probability, i.e. the probability of observing the path $\underline{\boldsymbol{\omega}}$ starting from the initial state $\boldsymbol{\omega}_0$. Hereafter, we consider Gaussian noises, and so completely determined by the first two moments, average and correlations, i.e. $\langle \boldsymbol{\eta} \rangle$ and $\nu_{ij}(t-s)$, respectively. Accounting for these assumptions, the path-probability reads:

$$\tilde{P}[\underline{\boldsymbol{\eta}}|\boldsymbol{\eta}_0] \propto \exp \left[-\frac{1}{2} \int dt \int ds \boldsymbol{\eta}(s) \mathbf{T}^{-1}(t-s) \boldsymbol{\eta}(t) \right], \quad (4.2)$$

dropping the normalization constant. The integrals in Eq. (4.2) are computed from t_0 to \mathcal{T} even if, also in what follows, we will drop the two extremes to simplify the notation. \mathbf{T}^{-1} is the operator representing the inverse of $\boldsymbol{\nu}$, defined as:

$$\int dt' \mathbf{T}^{-1}(t-t') \boldsymbol{\nu}(t'-s) = \mathbf{I} \delta(t-s),$$

being \mathbf{I} the unit matrix and $\delta(t)$ the Dirac delta function. The computation of \mathbf{T}^{-1} is reported in Appendix 4.A for several choices of $\boldsymbol{\nu}$ and, in general, needs to be evaluated in the Fourier space.

Changing variables by means of Eq. (4.1), $\boldsymbol{\nu}$ can be expressed in terms of the state variables $\boldsymbol{\omega}$ and their time derivatives $\dot{\boldsymbol{\omega}}$. From Eq.(4.1), we

have $\boldsymbol{\eta} = \boldsymbol{\eta}[\boldsymbol{\omega}, \dot{\boldsymbol{\omega}}]$ and, in addition, the two path probabilities satisfies the following relation:

$$\log P[\underline{\boldsymbol{\omega}}|\boldsymbol{\omega}_0] = \log \tilde{P}[\underline{\boldsymbol{\eta}}|\boldsymbol{\eta}_0] + \log \det \frac{\partial \boldsymbol{\eta}}{\partial \underline{\boldsymbol{\omega}}}, \quad (4.3)$$

being the last term the Jacobian of the transformation from $\boldsymbol{\eta}$ to $\underline{\boldsymbol{\omega}}$. Thus, the probability of a trajectory can be written only in terms of $\underline{\boldsymbol{\omega}}$ and $\dot{\boldsymbol{\omega}}$:

$$P[\underline{\boldsymbol{\omega}}|\boldsymbol{\omega}_0] \propto \exp \left[-\frac{1}{2} \int dt \int ds \boldsymbol{\eta}[\boldsymbol{\omega}, \dot{\boldsymbol{\omega}}](s) \cdot \mathbf{T}^{-1}(t-s) \cdot \boldsymbol{\eta}[\boldsymbol{\omega}, \dot{\boldsymbol{\omega}}](t) \right]. \quad (4.4)$$

In the change of variables leading to Eq.(4.4), the contribution of the determinant has been neglected. Indeed, this term plays only a marginal role under very general conditions and is completely irrelevant in the determination of the entropy production [207, 208, 209]. By considering Eq.(4.1), we can express Eq.(4.4) without loss of generality:

$$P[\underline{\boldsymbol{\omega}}|\boldsymbol{\omega}_0] \propto \exp \left[-\frac{1}{2} \int dt \int ds [\dot{\boldsymbol{\omega}} - \mathbf{F}](s) \cdot \mathbf{T}^{-1}(t-s) \cdot [\dot{\boldsymbol{\omega}} - \mathbf{F}](t) \right].$$

4.1.1 Time-reversal trajectory

In what follows, we introduce the probability associated to the reversed trajectory, i.e. the path which starts from the final state $\boldsymbol{\omega}_{\mathcal{T}}$ to end after a time interval $\mathcal{T} - t_0$. To compute this path-probability, we need to know how the state variables transform under time-reversal transformation. For notational convenience, we introduce the time-reversal operator, Θ , which acts on the generic observable, $o(t)$, as $\Theta o(t) = o(\mathcal{T} - t)$. We assume that each state variable transforms with a fixed prescription, even or odd variable, without loss of generality. Indeed, any complex variables written as a linear combination of even and odd variables can be decomposed in their sum. With these assumptions, the probability of observing the reverse-path reads:

$$P[\Theta \underline{\boldsymbol{\omega}}|\Theta \boldsymbol{\omega}_0] \propto \exp \left[\frac{1}{2} \int dt ds [\epsilon \dot{\boldsymbol{\omega}} + \mathbf{F}(\epsilon \boldsymbol{\omega})](s) \mathbf{T}^{-1}(t-s) [\epsilon \dot{\boldsymbol{\omega}} + \mathbf{F}(\epsilon \boldsymbol{\omega})](t) \right]$$

being $\Theta \boldsymbol{\omega}_0 = \epsilon \boldsymbol{\omega}_{\mathcal{T}}$ and ϵ a diagonal matrix with elements ± 1 for even and odd components under time reversal symmetry, respectively.

In what follows, we assume that the state variables, $\boldsymbol{\omega}$, are even under time reversal transformation (TRT), for the sake of simplicity: we are interested in such a case, even if the formalism could be easily applied in the more general case. In this way, ϵ is simply the identity matrix. The operator \mathbf{T}^{-1} is even under TRT because, by definition, $\boldsymbol{\nu}$ is even. Thus, the probability of the reversed path is:

$$P[\Theta \underline{\boldsymbol{\omega}}|\Theta \boldsymbol{\omega}_0] \propto \exp \left[\frac{1}{2} \int dt \int ds [\dot{\boldsymbol{\omega}} + \mathbf{F}](s) \mathbf{T}^{-1}(t-s) [\dot{\boldsymbol{\omega}} + \mathbf{F}](t) \right].$$

In practice, we are assuming that the deterministic force, \mathbf{F} , depends only on the even variables $\boldsymbol{\omega}$, without any explicit time-dependence.

4.1.2 Entropy Production and Dissipation

Following [187], we can estimate the entropy production of the medium, $\Sigma_{\mathcal{T}}$, as the log-ratio between the path-probability of the forward and the backward trajectories, generalizing the well-known result of [183] to non-Markovian noises. In practice, we get:

$$\begin{aligned}\Sigma_{\mathcal{T}} &= \log \frac{P[\underline{\omega}|\omega_0]}{P[\Theta\underline{\omega}|\Theta\omega_0]} \\ &= \frac{1}{2} \int dt \int ds \left[\dot{\omega}(t)\mathbf{T}^{-1}(t-s)\mathbf{F}(\omega(s)) + \mathbf{F}(\omega(t))\mathbf{T}^{-1}(t-s)\dot{\omega}(s) \right] \\ &+ \frac{1}{2} \int dt \int ds \left[\epsilon \dot{\omega}(t)\mathbf{T}^{-1}(t-s)\mathbf{F}(\epsilon\omega(s)) + \mathbf{F}(\epsilon\omega(t))\mathbf{T}^{-1}(t-s)\epsilon\dot{\omega}(s) \right].\end{aligned}\quad (4.5)$$

In the first passage, we have dropped irrelevant boundary terms, i.e. the quadratic terms $\omega\mathbf{T}^{-1}\omega$ and $\mathbf{F}\mathbf{T}^{-1}\mathbf{F}$, following the calculations of [187]. Restricting to even state variables, the two terms in the right-hand side of Eq. (4.5) are equal and we get:

$$\begin{aligned}\Sigma_{\mathcal{T}} &= \log \frac{P[\underline{\omega}|\omega_0]}{P[\Theta\underline{\omega}|\Theta\omega_0]} \\ &= \int dt \int ds \left[\dot{\omega}(t)\mathbf{T}^{-1}(t-s)\mathbf{F}(\omega(s)) + \mathbf{F}(\omega(t))\mathbf{T}^{-1}(t-s)\dot{\omega}(s) \right] \\ &= \int dt \left[\dot{\omega}(t) (\mathbf{T}^{-1} * \mathbf{F})(t) + \mathbf{F}(t) (\mathbf{T}^{-1} * \dot{\omega})(t) \right].\end{aligned}\quad (4.6)$$

The symbol $*$ indicates the convolution operator. Being \mathbf{T}^{-1} a decreasing function of $|t-s|$, the integrals can be extended from $-\infty$ to ∞ : this procedure is equivalent to add boundary terms, which in the limit of large \mathcal{T} does not contribute to $\Sigma_{\mathcal{T}}$. Then, the time-dependent entropy production rate can be expressed as follows:

$$\sigma(t) = \dot{\omega}(t) (\mathbf{T}^{-1} * \mathbf{F})(t) + \mathbf{F}(t) (\mathbf{T}^{-1} * \dot{\omega})(t). \quad (4.7)$$

We notice that the generalized Sekimoto's injection term resembles the first addend of Eq.(4.7), apart from a factor $1/2$. Instead, the second addend is a new term. Since \mathbf{T}^{-1} is an operator, the two addends are different except for special cases: in the case of white noise (passive Brownian motion), for instance, the two terms are equal since $\mathbf{T}^{-1}(t-s) \propto \mathbf{I}\delta(t-s)$. If $\mathbf{T}^{-1}(t-s) = \delta(t-s)\mathbf{G}^{-1}(t)$ is an operator local in time, Eq.(4.7) assumes the form:

$$\sigma(t) = \left[\dot{\omega} \mathbf{G}^{-1} \mathbf{F} + \mathbf{F} \mathbf{G}^{-1} \dot{\omega} \right](t) = \left[\dot{\omega} \mathbf{G}^{-1} \mathbf{F} + (\dot{\omega} \mathbf{G}^{-1} \mathbf{F})^{adj} \right](t), \quad (4.8)$$

where adj denote the adjoint operation. In the last equality we have used that $\mathbf{T}^{-1} = (\mathbf{T}^{-1})^{adj}$. We remark that, even when $\mathbf{T}^{-1}(t-s) = \delta(t-s)$

$s)\mathbf{G}^{-1}(t)$, the operator \mathbf{T}^{-1} can be a non-multiplicative operator, containing time derivatives, for instance.

Following Sekimoto [210, 211], we can also define the dissipation, I , as the imbalance between the power dissipated by the drag force and the power injected by the noise. This observable has been connected with the entropy production, originally for driven Langevin processes. Successively, such a connection have been generalized to particles immersed into a viscoelastic bath [212]. In the latter context, we can extend the generalized dissipation to systems whose dynamics is ruled by Eq.(4.1), obtaining:

$$I = \dot{\omega} \mathbf{G}^{-1} \mathbf{F} = -\dot{\omega} \mathbf{G}^{-1} \dot{\omega} + \dot{\omega} \mathbf{G}^{-1} \eta. \quad (4.9)$$

It is worthy to note that I is quite similar to the dissipation of particles in viscoelastic baths. Now, it is straightforward to express the entropy production in terms of I :

$$\sigma = I + I^{adj}. \quad (4.10)$$

Eq.(4.10) provides a generalization of Sekimoto's result originally obtained for a Brownian particle. Such a case will be reviewed in Sec.4.2 as a consistency check of the theory.

It is particularly convenient to express Eq. (4.6) in a more suitable way, switching from the time average of $\sigma(t)$ in the limit $\mathcal{T} \rightarrow \infty$ to its average over the space of the state variables:

$$\Sigma_{\mathcal{T}} \simeq \mathcal{T} \langle \sigma \rangle = \mathcal{T} \int d\omega p_s(\omega) \left[\dot{\omega} (\mathbf{T}^{-1} * \mathbf{F}) + \mathbf{F} (\mathbf{T}^{-1} * \dot{\omega}) \right]. \quad (4.11)$$

With the symbol \simeq we are referring to the steady-state entropy production, so neglecting any boundary and transient terms. The only assumption to switch from Eq.(4.6) to Eq.(4.11) is the ergodicity of the system. Eq.(4.11) is our final result for the entropy production and will be the starting point for the next Section.

4.2 Over-damped dynamics

In this Section, we consider the dynamics of particles in the over-damped regime, assuming that inertial terms are negligible. We restrict to the one-dimensional case, without loss of generality, since the results reported can be easily generalized to interacting particles in more dimensions. This simple choice means that the set ω contains only the position of the particle, x , a variable which is even under time-reversal transformation. In this way, there will be no arbitrary choices about the parity under TRT of the state variables. Thus, the general he dynamics treads:

$$\dot{x} = \frac{F}{\gamma} + \eta, \quad F = -U'(x), \quad (4.12)$$

being F the force due to the external potential $U(x)$ and γ the drag coefficient, in the same notation of the previous chapters. We remark that Eq.(4.12) is a generalization of any over-damped dynamics, including the case of the AOUP dynamics, for instance. The theory can be extended to driving deterministic forces, without complications. Nevertheless, such a generalization does not add anything to the following discussion. The term, η , encodes the whole source of stochasticity: the contribution of the solvent, the self-propulsion mechanism of the microswimmers or anything else noise source taking place in the dynamics. According to a recent interpretation, proposed by Di Leonardo et. al.[70, 71] and confirmed by several experiments, η can be alternatively considered as the effect of a bath of active particles on a tracer passive body, which evolves with Eq.(4.12). Assuming that F is a linear force, this choice can model the effect of an active gel [213, 214, 215, 216], as observed experimentally [217]. In what follows we consider three specific cases: i) passive Brownian particle, ii) AOUP particle in the absence of thermal noise, iii) AOUP particle in a thermal bath due to the solvent.

4.2.1 Example I: passive Brownian particles

As a consistency check for our theory, we consider the case of a passive Brownian particle in a thermal bath. In this case, the evolution assumes a very simple form, being η a Gaussian delta-correlated noise with zero average and correlation $\langle \eta(t)\eta(s) \rangle = 2(T_b/\gamma)\delta(t-s)$. This dynamics leads to

$$T^{-1}(t) = \gamma \frac{\delta(t)}{2T_b}, \quad (4.13)$$

which is derived in Appendix 4.A. Applying Eq. (4.7), the steady state entropy production rate reads:

$$\sigma(t) = -\frac{\gamma}{2T_b} \left[\frac{U'}{\gamma} \dot{x} + \dot{x} \frac{U'}{\gamma} \right] = -\frac{\dot{x}}{T_b} U' = -\frac{1}{T_b} \frac{d}{dt} U. \quad (4.14)$$

As expected, $\sigma(t)$ can be expressed as a time derivative and, thus, is a boundary term (b.t.), which gives only a vanishing contribution to the entropy production (4.6) in the steady-state:

$$\Sigma_{\mathcal{T}} \simeq \mathcal{T} \langle \sigma \rangle = - \int \frac{1}{T_b} \frac{d}{dt} U dt = b.t. \quad (4.15)$$

This is the only possible result since it is well-known that the detailed balance condition holds in such a system. Being the particle globally in equilibrium with the environment, no entropy can be produced in the steady-state.

Besides, using Eq.(4.9), the injected power, I , reads:

$$I = \dot{x} U' = \gamma \dot{x} (\dot{x} - \eta), \quad (4.16)$$

Eq.(4.16) coincides with Sekimoto’s result and is a consistency check for our general formula. Averaging Eq.(4.16) with the steady-state probability distribution, we obtain

$$\langle I \rangle = \frac{d}{dt} \langle U \rangle,$$

which vanishes in the stationary state, as expected.

4.2.2 Example II: Self-propelled particles without thermal noise

As a prototype of far equilibrium system, we apply our general theory to the dynamics of a self-propelled particle in a confined potential, considering the AOUP model in the absence of thermal noise. As already discussed in Chapter1, such an approximation holds for several experimental microswimmers.

The calculation of the entropy production of such dynamics gives rise to a recent debate, which has been solved in [192, 103] and confirmed in [193] with a different approach. The problem arises from the ambiguity concerning the parity under time reversal transformation of the active force, f_a . Indeed, starting from Eq.(2.28a) with zero thermal noise, it could be reasonable to fix arbitrarily the odd or even parity of f_a , a priori. Clearly, depending on the choice considered, we will obtain different results from the path-integral method [194, 218]. Instead, it is straightforward to calculate the entropy production rate from the transformed dynamics in variables (x, v) [101], due to the formal analogy with an underdamped passive Brownian system. In this case, no arbitrary choices have been performed, except for the reasonable assumption about the even parity of the microswimmer position x . Despite the clarity of the method, unphysical results occur: potential-free or harmonically confined particles display vanishing entropy production, in contrast with the fact that microswimmers consume energy from the environment, in both cases, being deeply far from the equilibrium in any experiments. To solve such a problem, the authors of [191] proposes to change arbitrarily the definition of the entropy production rate, from the path-integrals, modifying the backward-trajectory generator “by hands”. This procedure has already led to well-known results, for instance, in the presence of magnetic fields [219, 220, 221, 222], where its employment is based on strong and indisputable physical argument. Nevertheless, the meaning of these modified definitions of the entropy production is not clear in several cases, see for instance the discussion in [223]. We assert that this is also the case of self-propelled particles, where the procedure is even physically wrong. In what follows we develop an alternative way to perform the path integral applying the general theory developed in [187] for non-Markovian noises. We confirm the result of [101] and shed light on the parity of the self-propulsion, which is nor even nor odd.

The dynamics for the particle position, x , is given by Eqs.(2.28), which can be obtained from the general Eq.(4.12), replacing η with an exponentially correlated Gaussian noise, η_a . Below, we report the two-time correlation of η_a , in the same notation of the previous chapters.

$$\langle \eta_a(t)\eta_a(s) \rangle = \frac{D_a}{\tau} \exp(-|t-s|/\tau). \quad (4.17)$$

As shown in Appendix4.A, we can easily calculate the operator T^{-1} in the Fourier space, which reads

$$T^{-1}(t) = \delta(t)G^{-1}(t) = \frac{\delta(t)}{2D_a} \left(1 - \tau^2 \frac{d^2}{dt^2} \right). \quad (4.18)$$

We observe that T^{-1} is a differential operator, but for $\tau \rightarrow 0$ reduces to a multiplicative one, consistently with Eq.(4.13) for a passive Brownian particle with diffusion coefficient, D_a . Identifying the set $\boldsymbol{\omega}$ with the position, x , of the particle and \mathbf{F} with the force due to potentials, we obtain the entropy production rate:

$$\begin{aligned} \sigma(t) &= -\frac{1}{\gamma} \left[\dot{x}(t) (T^{-1} * U') (t) + U'(t) (T^{-1} * \dot{x}) (t) \right] \\ &= \frac{\tau^2}{\gamma} \left[\frac{\dot{x}(t)}{2D_a} \int ds \delta(t-s) \frac{d^2 U'(s)}{ds^2} + \frac{U'(t)}{2D_a} \int ds \delta(t-s) \frac{d^2 \dot{x}(s)}{ds^2} \right] - \frac{d}{dt} \frac{U}{D_a \gamma} \\ &= \frac{\tau^2}{2D_a \gamma} \left[\dot{x}^3(t) U'''(t) + \dot{x}(t) \ddot{x}(t) U''(t) + U'(t) \frac{d}{dt} \ddot{x}(t) \right] - \frac{d}{dt} \frac{U}{D_a \gamma} \\ &= \frac{\tau^2}{2D_a \gamma} \left[\dot{x}^3(t) U'''(t) + \frac{d}{dt} (\ddot{x}(t) U'(t)) \right] - \frac{d}{dt} \frac{U}{D_a \gamma}. \end{aligned} \quad (4.19)$$

Second and third addend of Eq.(4.19) are simply boundary terms while the first one is the only source of entropy production in the steady-state. We remark that we have not used arbitrary prescriptions about the parity under TRT of any terms. Thus there are no ambiguities in the procedure adopted since the position is the only variable involved in the calculations. Wondering what is the parity of f_a is meaningless. Instead, considering explicitly the dynamics of f_a , i.e. adopting a ‘‘Markovianization’’ of the AOUP, it is straightforward to see that f_a is nor even nor odd. Instead, is the sum of an even and an odd variable, because satisfies the relation:

$$f_a = \gamma \dot{x} + U'(x). \quad (4.20)$$

Coming back to the entropy production, we have:

$$\Sigma_{\mathcal{T}} = \int^{\mathcal{T}} ds \sigma(s) = \frac{\tau^2}{2D_a \gamma} \langle \dot{x}^3 U''' \rangle_{\mathcal{T}} + b.t. \quad (4.21)$$

where we have used the ergodicity to switch from the time average to the average over the space variables. Eq.(4.21) coincides with the entropy production calculated by Fodor et. al. [101], as already anticipated, which

is the only correct result for the AOUP dynamics in the approximation of vanishing thermal noise. Formula(4.21) shows that the entropy production vanishes both for potential-free and harmonically confined AOUP particles, i.e. the cases such that $U'''(x) = 0$. As already discussed by [191], this is an unphysical result: it does not match with biological systems, which are always far from equilibrium even in the absence of a confined mechanism. This fact does not mean that Eq.(4.21) is wrong or need to be modified, but this is only a failure of the model employed. Anyway, Eq.(4.21) predicts a positive entropy production for a general non-harmonic potential. Its value depends on the curvature of the potential and is larger as τ increases, according to our intuition. As an additional argument in favor of Eq.(4.21), Marconi et. al. [191] derive the analog result following a different approach based on the method introduced by Seifert [184], which comes directly from the manipulation of the Fokker Planck equation. This approach will be directly reviewed in Sec4.3.

Applying Eq.(4.7), we compute the dissipation of the AOUP model, which is quite similar to the one of a particle immersed into a viscoelastic bath:

$$\begin{aligned} I &= -\dot{x}G^{-1}U' - U'G^{-1}\dot{x} \\ &= -\frac{1}{2D_a\gamma^2} \left[\dot{x} \left(1 - \tau^2 \frac{d^2}{dt^2} \right) U' + U' \left(1 - \tau^2 \frac{d^2}{dt^2} \right) \dot{x} \right] \\ &= -\frac{\dot{x}U'}{D_a\gamma^2} + \frac{\tau^2}{2D_a\gamma^2} \left[\dot{x} \frac{d^2}{dt^2} U' + U' \frac{d^2}{dt^2} \dot{x} \right]. \end{aligned}$$

We remark that the above equation encodes an additional term with respect to the result of Fodor et al. [101], which comes from the second addend of Eq. (4.7).

4.2.3 Example III: Self-propelled particles in a suspension at fixed temperature

Even though Eq.(2.28) without thermal noise is often used in the literature, in a typical experimental setup self-propelled particles swim through a solvent even if its contribution could be very small with respect to the self-propulsion strength. Thus, the particle can be formally imagined in contact with two reservoirs, the thermal and the active one. As already discussed in Sec.3.2.1 of Chapter3, the presence of two baths led to non-trivial results in the framework of the accumulation near the walls.

For these reasons, we derive the entropy production for the AOUP dynamics in the presence of the thermal bath due to the environment. Also in this case, the particle remains far from equilibrium due to the active force and, thus, we expect a non-vanishing entropy production. The dynamics could be obtained by replacing the noise term η with $\eta_a + \eta_t$ in Eq. (4.12), where η_t is a white noise with $\langle \eta_t \rangle = 0$ and $\langle \eta_t(t)\eta_t(s) \rangle = 2(T_b/\gamma)\delta(t-s)$.

Instead, η_a is the colored noise already introduced in Sec. 4.2.2. It is straightforward to calculate the correlation matrix $\nu(t-s)$ of the whole noise:

$$\nu(t-s) = 2 \frac{T_b}{\gamma} \delta(t-s) + \frac{D_a}{\tau} \exp(-|t-s|/\tau). \quad (4.22)$$

Instead, T^{-1} simply reads:

$$T^{-1}(t) = \frac{\gamma}{2T_b} \delta(t) + K^{-1}(t), \quad (4.23)$$

where

$$K^{-1}(t) = -\frac{D_a \gamma^2}{2T_b^2} \left(\frac{1}{\zeta} \right) \left[\frac{1}{\tau} \sqrt{\zeta} \exp\left(-\frac{|t|}{\tau} \sqrt{\zeta}\right) \right], \quad (4.24)$$

$$\zeta = 1 + \frac{D_a \gamma}{T_b}.$$

The calculation of $T^{-1}(t)$ in the Fourier space is reported in Appendix 4.A. We observe that the first addend of Eq. (4.23) is determined by the thermal noise while the second one depends on both the reservoirs. At variance with the case of zero thermal noise, T^{-1} is non-local in time being not proportional to $\delta(t-s)$. Indeed, $K^{-1}(t)$ decays exponentially with a typical time given by $\tau/\sqrt{1 + D_a \gamma/T_b}$. Such a result has been derived in [218] and in [103], independently. Using the general expression (4.7), we obtain the entropy production rate:

$$\begin{aligned} \sigma(t) &= -\frac{\dot{x}(t)U'(t)}{T_b} - \frac{U'(t)}{\gamma} \int K^{-1}(t-s)\dot{x}(s)ds - \dot{x}(t) \int K^{-1}(t-s)\frac{U'(s)}{\gamma}ds \\ &= -\frac{U'(t)}{\gamma} \int K^{-1}(t-s)\dot{x}(s)ds - \dot{x}(t) \int K^{-1}(t-s)\frac{U'(s)}{\gamma}ds, \end{aligned} \quad (4.25)$$

where, as usual, we have neglected boundary terms. As a consistency check, we calculate the equilibrium limit, $\tau \rightarrow 0$, for which we expect a vanishing entropy production rate (unless of boundary terms). Since the expression within the square brackets in Eq. (4.24) approach to a delta-Dirac function, we get:

$$\lim_{\tau \rightarrow 0} T^{-1}(t) = \frac{\delta(t)}{(D_a + T_b/\gamma)}. \quad (4.26)$$

As we expect, the denominator of Eq.(4.26) is given by the sum of the solvent temperature and the effective temperature, $D_a \gamma$, due to the active force. Using the above expression of $T^{-1}(t)$ in the formula of the entropy production, Eq. (4.7), we obtain a boundary term, as in the case of a Brownian particle, Eq.(4.14). It is worthy to discuss the limit $D_a \gamma/T_b \ll 1$ in Eq.(4.25). We find that the entropy production rate decreases with the ratio $D_a \gamma/T_b$ because the amplitude of $K^{-1}(t)$ is proportional to this factor. In the end, we consider the singular limit $T_b \rightarrow 0$. In this case, we expect that the entropy

production rate converges to the result obtained at zero thermal noise. We have:

$$\lim_{T_b \rightarrow 0} \Sigma_{\mathcal{T}}(T_b \neq 0) = \frac{\tau^2}{2D_a\gamma} \langle \dot{x}^3 U''' \rangle \mathcal{T}, \quad (4.27)$$

neglecting boundary terms. In Appendix 4.C the limit is rigorously performed. Eq.(4.27) coincides with Eq.(4.21) of the previous section, derived directly in the case $T_b = 0$.

In what follows, we approximate Eq.(4.25) to extrapolate the largest contribution of the entropy production rate to express it as the average of an observable, which can be easily calculated by simulations. For each time history, we expect that the largest contribution occurs when the variables are strongly correlated. Since the memory kernel decays exponentially in time, this is achieved by the short time region, namely $t \sim s$. The kernel can be expanded in powers of $|t-s|/\tau_R \ll 1$, where τ_R is the correlation time of T^{-1} . For the sake of simplicity, we stop at the first order. In the same way, the only relevant contributions of the integral come from the time interval $[t - \tau_R, t]$. Using these approximations, we have:

$$\begin{aligned} \sigma(t) &= -2 \frac{U'(t)}{\gamma} \int_{t_0}^t K^{-1}(t-s) \dot{x}(s) ds - 2\dot{x}(t) \int_{t_0}^t K^{-1}(t-s) \frac{U'(s)}{\gamma} ds \\ &\approx 2 \frac{A}{\gamma\tau_R} \left[U'(t) \int_{t-\tau_R}^t \dot{x}(s) ds + \dot{x}(t) \int_{t-\tau_R}^t U'(s) ds \right] \\ &\approx 2 \frac{A}{\gamma} \left\{ U'(t) \left[\frac{x(t) - x(t - \tau_R)}{\tau_R} \right] - \dot{x}(t) [U'(t) - U'(t - \tau_R)] \right\}, \quad (4.28) \end{aligned}$$

where A is a constant which is:

$$A = \frac{D_a\gamma^2}{2T_b^2} \left(\frac{1}{1 + \frac{D_a\gamma}{T_b}} \right), \quad \tau_R = \tau \left(\sqrt{1 + \frac{D_a\gamma}{T_b}} \right)^{-1}. \quad (4.29)$$

The second time integral in Eq.(4.28) has been approximated in the simplest way as possible in the second equality. We remark that Eq.(4.28) is consistent with the equilibrium limit. Indeed, for $\tau \rightarrow 0$ the first term of Eq.(4.28) becomes the boundary term $\propto U'\dot{x}$ since $\tau_R \rightarrow 0$. In this limit, the second addend of Eq.(4.28) approaches to zero and the entropy production vanishes, as expected. Using the ergodicity, we can switch to the two-time state variables probability. Then, since the position $x(t - \tau_R)$ and $x(t)$ are roughly uncorrelated, the entropy production rate can be expressed as follows:

$$\langle \sigma \rangle \approx 2 \frac{A}{\tau_R\gamma} [\langle U'(x)x \rangle - \langle x \rangle \langle U'(x) \rangle + \tau_R \langle \dot{x} \rangle \langle U'(x) \rangle], \quad (4.30)$$

since the third addend of Eq.(4.28) is a boundary term.

In this case, the entropy production does not vanish even for a harmonic potential, as we expect for biological systems. We find that the leading order

of the entropy production is proportional to the x -variance of the distribution, because $\langle \dot{x} \rangle = 0$, as explicitly evaluated in [116]. Nevertheless, the potential-free case leads to vanishing entropy production, even in such a case. Such a failure is not due to the definition of the entropy production, which is unique upon specifying the dynamics, but rather to the poor modeling: its coarse-grained level cannot reproduce the real entropy production.

4.3 Energetics and local properties of the entropy production for the AOUP model

The energetics of a suspension of active particles, for instance the computation of heat-rate and stochastic work, is a controversial matter, currently under debate. Indeed, the generalization of such concepts to non-equilibrium systems is not so clear and some authors claim even that the equilibrium definitions are intrinsically ill-defined.

In the current Section, we restrict to the AOUP dynamics. We aim to define the heat-rate, following [102], and generalize the Clausius inequality to such systems [194]. Without loss of generality, we restrict our study to the one-dimensional case, even if generalizations to larger dimensionalities or interacting systems are straightforward. We also restrict to the case $D_t = 0$, for the sake of simplicity. We remark that it is not so clear if the methods could be applied to the ABP model, despite the AOUP dynamics is a good approximation of the ABP one.

4.3.1 The stochastic first thermodynamics law

It is convenient to rewrite the Smoluchowski equation for the probability distribution in the (x, v) representation as a continuity equation:

$$\frac{\partial}{\partial t} p = -\frac{\partial}{\partial x} I_x - \frac{\partial}{\partial v} I_v, \quad (4.31)$$

where $p = p(x, v, t)$ is the time-dependent solution of the equation and (I_x, I_v) are the components of the current in the space (x, v) . Both can be decomposed as the sum of reversible and irreversible contributions, denoted with the superscripts “*rev*” and “*irr*”, respectively. In particular, we get

$$(I_x^{rev}, I_v^{rev}) = \left(vp(x, v, t), -\frac{U'(x)}{\tau\gamma} p(x, v, t) \right), \quad (4.32)$$

while the irreversible currents are

$$(I_x^{irr}, I_v^{irr}) = \left(0, -\frac{D_a}{\tau^2} \frac{\partial}{\partial v} p(x, v, t) - v \frac{\Gamma(x)}{\tau} p(x, v, t) \right). \quad (4.33)$$

It is convenient to introduce the total stochastic energy, $e(t)$, as:

$$e(t) = \tau\gamma \frac{v^2}{2} + U(x, t). \quad (4.34)$$

Introducing a stochastic version of the first principle of the thermodynamics, e , can be expressed as the sum of the stochastic work and the stochastic heat. Then, differentiating their average values with respect to time we get:

$$\langle \dot{e}(t) \rangle = \langle \dot{W}(t) \rangle + \langle \dot{Q}(t) \rangle \quad (4.35)$$

being \dot{W} and \dot{Q} the stochastic work and heat rate, respectively. In particular, \dot{W} is given by the simple form:

$$\langle \dot{W} \rangle = \int dx dv p(x, v, t) \frac{\partial}{\partial t} U(x, t), \quad (4.36)$$

which vanishes if U does not depend explicitly on time, as in the case discussed in the previous Section. Instead, \dot{Q} reads:

$$\langle \dot{Q} \rangle = \int dx dv e(t) \frac{\partial}{\partial t} p(x, v, t) = \int dx dv e(t) \left[\frac{\partial}{\partial x} I_x + \frac{\partial}{\partial v} I_v \right], \quad (4.37)$$

where in the last equality we have used Eq.(4.31). Restricting to forces due to potentials as in Sec.4.2, the energy rate coincides with the heat rate being $\dot{W} = 0$. In this case, the contribution of the reversible currents vanishes and the expression of \dot{Q} reduces to:

$$\begin{aligned} \langle \dot{Q} \rangle &= - \int dx dv \left[\frac{\Gamma(x)}{\tau} v^2 p(x, v) + \frac{D_a}{\tau^2} v \frac{\partial}{\partial v} p(x, v, t) \right] \\ &= - \int dx \frac{\Gamma(x)}{\tau} \int dv \left[v^2 - \frac{D_a}{\tau \Gamma(x)} \right] p(v, x), \end{aligned} \quad (4.38)$$

where in the last equality we have only integrated by parts and used the zero flux boundary conditions at infinity. It is interesting to note that Eq.(4.38) approaches to zero in the limit $\tau \rightarrow 0$, in analogy with an equilibrium system. In this limit $p(x, v)$ approaches to a Gaussian with variance D_a/τ , meaning the two addends in Eq(4.44) cancel out at each position.

4.3.2 The stochastic second thermodynamics law: the generalized Clausius inequality

To find a version of the second principle in the framework of the stochastic thermodynamics, we introduce the Gibbs entropy

$$S(t) = - \int dx dv p(x, v, t) \log p(x, v, t).$$

Taking the derivative with respect to time, we get the Gibbs entropy production rate, $s(t) = \dot{S}(t)$:

$$\begin{aligned} s(t) &= - \int dx dv \frac{\partial}{\partial t} p(x, v, t) \log p(x, v, t) \\ &= \int dx dv \left[\frac{\partial}{\partial x} I_x + \frac{\partial}{\partial v} I_v \right] \log p(x, v, t), \end{aligned} \quad (4.39)$$

where we have used Eq.(4.31) in the last passage. Integrating by parts we can prove that the reversible currents do not provide any contributions to $S(t)$ and that the only relevant terms come from I_v^{irr} . Thus, using the definition of I_v^{irr} , we can express $s(t)$ as follows:

$$s(t) = \frac{\tau}{D_a} \int dx dv \left[\tau \frac{(I_v^{irr})^2}{p} + \Gamma(x) v I_v^{irr} \right]. \quad (4.40)$$

This expression allows us to decompose $s_s(t)$ in the sum of the entropy production of the whole system, $s_s(t)$, and the entropy production of the medium, $\sigma(t)$, i.e. the flux of entropy due to heat exchanges between the system and the surroundings, in analogy with equilibrium-like systems. In particular, we have $s(t) = s_s(t) - \sigma(t)$, where:

$$s_s(t) = \frac{\tau^2}{D_a} \int dx dv \frac{(I_v^{irr})^2}{p}, \quad (4.41)$$

$$\sigma(t) = -\frac{\tau}{D_a} \int dx dv \Gamma(x) v I_v^{irr}. \quad (4.42)$$

Even though such a decomposition could appear quite arbitrary, we observe that $s_s(t) \geq 0$, being the integral of a square. Then, since in the steady-state $s(t) = 0$, we simply obtain

$$\sigma(t) = s_s(t) \geq 0, \quad (4.43)$$

meaning that the entropy production of the medium coincides with the positive entropy production of the system in the steady-state. Using the definition of I_v^{irr} , Eq.(4.42) reads:

$$\sigma = \int dx dv \frac{\tau}{D_a} \Gamma(x) \left[\frac{\Gamma(x)}{\tau} v^2 - \frac{D_a}{\tau^2} \right] p(x, v) \geq 0, \quad (4.44)$$

We notice that Eq.(4.44) approaches to zero in the limit $\tau \rightarrow 0$, in analogy with an equilibrium system, and when $U(x)$ is chosen as zero, linear or harmonic potential, i.e. in the cases where $U'''(x) = 0$. For consistency with Sec.4.2, we can prove that Eq.(4.44) coincides with the result of the path-integral methods. The equivalence between Eq.(4.44) and Eq.(4.21) - apart from irrelevant boundary terms - is reported in Appendix 4.B. We remark that the formula (4.44) includes the contribution of the boundary terms and, thus, is the more suitable one to make a connection with the stochastic heat and work. Quite surprisingly, σ is proportional to \dot{Q} up to a function of x , which is nothing but the temperature, $\theta(x) = D_a/\tau\Gamma(x)^{-1}$, already introduced in Sec.2.5.1 by means of the UCNA approximation. Thus it is useful to introduce the space-dependent heat rate flux, $\dot{q}(x)$, as

$$\begin{aligned} \dot{q}(x) &= -\frac{\Gamma(x)}{\tau p(x)} \int dv \left[v^2 - \frac{D_a}{\tau^2 \Gamma(x)} \right] p(v, x) \\ &= -\frac{D_a \gamma}{\tau \Gamma(x)} \left[\tau \gamma \langle v^2 \rangle_x - \theta(x) \right], \end{aligned} \quad (4.45)$$

where $\langle v^2(x) \rangle_x = \int dv p(v, x) v^2 / p(x)$, is the conditional moment of v^2 , in the same notation of Chapter 3. Combining Eq.(4.45) and Eq.(4.44), it is straightforward to express the entropy production rate as follows:

$$\sigma(t) = - \int dx p(x) \frac{\dot{q}(x)}{\theta(x)} \geq 0. \quad (4.46)$$

Eq.(4.46) is the generalized version of the Clausius inequality for a system of self-propelled particles following the AOUP dynamics. This derivation provides dignity to the nomenclature “temperature” introduced in Sec.2.5.1 to denote $\theta(x)$, despite its space dependence.

Currently, also other interpretations of heat and work are diffused in the literature: some authors identify the work rate as the contribution of the active force and the remaining terms as the heat exchanged with the thermal bath. In our opinion, these definitions are quite unreasonable, preventing the derivation of a Clausius-like inequality. On the contrary, we stress the simplicity and the clarity of the present result holding for AOUP particles. Due to the evident connection between AOUP and ABP illustrated in the previous Chapter, we expect that similar results should be valid also for ABP active particles, even if, up to now, they are not known in the literature.

4.3.3 Local properties of the heat and the entropy production

Now, we adapt the general theory of Sec.4.3 to the system of confined self-propelled particles already studied in Chapter 2, to unveil the properties of the heat rate flux in this particular case. Since a harmonic potential does not produce a steady-state entropy production in the AOUP dynamics, being the system in equilibrium, as shown and discussed in Sec. 4.2.2, we consider a non-harmonic confinement. To perform our numerical study we start from the one-dimensional profile used in Sec.2.5.2 of Chapter 2, which is $U(x) \propto x^{2n}$, with positive integer n . We consider the case $n = 4$ even if the further results are independent on such a particular choice. We remind that the study performed in Sec.2.5.2 led to the distinction between Equilibrium and Non-Equilibrium regions where the conditional distribution, $p(v|x)$, is Gaussian or not, respectively. To confirm such a statement and the validity of our energetics relations for the heat-rate flux and the space-dependent temperature, we study Eq.(4.45) for such a system in the same condition of Sec.2.5.2. Fig.4.1(a) shows the profile of $\dot{q}(x)$ for different values of the persistence time, by means of the parameter $\nu \propto \tau$. As we expect, for the smaller ν the heat-rate flux does not show any profile and reads zero point by point, consistently with an equilibrium system. For $\nu \gtrsim 1$, instead, $\dot{q}(x)$ is a symmetric function of x . In the two accumulation regions, where the particles spend most of their life, $\dot{q}(x)$ is negative but very small (almost zero). Near the minimum of the potential $\dot{q}(x)$, in the origin of the reference

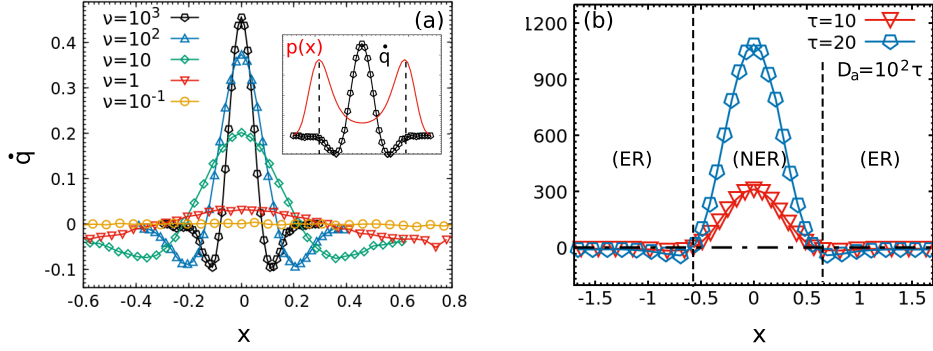


Figure 4.1: Heat-rate flux, $\dot{q}(x)$ as a function of the position for two different values of the parameters of the active force, as shown in the legends. Panel (a) and (b) are realized by means of a single-well quartic potential and a double-well potential, respectively. In both cases, the different curves are obtained at fixed D_a/τ , by varying τ (or equivalently $\nu \propto \tau$). The shape of the quartic potential is $U = kx^4/4$, with $k = 10$. Instead, the double potential has the profile of $U(x) = ax^4/4 - bx^2/2$, with $a = b = 10$.

frame, is very large and assumes positive values. As numerically checked in the steady-state, we have:

$$\dot{Q} = \int p(x)\dot{q}(x) = 0, \quad (4.47)$$

where the integral is performed over all the space. This condition gives dignity to our definition of \dot{Q} . Indeed, if the integral was different from zero in the stationary state, \dot{Q} would not be well-defined. Because of the ergodicity (note that $p(x)$ is peaked in the ER) we may conclude that a particle spends most of its life in the ER, where it accumulates a small amount of heat per unit time through the coupling with the fictitious bath. Instead, through fluctuations, the particle may overcome the effective barrier which separates the two effective symmetric wells, crossing the NER, where it returns all the heat, absorbed before, to the bath [77]. Such a scenario is consistent with the picture of Sec.2.5.2, since in the NER the heat-rate flux is very large while in the ER is approximatively zero.

Now, let us turn on the study of a non-convex potential. As a prototype case, we consider the double-well shape already studied in Sec. 2.6 of Chapter 2. Despite the fact that the UCNA temperature, $\theta(x)$, could assume negative values in the NER for τ large enough, becoming even zero, we remark that both $\dot{\sigma}(x)$ and $\dot{q}(x)$ are well-defined, remaining finite observables. As in the convex cases, in the two equilibrium-like regions occurring at $\Gamma > 0$, the heat rate flux $\dot{q}(x)$ (or equivalently $\dot{s}(x)$) is almost zero, assuming very small negative values. The NTR region, introduced in Sec. 2.6, is contained in the NER and displays large $\dot{q}(x)$ which assumes positive values. Indeed, both $-\theta(x)$ and $\langle v^2(x) \rangle$ in Eq. (4.45) have positive sign. As shown in Fig. 4.1(b), $\dot{q}(x)$ grows as τ increases. Indeed, evaluating the regime $\tau \gg 1$

in Eq. (4.45) in the NTR, $\dot{q}(x) \approx -\Gamma(x)\langle v(x) \rangle \sim \tau|U''(x)|\langle v^2(x) \rangle$, which shows the occurrence of an explicit τ dependence. Despite the fact that $\theta(x)$ approaches to infinity for $\Gamma(x) = 0$, we remark that $\dot{q}(x)$ remains finite and positive while $\dot{s}(x)$ becomes zero [104]. In the same way of the convex case, the Clausius inequality (4.46) holds because $p(x)$ is large in the ER and very small in the NER.

Therefore, both for convex and non-convex potentials the nomenclature “Equilibrium” and “Non-Equilibrium” regions, suggested by the shape of the probability distribution function of the velocities, is coherent with our energetics description in terms of heat-rate flux and entropy production rate flux. Besides, the validity of the Clausius relation (both for convex and non-convex potentials) enforces the idea that θ could be considered as the effective temperature of self-propelled particles. Since for negative curvature θ becomes negative, self-propelled systems seem to be an example of far equilibrium systems displaying regions with spontaneous negative temperature.

4.4 Linear Response Theory

In this Section, we briefly review the linear response theory and the generalized fluctuation relations to adapt these non-equilibrium tools to a system of confined active particles evolving with the AOUP self-propulsion. We shall present analytic and numerical results by applying the generalized fluctuation-dissipation relations (FDR) [224], discussing the controversial theme of its “violation” in such non-equilibrium dynamics. In particular, we compare the response function in the (x, f^a) and (x, v) representation illustrating a technical point which sheds light on the computation of such observable. Then, we calculate the response function using the UCNA dynamics. We anticipate that these procedures lead to different results, depending on the variables chosen, and invalidates the use of the UCNA approach to describe such a time-dependent observable at least in the large persistent regime [225].

First of all, let us introduce the FDR, commenting on its so-called “violation”. In its original version, the FDR describes the relation between a non-equilibrium observable, the response function due to a small perturbation, and an equilibrium one, a correlation function within the unperturbed dynamics: for instance, for a colloid in the overdamped regime immersed in a thermal bath, the response can be measured by means of the velocity-velocity correlation function. Several authors claimed that a “violation” of the FDR means that it is not possible to express R in function of such a special correlation. This statement is true for a non-equilibrium system under very general conditions since the shape of the correlation function is only related to the functional form of the distribution [224]. In particular, its gaussianity in equilibrium is the only reason which leads to the velocity

autocorrelation. Therefore, it is not so surprising that for self-propelled particles the equilibrium version of FDR is not satisfied since the system is far from equilibrium.

The FDR were generalized by Vulpiani et al. to far from equilibrium dynamics, originally in the framework of dynamical systems which admits a steady-state distribution [201], and independently derived for general stochastic dynamics by Agarwal [202]. Their result holds under very general conditions and connects the response function due to a small perturbation to a special correlation - obtained in the absence of the perturbations - which involves the derivative of the logarithm of the probability distribution function of the unperturbed system. The practical difficulty of such a procedure is related to the computation of the probability distribution function, which is in general unknown for non-equilibrium systems. Anyway, we expect that the generalized version of the FDR holds for self-propelled particles, as for any non-equilibrium systems, even if both the response function and the correlation need to be evaluated numerically. Therefore, we stress the following point: the natural application of the FDR to non-equilibrium systems occurs in its generalized version which will be discussed below. Thus, arguing about any violation is improper or trivial.

4.4.1 Linear Response Theory for self-propelled particles: the generalized fluctuation-dissipation relations

The response function of self-propelled particles was studied by Szamel [73] in the presence of a harmonic confinement and by Fodor et al. [101] in the interacting case. The former considered the only case which can be solved exactly, without revealing any surprises, while the latter focused on the regime of small persistence time, measuring the time-integral of the response in the (x, v) variables, i.e. the susceptibility.

Let us consider the dynamics of an AOUP self-propelled particle in the presence of a small perturbation acting at the initial time on the position of the microswimmer, i.e. an impulsive force with the form $h(t) = h\delta(t_0)$. The perturbed dynamics, neglecting the thermal noise due to the solvent, reads:

$$\gamma\dot{x}_h = -U'(x_h) + f^a + h(t), \quad (4.48)$$

$$\tau\dot{f}^a = -f^a + \gamma\sqrt{2D_a}\eta, \quad (4.49)$$

where h denotes a variable of the perturbed dynamics. We define the response function, $R(t)$, as

$$R(t) = \frac{\langle\delta x(t)\rangle}{\delta x(0)} \equiv \frac{\langle x_h(t) - x(t)\rangle}{x_h(0) - x(0)}, \quad (4.50)$$

where the symbol $\langle\cdot\rangle$ stems for the average over different trajectories starting at $x_h(0)$ or $x(0)$. $R(t)$ can be interpreted as a normalized measure of the

“distance” between the perturbed and unperturbed average trajectories and quantifies the effect of the small perturbation on the dynamics, measuring the time that the trajectory needs to collapse on the unperturbed one. As already mentioned, the generalized version of the FDR consists in a general relation which allows us to compute $R(t)$ in terms of a special correlation function performed using the unperturbed probability distribution function. Adapting the general form of the FDR to the self-propelled dynamics, we get:

$$R(t) = - \left\langle x(t) \left(\frac{\partial}{\partial x} \log P(x, f^a) \right) \Big|_{t=0} \right\rangle^{h=0}. \quad (4.51)$$

where the average $\langle \cdot \rangle^{h=0}$ is performed by means of the unperturbed dynamics, i.e. setting $h(t) = 0$ in Eq.(4.48). $P(x, f^a)$ is the probability distribution in the unperturbed (x, f^a) representation. The pedex $t = 0$ means that the observable is calculated at time zero. For a recent review see [224].

4.4.2 Perturbative expansion of $\mathbf{R}(t)$

Even if Eq.(4.51) holds, its predictive feature is related to the knowledge of $P(x, f^a)$, i.e. on the possibility of solving the unperturbed dynamics of a system of self-propelled particles. As already mentioned in Chapter 2, a general expression for $P(x, f^a)$ in the presence of external confinements is known only in the harmonic case, while for general non-harmonic potentials the Fokker Planck equation associated to the dynamics cannot be exactly solved. The only result available in the literature, and independently obtained by Fodor et al. [101] and Maggi et al. [102], is an expansion in power of $\sqrt{\tau}$ around a Gaussian probability distribution, i.e. the measure of the system for $\tau = 0$. Rescaling time and velocity as $t = \sqrt{\tau}s$ and $\tilde{v} = \sqrt{t}v$, respectively, the probability distribution function reads

$$P(x, \tilde{v}) \propto e^{-\frac{U}{\gamma D_a} - \frac{\tilde{v}^2}{2D_a}} \left\{ 1 - \frac{\tau}{2\gamma^2 D_a} \left[(U')^2 + (\gamma \tilde{v}^2 - 3\gamma D_a) U'' \right] + \frac{\tau^{3/2}}{6\gamma D_a} \tilde{v}^3 U''' - \frac{\tau^{3/2}}{2\gamma} \tilde{v} U''' \right\}, \quad (4.52)$$

where we have neglected terms $\propto \tau^2$. The result comes from a smart expansion in the basis of the Hermite polynomials in the transformed variable (x, \tilde{v}) (this result is known only for $D_t = 0$). Being a result near the equilibrium, holding for very small τ , Eq.(4.52) is not enough to understand the non-equilibrium phenomenology explained in the previous Chapters. Defining $\tilde{f}_a = \sqrt{\tau} f^a$, we can easily come back to the original representation in the (x, \tilde{f}_a) variables. Using the relation (2.28a) with $D_t = 0$ and observing

that such a change of variables is unitary, we obtain:

$$P(x, \tilde{f}_a) \propto e^{-\frac{U}{\gamma D_a} - \frac{(\tilde{f}_a - \sqrt{\tau} U' / \gamma)^2}{2 D_a}} \left\{ 1 - \frac{\tau}{2 \gamma^2 D_a} \left[(U')^2 + \tilde{f}_a^2 \gamma U'' - 3 \gamma D_a U'' \right] - \frac{\tau^{3/2}}{\gamma^2 D_a} \tilde{f}_a U' U'' + \frac{\tau^{3/2}}{6 \gamma D_a} \tilde{f}_a^3 U''' - \frac{\tau^{3/2}}{2 \gamma} \tilde{f}_a U''' \right\}, \quad (4.53)$$

where Eq.(4.53) holds up to orders $\sim \tau^2$. Both distributions (4.52) and (4.53) can be easily generalized to more dimensions and to a system of interacting particles.

Inserting the expression for $P(x, \tilde{f}_a)$ in Eq.(4.51) we are able to compute the FDR in power of $\sqrt{\tau}$, finding:

$$R(s) = \left\langle x(t) \left(\frac{U'}{\gamma D_a} - \frac{\sqrt{\tau} \tilde{f}_a}{\gamma D_a} U'' + \tau \left[2 \frac{U' U''}{\gamma^2 D_a} + \frac{\tilde{f}_a^2}{2} \frac{U'''}{\gamma D_a} - \frac{3}{2} \frac{U'''}{\gamma D_a} \right] + \tau^{3/2} \left[-\frac{\tilde{f}_a}{\gamma^2 D_a} (U''^2 + U' U''') - \frac{f_a^3}{6} \frac{U''''}{\gamma D_a} + \frac{f_a}{2} \frac{U''''}{\gamma D_a} \right] \right) \Big|_{t=0} \right\rangle_{h=0}, \quad (4.54)$$

which holds up to orders τ^2 . This expression remains implicit since the two-time propagator, associated to the dynamics, is unknown and we are not able to find the explicit expression as a function of time for a general potential. The only exception is the harmonic trap which will be considered separately.

4.4.3 Caveat: calculation of the response function in the (x, \tilde{v}) representation

The generality of the FDR allows us to compute the response function directly in the (x, \tilde{v}) representation. Since the change of variables is unitary, one can be tempted to use Eq.(4.51), by replacing $P(x, \tilde{f}_a)$ with $P(x, \tilde{v})$. In what follows, we show that this naive scheme is wrong and leads to unphysical results. Let us define, $R_v(s)$ as the response function obtained in the (x, \tilde{v}) variables by perturbing the transformed dynamics with an additional small force $h(s) = h \delta(s)$. Using the FDR we get:

$$R_v(s) = - \left\langle x(s) \left(\frac{\partial}{\partial x} \log P(x, \tilde{v}) \right) \Big|_{s=0} \right\rangle_v^{h=0} \quad (4.55)$$

where the average $\langle \cdot \rangle_v^{h=0}$ is performed using the two-time propagator in the (x, \tilde{v}) representation for $h(t) = 0$. Using the shape of $P(x, \tilde{v})$, given by

Eq.(4.52), we obtain a perturbative expression of $R_v(t)$ neglecting orders τ^2 :

$$R_v(s) = \left\langle x(s) \left(U' + \tau \left[U''U' + \frac{\tilde{v}^2}{2}U''' - \frac{3}{2}U'''' \right] - \tau^{3/2} \left[\frac{\tilde{v}^3}{6}U'''' - \frac{\tilde{v}}{2}U'''' \right] \right) \right|_{t=0} \right\rangle_{v}^{s=0}. \quad (4.56)$$

Suprisingly, Eq.(4.56) does not coincide with Eq.(4.54) and, in particular, we have

$$R(s) = R_v(s) - \sqrt{\tau} \left\langle x(s)\tilde{v}(0)U''(x(0)) \right\rangle_{v}^{h=0} - \tau^{3/2} \left\langle x(s)\tilde{v}(0)U'''(x(0))U'(x(0)) \right\rangle_{v}^{h=0}, \quad (4.57)$$

which holds up to orders τ^2 . This relation shows that $R(s)$ and $R_v(s)$ differ at least by terms of order $\sqrt{\tau}$. This means that the excess terms vanish in the equilibrium limit, $\tau \rightarrow 0$, where the two representations return the same response function. Such a result appears to be counterintuitive: how is it possible that the response of the system to an initial small perturbation depends on the coordinates used?

The explanation easily comes observing that the change of variables and the computation of the response do not commute. In general, let us introduce the probability of the perturbed system in (x, \tilde{f}_a) and (x, \tilde{v}) variables as $P'(x, \tilde{f}_a) = P(x - \delta x, \tilde{f}_a)$ and $P'(x, \tilde{v}) = P(x - \delta x, \tilde{v})$, respectively. Let us call $\tilde{W} = \tilde{W}[(x_0, \tilde{f}_0^a) \rightarrow (x, \tilde{f}_a)]$ and $W = W[(x_0, \tilde{v}_0) \rightarrow (x, \tilde{v})]$ the transition probabilities from the state at the initial time to the one at time s in the coordinates (x, \tilde{f}_a) and (x, \tilde{v}) , respectively. Following [224], the response R at time s in the variables (x, \tilde{f}_a) reads:

$$R(s)\delta x_0 = \int x \left(P'(x_0, \tilde{f}_0^a) - P(x_0, \tilde{f}_0^a) \right) \tilde{W} dx_0 d\tilde{f}_0^a dx d\tilde{f}_a. \quad (4.58)$$

Accounting for the unitarity of the Jacobinan of the transformation from (x, \tilde{f}_a) to (x, \tilde{v}) , we can switch variables, obtaining:

$$R(s)\delta x_0 = \int x \left(P'(x_0, \tilde{v}_0[x, \tilde{f}_0^a]) - P(x_0, \tilde{v}_0[x, \tilde{f}_0^a]) \right) W dx_0 d\tilde{v}_0 dx d\tilde{v}. \quad (4.59)$$

For a small increment due to the perturbation, namely δx_0 , we have:

$$\begin{aligned} P'(x_0, \tilde{v}_0[x, \tilde{f}_0^a]) - P(x_0, \tilde{v}_0[x, \tilde{f}_0^a]) &= -\delta x_0 \left[\frac{\partial}{\partial x} P(x, \tilde{v}[x, \tilde{f}_0^a]) + \frac{\partial \tilde{v}(x, \tilde{f}_a)}{\partial x} \frac{\partial P}{\partial \tilde{v}} \right] \\ &= -\delta x_0 \frac{d}{dx} P(x, \tilde{v}[x, \tilde{f}_0^a]), \end{aligned} \quad (4.60)$$

where d/dx is the total derivative which acts also on the velocity while $\partial/\partial x$ is the partial derivative. Thus, the response function $R(s) = \langle \delta x(s) \rangle / \delta x_0$ reads:

$$\begin{aligned} R(s) &= - \left\langle x(s) \left(\frac{d}{dx} \log P(x, \tilde{v}(x, \tilde{f}_a)) \right) \Big|_{s=0} \right\rangle_v \\ &\neq - \left\langle x(s) \left(\frac{\partial}{\partial x} \log P(x, \tilde{v}(x, \tilde{f}_a)) \right) \Big|_{s=0} \right\rangle_v = R_v(s), \end{aligned} \quad (4.61)$$

where the averages $\langle \cdot \rangle_v$ are both performed with $P(x, \tilde{v})$. In other words, since \tilde{f}_a is a function of x and \tilde{v} , the perturbation $(x, \tilde{v}) \rightarrow (x + \delta x_0, \tilde{v})$ does not coincide with the perturbation $(x, \tilde{f}_a) \rightarrow (x + \delta x_0, \tilde{f}_a)$. This fact emerges if we apply the change of variables directly to the perturbed system, Eq.(4.48): in the resulting transformed dynamics, the perturbation affects both the dynamics of x and \tilde{v} .

4.4.4 Response function of the UCNA dynamics

In Section 2.2.3 of Chapter 2, the UCNA approximation was developed and, in Sec.2.4, was successfully used to predict the steady state phenomenology in the presence of external convex potentials. This approximation works in the limit of small persistence time since coincides with the first leading terms of the expansion in power of $\sqrt{\tau}$ of the whole probability distribution function given by Eq.(4.52). Moreover, even in the regime of large τ this approximation predicts the steady-state phenomenology of confined self-propelled particles: UCNA provides the exact distribution in the case of harmonic traps and reproduces the accumulation far from the minimum of the potential for non-harmonic single well confinements. Even if UCNA may reproduce the stationary features of the AOUP dynamics, we will show that cannot be applied to estimate the time-dependent dynamical properties of the system, as the response due to a small perturbation [225]. This is not so surprising since the UCNA approximation is obtained employing the adiabatic elimination of the velocity in the (x, \tilde{v}) representation. Since we have already shown that $R(s)$ does not coincide with $R_v(s)$, we expect that also the response function obtained from UCNA displays differences from $R(s)$.

Let us introduce the UCNA dynamics in the presence of the small perturbation $h(s) = \delta(s)h$. Adapting Eq.(2.13) of Chapter2 to the rescaled variables introduced in this Section we simply get:

$$\dot{x} = \Gamma(x)^{-1} \left[-\sqrt{\tau} \frac{U'(x)}{\gamma} + \sqrt{2\tau^{1/2} D_a \eta} \right] + h(s). \quad (4.62)$$

The steady-state probability distribution, $P_U(x)$, associated to the UCNA unperturbed dynamics, i.e. Eq.(4.62) with $h = 0$, assumes the simple form:

$$P_U(x) = \mathcal{N} \exp \left(- \left[U(x) + \frac{\tau}{\gamma} U'(x)^2 - \gamma D_a \ln \left(1 + \frac{\tau}{\gamma} U''(x) \right) \right] \right), \quad (4.63)$$

being \mathcal{N} a normalization constant. Applying the general version of the FDR on Eq.(4.62), we obtain the response function, R_U , in terms of the unperturbed log-derivative of P_U

$$R_U(s) = - \left\langle x(s) \left(\frac{\partial}{\partial x} \log P_U(x) \right) \Big|_{s=0} \right\rangle_U \quad (4.64)$$

where $\langle \cdot \rangle_U$ means that the average is performed using the unperturbed UCNA dynamics. Using the expression (4.63) in Eq.(4.64), we get:

$$R_U(s) = \langle x(s) (U'(x(0))) \rangle_U + \tau \langle x(s) (U'(x(0))U''(x(0))) \rangle_U - \tau \left\langle x(s) \left(\frac{U'''(x(0))}{1 + \tau U''(x(0))} \right) \right\rangle_U. \quad (4.65)$$

It is worthy to compare $R_U(s)$ [Eq.(4.65)] with $R_v(s)$ [Eq.(4.56)] and $R(s)$ [Eq.(4.54)]: R_U coincides with R_v up to the orders τ and, thus, the first discrepancy with the correct response function, R , occurs at the lower order in $\sqrt{\tau}$. Therefore, we expect that the UCNA response function cannot reproduce the behavior of $R(s)$ in the large persistence regime.

4.4.5 Numerical study of the response function

We study the response of an AOUP system of independent particles confined by the three different potentials, whose stationary properties have been already described in Chapter 2. We start from the harmonic trap, $kx^2/2$ [case (a)], which can be solved exactly, then we study the quartic potential, $kx^4/4$ [case (b)], and the double-well potential, $k(x^4/4 - x^2/2)$ [case (c)]. For both cases (b) and (c), we can apply the FDR only perturbatively in powers of $\sqrt{\tau}$, while the regime of large persistence needs to be studied numerically.

In panels (a), (b) and (c) of Fig.4.2, we show $R(t)$ for several values of $\zeta = 1/\sqrt{\tau}$ in the cases (a), (b) and (c), respectively. In the case (a), the unperturbed probability distribution of the system can be computed exactly, as shown in Sec.2.3 of Chapter 2, and we are also able to calculate the correlation and the response in function of time: the gaussianity of the distribution leads all the correlations to decay exponentially. In particular, the response has the form $R(s) \sim e^{-s\sqrt{\tau}k/\gamma}$, as clearly emerged in panel (a) of Fig.4.2. In this case, the analytical calculations are explicitly reported and commented in Sec.4.4.6. Therefore, in these rescaled units, the growth of ζ , i.e. the decrease of $\sqrt{\tau}$, induces the increase of the correlation time which dominates the exponential decay of $R(s)$.

In the cases (b) and (c), we can distinguish between two regimes in analogy with the discussion of Chapter 2. When τ is small (or $\nu \lesssim 1$ in the notation of Chapter 2) we are in a near-equilibrium regime, where the self-propulsion can be approximated by thermal noise. In this case, there are no differences with the typical response function of a passive suspension of

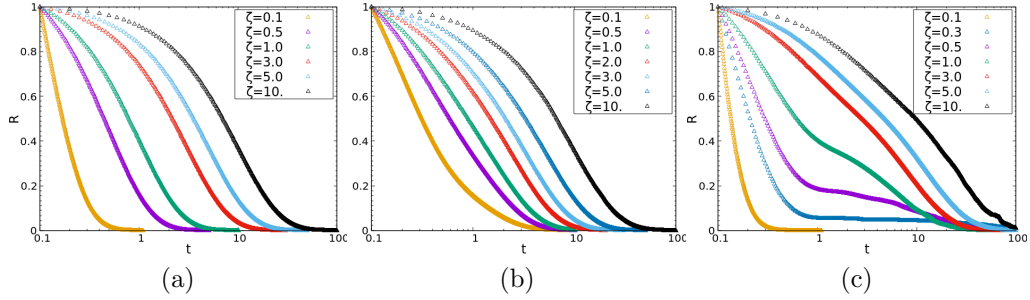


Figure 4.2: Responses $R(s)$ for the AOUP model computed, via numerical simulation, for different values of $\zeta = 1/\sqrt{\tau}$ by setting $k/\gamma = 1$. In figure (a) are plotted the responses for the harmonic potential $U(x) = kx^2/2$. The plots (b) and (c) correspond to a quartic potential $U(x) = kx^4/4$ and a double well potential $U(x) = k(x^4/4 - x^2/2)$, respectively.

particles. In particular, in the case of a quartic potential, the decrease of ζ (or equivalently the increase of $\sqrt{\tau}$) leads simply to slower decays of $R(s)$ which is ruled by a single time-scale, with roughly exponential profiles. Instead, in the double-well potential the situation is slightly richer: we can distinguish two different decay behaviors (roughly exponential). In the first stage, the typical decay time is related to the relaxation in one of the two wells and is determined by the curvature of the potential around their minima, namely $U''(x_{min})$. For longer times, roughly of the order of the Kramers escape rate, the decay is influenced by the jumps of particles between the two symmetric minima of the potential and a second slower regime occurs.

In the far from equilibrium regime, when ζ becomes smaller (large values of $\sqrt{\tau}$), we find a richer phenomenology. Let us start from the case (b) shown in panel (b) of Fig.4.2: we observe the occurrence of two decay regimes as if the dynamics was ruled by an effective bistable potential. As already described in Section 2.3 of Chapter 2, this is exactly what happens in the large persistence regime, where particles accumulate far from the minimum of the potential. Not so surprisingly the phenomenology of $R(s)$ is perfectly in agreement with what we expected. The occurrence of two decay regimes is also evident in the case (c), [see panel (c) of Fig.4.2], where the second regime is even more marked with respect to the $R(s)$ of the quartic potential. Interestingly, for the smallest value of ζ a single decay occurs again. This means that the relaxation is completed before a Kramers time.

In each panel of Fig.4.3b, we plot the responses for two different values of ζ (i.e. $1/\sqrt{\tau}$): one large and another small, representing the equilibrium-like and the far from equilibrium regime, respectively. In particular, panel (a) is obtained with a harmonic trap [case (a)] and is just a numerical test while panel (b) is obtained with the quartic confinement [case (b)]. We compare $R(s)$ and $R_U(s)$ to check their relation: we confirm that in the small persistence regime (large ζ and small τ), UCNA provides a good

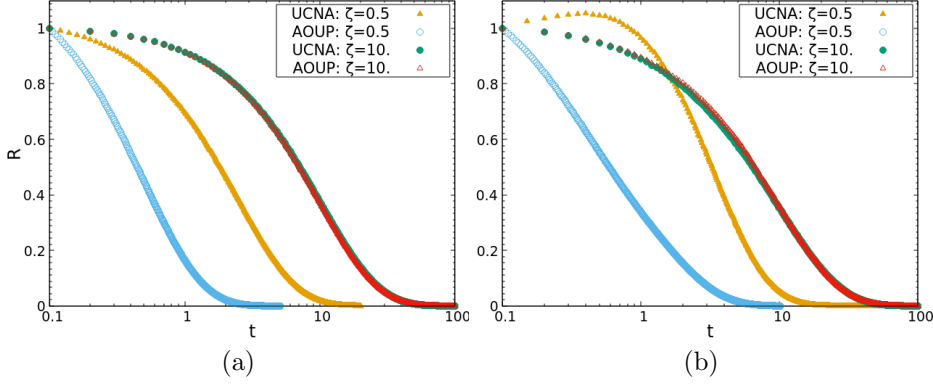


Figure 4.3: Responses functions computed via numerical simulations, R and R_U , for different values of ζ : $\zeta = 10, 0.5$ and $k/\gamma = 1$. The graphs are obtained for systems under the action of a harmonic potential $U(x) = kx^2/2$ (panel (a)) and a potential $U = kx^4/4$ (panel (b)).

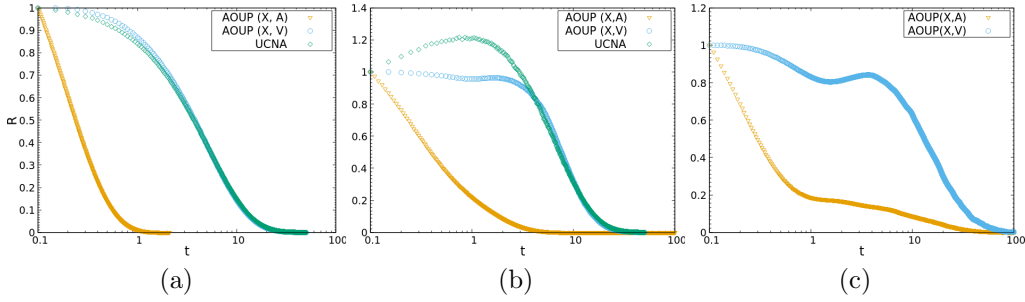


Figure 4.4: Response functions R , R_v and R_U in the case of small ζ : $\zeta = 0.2$ and $k/\gamma = 1$. The graphs (a) and (b) are obtained for systems under the action of a harmonic potential $U(x) = kx^2/2$ and a quartic one $U(x) = kx^4/4$, respectively. The graph (c) is obtained for the double well potential $U(x) = k(x^4/4 - x^2/2)$, for $\zeta = 0.5$.

approximation for the response function. Instead, UCNA underrates the response in the long-persistence regime, predicting a slower decay both in the harmonic and in the quartic potential. In the first case, the decay is again exponential but with larger correlation times, while, in the second case, even the shape of the decay is strongly modified. In particular, R_U reveals an unphysical non-monotonicity for small times.

In Fig.4.4, we show a comparison between $R(s)$, $R_v(s)$ and $R_U(s)$ to check the inequality (4.61) also in the large persistence regime. In panels (a), (b) and (c) we plot the responses for the harmonic, quartic and double-well potentials, respectively. In every case, $R_v(s)$ and $R(s)$ display large differences, as we expect, being in particular $R_v(s)$ always slower than $R(s)$. The explanation of such a slow down is quite clear in the case (a) since the correlation between x and \tilde{v} gives a negative contribution to the calculation

of R . In this case, $R_U(s)$ is a very good approximation of $R_v(s)$. This is no longer true in the case (b) where UCNA reproduces only the second decay regime completely underrating the response behavior for small times.

4.4.6 The harmonic potential: exact results

When the confinement is harmonic, $U(x) = kx^2/2$, we can compute exactly correlations and responses in function of time, without the employment of any approximations [73]. The linearity of the system implies that these observables are just combinations of exponentials. As already studied in Sec.2.3 of Chapter2, we can compute exactly the steady-state probability distribution function, which is a Gaussian both in x and \tilde{v} in the (x, \tilde{v}) representation, while is a multivariate Gaussian in the (x, \tilde{f}_a) one.

In this case, we can apply the FDR without power expansions determining the exact expression of $R(s)$ and $R_v(s)$ in terms of unperturbed correlation functions. Adapting Eq.(4.54) and Eq.(4.56) to the harmonic potential, we get:

$$R(s) = R_v(s) - \beta \frac{\sqrt{\tau}k}{\gamma} \langle x(s)\tilde{v}(0) \rangle_v, \quad (4.66)$$

where $R_v(s)$ reads:

$$R_v(s) = \beta \langle x(s)x(0) \rangle_v, \quad (4.67)$$

and β is a constant related to the xx element of the covariance matrix of the steady-state distribution function. R_v and R differ by a term $\propto \sqrt{\tau}$ which disappears only in the equilibrium limit $\tau \rightarrow 0$. The explicit expressions as a function of time are:

$$R(s) = e^{-s\sqrt{\tau}k/\gamma}, \quad (4.68)$$

and

$$R_v(s) = \frac{\sqrt{\tau}}{1 - \tau \frac{k}{\gamma}} \left(e^{-s/\sqrt{\tau}} - e^{-s\sqrt{\tau}k/\gamma} \right) \quad (4.69)$$

if $\tau k/\gamma \neq 1$. The details of the calculations are reported in Appendix4.D.

In the two panels of Fig.4.5, we compare numerically correlations and response functions for two different values of ζ . Both panels show that the generalized version of the FDR holds, as shown by the numerical comparison between the Response and the correlation given by Eq.(4.66). It is interesting to note that the cross correlation $\langle x(s)\tilde{v}(0) \rangle$ is almost zero for the larger value of ζ , as shown in panel (a). Instead, assumes larger negative values for the smaller values of ζ , i.e. when the system is far from equilibrium. Only in the latter case, R is strongly different from R_v .

It is worthy to mention that the dimensional version of Eq.(4.68) reads:

$$R(t) = e^{-tk/\gamma}, \quad (4.70)$$

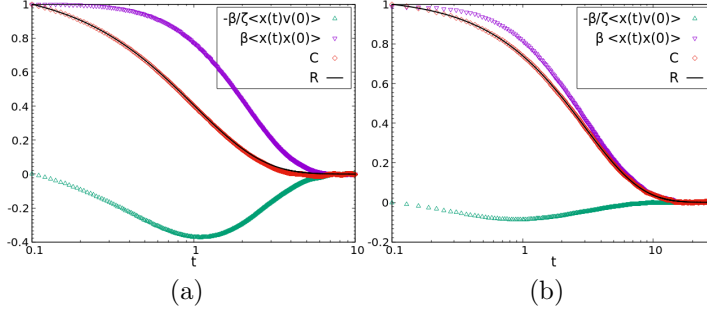


Figure 4.5: Response function $R(s)$ computed via numerical simulation for a harmonic potential $kx^2/2$ with $k = 1$ (black line). The red diamonds (C) represent the sum of the correlation functions, i.e. $R(s) = \beta k/\gamma \left(\langle x(s)x(0) \rangle_v - \sqrt{\tau} \langle x(s)\tilde{v}(0) \rangle_v \right)$, a test employed in order to verify FDR. The green triangles represent the correlation $\beta \langle x(s)\tilde{v}(0) \rangle_v$ and the violet inverse triangles represent the correlation $\beta \langle x(s)x(0) \rangle_v$ and . Panel (a) corresponds to $\zeta = 1$ and panel (b) to $\zeta = 3$.

i.e. the response in the original variables is independent of τ . The relaxation towards zero depends only on the ratio k/γ , i.e. on the parameters of the quadratic potential.

In Sec.4.4.4, we have concluded that we cannot use the UCNA dynamics to approximate the response function in the large persistence regime (small ζ or large $\sqrt{\tau}$). Below, we check this statement in the case of the harmonic oscillator where we can perform the calculations analytically. Indeed, the autocorrelation function of the position following the UCNA dynamics reads:

$$\beta \langle x(t)x(0) \rangle_U = \frac{\gamma}{k} e^{-\frac{k}{\gamma} \frac{s\sqrt{\tau}}{1+\tau k/\gamma}}. \quad (4.71)$$

Then, applying Eq.(4.65) to the harmonic potential of this Section, we get R_U :

$$R_U(s) = e^{-\frac{k}{\gamma} \frac{s\sqrt{\tau}}{1+\tau k/\gamma}} \quad (4.72)$$

As expected, R_U is consistent with R only in the small persistence regime, while for large τ the two expressions are not in agreement.

4.5 Conclusions

In this Chapter, we have reviewed several tools of non-equilibrium statistical mechanics, applying them on systems of non-interacting self-propelled particles evolving with the Active Ornstein-Uhlenbeck dynamics (AOUP model).

We have started by reviewing the path-integral approach to estimate the probability of the forward and the backward trajectory through which have focused on the calculation of the entropy production rate. Following

[187], we extend the well-known results originally developed for Gaussian white noises to the case of non-Markovian noises. In particular, we have studied the entropy production rate of a confined self-propelled particle in the absence of thermal noise, which recently has been a matter of intense debate [101, 191, 194]. This was solved in [192] and, successively, using a different approach in [193]. Indeed, the change of variables reviewed in Sec.2.2 of Chapter 2 introduces the ambiguity regarding the parity under time-reversal symmetry of the active force, whose choice could determine different results for the entropy production. In the present Chapter, we discover that the self-propulsion is neither even nor odd, being a combination of even and odd variables. Thus, following our technique, we confirm the results obtained with independent methods in [101] and [102], which differ from irrelevant boundary terms. Our method allows us to generalize the calculation of the entropy production to active systems in the presence of the additional thermal noise due to the environment where self-propelled particles are immersed [103].

Shedding light on the use of path-integral techniques is important in the study of non-equilibrium systems. Indeed, the path-probability can be used to calculate several interesting observables, such as the response due to a small perturbation or the escape time from a bistable potential. Recently, both these observables have been studied for a system of Active Brownian particles: the authors of [226] focused on the response under small shear flows, while the authors of [127] employed path integrals to compute the Kramers time. Moreover, the problem of arbitrarily fixing the parity of the self-propulsion appears also in the framework of ABP [227, 228, 229, 230] dynamics. Since, in the AOUP model, this matter has solved, we expect that the same may be true for the ABP dynamics. We mention that the entropy production of active matter has been calculated also for other models, for instance, considering the role of chirality [231], hydrodynamic interactions [232], or by accounting for the chemical origin of the active force in some specific cases [233, 234].

Several works have focused on the extending of many concepts of stochastic thermodynamics to a system of self-propelled particles, such as heat-rate and stochastic work. In the present Chapter, we have reviewed such concepts, following [102]. Using these tools, we confirm one of the leading observations illustrated in Chapter 2: even if the system is globally far from equilibrium, we can identify regions where the detailed balance condition is locally satisfied and other where it is violated. As a confirmation, the heat rate density (or equivalently the density of entropy production rate) almost vanishes in the equilibrium-like regions and is very large in the non-equilibrium one both for convex [77] and non-convex potentials [104]. Besides, the equilibrium-like regions coincide with the accumulation regions where the particles spend most of their life. Testing this principle in other far equilibrium stochastic dynamics could be an interesting research line.

In the final part of the Chapter, we have applied the generalized version

of the fluctuation-dissipation relations to study the response due to a small perturbation for a system of AOUP particles. After illustrating some technical points regarding its correct calculation, we study perturbatively the regime near-equilibrium and, then, evaluate numerically the regime of large persistence. We, also, discover that the UCNA dynamics cannot be used to approximate the real response function in the large persistence regime, but only to estimate such an observable near-equilibrium [225].

The extension of the whole study on interacting self-propelled particles could be an intriguing next point. The study of the entropy production in systems displaying clustering or motility induced phase-separation has been partially performed in the framework of ABP particles. Anyway, in this case, the question about the parity of the self-propulsion has not yet been solved and the available studies are quite incomplete. Our idea is that for AOUP particles, the entropy production rate is larger on the boundary of the mean cluster, while should be quite small both inside and outside of it. In particular, we expect that the MIPS configuration minimizes the entropy production. It may be also interesting to understand what happens by applying a local perturbation in space, where MIPS occurs: we wonder if the relaxation occurs faster or not when the collective phenomenon takes place.

Appendices

4.A Computation of \mathbf{T}^{-1}

In this Appendix, we derive the expression for the operator \mathbf{T}^{-1} for the three cases discussed along with this Chapter. Since \mathbf{T}^{-1} is defined as the inverse of the correlator $\boldsymbol{\nu}$, its computation comes directly from the definition of the inverse operator:

$$\int \mathbf{T}^{-1}(t-t')\boldsymbol{\nu}(t'-s)dt' = \boldsymbol{\delta}(t-s). \quad (4.73)$$

The simplest way to compute \mathbf{T}^{-1} is to switch in the Fourier space. Denoting as \mathcal{FT} the Fourier transform operator and \mathcal{FT}^{-1} the inverse-Fourier transform one and using a tilde to denote the Fourier transform of a given function, we get:

$$\mathbf{T}^{-1}(t) = \mathcal{FT}^{-1}(\tilde{\mathbf{T}}^{-1}) = \int \frac{d\omega}{2\pi} \tilde{\mathbf{T}}^{-1}(\omega) e^{-i\omega t}. \quad (4.74)$$

We can evaluate the convolution in the \mathcal{FT} -space, obtaining:

$$\tilde{\mathbf{T}}^{-1}(\omega) = \frac{1}{\tilde{\boldsymbol{\nu}}(\omega)}, \quad \tilde{\boldsymbol{\nu}}(\omega) = \int dt e^{i\omega t} \boldsymbol{\nu}(t). \quad (4.75)$$

Now, we are ready to calculate \mathbf{T}^{-1} in the three cases discussed in this Chapter, considering the scalar case, for the sake of simplicity:

1. Passive Brownian particle. The dynamics comes from the general Eq.(4.12), replacing η with $\sqrt{2T_b/\gamma}\eta$, where the last η is a thermal noise with unitary variance and zero average. Applying Eqs.(4.74), we obtain:

$$\tilde{\nu}(\omega) = 2T_b, \quad T^{-1} = \frac{\delta(t)}{2T_b}. \quad (4.76)$$

2. Active particle evolving with the AOUP dynamics in the absence of thermal noise. Replacing η in Eq.(4.12) with η_a , i.e. a noise with zero average and two-time correlation $\nu(t-s) = \gamma^2(D_a/\tau)e^{-|t-s|/\tau}$, we get the dynamics. Then, Eq.(4.74) gives rise to the following expression:

$$\tilde{\nu}(\omega) = \frac{2D_a}{1 + \tau^2\omega^2}, \quad T^{-1}(t) = \frac{\delta(t)}{2D_a} \left(1 - \tau^2 \frac{d^2}{dt^2} \right). \quad (4.77)$$

We remark that, in this case, T^{-1} is even in its argument but is a differential operator, containing the second time derivate.

3. AOUP dynamics with the additional thermal bath. The dynamics is obtained by replacing η in Eq.(4.12) with $\sqrt{2T_b/\gamma}\eta + \eta_a$, i.e. the sum of the two previous noises. The correlation of the noise is given by $\nu(t-s) = 2(T_b/\gamma)\delta(t-s) + (D_a/\tau)e^{-|t-s|/\tau}$. Thus, using Eq.(4.74), we have:

$$\tilde{\nu}(\omega) = \frac{2D_a}{1 + \tau^2\omega^2} + \frac{2T_b}{\gamma}, \quad (4.78)$$

$$T^{-1}(t) = \frac{\gamma}{2T_b}\delta(t) - \frac{D_a\gamma^2}{2T_b^2} \left(\frac{1}{1 + D_a\gamma/T_b} \right) \times \quad (4.79)$$

$$\times \left[\frac{1}{\tau} \sqrt{1 + \frac{D_a\gamma}{T_b}} \exp\left(-\frac{|t|}{\tau} \sqrt{1 + \frac{D_a\gamma}{T_b}}\right) \right].$$

It is worthy to mention that the sum of the thermal and the active bath leads to a shape of T^{-1} not proportional to a delta-Dirca function.

We also remark that we can generalize all the previous calculations and definitions to a multi-dimensional case with inter-particles interactions.

4.B Equivalence between Fokker-Planck and path-integral approaches in the computation of the entropy production

The entropy production rate of the medium can be computed using a path-integral technique or by considering a Fokker-Planck approach, as shown in Sec.4.2 and Sec.4.3, respectively. The two methods seem to lead to different expressions. Instead, in this Appendix, we show that the two results, i.e. Eq.(4.21) and Eq.(4.44), coincide unless of irrilevant boundary terms.

Before proceeding to the equivalence, we develop a formal relation which will be useful in what follows. Comparing different formulations of the linear response theory due to a small perturbation of a generic observable, O , which depends on the dynamical variables. From one hand, we have Eq.(4.55), which has been discussed in Sec.4.4 (see also [224] for a reference), which we rewrite for completeness:

$$\mathcal{R}_{Ov}(t-s) = -\langle O(t) \frac{d}{dv} \log p(x, \dot{x})(s) \rangle, \quad (4.80)$$

where p is the probability in the sapce (x, v) . From the other hand, other relations have been recently derived [189, 188], for instance:

$$\mathcal{R}_{Ov}(t-s) = \frac{2\tau}{\sqrt{2D_a}} \langle O(t)\eta(s) \rangle, \quad (4.81)$$

already adapted to the specific case we are considering. We recall that $\eta(s)$ is a white with zero average and unitary variance. Identifying the right-hand

side of the two formulations and noticing that both are valid for a generic observable, $p(x, \dot{x})$ and ξ appear to be related by an integral equation, which is

$$\int dx d\dot{x} \frac{\sqrt{2\tau}}{\sqrt{D_a}} \eta p(x, \dot{x}) O(x, \dot{x}) = - \int dx d\dot{x} \frac{\partial}{\partial \dot{x}} p(x, \dot{x}) O(x, \dot{x}). \quad (4.82)$$

Taking in mind Eq.(4.82), we are ready for the proof. Starting from Eq.(4.44), for instance, we get:

$$\begin{aligned} \langle \sigma(t) \rangle &= \int dx d\dot{x} \frac{\tau}{D_a} \Gamma(x) \left[\frac{\Gamma(x)}{\tau} \dot{x}^2 - \frac{D_a}{\tau^2} \right] p(x, \dot{x}) \\ &= \int dx d\dot{x} \frac{\tau}{D_a} \Gamma(x) \dot{x} \left[\frac{\Gamma(x)}{\tau} \dot{x} p(x, \dot{x}) + \frac{D_a}{\tau^2} \frac{\partial}{\partial \dot{x}} p(x, \dot{x}) \right] \\ &= \int dx d\dot{x} \frac{\tau}{D_a} \Gamma(x) \dot{x} \left[\frac{\Gamma(x)}{\tau} \dot{x} - \frac{\sqrt{2D_a}}{\tau} \eta \right] p(x, \dot{x}) \\ &= -\frac{1}{\mathcal{T}} \int^{\mathcal{T}} dt \frac{\tau}{D_a} \Gamma(x) \dot{x} \left[\ddot{x} + \frac{\Psi'}{\tau} \right] \\ &= -\frac{1}{\mathcal{T}} \int^{\mathcal{T}} dt \frac{\tau}{D_a} [1 + \tau \Psi''(x)] \dot{x} \left[\ddot{x} + \frac{\Psi'}{\tau} \right] \\ &= -\frac{1}{\mathcal{T}} \int^{\mathcal{T}} dt \frac{\tau}{D_a} \left[\frac{d}{dt} \frac{\dot{x}^2}{2} + \tau \dot{x} \ddot{x} \Psi''(x) + \frac{d}{dt} \frac{\Psi(x)}{\tau} + \frac{d}{dt} \frac{\Psi'^2}{2} \right] \\ &= -\frac{1}{\mathcal{T}} \int^{\mathcal{T}} dt \frac{\tau^2}{2D_a} \dot{x}^3 \Psi'''(x) + b.t. \end{aligned} \quad (4.83)$$

As usual in this Chapter, *b.t.* means boundary terms. In the second equality of Eq.(4.83) we have performed an integration by parts while in the third we have used Eq.(4.82). Then, in the fourth equality the content of the square brackets has been replaced by the equation of motion and, assuming the ergodicity, we have switched from the average in the variable space to the time integral, i.e. $\mathcal{T} \int dx d\dot{x} p(x, \dot{x}) = \int^{\mathcal{T}} dt$. Last equalities are obtained integrated again by parts. As claimed, Eq.(4.21) coincides with Eq.(4.44), unless of boundary terms, meaning that the Fokker Planck approach and the path-integral method are equivalent.

4.C Entropy production in the limit of zero thermal noise

In this Appendix, we report the derivation of the equality (4.27). To get the proof, It is sufficient to prove the following:

$$\lim_{T_b \rightarrow 0} K^{-1}(t) \approx -\frac{\tau^2}{2D_a} \frac{d^2}{dt^2} \delta(t) \equiv -\frac{\tau^2}{2D_a} \delta(t) \frac{d^2}{dt^2},$$

According to the notation of this Chapter, the symbol \approx means that the result is obtained unless of terms which leads to irrelevant boundary terms in the computation of the entropy production, whose computation is the final goal of the Section. Thus, in the form of K^{-1} we neglect addends $\propto \delta(t)$. Now, using the following identity:

$$\frac{d^2}{dt^2} \left[\frac{1}{\tau_R} \exp \left(-\frac{t}{\tau_R} \right) \right] = \frac{1}{\tau_R^2} \left[\frac{1}{\tau_R} \exp \left(-\frac{t}{\tau_R} \right) \right], \quad (4.84)$$

we can rewrite $K^{-1}(t)$ in a more suitable way:

$$K^{-1}(t) = -\frac{D_a \gamma^2}{2T_b^2} \left(\frac{1}{1 + \frac{D_a \gamma}{T_b}} \right)^2 \frac{d^2}{dt^2} \left[\frac{1}{\tau_R} \exp \left(-\frac{t}{\tau_R} \right) \right], \quad \tau_R = \frac{\tau}{\sqrt{1 + \frac{D_a \gamma}{T_b}}}.$$

This concludes the derivation. We remark that in the limit $T_b \rightarrow 0$, or equivalently $\tau_R \rightarrow 0$, the term inside the square bracket approaches to a δ -Dirac function and the prefactor of the whole expression becomes $-\tau^2/2D_a$.

4.D Computations of correlations functions and response for the harmonic potential

In the harmonic potential case, $P(x, v)$ is a Gaussian with respect to x and v , while $P(x, f_a)$ is a multivariate Gaussian. The dynamics is equivalent to the one of a passive Brownian particle in the underdamped regime with an effective temperature depending on the strength of the potential and the parameters of the active force. The linearity of the dynamics allows us to compute the correlation vs time as a simple combination of exponential functions. In particular, writing explicitly the dynamics in terms of \tilde{f}_a and s we get:

$$\gamma \dot{x} = -\sqrt{\tau} x + \tilde{f}_a \quad (4.85)$$

$$\dot{\tilde{f}}_a = -\frac{f_a}{\sqrt{\tau}} + \frac{\sqrt{D_a}}{\tau} \eta, \quad (4.86)$$

where, for the sake of simplicity, we have used the dot for the time derivative with respect to s . Multiplying Eq.(4.85) and Eq.(4.86) by $x(0)$ and taking the average with respect to the steady state propagator in the (x, \tilde{v}) representation we obtain a set of coupled ordinary differential equations for the correlations:

$$\frac{d}{ds} \langle x(s)x(0) \rangle_v = \langle \tilde{f}_a(s)x(0) \rangle_v - \frac{k\sqrt{\tau}}{\gamma} \langle x(s)x(0) \rangle_v \quad (4.87)$$

$$\frac{d}{ds} \langle \tilde{f}_a(s)x(0) \rangle_v = -\frac{1}{\sqrt{\tau}} \langle \tilde{f}_a(s)x(0) \rangle_v \quad (4.88)$$

The solution of Eq.(4.88) reads:

$$\langle \tilde{f}_a(\tilde{t})x(0) \rangle_v = B e^{-\tilde{t}/\sqrt{\tau}}, \quad (4.89)$$

where B is a constant to be fixed by the initial conditions. Substituting the expression (4.89) in Eq.(4.87), we obtain:

$$\frac{d}{d\tilde{t}} \langle x(\tilde{t})x(0) \rangle_v = \frac{\sqrt{\tau}k}{\gamma} \langle x(\tilde{t})x(0) \rangle_v + B e^{-\tilde{t}/\sqrt{\tau}}, \quad (4.90)$$

whose solution is:

$$\langle x(\tilde{t})x(0) \rangle_v = C e^{-\tilde{t}\sqrt{\tau}k/\gamma} - \frac{B}{\frac{1}{\sqrt{\tau}} - \frac{\sqrt{\tau}k}{\gamma}} e^{-\tilde{t}/\sqrt{\tau}}, \quad (4.91)$$

where C is the second constant to be determine by the initial conditions. The initial conditions to deal with a steady-state can be obtained by the covariance-matrix of the distribution:

$$\frac{k}{\gamma} \langle x(0)x(0) \rangle_v = \frac{1}{\beta}, \quad (4.92)$$

$$\langle \tilde{v}(0)x(0) \rangle_v = \langle \tilde{f}_a(0)x(0) \rangle_v - \frac{\sqrt{\tau}k}{\gamma} \langle x(0)x(0) \rangle_v = 0. \quad (4.93)$$

where β is an irrelevant constant related to the xx element of the covariance matrix of the probability distribution function. Eq.(4.92) means that the potential energy obeys a sort of equipartition principle, while Eq.(4.93) that the position is not correlated with the velocity. In this way, we can determine the values of the two constants in terms of the parameters of the model:

$$\beta B = \sqrt{\tau} \quad (4.94)$$

$$\beta C = \frac{\gamma}{k\sqrt{\tau}} \frac{1}{\frac{1}{\sqrt{\tau}} - \frac{\sqrt{\tau}k}{\gamma}}, \quad (4.95)$$

from which we have:

$$\beta \langle x(s)x(0) \rangle_v = \frac{1}{\frac{1}{\sqrt{\tau}} - \frac{\sqrt{\tau}k}{\gamma}} \left(\frac{\gamma}{k\sqrt{\tau}} e^{-s\sqrt{\tau}k/\gamma} - \sqrt{\tau} e^{-s/\sqrt{\tau}} \right) \quad (4.96)$$

and

$$\beta \langle v(s)x(0) \rangle_v = \frac{1}{\frac{1}{\sqrt{\tau}} - \frac{\sqrt{\tau}k}{\gamma}} \left(e^{-s/\sqrt{\tau}} - e^{-s\sqrt{\tau}k/\gamma} \right) = \frac{\gamma}{k} R_v(s). \quad (4.97)$$

Being in equilibrium, we can use the reversibility condition $\langle \tilde{v}(s)x(0) \rangle = -\langle x(s)\tilde{v}(0) \rangle$, to get the final expression for the response function:

$$R(s) = \beta \frac{k}{\gamma} \langle x(s)x(0) \rangle_v - \beta \frac{k}{\gamma} \sqrt{\tau} \langle x(s)\tilde{v}(0) \rangle_v = e^{-s\sqrt{\tau}k/\gamma}. \quad (4.98)$$

Part II

An overlook of collective phenomena

Chapter 5

High densities active matter

The dynamics of passive Brownian particles at high densities have been largely explored, both theoretically and experimentally, in the last decades [235]. Even if the Mermin-Wagner theorem excludes the existence of a crystalline phase, featuring Bragg peaks and long-range positional order [236], two dimensional spherical equilibrium particles undergo two phase transitions: one from the liquid phase - with short-range positional and orientational order - to the hexatic phase - with short-range positional and quasi-long-range orientational order - and a second from the hexatic to the solid (albeit non-crystalline) phase - which has quasi-long range positional and long-range orientational orders [237]. Density and temperature have recognized to be the two leading parameters to move from liquid to hexatic and, then, to solid-like aggregation phases, where particles are arranged in a periodic hexagonal lattice. Experimental verifications have obtained using dense suspensions of equilibrium colloids [238, 239], which are known to be the experimental platform to test Brownian dynamics.

Recently, also the experimental study of two dimensional systems of self-propelled particles at large densities has attracted the attention of the active matter community. The study of artificial microswimmers in these regimes may offer interesting engineering applications, for instance, in the design of new materials, whose properties are under investigations. To make some example, even if most of the studies are restricted to smaller regimes of densities, recently, Janus particles have been investigated also in the case of very dense suspensions [240]. Another class of artificial self-propelled systems, studied at very high densities, belongs to the category of driven granular media. Monodisperse polar grains shows persistent motion under shaking [241]. Dauchot's group provides one of the first study of artificial microswimmers at this very high densities [242], revealing a new intriguing experimental scenario for non-equilibrium dense aggregation phases. Specimens of active matter systems at very high densities are very interesting also in the biological realm. Typical examples are tissues and cells, even if the scenario is rather complex in these cases: in experiments, both tissues and cells may dynamically deform and cells are usually proliferating or dying in

such a way that their numerical density is a function of time. Particular attention has been devoted to the dynamics of a confluent epithelial cell sheet [243, 244], which slow down when their densities increases. More recently, an amorphous “solidification” process has been investigated during the process of vertebrate body axis elongation [245], where the cells become solid-like.

Modeling the behavior of these different systems using simplified stochastic dynamics is a great deal, aimed to understand the features of the high-density aggregation phases of these non-equilibrium systems, all united to be formed by self-propelled units. Even if biological specimens need more refined models, accounting for deformability effects [246] for instance, the ABP dynamics remains the minimal model to unveil the basic features of dense non-equilibrium systems, providing, at least, a high-level coarse-grained description. Instead, it is paradigmatic for artificial microswimmers which are the best platform to test numerical studies. Despite the existence of many works in the regime of moderate packing fractions, the ABP dynamics in the high-density regimes is less explored. First work on active crystallization appears in [247], revealing a shift towards larger densities with respect to the Brownian counterpart to obtain the transition from liquid to solid structures. Besides, this transition is accompanied by a pure non-equilibrium phenomenon: liquid and solid phases are separated by a region where the suspension is globally ordered but unordered bubbles of “liquid” still persist. Successively, a deeper analysis about active solids shows the occurrence of traveling crystals [248, 249], accompanied by the transition to rhombic, square and even lamellar patterns. This phenomenology has been recently confirmed by experiments realized with vibrating granular disks [250]. Recent studies have been focused on the construction of the phase diagram of self-propelled particles employing the ABP dynamics [251, 252, 253], focused on the generalization of equilibrium phases to non-equilibrium systems [254]. For small active forces, the scenario seems to resemble the one of passive Brownian particles with the occurrence of “gas-like”, “liquid-like”, “hexatic-like” and “solid-like” phases, with a shift of the transition points towards larger densities [251]. Instead, for large self-propulsions (but moderate densities) an unexpected phase occurs, the so-called Motility Induced Phase Separation (MIPS) - in the absence of attractive interactions -, which will be the main object of Chapter 6. Instead, even far from equilibrium, crystallization seems to occur at high densities [247, 251]. Such a study suggests a natural extension of the picture of equilibrium aggregation phases from passive Brownian particles to active non-equilibrium systems in the regime of large densities, providing that self-propulsion at high densities has the only effect to destabilize the ordered phases or produce a phase-separation.

In this Chapter, we focus on the high-density regimes varying the persistence of the active force and the packing fraction. While the proposed scenario is fairly confirmed in the small persistence regime, new and unexplored phenomenologies arise when the persistence time is large. We change the widespread idea that equilibrium-like concepts, such as equi-

librium phases, can be simply used to describe high-density suspensions of self-propelled particles. Despite the internal structure resembles the one of a liquid phase, we discover that the increasing of the persistence breaks down the global translational symmetry which is at the basis of the liquid definition. Here, empty moving regions form and travel along with the whole systems. This phenomenon cannot be considered simply as a manifestation of MIPS: this is not a phase separation since all the particles belong to the dense phase even if they do not explore the whole box. We, also, discover a new intriguing emergent order, which supports the pure non-equilibrium scenario: particles velocities form pattern arranging in aligned or vortex-like domains, whose size depends on the parameters of the active force. This order is absent in any passive Brownian suspensions and is a confirmation of the pure non-equilibrium features of self-propulsive systems even in the denser regimes, which hinders any generalization of the equilibrium phases to self-propelled particles. This study shows, also, a strong connection between ABP (or AOUP) particles in the dense regimes and Vicsek-like models [21, 255]: while, in the latter, a velocity alignment force is explicitly introduced [256], in the former, an effective Vicsek-like force naturally emerges from the interplay between self-propulsion and steric interactions. We will show that an explicit force - as in the seminal work of Vicsek [257] - is not required to induce a flock or simply a velocity alignment.

The Chapter is structured as follows: after introducing the ABP model for interacting self-propelled particles in Sec.5.1, we numerically study the phenomenology of self-propelled particles at large packing fraction in Sec.5.2, varying the persistence of the active force and the density. In Sec.5.3, we show the pattern formation of the velocity alignment studying such long-range order using a suitable order parameter. Sec.5.4 is devoted to the theoretical understanding of such an intriguing phenomenology. Finally, in Sec.5.5, we confine the system using an external trap before presenting some conclusions in the final Section.

5.1 Interacting systems of self-propelled particles

We study a system of N interacting self-propelled particles, for simplicity and without loss of generality, in two dimensions. The position of each microswimmer, \mathbf{x}_i , representing its center of mass, is described by Eq.(1.1) where \mathbf{F}_i is given by any deterministic force contribution taking place in the dynamics. The self-propulsion forces of each microswimmer evolve with independent ABP or AOUP dynamics, given by Eq.(1.3) and Eq.(1.5), respectively. For completeness, we report below the dynamics in both cases.

In particular, the ABP suspension of interacting particles evolves with:

$$\gamma \dot{\mathbf{x}}_i = \mathbf{F}_i + \gamma U_0 \mathbf{n}_i, \quad (5.1a)$$

$$\dot{\theta}_i = \sqrt{2D_r} \xi_i, \quad (5.1b)$$

while, according to the AOUP scheme, the dynamics is given by:

$$\gamma \dot{\mathbf{x}}_i = \mathbf{F}_i + \mathbf{f}_i^a, \quad (5.2a)$$

$$\tau \dot{\mathbf{f}}_i^a = -\mathbf{f}_i^a + \gamma \sqrt{2D_a} \xi_i. \quad (5.2b)$$

In both equations of motion, we have used the same notation of the previous Chapters. The interacting feature of the dynamics is enclosed in the force term, \mathbf{F}_i , chosen to be purely repulsive. We remark that no explicit aligning forces are included in the dynamics. This is the main difference with respect to Vicsek-like models for which each θ_i depends on the orientational angle of the surrounding particles [21, 256], in such a way that each θ_i is attracted towards the value $\sum_j \theta_j$, where the sum is performed over particles inside a circle around the target microswimmer. So, according to the current nomenclature, the dynamics (5.1) (or (5.2)) does not show an average polarization, at variance with the Vicsek-like models.

The dynamics of different particles are coupled only by the force term, $\mathbf{F}_i = -\nabla_i U_{tot}$, being U_{tot} the total interacting potential depending on the whole set of the particles' positions. U_{tot} usually depends only on the inter-particle distances and can be expressed as:

$$U_{tot} = \sum_{i < j} U(|\mathbf{r}_{ij}|), \quad (5.3)$$

where $\mathbf{r}_{ij} = \mathbf{x}_i - \mathbf{x}_j$. The choice of $U(r)$ is determined by the physical properties of the system: it could be set as a long-range potential $\propto 1/r$ to account for electric repulsion or attraction, as a Lennard-Jones-like potential, as usual in liquid theory, i.e. a repulsive potential for short distances with an attractive components, or as a purely repulsive short-range potential to simply account for the impenetrable size of the particles. In what follows, we restrict to the latter case. In particular, we choose $U(r)$ as a WCA potential in such a way that \mathbf{F}_i models steric interactions. Following previous studies, we choose:

$$U(r) = 4\epsilon \left[\left(\frac{\sigma}{r} \right)^{2b} - \left(\frac{\sigma}{r} \right)^b \right] + \epsilon \quad \text{for } r \leq 2^{1/b} \sigma \quad (5.4)$$

and zero for $r \geq 2^{1/b} \sigma$, where b is a positive integer number. In this way, the potential approaches continuously to zero and then is truncated. The constant σ represents the nominal particle diameter while ϵ is the energy scale due to interactions. For numerical convenience, both these parameters are set to one in the simulations along the rest of the thesis. The shape

of $U(r)$ guarantees that the potential is short-range, assuming at least that $b = 6$ as in Sec.5.2. In this way, a target particle can interact only with its first neighbors even in a very packed configuration. We remark that such a choice of U is very common in the literature of liquid theory and active matter studies.

5.1.1 The coarse-grained velocity of the particle

Following Chapter 2, we can adapt the change of variables, introduced in Sec. 2.2, to the interacting case. Adapting the derivation reported in Appendix 2.A, we can switch from the set of variables $\{\mathbf{x}_i, \mathbf{f}_i^a\}$ to the transformed variables $\{\mathbf{x}_i, \mathbf{v}_i\}$ eliminating the self-propulsions both for the AOUP and ABP models in favor of the microswimmer velocities, $\mathbf{v}_i = \dot{\mathbf{x}}_i$. In what follows, we restrict to the case $D_t = 0$ for the sake of simplicity, even if the above results could be easily generalized to the presence of additional thermal noises. The dynamics of \mathbf{v}_i can be expressed in a compact formalism accounting for both AOUP and ABP dynamics, as

$$\dot{\mathbf{v}}_i = -D_r \sum_{j=1}^N \Gamma_{ij}(\mathbf{r}_{ij}) \mathbf{v}_j + D_r \frac{\mathbf{F}_i}{\gamma} + \mathbf{k}_i, \quad (5.5)$$

here both \mathbf{v}_i and \mathbf{x}_i belong to the plane xy . Γ is a $2 \times N$ dimensional matrix, whose elements are:

$$\Gamma_{ij}^{\alpha\beta}(\mathbf{r}_{ij}) = \delta_{ij} \delta_{\alpha\beta} + \frac{1}{D_r \gamma} \nabla_{i\alpha} \nabla_{j\beta} U(|\mathbf{r}_{ij}|), \quad (5.6)$$

where Latin and Greek indices refer to the particle number and the spatial vector components, respectively. The last addend, \mathbf{k}_i , is a noise term which reads:

$$\mathbf{k}_i = v_0 \sqrt{2D_r} \boldsymbol{\xi}_i \times \mathbf{n}_i = v_0 \sqrt{2D_r} \boldsymbol{\xi}_i \times \frac{\gamma \mathbf{v}_i - \mathbf{F}_i}{\gamma} \quad (5.7)$$

for the ABP model. In the same notation of Sec.2.2, $\boldsymbol{\xi}_i$ is the stochastic vector with components $(0, 0, \xi_i)$ normal to the motion plane. Instead, for the AOUP model \mathbf{k}_i belongs to the plane xy and is given by:

$$\mathbf{k}_i = \frac{\sqrt{2D_a}}{\tau} \boldsymbol{\eta}_i \quad (5.8)$$

where $\boldsymbol{\eta}_i$ is a two-dimensional white noise vector with independent components.

As already explained in Sec.2.2, the original equation of motion have been mapped in the dynamics of an underdamped passive particle under the action of a space-dependent Stokes force which, now, depends on the space coordinates of all the particles. Indeed, the first addend of the right-hand side of Eq.(5.5) can be split as follows:

$$-\frac{1}{\tau} \sum_{j=1}^N \Gamma_{ij}(\mathbf{r}_{ij}) \mathbf{v}_j = -\frac{1}{\tau} \Gamma_{ii}(\mathbf{r}_{ij}) \mathbf{v}_i - \frac{1}{\tau} \sum_{j \neq i}^N \Gamma_{ij}(\mathbf{r}_{ij}) \mathbf{v}_j. \quad (5.9)$$

The first term represents a generalized Stokes force acting on the i -th particle because is proportional to \mathbf{v}_i . In analogy with the non-interacting system, its amplitude is not constant but, now, is determined by the positions of the surrounding particles. Besides, an external force depending on the velocities of the neighboring particles affects the dynamics of v_i . Understanding its effect is very complicated and the consequences of such a term are not clear at this level. The numerical study of Sec.5.3 and the theoretical methods of Sec.5.4 will shed light on such a point.

The only difference between ABP and AOUP dynamics arises from the noise term \mathbf{k} . In the latter case, it is a simple white noise term which acts on the velocity as an effective thermal bath. Instead, in the former, \mathbf{k}_i acts always perpendicularly to \mathbf{n}_i , i.e. the orientation of the active force. Formally, we deal with multiplicative noise, since its amplitude depends both on \mathbf{v} and \mathbf{F}_i through the unitary vector \mathbf{n}_i . Because of this property, it is worthy to note that the amplitudes of two noises coincide using the mapping of the parameters which states the “equivalence” between the two models: $D_r = 1/\tau$ and $U_0^2/2 = D_a/\tau$. We observe that fixing U_0 , the amplitude of \mathbf{k}_i scales as $1/\sqrt{\tau} = \sqrt{D_r}$, meaning that its value decreases in the large persistence regime. From this observation, it is straightforward to conclude that the differences between ABP or AOUP models vanish for small D_r . Indeed, in this regime, the velocity-dependent force (common to both dynamics) becomes dominant since all the other terms are $O(D_r)$.

5.2 Self-propulsive systems at high densities

In this Section, we integrate Eqs.(5.1) (or equivalently Eqs.(5.2)) in a box of size L with periodic boundary conditions to simulate an infinite system. For the moment, we restrict to regimes of very large densities where particles are extremely packed, while regimes with smaller densities will be the main objects of Chapter6. In particular, we define the packing fraction (or area fraction), ϕ , as the product between the nominal area of a single particle with radius $\sigma/2$ and the numerical density of the system, namely $\phi = N/L^2\pi\sigma^2/4$. The values of ϕ are fixed in the interval $(1, 1.4)$, in the conditions of the so-called “extreme active matter” [258]. At these values of the packing fraction, a passive Brownian suspension of particles exhibits liquid, hexatic and solid phase depending on its temperature which is related to the diffusion coefficient by the Einstein relation. This Section aims to unveil the effect of the self-propulsion force on the structure of the system roughly understanding if there are new insights in the aggregation phases due to the non-equilibrium features of self-propelled systems.

5.2.1 Phase diagram: effective temperature and density non-homogeneities

In panel (a) of Fig.5.1, we illustrate the phase diagram in terms of Snapshot configurations in the motion plane, varying the persistence time of the active force, $\tau = 1/D_r$, and ϕ . The colors of the particles represent their orientation, i.e. the direction of the self-propulsion.

When the persistence is smaller than the time-scale induced by the potential, i.e. when the dimensionless parameter $\nu = \tau \nabla^2 U_{tot} / \gamma$ is roughly smaller than one, we expect the same behavior of passive Brownian particles: particles are homogeneously distributed in the box and arranged in the solid, hexatic or liquid phases. The orientations of the self-propulsions are randomly distributed being their dynamics independent. As already explained in Chapter 2, the active force acts as a thermal bath with amplitude $\sim v_0 / \sqrt{D_r} = \sqrt{2D_a}$ in this regime. Thus, the growth of $\tau = 1/D_r$, at fixed $D_a/\tau = v_0^2/2$, induces the increase of the effective temperature and, so, simply the warming of the system at any densities, in analogy with passive Brownian particles. Depending on the interplay between ϕ and the effective temperature, the system is in the liquid, hexatic or solid phase. To confirm such a phenomenology we study the internal structure of the system using the pair correlation function, $g(r)$. For a definition and a discussion of this observable for a system of passive Brownian particles see Appendix.5.A. The $g(r)$ reveals the typical shape of an equilibrium solid, since the second peak is split, for the larger values of the densities (left bottom panels in Fig.5.1(a), below the blue line). Because particles are arranged in the hexagonal lattice, the peaks are placed at positions $\bar{x}, \sqrt{3}\bar{x}, 2\bar{x}, \sqrt{7}\bar{x}, \dots$ and so on, where \bar{x} is the typical distance between neighboring particles. It is worthy to note that \bar{x} is quite smaller than σ , meaning that particles climb on the interacting potential due to the large density. Anyway, they interact with their six neighbors only, since the short-range property of $U(r)$ allows us to neglect the contribution of the second and further neighbors. Instead for the smaller densities, the $g(r)$ displays the typical liquid structure with the occurrence of a second no-split peak (left top panels in Fig.5.1(a), above the blue line). In both phases, the peaks of the $g(r)$ decrease as τ is enlarged, in agreement with the interpretation of the self-propulsion in terms of effective temperatures: fluidization occurs. This analysis is shown in panels (b) and (d) of Fig.5.1 for the lower and higher value of ϕ , respectively.

In the large persistence regime, $\nu \gg 1$, ((right panels of Fig.5.1) the phenomenology is richer from many points of view. Let us start to discuss the first row from below of Fig.5.1, i.e. the larger value of ϕ . In this case, the $g(r)$ roughly saturates for $\tau \gtrsim 1$ and, thus, the active force becomes irrelevant for the structure of the system, as shown in panel (d) of Fig.5.1. Anyway, the whole hexagonal pattern moves coherently in space, in spite of the fact that each self-propulsion vector points randomly. The hexagonal pattern changes the direction of its motion, roughly after a time which grows as τ ($1/D_r$) and

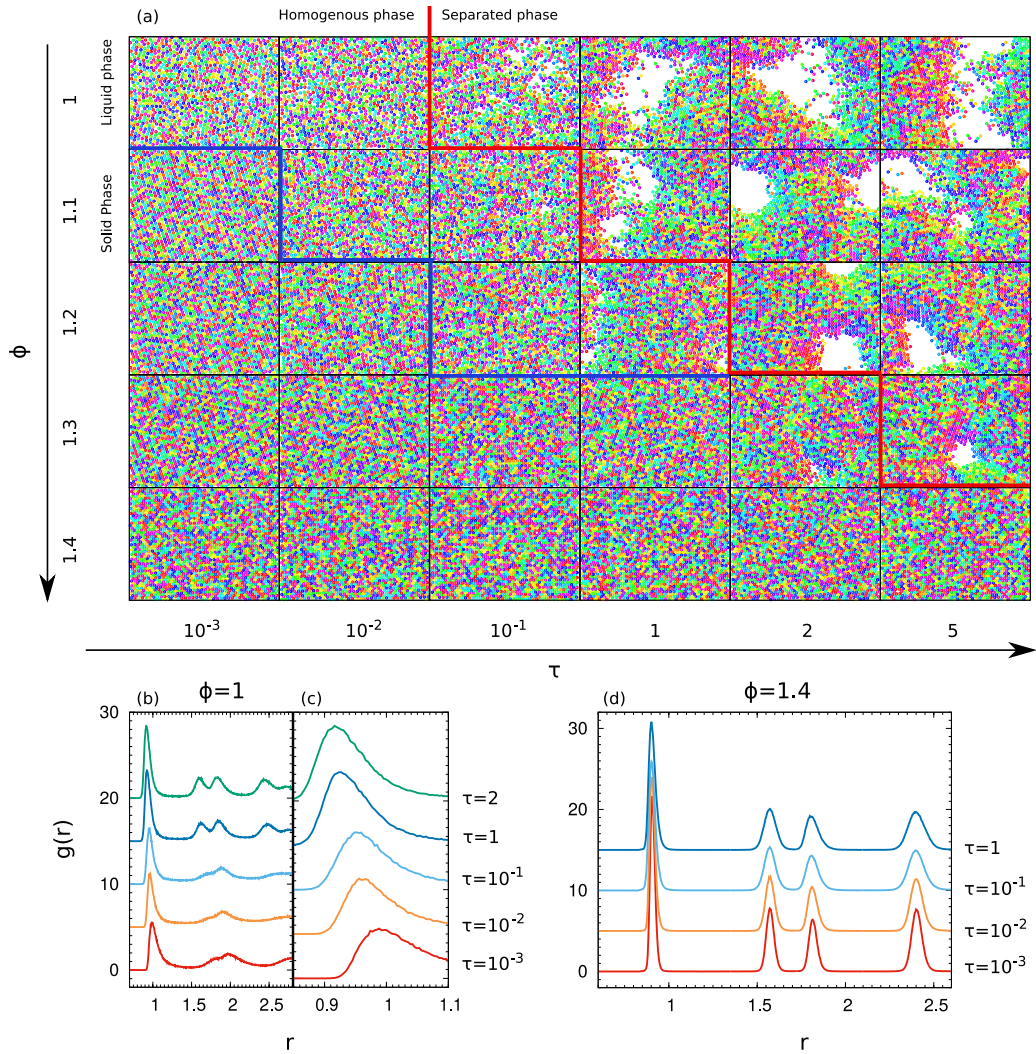


Figure 5.1: In panel (a), we plot the phase diagram in function of τ and ϕ in terms of Snapshots configuration in the motion plane. The colors encode the self-propulsion orientation of the active force. Blue and red lines denote the solid-liquid transition and passage from the homogenous and the non-homogenous phase. Panel (b) and (c) represent the $g(r)$ for $\phi = 1$, while panel (d) the $g(r)$ for $\phi = 1.4$, both varying the persistence time τ , as shown in the two legends. Each $g(r)$ is shifted along the y axis for presentation reasons.

follows the direction of the total self-propulsion, obtained averaging over the active forces of the whole systems. The first time, such a phenomenon has been numerically observed in [248, 249] and, recently, experimental evidence of this effect has been revealed by suspensions of micro-disks subjected to vertical vibrations [250]. The use of density functional theory predicts such a phenomenology and, in particular, the transition to rhombic, quadratic, and lamellar patterns with the increasing of the active force [248, 249].

The configurations for smaller ϕ of Fig.5.1(a) reveal intriguing challenges with respect to the equilibrium liquid phase corresponding to the same values of the packing fraction. Starting from $\phi \approx 1.3$ towards smaller values of ϕ , the translational symmetry of the system breaks down and moving empty regions appear in the steady-state configurations, as we can see in the right columns of Fig.5.1(a). The empty regions move along the box continuously in time, their shapes feature dynamical changes and their typical sizes depend on the active force parameters and mostly on the density values. Decreasing ϕ its area grows, sometimes splitting into two parts, until to form a very large empty region which can occupy also one-half of the box. At fixed ϕ , the hole appears increasing τ . It is worthy to note that, in spite of the absence of global polarization - there are no explicit alignment interactions -, the orientations of the particles show a clear organization in the layer of particles near the empty region. The orientations are directed almost radially with respect to the center of the hole. We also remark that the emergence of empty regions determines the suppression of any global pattern movement. In these density regimes, the structure function changes when the persistence is increased revealing a freezing-like effect in the regime of large persistence: the peaks of the $g(r)$ become more pronounced as shown in panel (b) of Fig.5.1. Besides, in panel (c) of the same figure, we focus on the main peak showing its shift towards smaller distances as τ is increased. Particles climb on the potential, a well-known phenomenon in self-propelled systems. This observation is consistent with the existence of empty regions: being the numerical density fixed, particles are more packed.

Summarizing, at variance with a passive Brownian liquid, the long-range translational invariance is broken by the presence of a very persistent self-propulsion. Thus, even the nomenclature “non-equilibrium liquid” is questionable, since the leading property of such an aggregation phase is lost. In the same way, the solid-like phase displays a strange coherent movement of the pattern even if, at least in this case, the quasi long-range translational order is not broken. We do not discuss the hexatic phase: we expect that even this equilibrium aggregation is hard to extend to such a non-equilibrium system. Building a whole phase-diagram for self-propelled particles in the large persistence regime requires the introduction of purely non-equilibrium aggregation phases, going beyond the well-known equilibrium-like picture. The next Section will show another clear evidence of such a statement unveiling a new phenomenology which has not a Brownian counterpart.

Instead, the well-known theory of equilibrium phases can be easily generalized to active systems in the small persistence regime, where the active force plays only the role of an effective temperature, which grows as τ is enlarged. Anyway, we point out that it is just a trivial regime for self-propelled systems, as discussed also in previous Chapters.

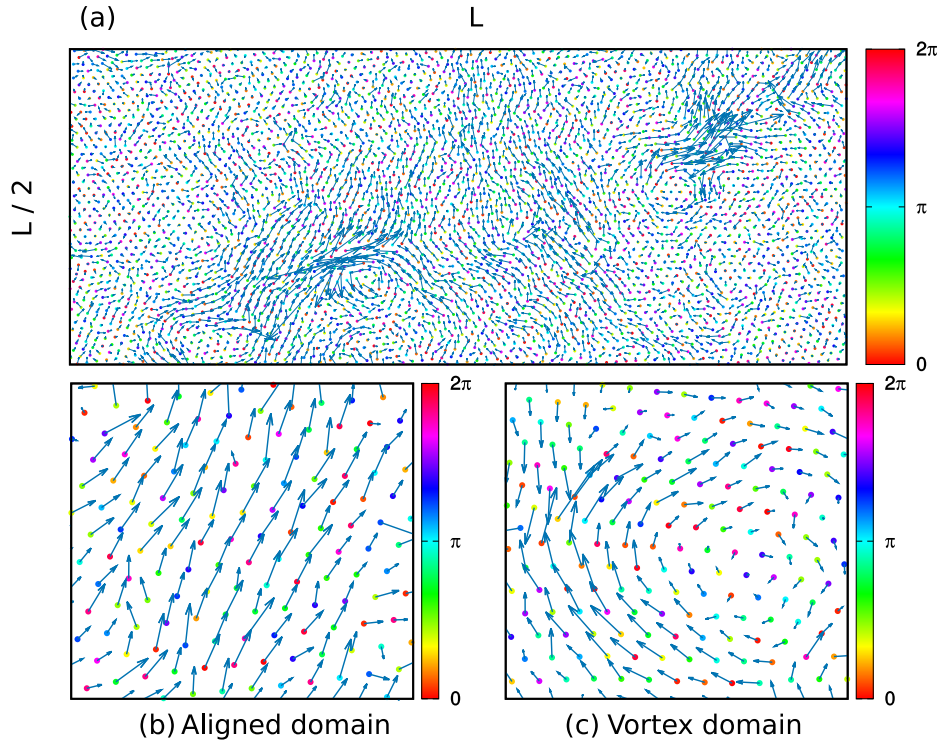


Figure 5.2: In panel (a), we plot a snapshot of the particles' configuration in a box of size $L, L/2$, obtained for $D_r = 0.5$, $U_0 = 50$ and the inter-particles interaction discussed in the main text. Colors encode the orientation of the self-propulsion while the blue arrows represent the velocity vectors. Panels (b) and (c) enlarge a small region showing an aligned domain and a vortex-like structure in the pattern of the particles' velocities.

5.3 Self-propulsion induced velocity alignment at high densities

In the previous Sections, we argue about the difficulty of defining non-equilibrium aggregation phases simply from the analogy with the equilibrium ones. In particular, a new phenomenology takes place even at the level of the structure of the system, whose homogeneity is lost. To enforce this concept, in this Section, we will show the occurrence of a new long-range order occurring, at least, in the regime of high packing fraction discussed in this Chapter.

In Fig.5.2 (a), we give evidence of the main novel phenomenon discussed in this Section, reporting a Snapshot configuration in the motion plane for a simulation with large persistence obtained at $\phi = 1.4$, i.e. when the empty regions do not form. We draw with blue arrows the velocities of the particles, $\dot{\mathbf{x}}_i$, which is in general different from the active forces, \mathbf{f}_i^a , when inter-particles interactions take place. In spite of the absence of any alignment interactions, the velocities of the microswimmers align, self-organizing in large oriented

domains even though each \mathbf{n}_i points randomly. Particles move in the same direction forming large groups, as illustrated in panel (b) of Fig.5.2, i.e. they flock. Such domains self-arrange continuously in time and, sometimes collapse into vortex structures as shown in panel (c) of the same figure. Thus, they are not stable at variance with the well-known traveling bands occurring in the Vicsek-like models [256, 259, 260, 261]. In what follows, such a velocity order will be studied quantitatively in terms of spatial alignment velocity correlations and a suitable order parameter. Then, some theoretical arguments will shed light on this effect showing the occurrence of effective Vicsek-like interactions in the dynamics of \mathbf{v} .

In addition, such a picture is quite coherent with the traveling crystals scenario, discussed in Sec.5.2, and, somehow, provides a physical explanation for the global movement observed. The size of such domains has a non-trivial dependence on the active force parameters and ϕ , as will be shown in details in the further sections. Roughly speaking, their sizes increase as τ grows, as emerged in panels (c), (d) and (e) of Fig.5.3: the pattern movement occurs when such a size overcomes the value of the box meaning that it is not possible to observe such a phenomenology in a real infinite system: traveling crystals are just a finite size effect. Anyway, systems with a small number of particles which move maintaining their solid-like structure have been experimentally observed [250], supporting such a phenomenology.

5.3.1 Spatial correlation of the velocity orientation

For Vicsek-like models, the global alignment of the particles, also known as polarization, is commonly measured by the following order parameters:

$$\langle \Theta \rangle = \left| \sum_{k=1}^N e^{i\theta_k} \right| \quad (5.10)$$

where i is the imaginary unit. This observable is almost zero for particles without any alignment, typically before the band formation at low numerical densities, and returns one, for perfectly aligned particles, typically for large values of ϕ when bands form. Several studies have revealed that these systems exhibit a first order transition with ϕ as order parameter [259]. This observable is zero for a system of self-propelled particles, being the orientational angles independent. Adapting this definition to the microswimmers velocities means to replace θ_k with ψ_k in Eq.(5.10), where ψ_k is the angle formed by the velocity of the particle with respect to the x axis. Even in this case, we cannot obtain a clear velocity-polarization because of the presence of several domains with different orientations, even in the regimes of larger persistence. Fixing the time, we can in principle obtain a large oriented domain along with the whole box for very large persistence. Nevertheless, this is a finite size effect which can be obtained only when $\sqrt{D_a\tau} \gtrsim L$, i.e. when the persistence length overcomes the box size.

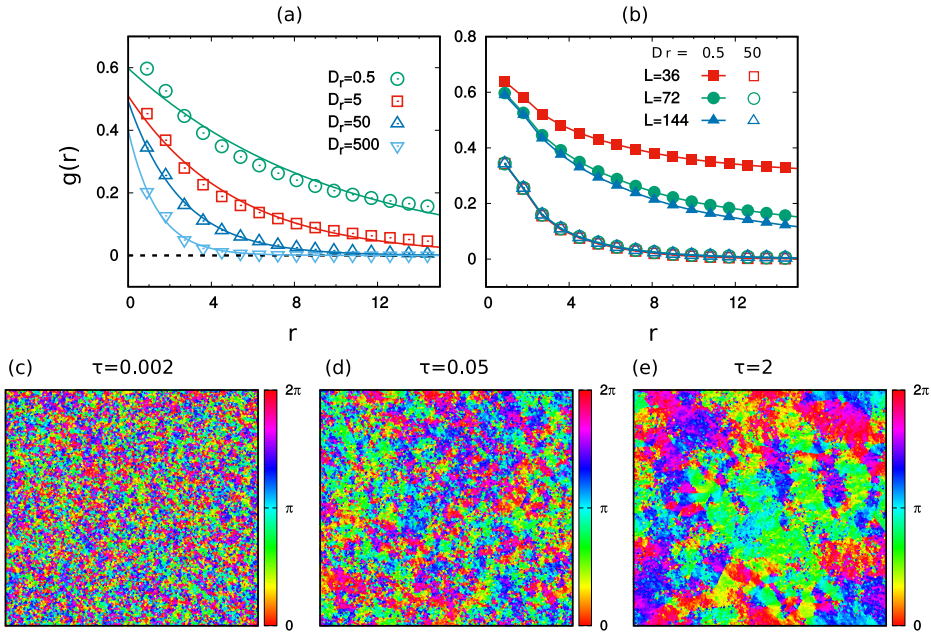


Figure 5.3: In panels (a) and (b), we plot $Q(r)$ for $\phi = 1.4$ and $U_0 = 50$. In particular, in panel (a) we show the function $Q(r)$ for different values of D_r , as illustrated in the legend. Instead, in panel (b), we show two configurations for $D_r = 0.5, 50$, for three different values of L (keeping fixed the value of ϕ). Panels (c), (d) and (e) plot three different snapshot configurations in the motion plane for $\tau = 0.002, 0.05, 2$, respectively. The snapshots are realized with $U_0 = 50$ and $\phi = 1.4$ with the interactions discussed in the text.

To overcome this difficulty, taking into account that particles are more aligned depending on their distance, we introduce the spatial correlation function of the velocity orientation, $Q_i(r)$, i.e. an observable which can quantify the local alignment even in absence of global polarization. In particular, we measure the velocity alignment between the particle i and its neighboring particles in the circular crown of thickness \bar{r} and mean radius $r = k\bar{r}$, being k an integer positive number. In this way, we get:

$$Q_i(r) = 1 - 2 \sum_j \frac{d_{ij}}{\mathcal{N}_k \pi} \quad (5.11)$$

where the sum runs over the particles in the circular crown selected by k and \mathcal{N}_k is the number of particles in that shell. The term d_{ij} is the angular distance between the two angles of particles i and j , calculated as $d_{ij} = \min[|\psi_i - \psi_j|, 2\pi - |\psi_i - \psi_j|]$. Then, we define $Q(r) = \sum_i Q_i(r)/N$, which, at each r , reads 1 and -1 for perfectly aligned and antialigned particles, respectively, and 0 in absence of any form of alignment. In panel (a) of Fig.5.3, we show the shape of $Q(r)$ for different values of the persistence time, $1/D_r$. As expected, $Q(r)$ is a decreasing function of r , being the far particles less aligned than the close ones. For the smaller values of τ , the alignment is

quite absent, affecting no more than the first shells: this is consistent with the effective Brownian scenario when the self-propulsion plays only the role of effective temperature. Instead, for large τ , the function $Q(r)$ assumes very large values in the first shell and shows a roughly exponential decay towards zero, with a typical length which roughly represents the average size of one domain. The enlarging of τ produces both the increasing of the $Q(r)$ value in the first shell ($k = 1$) and the slower decay of the whole function. This observation is, also, qualitatively confirmed in three snapshot configurations obtained for increasing values of τ from panel (c) to panel (d) and (e) of Fig.5.3, i.e. from the left to the right panels. There, the colors encode the velocity orientations, showing the increase of the alignment for larger and larger distances as τ is increased.

In what follows, we investigate the nature of this ordering phenomenon by introducing a suitable order parameter, R , obtained integrating the correlation $Q(r)$:

$$R = \int Q(r)dr, \quad (5.12)$$

where the integral is performed along with the whole box. Such a parameter displays a monotonic increasing behavior as τ grows and roughly represents the correlation length associated with the exponential decay of $Q(r)$, as shown in Fig.5.4. In this Figure, we compare the shape of R for three different configurations increasing the box size but keeping fixed the packing fraction value to $\phi = 1.4$ to unveil the presence of size effects. They are irrelevant in the small persistence regime, as emerged evaluating both $Q(r)$ in panel (b) of Fig.5.3, and R in panel (a) of Fig.5.4. Instead, clear size effects occur in the large persistence regime, namely when the persistence length, U_0/D_r , is of the order of L . The black curve shows that such an order parameter roughly increases as $\sqrt{\tau}$, an approximation which works quite well in the regime of small persistence and breaks down for large values of τ .

We study the behavior of such a velocity alignment order varying the density, exploring, in particular, the configuration for which the translational symmetry is broken. In particular, in panel (b) of Fig.5.4, we plot the order parameter, R , in function of D_r for three different values of the packing fraction. for the smaller ϕ , after a first slow monotonic growth, R reveals a sharp increase. This occurs in correspondence of the value of D_r for which the homogenous liquid-like phase breaks down in favor of a non-homogenous phase. As a confirmation, this effect does not occur for $\phi = 1.4$ where the empty regions do not appear.

The occurrence of such a velocity order is a clear evidence of the non-equilibrium nature of the dense phases studied in this Chapter. Even if the internal structure - roughly measured by the $g(r)$ - could resemble the one of equilibrium liquids or solids - with the important differences already discussed in Sec.5.2 - we point out that there is no a passive counterpart of such an ordering phenomenon. This enforces the impossibility of referring to liquid and solids in order to denote non-equilibrium phases at very high

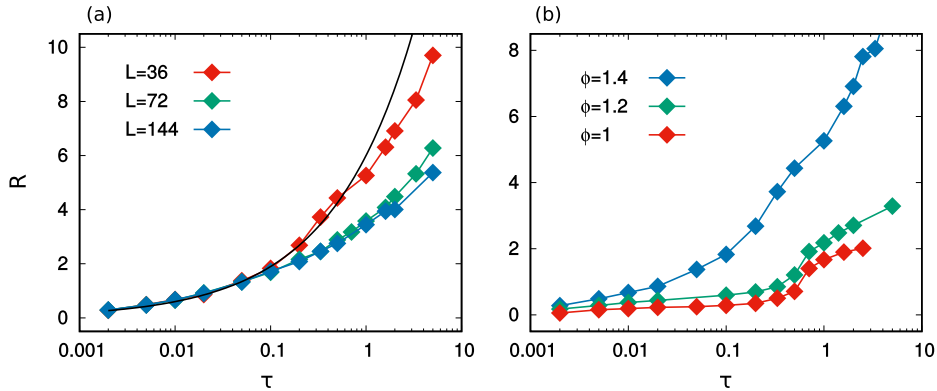


Figure 5.4: In panel (a), we plot R in function of τ for $\phi = 1.4$. Each curve is realized with a different value of L keeping fixed the value of ϕ . The black line represents the numerical fit of the function $\sim \sqrt{D_r}$. Instead, panel (b) shows R in function of τ for three different values of $\phi = 1, 1.2, 1.4$. Each simulation of both panels is realized with $U_0 = 50$ and the interaction potential discussed in the main text.

densities.

In addition, we challenge the widespread idea that explicit alignment interactions are necessary to observe the orientational order of the velocities, or, in other words, the flocking patterns typical of Vicsek-like dynamics. The simplest models for self-propelled particles with independent orientations (both ABP or AOUP) lead to this effect in the high-density regimes, because of the interplay between self-propulsion and repulsive inter-particles interactions.

5.4 Theoretical explanation: effective Vicsek-like interactions

To explain the above phenomenology, we start from the dynamics of the coarse-grained velocity, given by Eq.(5.5), applying some simplifications based on the regular structure of the system. In the densest configurations or equivalently in the non-empty regions, we can take advantage of the hexagonal spatial order. Assuming an ideal lattice, a target particle, at position \mathbf{r} has six neighbors at distance $\mathbf{r}_j = \mathbf{r}_j - \mathbf{r}$ with $j = 1..6$, with constant modulus $\bar{r} = |\mathbf{r}_j| < \sigma$. This assumption is confirmed by the study of the $g(r)$ and means that a target particle interacts with its six neighbors placed in the first shell. The interactions with further particles are zero due to the short-range feature of the potential. With these assumptions, the elements of the matrix $\mathbf{\Gamma}$ taking place in the dynamics of a target particle are only six and can be calculated, while the contributions of the external force cancel out. For notational convenience, the particle with $j = 1$ is placed on the x direction at coordinates $(\bar{r}, 0)$, while the others are placed sequentially in

the anti-clockwise sense at reciprocal angular distance $\pi/3$ and at distance \bar{r} from the origin of the reference frame. Thus, Eq.(5.5) can be simplified and reads:

$$\dot{\mathbf{v}} = -\frac{1}{\gamma} \sum_{j=1}^6 \hat{H}_j \cdot (\mathbf{v} - \mathbf{v}_j) - D_r \mathbf{v} + \mathbf{k}, \quad (5.13)$$

where we have dropped the index i of the target particle, for the sake of simplicity. The matrix \hat{H}_j comes from a manipulation of the interacting part of $\mathbf{\Gamma}$ - see Eq.(5.6) -, which is the term coupling the target particle to the j -th particle. In this way, its element are:

$$\hat{H}_j = \begin{pmatrix} U''(\bar{r}) \cos^2(\frac{j\pi}{3}) + \frac{U'(\bar{r})}{|\bar{r}|} \sin^2(\frac{j\pi}{3}) & \left[U''(\bar{r}) - \frac{U'(\bar{r})}{|\bar{r}|} \right] \cos(\frac{j\pi}{3}) \sin(\frac{j\pi}{3}) \\ \left[U''(\bar{r}) - \frac{U'(\bar{r})}{|\bar{r}|} \right] \cos(\frac{j\pi}{3}) \sin(\frac{j\pi}{3}) & U''(\bar{r}) \sin^2(\frac{j\pi}{3}) + \frac{U'(\bar{r})}{|\bar{r}|} \cos^2(\frac{j\pi}{3}) \end{pmatrix} \quad (5.14)$$

The derivations of Eq.(5.13) and Eq.(5.14) are reported in Appendix 5.C. To unveil the physical meaning of the \mathbf{v} -dynamics it is useful to rewrite Eq.(5.13) in terms of the average velocity vector of the six neighbors of the target particle:

$$\mathbf{v}^* = \sum_{j=1}^6 \mathbf{v}_j / 6.$$

Following Appendix 5.C, we get

$$\dot{\mathbf{v}} = -\frac{1}{\gamma} \hat{J} \cdot (\mathbf{v} - \mathbf{v}^*) + \frac{1}{\gamma} \sum_{j=1}^6 \hat{H}_j \cdot (\mathbf{v}_j - \mathbf{v}^*) - D_r \mathbf{v} + \mathbf{k}, \quad (5.15)$$

where the diagonal matrix \hat{J} is defined as:

$$\hat{J} = \sum_j \hat{H}_j = 3 \left[U''(\bar{r}) + \frac{U'(\bar{r})}{|\bar{r}|} \right] \mathcal{I}, \quad (5.16)$$

being \mathcal{I} the identity matrix. We notice that the diagonal components of \mathbf{J} are strictly positive, for our potential choice. This means that the first addend of Eq.(5.15) has the effect of an alignment Vicsek-like force: the dynamics of \mathbf{v} is forced to converge to \mathbf{v}^* by means of a harmonic attracting force and, thus, the target velocity aligns to the surrounding. This is exactly what happens in the Vicsek-like models, where the alignment is induced by an explicit force in the dynamics. Instead, in the ABP dynamics, such alignment is produced by the interplay between inter-particles interactions and self-propulsion in a dense suspension of self-propelled microswimmers.

To enforce our statement we show that the other terms are negligible in the large persistence limit. Indeed, both the third and the fourth addends in Eq.(5.15) are sub-dominant respect to the first two forces: the latter ones do not vanish in the limit of small D_r (large τ). Since, the noise

term, \mathbf{k} , embodies the differences between ABP and AOUP dynamics, it is not surprising that both models show the same phenomenology. Thus, the dynamics could be dominated only by the first two forces in the right-hand side of Eq. (5.15). We notice that the second one vanishes in two cases: i) when the six neighboring particles have all identical velocities $\mathbf{v}_j = \mathbf{v}^*$; ii) when these velocities are arranged according to a vortex-like pattern, defined for instance by the profile $\mathbf{v}_j = v_0(-\sin(j\pi/3), \cos(j\pi/3))$, i.e. in the two typical configurations of the small persistence regime. See Appendix 5.D for more details about the proof. In both cases, the dynamics of $\mu\dot{\mathbf{v}}$ is ruled by the Vicsek-like aligning force at small $1/D_r$, which induces the rapid convergence $\mathbf{v} \rightarrow \mathbf{v}^*$. When \mathbf{v} is aligned with the neighbors' velocities, the aligning force vanishes and the sub-dominant bath-like terms, i.e. $-\gamma\mathbf{v} + \mathbf{k}$, perturb the target velocity. At this stage, the Vicsek-like force restores the alignment.

In the more general case, where the six neighboring particles are not aligned or in the vortex pattern, the second force appears in the dynamics. Anyway, when particles are close to alignment this term is small with respect to the attractive point of the Vicsek-like force: in particular, the first two addends of Eq.(5.15) can be rewritten as

$$-\frac{1}{\gamma}\hat{J} \cdot (\mathbf{v} - \mathbf{v}^*) + \frac{1}{\gamma} \sum_{j=1}^6 \hat{H}_j \cdot (\mathbf{v}_j - \mathbf{v}^*) = -\frac{1}{\gamma}\hat{J} \cdot [\mathbf{v} - \mathbf{v}^* + \mathbf{v}_{ex}^*] \quad (5.17)$$

$$\mathbf{v}_{ex}^* = \hat{J}^{-1} \cdot \frac{1}{\gamma} \sum_{j=1}^6 \hat{H}_j \cdot (\mathbf{v}_j - \mathbf{v}^*), \quad (5.18)$$

being \mathbf{v}_{ex}^* the excess part respect to the attraction point of interaction with Vicsek's form. If \mathbf{v}_j is close to \mathbf{v}^* for every j , then we have:

$$|\mathbf{v}^*| \gg \mathbf{v}_{ex}^*. \quad (5.19)$$

Even if a rigorous general estimate of the fate of Eq. (5.15) is very complicated, the above argument suggests that when the system is close to the cases i) and ii) the dynamics of the velocities develops a spontaneous aligning mechanism which dominates over the other terms.

Eq.(5.15) establishes a strong analogy with Vicsek-like models, showing that the emergence of flocking could occur even in the absence of explicit aligning interactions. For ABP (or AOUP) spherical particles, this is simply caused by the interplay between strong interactions and self-propulsions.

5.4.1 A further approximation: predicting the shape of R

Hereafter, we develop a suitable approximation to roughly predict analytically the behavior of the spatial velocity correlations as a function of D_r (or

τ), shown in Fig.5.4. In particular, we assume that particles maintain their positions on a hexagonal lattice whose orientation is fixed a priori, as in the previous Section. Calculations are performed using the AOUP form of \mathbf{k}_i , i.e. a white noise vector with independent components. The lattice assumption implies that we can replace \mathbf{v} with a velocity field $\mathbf{v}(\mathbf{x})$ and the noise \mathbf{k} with $\mathbf{k}(\mathbf{x})$, in Eq.(5.13). Now, applying the discrete Fourier transform, we get:

$$\mu \frac{\partial}{\partial t} \tilde{\mathbf{v}}(\mathbf{k}, t) = -\gamma \tilde{\mathbf{v}}(\mathbf{k}, t) - \frac{1}{D_r} \tilde{H}(\mathbf{k}) \tilde{\mathbf{v}}(\mathbf{k}, t) + \sqrt{2\gamma\mu v_0^2} \tilde{\boldsymbol{\xi}}(\mathbf{k}, t), \quad (5.20)$$

where $\tilde{\mathbf{v}}(\mathbf{k}, t)$, $\tilde{\boldsymbol{\xi}}(\mathbf{k}, t)$ and $\tilde{H}(\mathbf{k})$ are the Fourier transform of $\mathbf{v}(\mathbf{x})$, $\boldsymbol{\xi}(\mathbf{x})$ and $H(\mathbf{x})$, respectively. The symmetric matrix $\tilde{H}(\mathbf{k})$, has the following elements according to Eq.(5.14):

$$\tilde{H}_{xx}(\mathbf{k}) = \left(U''(\bar{r}) + 3 \frac{U'(\bar{r})}{\bar{r}} \right) \left[\cos\left(\frac{k_x \bar{r}}{2}\right) \cos\left(\frac{\sqrt{3}k_y \bar{r}}{2}\right) - 1 \right] + \quad (5.21)$$

$$+ 2 U''(\bar{r}) [\cos(k_x \bar{r}) - 1],$$

$$\tilde{H}_{yy}(\mathbf{k}) = \left(3U''(\bar{r}) + \frac{U'(\bar{r})}{\bar{r}} \right) \left[\cos\left(\frac{k_x \bar{r}}{2}\right) \cos\left(\frac{\sqrt{3}k_y \bar{r}}{2}\right) - 1 \right] + \quad (5.22)$$

$$+ 2 \frac{U'(\bar{r})}{\bar{r}} [\cos(k_x \bar{r}) - 1],$$

$$\tilde{H}_{xy}(\mathbf{k}) = \sqrt{3} \left(U''(\bar{r}) + 3 \frac{U'(\bar{r})}{\bar{r}} \right) \sin\left(\frac{k_x \bar{r}}{2}\right) \sin\left(\frac{\sqrt{3}k_y \bar{r}}{2}\right). \quad (5.23)$$

Eq. (5.20) can be formally solved and its solution reads:

$$\tilde{\mathbf{v}}(\mathbf{k}, t) = \tilde{\mathbf{v}}(\mathbf{k}, 0) e^{-\alpha(\mathbf{k})t} + \sqrt{2\gamma\mu v_0^2} \int_0^t dt' e^{-\alpha(\mathbf{k})(t-t')} \tilde{\boldsymbol{\xi}}(\mathbf{k}, t'). \quad (5.24)$$

To get simple analytical results, we calculate $\alpha(\mathbf{k})$ in the small \mathbf{k} limit, obtaining:

$$\alpha(\mathbf{k}) = D_r + \frac{3}{4\gamma} \left(U''(\bar{r}) + \frac{U'(\bar{r})}{\bar{r}} \right) |\mathbf{k}|^2 \bar{r}^2. \quad (5.25)$$

The corresponding equal time velocity-correlation in the Fourier space is

$$\langle \hat{v}_x(\mathbf{k}, t) \hat{v}_x(-\mathbf{k}, t) \rangle + \langle \hat{v}_y(\mathbf{k}, t) \hat{v}_y(-\mathbf{k}, t) \rangle = \frac{2v_0^2}{1 + \lambda_s^2 |\mathbf{k}|^2}, \quad (5.26)$$

where

$$\lambda_s \approx \bar{r} \left[\frac{3}{4\gamma} \frac{1}{D_r} \left(U''(\bar{r}) + \frac{U'(\bar{r})}{\bar{r}} \right) \right]^{1/2}. \quad (5.27)$$

Coming back to the representation in the real space, Eq. (5.26) turns into:

$$\langle \mathbf{v}(\mathbf{x} + \mathbf{r}, t) \mathbf{v}(\mathbf{x}, t) \rangle \approx 2v_0^2 \left(\frac{\lambda_s}{8\pi r} \right)^{1/2} e^{-r/\lambda_s}. \quad (5.28)$$

We outline that the correlation length, Eq. (5.27), and the exponential shape of the space correlation, Eq. (5.28), are the results of the expansion for small \mathbf{k} . We suspect that terms at small wavelengths can be important, for instance, in the explanation of the vortex structures. The prediction given by Eq.(5.27) suggests a correlation length which increases as $1/D_r$ grows. In spite of the numerous approximations, the comparison between data and Eq.(5.27) shows a good agreement in the small persistence regime, where the profile of R scales as $\sqrt{\tau}$. As shown in Fig.5.4, first discrepancies occur for large values of τ .

We remark that such an argument can be extended to the ABP dynamics because \mathbf{n} and \mathbf{v} are roughly uncorrelated, as confirmed by simulations and from the fact that the noise term plays a marginal role in the large persistence limit. Anyway, a formal derivation in the ABP case, i.e. using a multiplicative noise, is unknown.

5.4.2 Distribution functions of the velocity modulus

It is worthy to note that the typical value of the average single-particle velocity modulus, $|\mathbf{v}|$, is smaller than U_0 , i.e. the amplitude of the average - only in the AOUP dynamics - modulus of the self-propulsion. The two objects coincide only in the absence of external or inter-particles forces. This is in agreement with what we expect from the transformed equation of motion, Eq.(5.5), where the occurrence of very large Stokes forces in the dynamics depresses the values of $\dot{\mathbf{x}}_i = \mathbf{v}_i$. The slow-down due to the interactions is a well-known phenomenon for systems of active particles, which thanks to Eqs.(5.5) is common to ABP and AOUP models.

In Fig.5.5, we show the distribution of the velocity modulus for several values of τ at fixed U_0 . Increasing the persistence, the distribution moves towards smaller $|\mathbf{v}|$, meaning that the system slows down. A clear monotonic behavior occurs both in the small and in the large persistence regimes. In all cases, the distribution is fairly described by a Gaussian in cartesian coordinates centered at $\mathbf{v} = 0$ with some effective temperature, as confirmed by the numerical fits. While this is less surprising for the AOUP dynamics - where the non-interacting particle follows the same distribution - this is unexpected for the ABP one - since, in this case, the velocity modulus of a non-interacting particle is distributed as a δ -Dirac function centered at U_0 . Small discrepancies from the Gaussian profile appear in the right tails of $p(|\mathbf{v}|)$, revealing that, sometimes, particles are faster than any equilibrium-like gaussian distributed suspension of packed particles.

Using the approximate dynamics, given by Eq.(5.15), and the condition (5.19), the equation of motion can be roughly simplified and the dynamics of \mathbf{v} depends on its neighbors' velocities only through \mathbf{v}^* . Recurring to a sort of mean-field approximation means to average over the whole domains with aligned particles. This implies that $\langle \mathbf{v}^* \rangle = 0$ since the average is performed over the whole box supposed to be always larger than the typical size of the

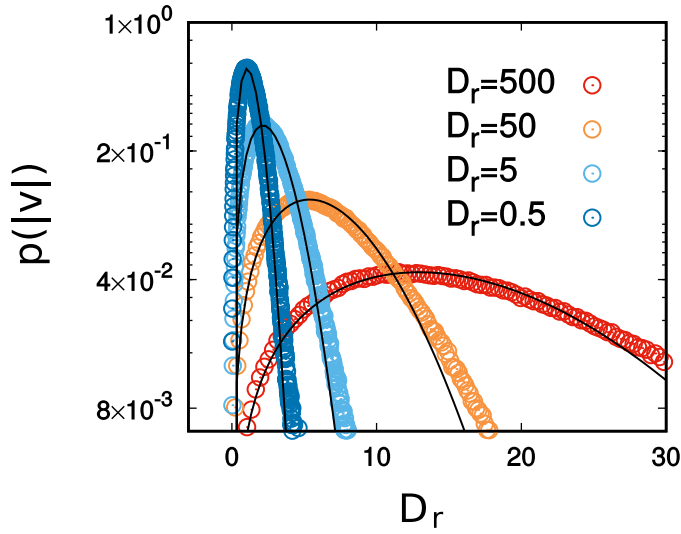


Figure 5.5: Probability distribution of the velocity modulus, $p(|\mathbf{v}|)$, for the different values of D_r shown in the legend. Black lines are the results of numerical fits performed with the Gaussian distributions, predicted by Eq.(5.30). Simulations are realized with $U_0 = 50$ at $\phi = 1.4$ with the interacting potential described in this Chapter.

aligned domains. In this way, any local structure of the velocity is lost, but we can trivially close the original equation obtaining the dynamics of the mean-field velocity, \mathbf{v}_m :

$$\dot{\mathbf{v}}_m = -\frac{1}{\gamma} \mathbf{J} \cdot \mathbf{v}_m - D_r \mathbf{v}_m + \mathbf{k}. \quad (5.29)$$

being J the value of two diagonal elements of the matrix \hat{J} . While the solution of Eq.(5.29) is unknown for the ABP dynamics, it can be easily solved using the AOUP one, i.e. choosing \mathbf{k} as white noise. In this case, the steady-state probability distribution of \mathbf{v}_m is simply given by a Gaussian:

$$P(\mathbf{v}_m) \propto \exp\left(-\frac{\tau}{\gamma D_a} \left(1 + \frac{\tau}{\gamma} \hat{J}\right) \frac{|\mathbf{v}_m|^2}{2}\right) \quad (5.30)$$

Introducing the effective mass $\mu = \tau\gamma$, it is straightforward to generalize the effective temperature described in Sec.2.37 to high dense suspensions of interacting self-propelled particles:

$$\theta_m = \gamma \frac{U_0^2}{2} \frac{\tau}{1 + \frac{\tau}{\gamma} \hat{J}(\bar{r})} \quad (5.31)$$

This expression is in agreement with the effective temperature introduced by numerical fits in the framework of active glassy systems [258]. Eq.(5.31) predicts its value in terms of the active force parameters and \bar{r} and no

numerical fits are involved. This prediction is only based on the hexagonal lattice assumption and, thus, we expect that its range of validity should be restricted to the freezing regime. Since in the large persistence regime θ_m returns:

$$\theta_m \approx \gamma^2 \frac{U_0^2}{2\hat{J}(\bar{r})}, \quad (5.32)$$

our prediction is in agreement with the phenomenology reported in the study of the $g(r)$ (see Fig.5.1): in the homogenous phase, the internal structure saturate to a fixed value in the limit of large τ , as if a saturation in the effective “temperature” occurs. Instead, in the small persistence regime, θ_m becomes:

$$\theta_m \approx \gamma\tau \frac{U_0^2}{2}, \quad (5.33)$$

Again, Eq.(5.33) is in agreement with the phenomenology of the structure-function, reported in Fig.5.1: in this regime, the increasing of τ leads to fluidization as if the effective temperature was increased.

In the latter case, the prediction (5.32) does not depend on the shape of the interactions as we expect in the small persistence regime. On the contrary, the shape of (5.33) is strongly influenced by U through the matrix element J , as in the case of non-interacting particles in external potentials. Nevertheless, the lattice assumption reduces the positional dependence simply to \bar{r} , which is fixed by the numerical density in any homogenous configurations.

5.5 Confined interacting particles: activity induced freezing

In previous Sections, we have shown that even pure repulsive interactions induce non-trivial phenomena in the internal structure of an infinite system breaking the translational symmetry and, mostly, producing intriguing patterns of aligned or vortex-like velocities. In this Section, we confine the interacting system of self-propelled particles discussed in the previous Sections using an external trap centered at the origin of the reference frame. We set the external potential as in Sec.2.4 of Chapter2, namely

$$U(\mathbf{x}) = k/n |\mathbf{x}|^n, \quad (5.34)$$

being n a positive integer number. The inter-particle interactions are fixed by the functional form (5.4), for the sake of simplicity, with $b = 3$.

Such a study is motivated by a recent experiment of Takatori et. al. [110]: they consider a dilute suspension of Janus particles, confined by an optical trap, observing the “accumulation” far from the minimum of the potential, already discussed in Sec.2.4. In Chapter 2, we have qualitatively reproduced such a phenomenon using both independent ABP and AOUP

dynamics. Such an approximation is consistent with [110] since the number of particles employed in the numerical study is low enough to neglect any interactions among Janus particles. This Section aims to extend the study of Chapter 2 even to very packed systems to unveil the role of inter-particle interactions and their influence on such a non-equilibrium phenomenon.

The study reported below [77] is performed using the AOUP dynamics, for the sake of simplicity, even if all the results illustrated are valid also for the ABP one. Let us briefly recall the AOUP model used in this Section, for completeness. Extending Eqs(5.2) to the presence of an external trap (5.34), we get:

$$\gamma \dot{\mathbf{x}}_i = \mathbf{F}_i + \mathbf{f}_i^a - k |\mathbf{x}_i|^{n-1} \hat{\mathbf{x}}_i, \quad (5.35)$$

where \mathbf{f}_a evolves with Eq.(5.2b). In the following numerical study we fix $\gamma = 1$ and keep the ratio $D_a/\tau = 10^2$ (corresponding to $v_0 = 10$). The relevance of the active force is determined by the value of τ and, to be specific, by the adimensional parameter $\nu = \tau U''(l)/\gamma$. In the non-interacting case, the analysis of such a system has been already performed in Chapter 2, showing equilibrium-like regimes for $\nu \lesssim 1$ which can be explained in terms of an effective temperature due to the self-propulsion. Instead, for $\nu \gtrsim 1$, marked non-equilibrium phenomena occur: particles accumulate far from the minimum of the potential arranging on a circular crown. The non-Boltzmann shape of the whole distribution could be considered as evidence of the failure of any global effective temperature approaches. Anyway, the discovery of regions where equilibrium is approximatively restored - the accumulation regions to be specific - allows us to claim that such an equilibrium-like approach could lead to interesting results.

In any infinite system with fixed inter-particle interactions, the control parameters of the dynamics are three: the two coming from the active force and the packing fraction, ϕ (density). In a confined system, things are more complicated: the density is not a “good” parameter since the available space mostly depends on the interplay between the force exerted by the external trap, the active force and the interacting one. In other words, in the definition of the density (or packing fraction), at least, we should replace the size of the box with the “size” of the volume available because of the external potential. We denote with l such a size which will be set to one in the numerical study. Besides, it is worthy to note that the number of particles, N , plays a role itself since the system is not translationally invariant. For this reason, we consider a small system, setting $N = 10^3$, for the sake of simplicity. Then, we keep fixed the parameters of the external potential, i.e. k (in such a way that $l = 1$), varying only the parameters of U : to explore larger packing fraction we simply increase the effective length due to the interaction, i.e. the nominal particle diameter σ .

5.5.1 Phase diagram: self-propulsion induced freezing

In Fig.5.6, we display pictorially the phase diagram varying ν and the radius of the inter-particles interactions rescaled with the typical external potential length, i.e. the ratio R/l . The former parameter tunes the relevance of the self-propulsion while the latter controls the excluded volume of the system.

For completeness, we discuss the dilute regime which is consistent with the phenomenology of Chapter2 obtained directly in the non-interacting case. Where R/l is very small, the regime of $\nu \lesssim 1$ is consistent with a Brownian-like picture and does not reveal any surprises: particles accumulate around the minimum of the external potential and explore an effective average volume determined by the interplay between the external potential and the self-propulsion. The latter behaves as an effective temperature given by $\gamma D_a \propto \gamma U_0^2 / D_r$, which increases as the persistence time grows. Thus, the system explores the area close to the origin by the means of activity-induced effective thermal fluctuations: the increasing of τ enlarges the visited area. Instead, when $\nu \gtrsim 1$, the area close to the potential minimum empties and the system shows a strong delocalization in favor of a peripheric annular region. The size of the circular crown increases for larger values of ν until to saturate at an average distance, r^* , from the origin determined by the balance between the average modulus of the self-propulsion and external force. A further increase of ν produces only the slow down of the particles. This effect is consistent with the definition of the effective space-dependent temperature, already introduced and discussed in Sec.2.5.1.

Let us consider a regime for larger values of R/l where the interactions are not negligible. At first, we discuss the equilibrium-like regimes for $\nu \lesssim 1$: also in this case, the self-propulsion behaves as an effective thermal bath. In analogy with the infinite system studied in Sec.5.2, also in the presence of a confining mechanism we recover the usual equilibrium-like aggregation phases in this small persistence regime. Each phase is denoted with different colors in panel (a) of Fig.5.6: in the dilute phase (red), the interactions are rare events and the volume explored by the particles is only determined by the self-propulsion. In the solid phase (green) the effective random force is small compared to the inter-particles interactions producing only oscillations around the particles' positions, which are almost fixed. Finally, an intermediate phase between the previous two, i.e. the liquid phase (blue), occurs, where both these forces are comparable producing a complex and correlated dynamics. The three aggregation phases can be detected by the pair correlation function, $g(r)$, in a similar way to the infinite case, assuming the same criteria to distinguish them. Since the system is not translational invariant due to the presence of the external potential, in this regime, we evaluate the $g(r)$ in the densest part of the system, i.e. a small region around the origin. The increasing of ν from 10^{-2} to 1 shows a fluidization effect for each phase. As in the non-interacting regime, this phenomenon can be understood in terms of the effective temperature approach. In particular, from the smaller

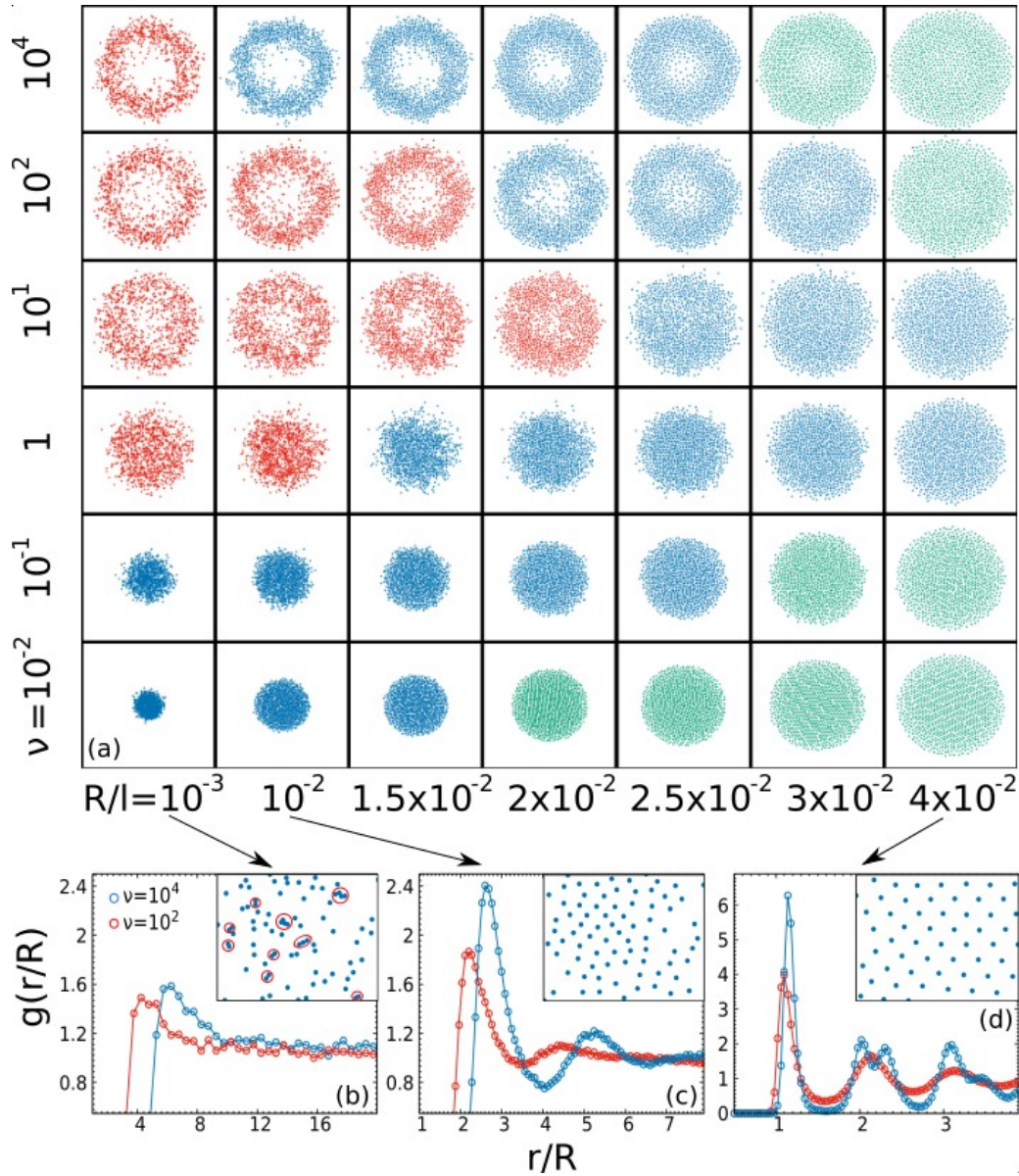


Figure 5.6: In panel (a) we display the phase diagram in terms of snapshot configurations in the motion plane, varying the adimensional parameter ν and the ratio R/l . In panels (b), (c) and (d), we show the $g(r)$ in the large persistence regime for three different values of $R/l = 10^{-3}, 10^{-2}, 4 \times 10^{-2}$, respectively. In each panel we report two $g(r)$ obtained in the large persistence regime, for $\nu = 10^2, 10^4$. Simulations are realized with $U_0^2/2 = D_a/\tau = 10^2$, $b = 4$, $l = 1$.

values of R/l , namely the first two columns of Fig.5.6(a), we pass from the liquid to the gas phase: the $g(r)$ displays a second marked peak in the former case and a flat-like shape in the latter. This transition is accompanied by an enhancement of the effective volume occupied: the effective temperature leads particles to explore larger areas until the interactions become rare in

the gas. For larger values of R/l , the transition from the solid to the liquid phase occurs, as shown in the last two columns in Fig.5.6(a): this happens when the second split peak of the solid $g(r)$ collapses into a single peak. We remark that, in the solid phase, the occupied volume is purely determined by the balance between the inter-particles repulsion and external potential, which pushes particles towards the origin of the reference frame.

Let us consider the large persistence regime $\nu \gtrsim 1$. The delocalization phenomenon reexists to the presence of the interactions as shown in panel (a) of Fig.5.6. Anyway, when R/l brings the system to an effective close packing, the radial delocalization is completely suppressed and the system arranges again into a homogenous phase with ordered solid-like internal structure. This phenomenon is not so surprising: for these values of R/l , the self-propulsion is negligible with respect to the interactions and there are no reasons to expect the delocalization. At variance with the dense infinite systems discussed in Sec.5.2, the confinement denies the formation of traveling crystals. Also in this non-equilibrium regime, we study the $g(r)$ to unveil the effect of ν on the internal structure of the system. The $g(r)$ is always calculated in one of the densest regions, which, in this regime, corresponds to a small square of the circular crown where particles accumulate. As argued in Sec.5.2 for an infinite system, the introduction of non-equilibrium like phases simply by the analogy with the equilibrium picture is rather questionable. Anyway, here, we call “solid-like”, “liquid-like” and “gas-like” the aggregation phases whose internal structures have the same features of the equilibrium phases. We remark that such a nomenclature does not mean that we are dealing with “real” solid, liquid, or gas phases since large differences occur at several levels of description. In the large persistence regime, the increasing of ν has an opposite effect than the small persistence one: the peaks of the $g(r)$ become more pronounced in all the aggregation phases. Such an effect resembles the phenomenology of the equilibrium cooling induced by decreasing the temperature of the system. We can observe the transition from “gas-like” to “liquid-like” (first columns of Fig.5.6 (a)) and the one from “liquid-like” to “solid-like” structures (last columns of Fig.5.6 (a)). In panels (c) and (d) of Fig5.6, we report the $g(r)$ study to unveil the transitions: in particular, we plot two $g(r)$, obtained for $\nu = 10^2, 10^4$, in each panel. We also enlarge a typical snapshot configuration showing few particles in the more persistence case, evidencing the typical configuration of a “liquid” and the perfect hexagonal pattern in panels (c) and (d), respectively. Instead, in panel (b) we show two typical configurations in the “gas-like” case which will be mostly discussed in the next Section.

Summarizing, first, the delocalization reexists to the presence of interactions. Second, in all the aggregation phases, i.e. for all the values of R/l , we discover a reentrant behavior of the structural properties of the system induced by the active force persistence [77]. For $\nu \lesssim 1$ the fluidization of the structures occurs, in agreement with the effective temperature approach, while, for $\nu \gtrsim 1$, an induced far from equilibrium freezing takes place. The

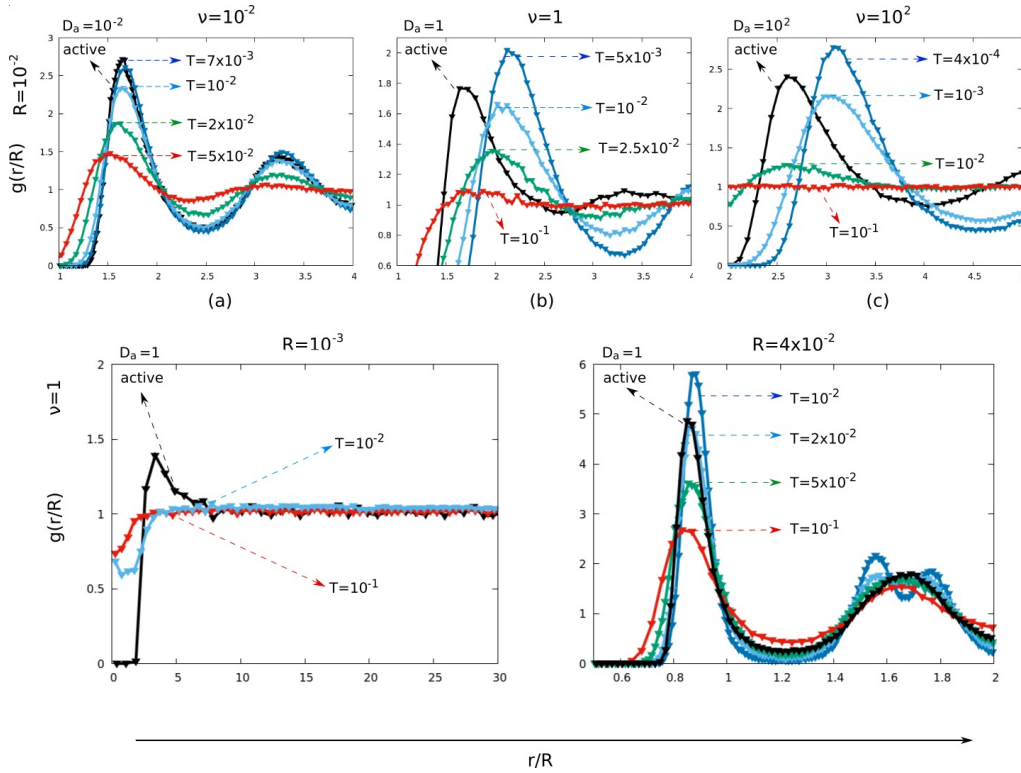


Figure 5.7: $g(r)$ for an active system (black line) compared with the equivalent Brownian systems at different temperatures (colored line as shown in each graph). Top Panel: $R = 10^{-2}$, graph(a),(b) and (c), respectively, at $\nu = 10^{-2}, 1, 10^2$. Bottom panels: $\nu = 1$. Graph(d) at $R = 10^{-3}$ and graph(e) at $R = 4 \cdot 10^{-2}$. Other parameters: $k = 10^2/4$, $D_a/\tau = 10^2$, $b = 4$.

occurrence of this non-monotonicity is entirely due to the presence of the external trapping being completely absent in any infinite systems at high densities.

5.5.2 Study of the pair correlation function

As already mentioned, the identification of “non-equilibrium phases” based on the analogy with the internal structure of passive Brownian particles is rather questionable. Even if the $g(r)$ shows one or two peaks and a second split peak depending on R/l and τ , the differences between passive and active structure are evident.

To give consistency to this statement, we compare the $g(r)$ of self-propelled particles following the dynamics (5.35) with an equivalent passive Brownian suspension. In this context, “equivalent” means at the same effective packing - same external potential and interaction length. Being not clear what is the effective temperature of active particles in the large persistence regime, we explore different diffusive constants (i.e. different temperatures) trying to obtain the same structure in the liquid, solid a diluted aggregation

phases.

Let us start from the “gas-like phase” when R/l is very small, as shown in panel (d) of Fig. 5.7. The active $g(r)$ displays a first peak at $r \approx R$ before approaching to one, which does not have a Brownian counterpart. Indeed, the passive $g(r)$ are peak-less also for very low temperatures, which is not so surprising since the interactions are very small. The occurrence of such an active peak is a consequence of the slow-down of the particles when they interact with each other. This introduces a discrepancy in the probability of finding two particles close to each other, forming couples or even small groups. Anyway, these couples should have a finite life-time, otherwise, the formation of an infinite cluster could not be arrested. In the inset of Fig.5.6 (b), we enlarge a small region in a snapshot configuration evidencing the occurrence of a large number of couples which has not a Brownian counterpart. This point will be further analyzed in Chapter 6, where more details about the instability of the couples will be provided. In the same panel, we also observe the role of ν : the main peak shifts towards larger distances. From this analysis, we conclude that the “gas-like” phase is fairly different from the equilibrium one. In spite of the small values of R/l , interactions are not so rare and very small structures form.

In the top panel of Fig. 5.7, we perform the same analysis with larger values of the interaction length to explore the feature of the “liquid-like” structure in the non-equilibrium phase. In the regime $\nu \lesssim 1$, the shape of the $g(r)$ is obtained with a Brownian simulation, as shown in panel (a) of Fig.5.7. This is in agreement with the effective temperature approach holding in this limit. Instead, for $\nu \gtrsim 1$, the shape of the active $g(r)$ cannot be reproduced changing the diffusion coefficient as shown in panel (b) and (c) of the same figure. The active peak is always shifted towards smaller distances, meaning that particles are more close to each other with respect to the equivalent passive counterpart. This is fairly in agreement with the phenomenology of the infinite system of Sec.5.2, where the occurrence of empty regions means that the system is more packed. The only exception regards a more packed configuration reported in panel (e), where we can find a numerical temperature value through which we can roughly reproduce the active shape of the $g(r)$.

We may conclude that when the packing fraction is large enough the microscopic structure, represented by the $g(r)$, is the same as the one of an equivalent Brownian system with some effective temperature. This is in agreement with the phenomenology of Sec.5.2: for the larger values of ϕ the increasing of τ does not change the peak positions. Nevertheless, there is no way to reproduce the active $g(r)$ in the gas-like and liquid-like regime induced by the activity, with an equivalent Brownian simulation under the same condition: these structural changes are entirely due to the activity and are genuine non-equilibrium effects [77].

5.6 Conclusion

In this Section, we have studied systems of self-propelled particles at high packing fractions, the so-called “extreme active matter” [258]. With this nomenclature, we refer to very packed systems displaying liquid or solid-like structures for passive Brownian suspension of particles. We discover that the self-propulsion plays the role of an effective temperature only in the regime of small persistence: the increase of τ induces the “warming” of the internal structure of the system. Instead, the phenomenology in the high persistence regime is richer revealing interesting novelties both in the internal structure and in the occurrence of a new long-range order, which has not a Brownian counterpart. In particular, the translational order common of the liquid phase breaks down with the occurrence of empty regions, whose sizes depend on the density and on the parameters of the active force. In addition, velocities exhibit intriguing patterns, forming aligned domains or vortex-like arrangements, which become more pronounced as the persistence is increased. We study such an emerging long-range order introducing a suitable order parameter in terms of the spatial correlations of the velocity orientations. These numerical observations, confirmed by suitable theoretical approximations, call for experimental verifications: as already mentioned, biological specimens of extreme active matter are not suitable for any controlled experiments, because their numerical density is a function of time. Instead, Janus particles [110, 240] or vibrated polar granular disks [242] offer a real platform to confirm such a long-range order. We stress that both density heterogeneity and velocity alignment suggest that extreme active matter does not deal with the usual equilibrium aggregation phases and that new “non-equilibrium phases” need to be introduced.

Several works have been devoted to the generalization of the well-known glass transition [262, 263] for passive Brownian particles to suspensions of non-equilibrium self-propelled units [264] evolving with AOUP [265, 266, 263] or ABP [267, 268, 269] dynamics. Considering a binary mixture - two species with different sizes - of spherically symmetric active particles, they show the leading features of a glass transition: a dramatic slowing down of the liquid’s dynamics with small changes in the structure of the pair correlation function upon a little change in the density and/or “temperature” - with this term several authors simply denote a combination of the active force parameters, assuming for instance the amplitude of the mean square displacement as “temperature”. In spite of the different results - monotonicity or non-monotonicity of the relaxation time due to the different protocols used in the variation of the control parameters - the adaptation of the present velocity analysis to this case could offer a new challenge in the phenomenology of active glasses, shedding light on the non-equilibrium nature of such a transition. Understanding how the velocity alignment modifies in the glassy state is an intriguing generalization of the present study. Even the breaking down of the translational symmetry, induced by the increase of the persis-

tence time, is another interesting question: evaluating the suppression or not of a non-homogeneous glassy dynamics is another interesting question.

As an additional point, we extend the study of Chapter 2 - in the presence of a confinement trap - to the interacting case to account for the excluded volume of a microswimmer. The accumulation far from the minimum of the potential, experimentally confirmed by suspensions of diluted Janus particles confined by acoustic traps [110], persists in the presence of pure repulsive interactions: particles accumulate in circular crowns whose sizes are determined by the interplay between confinement and self-propulsion. The system shows internal structures which resemble the liquid and the solid ones in the passive Brownian counterparts. Even if we cannot talk about “liquid” or “solid”, as already discussed for infinite systems, the increase of the self-propulsion persistence induces a non-monotonic behavior in the structure-function which is absent in the confinement-free system. A first fluidization, in the regime of small persistence, is followed by an induced freezing [77], due to the interplay between self-propulsion, interactions and confinement. Such a study calls for verifications using the same experimental setup of [110], i.e. Janus particles confined by acoustic traps, or using bacteria.

Appendices

5.A The pair correlation function

In the framework of liquid theory, the internal structure of a system of interacting particles can be well-described by the pair correlation function, $g(r)$, which measures the probability of finding a couple of particles at distance r . In particular, the $g(r)$ is defined as [235]:

$$g(r) = \frac{V}{N} \left\langle \frac{1}{N} \sum_{i \neq j} \delta[\mathbf{r} - (\mathbf{r}_i - \mathbf{r}_j)] \right\rangle. \quad (5.36)$$

where \mathbf{r}_i is the position of a target particle and $\langle \cdot \rangle$ denotes both the average over all the particles and a time average. Such a definition could be adapted to a specific portion of space, a square for instance, simply replacing N as the number of particles in that region and L with its size.

In a system of passive Brownian particles, such observable could be roughly used to describe the “transition” from gas to liquid and even to “solid” state, by decreasing the temperature or increasing the density of the system, which are the two leading control parameters. In particular, the $g(r)$ in the gas-phase is characterized by a flat profile: for $r > \sigma$, being σ the typical diameter of the particle, $g(r)$ is one, or displays a small initial peak around $r \sim \sigma$ which rapidly decreases towards one. The height of such a peak increases as the temperature decreases or the density grows. This shape of the $g(r)$ describes a homogenous gas phase where interactions are rare and binary-like and particles move around the accessible volume by means of thermal fluctuations. For further values of the control parameters (small temperatures or higher densities), the first peak becomes narrow and a second peak in the shape of the $g(r)$ occurs, which can be roughly considered as the starting point of the liquid-phase. In this case, particles move around the available volume and their positions are strongly correlated: the position of the first peak states the typical average distance between two neighboring particles. For smaller temperatures (or higher packing fractions), several peaks appear before that the $g(r)$ approaches to one. The transition point from liquid to solid-like phases is obtained when the second peak starts to split. Now, the peaks of the $g(r)$ are placed at the typical distances between particles determined by the structure of the lattice and they become narrow as the temperature is decreased, ideally approaching to δ -Dirac functions. In two dimensions, with interactions depending only on inter-particle distances, particles arrange into a hexagonal pattern, fluctuating around their fixed equilibrium positions.

Let us remark that the identification of the microscopic structures with the macroscopic phases (and in particular, the occurrence of transitions between different phases) makes sense just if we consider the infinite volume

limit, numerically by means of periodic boundary conditions. If we apply an external potential, particles can explore just an effective volume, depending on the inter-particles interactions and on the potential itself. Therefore, fixing the number of particles to $\sim 10^2 - 10^4$ (typical numbers of a simulation), means to study a system with few degrees of freedom, whose importance, nowadays, is well known. With these motivations, studying the internal structure of such a system, for instance through the $g(r)$, makes sense and could be useful to understand the role of the interactions.

5.A.1 Details about the $g(r)$ computations for confined systems

In the presence of external confinements, i.e. in Sec.5.5, the translational symmetry is broken and, so, to evaluate the internal structure of the system (both for passive and active particles), we have computed numerically the $g(r)$ using the following protocol:

1. We chose a square inside the dense region of a configuration: a disk or a circular crown (if the radial delocalization occurs or not). Such a square is chosen not too big, in such a way we can neglect the boundary of the region.
2. We compute numerically the $g(r)$ in this region, using Eq.(5.36) [235]. The normalization is estimated by numerically computing the number of particles inside the square for each configuration.
3. In order to check the result, we perform the same analysis for different (but dense) regions, verifying that there are no big changes.

In the following, we describe the protocol adopted to compare an AOUP system with a passive Brownian one, giving more details about the study performed in Sec.5.5.2. To compare the active $g(r)$ with its passive Brownian counterpart, we simulate a passive suspension with the same packing fraction of the active system, choosing the same potentials and the same number of particles. Being not so clear the definition of the effective temperature in active systems, we look for some diffusion coefficients - i.e. temperatures - able to reproduce the active $g(r)$. To be specific, we adopt the following protocol:

1. We compute the $g(r)$ in the active case, with the procedure described above, selecting a square space region of area A_r , and computing the average number of particles, N_r , in that region.
2. We compute the $g(r)$, for the following system: N_r overdamped passive Brownian interacting particles in a square region of area, A_r , under the action of the confining potential. In this way, the self-propelled system and the equivalent passive Brownian one has the same effective packing fraction.

3. We compute the $g(r)$ of the Brownian system for different values of the diffusion coefficient, checking if there is some temperature value which reproduces the active $g(r)$.

5.B Derivation of Eq.(5.5)

Eq. (5.1b) for the angle θ_i corresponds to the following vectorial equation for the associated orientation vector \mathbf{n}_i :

$$\dot{\mathbf{n}}_i = \sqrt{2D_r}\boldsymbol{\xi}_i \times \mathbf{n}_i, \quad (5.37)$$

being $\boldsymbol{\xi}_i$ a three dimensional vector with components $(0, 0, \xi_i)$ and $\langle \xi_i(t)\xi_j(t') \rangle = \delta(t-t')$, while \mathbf{n}_i is a unit vector belonging to the xy -plane. In Eq. (5.37) the noise has multiplicative character and is integrated with the Stratonovich convention. Taking the time derivative of Eq. (5.1a) and defining $\mathbf{v}_i = \dot{\mathbf{x}}_i$, we get:

$$d\mathbf{v}_i = -\frac{1}{\gamma} \sum_j \nabla_i \nabla_j U_{tot} \cdot \mathbf{v}_j dt + v_0 d\mathbf{n}_i. \quad (5.38)$$

In order to compute the variation $d\mathbf{n}_i$ we switch to Ito calculus and find after some standard manipulations:

$$d\mathbf{n}_i = \sqrt{2D_r} \boldsymbol{\xi}_i dt \times \mathbf{n}_i - D_r \mathbf{n}_i dt, \quad (5.39)$$

where by $\boldsymbol{\xi}_i dt$ we denote the Wiener process $d\mathbf{W}_i = \boldsymbol{\xi}_i dt$. Putting Eq.(5.39) into Eq. (5.38), we obtain:

$$d\mathbf{v}_i = -\frac{1}{\gamma} \sum_j \nabla_i \nabla_j U_{tot} \cdot \mathbf{v}_j dt - D_r v_0 \mathbf{n}_i dt + v_0 \sqrt{2D_r} \boldsymbol{\xi}_i dt \times \mathbf{n}_i.$$

Finally, using Eq. 5.1a, we get:

$$\frac{\gamma}{D_r} d\mathbf{v}_i = -\gamma \mathbf{v}_i dt - \frac{1}{D_r} \sum_j \nabla_i \nabla_j U_{tot} \cdot \mathbf{v}_j dt - \nabla_i U_{tot} dt + v_0 \sqrt{2\frac{\gamma^2}{D_r}} \boldsymbol{\xi}_i dt \times \mathbf{n}_i.$$

Considering the definition of the matrix $\boldsymbol{\Gamma}$ given by Eq. (5.6), we obtain Eq. (5.5).

5.C Effective equations in the cluster: derivation of Eq.(5.13) and Eq.(5.15)

Let us start from Eq. (5.5) for a system of particles placed on a perfect hexagon, as in the bulk of the cluster. A target particle interacts only with its six neighbors at distance $\bar{r} < \sigma$ due to the nature of the potential that cuts off the interactions with particles located at distances larger than σ . By

symmetry, in Eq. (5.5) the external force contribution, \mathbf{F}_i , on the target particle, turns out to be zero and the only contribution to the dynamics comes from the noise source and from the velocities-dependent terms, $\sum_j \mathbf{\Gamma}_{ij} \cdot \mathbf{v}_j$, which explicitly read:

$$\begin{aligned} \sum_j \mathbf{\Gamma}_{ij} \cdot \mathbf{v}_j &= \sum_j \mathbf{v}_j \cdot \left[\mathcal{I} + \frac{\gamma}{D_r} \nabla_i \nabla_j U_{tot} \right] \\ &= \mathbf{v}_i + \frac{\gamma}{D_r} \sum_{j=1}^6 \mathbf{v}_i \cdot \nabla_i \nabla_i U(r_{ij}) + \frac{\gamma}{D_r} \sum_{j=1}^6 \mathbf{v}_j \cdot \nabla_i \nabla_j U(r_{ij}), \end{aligned} \quad (5.40)$$

being r_{ij} the distance between the i -th and j -th particle. The last two terms of Eq. (5.40) can be explicitly evaluated by considering the derivative with respect to the spatial components denoted by Greek upper indices:

$$\nabla_i^\alpha \nabla_i^\beta U(r_{ij}) = \left[U''(r_{ij}) + \frac{U'(r_{ij})}{|r_{ij}|} \right] \frac{r_{ij}^\alpha r_{ij}^\beta}{|r_{ij}|^2} - \delta_{\alpha\beta} \frac{U'(r_{ij})}{|r_{ij}|}, \quad (5.41)$$

being $r_{ij}^\alpha = r_i^\alpha - r_j^\alpha$, with $\alpha = x, y$. Denoting with δ_j the angle formed (with respect to the x -axis) between the j -th and the i -th particle, we can note that $r_{ij}^\alpha/|r_{ij}|$ reads $\cos(\delta_j)$ and $\sin(\delta_j)$ for $\alpha = x, y$, respectively. Since particles belong to a perfect hexagon we can express the angle as a function of j in such a way that $\delta_j = \delta_0 + j\pi/3$. The orientation of the hexagon with respect to the reference frame is fixed by the angle δ_0 , which we set to zero for the sake of simplicity. Writing Eq. (5.41) in terms of trigonometric function we get the matrix elements of Eq. (5.6). Since the potential depends only on the inter-particle distance the following property holds:

$$\nabla_i^\alpha \nabla_j^\beta U = -\nabla_i^\alpha \nabla_i^\beta U, \quad (5.42)$$

and we can easily find Eq. (5.13), assuming that $r_{ij} = \bar{r}$, for every j , and defining the element of H_j from Eq (5.41).

The derivation of Eq.(5.15) comes directly from Eq. (5.13), in particular, by separating the force $\propto \mathbf{v}$ from the one $\propto \mathbf{v}_j$. We observe that the sum over j of the matrix element of \hat{H}_j gives rise to a very simple shape in the hexagonal configuration:

$$\sum_{j=1}^6 \hat{H}_j = 3 \left(U'' + \frac{U'}{\bar{r}} \right) \mathcal{I} \equiv \hat{J}. \quad (5.43)$$

Such a simplification comes from the following properties holding in general for every δ_0 :

$$\sum_{j=1}^6 \cos^2 \left(\delta_0 + \frac{j\pi}{3} \right) = \sum_{j=1}^6 \sin^2 \left(\delta_0 + \frac{j\pi}{3} \right) = 3, \quad (5.44)$$

$$\sum_{j=1}^6 \cos \left(\delta_0 + \frac{j\pi}{3} \right) \sin \left(\delta_0 + \frac{j\pi}{3} \right) = 0. \quad (5.45)$$

Finally, adding and subtracting $J \cdot \mathbf{v}^*$, being $\mathbf{v}^* = \sum_{j=1}^6 \mathbf{v}_j$, we obtain Eq. (5.15).

5.D Forces contributions in the aligned and vortex domains

In this Section, we calculate the velocity-dependent force on a target particle due to the six surrounding particles having velocities, \mathbf{v}_j , with $j = 1, \dots, 6$. We recall that the particle with $j = 1$ is placed on the x direction at coordinates $(\bar{r}, 0)$. The others are placed sequentially in the anti-clockwise sense at reciprocal angular distance $\pi/3$ and at distance \bar{r} from the origin of the reference frame. We check that in the ideal cases of aligned domains and vortex-like structures the only relevant force contribution in Eq. (5.15) is the alignment term, $\propto \hat{J} \cdot (\mathbf{v} - \mathbf{v}^*)$, while the other forces vanish or are irrelevant. Let us start from Eq. (5.15), which we rewrite below, for completeness:

$$\mu \dot{\mathbf{v}} = -\frac{1}{D_r} \hat{J} \cdot (\mathbf{v} - \mathbf{v}^*) + \frac{1}{D_r} \sum_{j=1}^6 (\hat{H}_j - \frac{\hat{J}}{6}) \cdot \mathbf{v}_j - \gamma \mathbf{v} + \sqrt{2\gamma(\mu v_0^2)} \boldsymbol{\xi} \times \mathbf{n}, \quad (5.46)$$

The last two terms of the right-hand side of Eq. (5.46) are irrelevant in the large persistence regime, where D_r is small. Instead, the second addend of the right-hand side of Eq. (5.46) needs to be computed:

$$\mathbf{T} \equiv \frac{1}{D_r} \sum_{j=1}^6 (\hat{H}_j - \frac{\hat{J}}{6}) \cdot \mathbf{v}_j. \quad (5.47)$$

By symmetry, the contributions on \mathbf{T} due to the particles placed at the opposite vertices of the hexagon are equal. Thus, in our notation, we have $H_1 = H_4$, $H_2 = H_5$ and $H_3 = H_6$. Below, we write explicitly each term:

$$\hat{H}_1 - \frac{\hat{J}}{6} = \hat{H}_4 - \frac{\hat{J}}{6} = (U''(\bar{r}) - \frac{U'(\bar{r})}{\bar{r}}) \begin{pmatrix} -\frac{1}{4} & \frac{\sqrt{3}}{4} \\ \frac{\sqrt{3}}{4} & \frac{1}{4} \end{pmatrix}, \quad (5.48)$$

$$\hat{H}_2 - \frac{\hat{J}}{6} = \hat{H}_5 - \frac{\hat{J}}{6} = (U''(\bar{r}) - \frac{U'(\bar{r})}{\bar{r}}) \begin{pmatrix} -\frac{1}{4} & -\frac{\sqrt{3}}{4} \\ -\frac{\sqrt{3}}{4} & \frac{1}{4} \end{pmatrix}, \quad (5.49)$$

$$\hat{H}_3 - \frac{\hat{J}}{6} = \hat{H}_6 - \frac{\hat{J}}{6} = (U''(\bar{r}) - \frac{U'(\bar{r})}{\bar{r}}) \begin{pmatrix} \frac{1}{2} & 0 \\ 0 & -\frac{1}{2} \end{pmatrix}. \quad (5.50)$$

Using the above expressions for H_j we get:

$$T_x = \frac{1}{4D_r} \left(U''(\bar{r}) - \frac{U'(\bar{r})}{\bar{r}} \right) \left(2v_{6x} + 2v_{3x} - v_{1x} - v_{2x} \right. \\ \left. - v_{4x} - v_{5x} + \sqrt{3}(v_{1y} + v_{4y} - v_{2y} - v_{5y}) \right), \quad (5.51)$$

$$T_y = -\frac{1}{4D_r} \left(U''(\bar{r}) - \frac{U'(\bar{r})}{\bar{r}} \right) \left(2v_{6y} + 2v_{3y} - v_{1y} - v_{2y} \right. \\ \left. - v_{4y} - v_{5y} + \sqrt{3}(v_{1x} + v_{4x} - v_{2x} - v_{5x}) \right). \quad (5.52)$$

Both components of the force vanish in the following cases: i) when all velocities are identical, i.e. in the case of aligned domains. ii) When the velocities of the six neighboring particles are arranged in a vortex configuration, for instance, described by the following velocity profile:

$$\mathbf{v}_j = v_0(-\sin(j\pi/3), \cos(j\pi/3)). \quad (5.53)$$

In this last case, the corresponding average velocity vanishes, i.e. $\mathbf{v}^* = 0$.

Chapter 6

Motility Induced Phase Separation

Several living organisms prefer organizing in cohesive and stable structures instead of spending their life as single, independent unities [21]. Cooperation is recognized to be an important ingredient in species evolution, a typical feature of some living organisms occurring both at macroscopic and mesoscopic length scales.

Several animals move coherently in ordered structures, manifesting intriguing and variegated collective phenomena, which recently has attracted the attention of the Statistical Physics community. School of fishes [270] and birds [271] or insects [272] usually arrange in complex three-dimensional space structures displaying fascinating collective behaviors such as flocking [271, 273] and swarming [274]. To describe such complex dynamics a particularly successful model has been introduced by Vicsek in 1995 in the framework of non-equilibrium stochastic processes with effective interactions [257]. Vicsek-like models consist of constant-speed point particles that locally align their velocities, through a short-range force in competition with noise. The dynamics manifests long-range polar order [255] and a coexistence phase made of quantized traveling bands [256, 275]. More refined modelizations [276, 277] are able to account for the propagation of the information in real flocks of birds [278], showing a fair agreement with experimental data.

Recently, large attention has been dedicated to systems at mesoscopic length scales, principally micro-organisms coming from biology and microbiology [20]. Bacterial colonies [279], such as *E. Coli* [16] among the others, shows the emergence of intriguing pattern, while cluster formation is also observed for *Myxococcus xanthus* [280] or *Thiovulum majus* [281]. The study of Bacteria colonies in vitro has a very important role in several areas of medical and pharmaceutical sciences, being for instance at the basis of histological cultures to detect and identify bacterial infections in tissues. Understanding their aggregation and the growth of their colonies is particularly important for medical applications. We also mention some species of

motile cells, which lives in aquatic habitats, such as *Heterosigma akashiwo* or *Chlamydomonas reinhardtii* [138], as other examples of microswimmers showing the formations of stable clusters. Besides, several colloidal particles have been activated [282] using external fields, lights [48], or by chemical reactions occurring on the colloidal surfaces. We mention self-phoretic artificial spherical microswimmers, the so-called Janus particles [283, 284, 110]. These last examples are particularly interesting for the current study, being the experimental specimens nearer to the models adopted along with this thesis. Thus, their phenomenology will receive much attention in Sec.6.1. We remark that the occurrence of stable, artificial clusters and even stable chain or vortices [285] offers an interesting challenge in the formation of new materials.

Even if the microscopic details of each microswimmer differs case by case, a common coarse-grained feature of such systems manifests in the formation of clusters at moderate concentrations and, even, in phase-separation: a dense large cluster coexists with a dilute phase. Finding minimal models to reproduce and shedding light on the rich phenomenology observed in these new class of systems has been a key point in active matter research. Among the others, ABP (and so AOUP) dynamics [19, 17, 20] has played an important role in the understanding of such a phenomenology, in the framework of non-equilibrium stochastic processes. This point will be further investigated in Sec.6.2. We just anticipate that the interplay between steric interactions and self-propulsion produces clustering and phase-separation [286]. Such a phenomenon, often know as Motility Induced Phase Separation (MIPS) has been largely investigated [287], starting from the pioneering work of C. Marchetti [69]. The use of different pure-repulsive interaction potentials [247, 288, 286, 251, 101], even in the presence of attractive components [289], have revealed the robustness of the mechanism, which is only quantitatively affected by the microscopic details of the system.

Recent studies have been often focused on the consequences of inertia [290], chirality [291, 292], hydrodynamic interactions [92, 293] or inter-particle torques [294], all ingredients of the dynamics which in general are responsible for the MIPS suppression. On the contrary, the presence of explicit alignment interactions seems to favors MIPS [295, 296, 297] and, recently, even the possibility of freezing a flock of particles has been explored [298]. The particle shape has been also considered and polar particles [299] have revealed the occurrence of a polarized phase, where clusters of aligned particles occur as the shape of the microswimmers becomes more elongated [299]. In the same spirit, MIPS transition has been investigated for complex structures such as active molecules [300], dumbbells [252, 301], actived semi-flexible [302] or flexible filaments[303] or simply self-propelled polymers [304, 305], modeling, for instance, actin filaments and fluorescently labelled reporter filaments that are propelled by motor proteins [306] or microtubules propelled by surface-bound dyneins [307].

Even if some features of the dynamics could affect some details of the

phase separation, often rather important, the common denominator of the transition cannot be ignored. In general, the complexity of the models, often adapted to the specific systems under investigation, does not change the qualitative picture behind the cluster formations or MIPS, whose leading mechanism even in the simpler case of spherical particles is still an open issue. Some authors studied equilibrium-like approaches in terms of effective interactions with the occurrence of an attractive components between particles [90, 308], developed an effective free-energy functional [62, 68, 309] using the well-known bifurcation theory to predict the stability of the two coexisting phases [310, 107] or studied an Effective Cahn-Hilliard equation for self-propelled particles [311]. Anyway, such strategies are not able to capture the rich non-equilibrium phenomenology behind the phase separation and even if such results sound particularly interesting some very important aspects of MIPS are clearly missed at this level. Observables as pressure [106, 107] or interfacial tension between the two coexisting phases [312, 313] cannot be not consistent with any equilibrium-like scenario. Moreover, a recent study even revealed the presence of two different temperatures inside and outside the cluster, even for simple spherical ABP particles [290] or the occurrence of un-expected hexatic phases [254] in two dimensions. In particular, the failure of any equilibrium-like approaches to generalize standard concepts of thermodynamics comes directly from the intrinsic non-equilibrium feature of the dynamics. With this idea, the MIPS transition has been studied with coarse-grained models in the framework of a scalar field theory approach [314, 315, 316, 317, 318] and a fundamental role in the phase separation has been connected to the violation of the Detailed Balance.

The emergence and the understanding of non-equilibrium collective behaviors are currently an open issue, even for very simplified dynamics and a general thermodynamics theory for such biological microswimmers is under development but is quite far from a full comprehension. Indeed, the adaptation of usual thermodynamics concepts often lacks consistency and the need for going beyond the well-known notions coming from Equilibrium Statistical Mechanics appears to be evident.

Up to now, Vicsek-like and self-propelled models are considered two distinct pillars in the modelizations of active matter systems. The former employs an explicit alignment interaction among the orientations of the microswimmers and is commonly employed to model systems which exhibit flocking or swarming. The latter does not involve any explicit alignment forces and, thus, any form of velocity order is not expected. In this Chapter, we change this a widespread idea. Also in self-propelled particles, an effective alignment force, with a Vicksek-like form, is induced by the interplay between steric interactions and self-propulsion, even if the system does not show a global polarization. Particles' velocities align in oriented domains, featuring coherent structures with aligned or vortex-like velocities. In particular, we unveil the hindered structure of MIPS, showing that the

phase-separation occurs together with a new long-range order in the orientations of the velocities triggered by active forces. As a consequence, the MIPS transition cannot be simply studied in terms of a scalar field, the density, but the presence of an additional field, taking into account the collective orientation of the velocities, is needed to describing MIPS even at the lower coarse-grained level.

The Chapter is structured as follows: In Sec.6.1, we briefly describe some experiments about clustering or phase separation, mostly obtained for spherical artificial microswimmers. In Sec.6.2, after the introduction of ABP and AOUP interacting dynamics, we describe the MIPS transition, while, in Sec.6.3, we briefly review existing theories (mostly focused on equilibrium approaches) to explain MIPS. Then, Sec.6.4 contains our first original contribution of this chapter: exploring MIPS in the large persistence regime gives rise to some novelties, which we denote as “dynamical MIPS”. In Sec.6.5, we show the occurrence of the new long-range order (already found in Chapter 5 at higher densities) in the alignment of the velocities occurring in concomitance with the phase-separation. Instead, Sec.6.6 is devoted to the theoretical study of the dilute regime outside the cluster. Finally, we report a discussion in the conclusive section.

6.1 Experimental evidence of clustering

The aggregation in large clusters at moderate packing fraction in absence of explicit alignment - and eventually phase-separation - is the leading feature of any specimens known as self-propelled microswimmers. This behavior, manifests both in biological entities, such as cells or bacteria, both in artificial microswimmers. The microscopic details of the systems do not change the qualitative clustering picture and, in many cases, affect just marginally - often just quantitatively - such a phenomenon.

In the case of artificial microswimmers, experimental evidence of clustering was obtained using Janus Particles, where chemical reactions create self-phoretic local chemical motors due to the combined effect of diffusiophoresis and self-electrophoresis. For instance, in the experiments of Theurkauff et. al. [319, 320] and the recent experiment of Ginot et. al. [284], gold colloids half-coated with Platinum, immersed in hydrogen peroxide solutions, were studied. They showed the occurrence of cohesive and stable clusters starting from area fractions within the range 5 – 10%. This class of microswimmers degrades in passive suspensions where the molecular solute is consumed. To overwhelm this problem, suspension of carbon-coated colloidal Janus particles dispersed in a near-critical mixture of water and lutidine [283, 282] has been investigated. Here, self-propulsion is induced by illuminating the whole sample with a laser beam. Also in this case, clustering occurs at rather low values of area fraction and, additionally, the first evidence of phase separation takes place. Alternatively, synthetic photoactivated colloidal particles

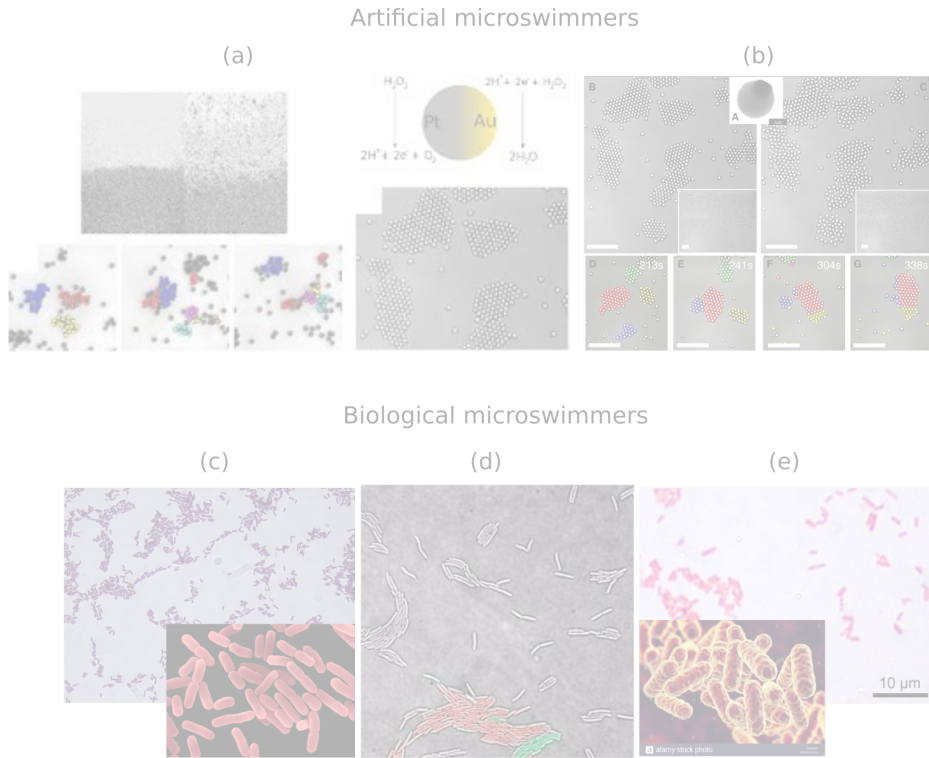


Figure 6.1: Panel (a) shows snapshots of experiments performed with a suspension of gold Janus particles half-coated with Platinum immersed in hydrogen peroxide, while panel (b) displays the same scenario for photo-activated colloidal particles with an embedded hematite cube immersed in basic solutions. Panel (c), (d) and (e) reported experimental samples of *Bacillus subtilis*, *Myxobacteria* and *Serratia marcescens* cells, respectively.

(in particular, colloids with an embedded hematite cube immersed in basic solutions) have been studied [48]. In this case, organized almost-crystallite structures are formed under illumination starting from packings $\gtrsim 10\%$. These clusters are not static, translating and rotating, and even splitting and joining, and for these features were named “living crystals”. This class of systems does not show phase separation since a single stable cluster does not form.

Other important evidence for clustering and, eventually, phase separation appears in the framework of biological specimens. In general, biological experiments involve more complex phenomena, since typically particles have elongated or even deformable shapes. Bacteria or cells could die or reproduce and generally interact through more complex mechanisms with respect to artificial microswimmers. For instance, hydrodynamic interactions often play an important role and several bacteria interact using quorum sensing mechanisms [321]. Anyway, even, fast-moving bacteria self-organize into two-dimensional clusters, as in the case of *Serratia marcescens* cells near an air-liquid interface [322]. Anyway, depending on the specimens, the dynam-

ics of these structures could show interesting behaviors: these clusters could rotate [281] in the case of *Thiovulum majus*, for instance. The large part of experiments has been realized with rod-shaped bacteria, such as *E.Coli*, myxobacteria or *Bacillus subtilis*. The latter exhibit giant density fluctuations [323] and scale-invariant clusters [324] Instead, myxobacteria shows a scale-free size distribution [280].

These are only a few examples of artificial or living microorganisms giving rise to cluster formation and, sometimes, phase separation. Samples of these active matter specimens are reported in Fig.6.1, where direct images show the phenomenology described in this Section. We remark that, in several cases, the crossover from clustering and phase-separation (MIPS) is not so clear.

6.2 Minimal microscopic models for MIPS

Phase-separation or clustering represents the typical feature of interacting self-propelled particles, common to a large class of both artificial and biological microswimmers, as described in Sec.6.1. Despite the specific physical or chemical mechanisms involved in the self-propulsion could affect the microscopic details of the cluster formation, the identification of minimal ingredients in the microscopic dynamics to reproduce such a phenomenon has attracted the active matter community, in the last years.

First dynamics reproducing such behavior appeared in the framework of bacteria, such as *E.Coli*, described by Run&Tumble models [325, 326]. A coarse-grained theory with density-dependent swim velocities (or equivalently density-dependent effective diffusion coefficients) have been derived and used to numerically and theoretically explore clustering or phase separation [62, 68, 287].

Then, in 2012, the pioneering work of C.M. Marchetti and Y. Fily [69] reproduced MIPS employing ABP particles with pure repulsive forces in the absence of any alignment interactions. Successive works reveal such a phenomenology for a large class of interacting potentials [289, 251, 327], confirming the leading mechanism behind phase-separation: the interplay between random persistence forces and steric interactions produces the particles' slow down which, at large enough packing fraction, leads to MIPS. As already mentioned in the introduction, MIPS could be enhanced or suppressed by other microscopic ingredients of the dynamics - chirality, hydrodynamic interactions, aligning forces, inertia, polar shapes, etc.. They are not fundamental for the MIPS-transition and could be considered as irrelevant details in its explanation.

Following the existing literature - in particular, [288] -, in this Section, we numerically study a suspension of self-propelled interacting particles in a square box of size L with periodic boundary conditions, setting the same computational setup of Chapter5. Here, we explore smaller packing fraction

regimes with respect to Sec.5.2, using the same interacting potential:

$$U_{tot} = \sum_{i < j} U(r_{ij}),$$

where r_{ij} is the distance between particle i and particle j and $U(r)$ has the WCA shape:

$$U(r) = \begin{cases} 4\epsilon \left[\left(\frac{\sigma}{r}\right)^{12} - \left(\frac{\sigma}{r}\right)^6 \right] + \epsilon, & \text{for } r \leq 2^{1/6}\sigma, \\ 0, & \text{for } r > 2^{1/6}\sigma. \end{cases} \quad (6.1)$$

As already discussed in Sec.5.1, σ represents the nominal particle diameter and ϵ the energy scale of the potential, which models steric interactions between particles. As largely discussed along with this thesis, the self-propulsion force follows the ABP or AOUP dynamics, given by Eq.(1.3) or Eq.(1.5), respectively, while the dynamics of the particle center of mass, \mathbf{x}_i , is ruled by Eq.(5.1). To be specific, the dynamics reads:

$$\gamma \dot{\mathbf{x}}_i = \mathbf{F}_i + \mathbf{f}_i^a, \quad (6.2)$$

where $\mathbf{F}_i = -\nabla U_{tot}$ and \mathbf{f}_i^a is the self-propulsion force which is given by

$$\mathbf{f}_i^a = \gamma U_0 \mathbf{n}_i \quad (6.3)$$

$$\dot{\mathbf{n}}_i = \sqrt{2D_r} \mathbf{n}_i \times \boldsymbol{\xi}, \quad (6.4)$$

for the ABP, while it evolves as a vectorial Ornstein-Uhlenbeck process in the AOUP case:

$$\tau \dot{\mathbf{f}}_i^a = -\mathbf{f}_i^a + \gamma \sqrt{2D_a} \boldsymbol{\xi}_i. \quad (6.5)$$

A detail discussion about the two different dynamics to model the self-propulsion force is given in Chapter1. Here, we skip the model description, recalling only the relations between the control parameters of the two dynamics, which will be always assumed along with the rest of the chapter. In particular, the ABP dynamics is fairly approximated by the AOUP one if $D_r = 1/\tau$ and $v_0^2/2 = D_a/\tau$.

In the same way of Chapter 5, we describe dynamics directly in terms of the microswimmers' velocities, $\dot{\mathbf{x}}_i = \mathbf{v}_i$. For completeness, we report the dynamics of \mathbf{v}_i derived in Appendix 5.B, which has the same structure for AOUP and ABP dynamics:

$$\dot{\mathbf{v}}_i = -D_r \sum_{j=1}^N \Gamma_{ij}(\mathbf{r}_{ij}) \mathbf{v}_j + D_r \frac{\mathbf{F}_i}{\gamma} + \mathbf{k}_i. \quad (6.6)$$

The difference between the two dynamics is embodied in the noise term \mathbf{k}_i , which is a Gaussian white noise vector with independent components and

variances $2D_a/\tau^2$ in the AOUP case, while it is a multiplicative noise vector for the ABP self-propulsion, which reads:

$$\mathbf{k}_i = v_0 \sqrt{2D_r} \boldsymbol{\xi}_i \times \frac{\gamma \mathbf{v}_i - \mathbf{F}_i}{\gamma}. \quad (6.7)$$

Besides, we remark the absence of any kind of attracting forces in the equation of motion and the absence of explicit alignment interactions in the dynamics of each self-propulsion which evolves independently of each other.

6.2.1 Qualitative picture: cluster formation and dilute phase

In the numerical study of the dynamics (6.2), we fix the packing fraction at the value $\phi = N/L^2\pi\sigma^2/4 = 0.65$, i.e. in a smaller regime with respect to Chapter 5. At this value of ϕ , a passive Brownian suspension of interacting particles - with the same packing fraction and repulsive interactions - arranges into a homogeneous phase with the typical internal structure of a liquid - characterized by more than one peak in the shape of the $g(r)$, for instance (depending on the temperature value).

As already explained in Chapter 2, the small persistent regime with $\nu \lesssim 1$ (small τ) shows a passive Brownian-like phenomenology, where the active force behaves as an effective temperature with amplitude $\gamma D_a = \gamma U_0^2 D_r / 2$. In this regime, the non-equilibrium features of active systems do not emerge and the increasing of the persistence time leads only to the fluidization of the structure because of the temperature increase.

Interesting novelties appear even in the regime of moderate large persistence with $\nu \approx 1$ ($\tau \approx 1$). In this regime, strong non-equilibrium phenomenologies have been revealed also in Chapter 5 in denser regimes, where empty regions form and travel along with the whole box, breaking the homogeneity of the system. In Sec.5.2, it has been shown that their sizes grow as ϕ is decreased. Instead, in the regime of ϕ discussed in this Chapter, a “real” phase-separation occurs: starting from a homogeneous configuration with U_0 large (with respect to the inter-particles interactions) and D_r small (in such a way that $\nu \lesssim 1$), particles spontaneously form a very dense cluster at effective packing fractions larger than ϕ . When the nucleation process is completed, a stable large cluster coexists with a dilute phase with packing smaller than ϕ . Such a non-equilibrium phase separation, obtained even in the absence of any attracting interactions, is commonly known as Motility Induced Phase Separation (MIPS). The large cluster reaches a typical size and population determined by the parameters of the active force and the packing fraction: from one hand, a larger U_0 determines more packed clusters, while larger τ increases the average cluster population. The latter effect is also induced by the growth of ϕ .

Particles inside the cluster display a hexagonal structure [288] with typical distances between neighboring particles $\bar{r} < \sigma$, i.e. smaller than the non-

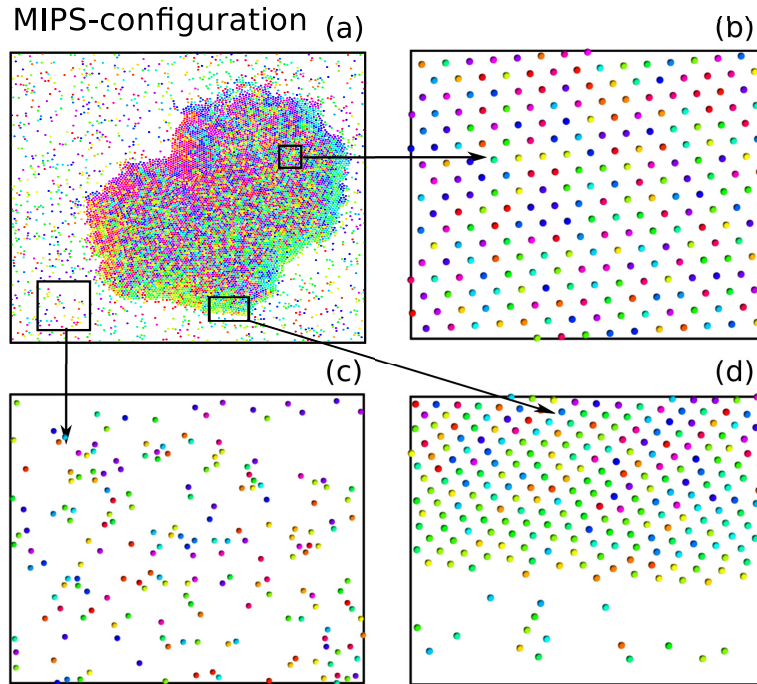


Figure 6.2: In panel (a) we show a typical snapshot configuration displaying the MIPS transition. The simulation is realized with $U_0 = 50$, $D_r = 0.5$, $\phi = 0.65$, in square box of size $L = 125$. Particles interact by means of the potential described in the text. Panel (b), (c) and (d) enlarges small regions inside the cluster, on its boundary and in the dilute phase. Colors encode the orientations of the self-propulsion.

inal particles' diameter [77]. As a consequence, microswimmers are partially overlapped attaining stationary configurations with larger potential energies: at variance with any form of passive Brownian suspensions, self-propelled entities climb on the potential in analogy with the dynamics confined by convex external traps. Each self-propulsion force, \mathbf{f}_i^a , points randomly both inside and outside the cluster, being their dynamics independent. While, in the dilute regime, \mathbf{f}_i^a roughly determines the velocity of each particle, this is no longer true in the packed regime. Indeed, inside the cluster, active microswimmers have typical velocities slower and slower than self-propelled entities in the dilute phase. Again, such a phenomenology is consistent with the confined dynamics, studied in Chapter 2: there, the slow down is induced by the interplay between self-propulsion and external force, featuring in a space-dependent Stokes force. Here, a similar mechanism occurs, this time, due to the interplay between convex inter-particle interactions and active forces, even if the modulus (or its average) of \mathbf{f}_i^a is fixed to U_0 .

Besides, it is worthy to spend some words about the cluster boundary. in spite of the average cluster stability, particles leave and join the cluster continuously in time: in the steady-state, the inner flux of particles inside

the cluster is compensated by the exit flux, a condition which guarantees the saturation of the cluster population except for fluctuations. The shape of the boundaries will be further investigated in Sec.6.4.

Such a scenario displays some analogies to the phase-separation of passive Brownian particles in the presence of attractive interactions (Lennard Jones potentials, for instance), even if there is no way to find the same phenomenology with purely repulsive interactions. Such an observation has led to the generalization of existing equilibrium theories to such a class of non-equilibrium systems. Some of these approaches will be reviewed in Sec.6.3.

Packing fraction distributions

As a criterion to determine the occurrence of a phase-separation [288], we study the distribution of $\hat{\phi}$, the effective packing fraction of the whole self-propulsive system, namely $\mathcal{P}(\hat{\phi})$. Before MIPS, when the system is almost-homogeneous, $\mathcal{P}(\hat{\phi})$ has a unimodal shape: roughly a Gaussian-like distribution around the nominal packing fraction $\phi = N/L^2\pi\sigma^2/4$, consistently with a Brownian suspension of particles. In this case, its average value ($\langle\hat{\phi}\rangle \approx \phi$) corresponds to a measure of the system packing. Instead, when a dense cluster forms, $\mathcal{P}(\hat{\phi})$ is a bimodal function of $\hat{\phi}$, with a first peak for $\hat{\phi} < \phi$ and a second peak for $\hat{\phi} > \phi$. The former quantifies the effective packing fraction of the dilute phase while the latter the effective packing of the dense cluster. In this case, $\mathcal{P}(\hat{\phi})$ roughly results from the superposition of two Gaussians. Their averages (or quite equivalently their peak positions) will be denoted as ϕ_g and ϕ_c , respectively. We remark that around a very small region before the “critical” $\hat{\phi}$, the distribution $\mathcal{P}(\hat{\phi})$ is still unimodal but larger differences from a Gaussian-like shape occurs.

Following [288], two cases could occur: i) for smaller values of ϕ , ϕ_g increases following almost-continuously ϕ , while ϕ_c is discontinuous. ii) for larger values of ϕ , the opposite situation occurs. Our choice, $\phi = 0.65$, restrict to the case i).

6.3 Effective equilibrium theories for MIPS

The theoretical explanation of MIPS starting from some simplified dynamics has attracted the attention of the active matter community in the last years. First existing theories have been formulated starting from Run&Tumble dynamics by M. E. Cates and J. Tailleur [62, 68]. Their strategy consists in a hydrodynamic-like approach for self-propelled particles, finding coupled equations for the density field, $\rho(\mathbf{x})$, and the polarization field, $\mathbf{p}(\mathbf{x})$, closed under suitable approximations. Denoting as $\Psi(\mathbf{x}, \theta)$ the probability of finding a particle at position \mathbf{x} with self-propulsion orientation θ , we can write the Ψ evolution in the absence of interactions:

$$\partial_t \Psi = -\nabla \cdot [U_0 \mathbf{n} \Psi] + \nabla_\theta [D_r \nabla_\theta \Psi] + \nabla (D_t \nabla \Psi) . \quad (6.8)$$

Following [62], we have assumed that U_0 , D_r and D_t could depend on \mathbf{x} but not on \mathbf{n} , even if they are constant coefficients for ABP particles. Such a dependence will be a key point to generalize the theory to interacting systems. Then, we have assumed $\gamma = 1$, for the sake of simplicity. To proceed further, we introduce the density field:

$$\rho(\mathbf{x}, t) = \int_0^{2\pi} d\theta \Psi(\mathbf{x}, \theta, t), \quad (6.9)$$

the orientational field

$$\mathbf{p}(\mathbf{x}, t) = \int_0^{2\pi} d\theta \mathbf{n} \Psi(\mathbf{x}, \theta, t) \quad (6.10)$$

and the orientational tensor \mathbf{Q} :

$$\mathbf{Q}(\mathbf{x}, t) = \int_0^{2\pi} d\theta \mathbf{n} \Psi(\mathbf{x}, \theta, t) \mathbf{n}. \quad (6.11)$$

Then, we decompose Ψ in the first components of the basis of spherical harmonics defined by ρ , \mathbf{p} and \mathbf{Q} , obtaining:

$$\Psi = \rho + \mathbf{p} \cdot \mathbf{n} + \mathbf{Q} : (\mathbf{n} \mathbf{n} - \mathcal{I}/2) + \dots \quad (6.12)$$

where we have neglected higher harmonic components. Projecting on the above basis we can obtain a set of coupled hydrodynamic equations, i.e. an infinite hierarchy. In particular, integrating Eq.(6.8) over θ , we get:

$$\dot{\rho} = -\frac{1}{2} \nabla \cdot (U_0 \mathbf{n}) + \nabla \cdot (D_t \nabla \rho), \quad (6.13)$$

while multiplying Eq.(6.8) by \mathbf{n} and integrating, we get equations for each component of \mathbf{p} (not reported) In the same way, we can derive the equation for each component of \mathbf{Q} . More details are contained in [68]. It is straightforward to see that ρ is the only slow mode, while higher-order harmonics relax faster as a result of a gradient expansion [62]. Thus, assuming that $\dot{\mathbf{p}} = 0$ and $\dot{\mathbf{Q}} = 0$, two constitutive equations arise. In particular, \mathbf{p} reads:

$$\mathbf{p} = -\frac{1}{D_r} \nabla (U_0 \rho) + O(\nabla^2), \quad (6.14)$$

so that Eq.(6.13) turns into:

$$\dot{\rho} = \nabla \cdot \left[\frac{U_0}{2D_r} \nabla (U_0 \rho) + D_t \nabla \rho \right], \quad (6.15)$$

which is a self-consistent equation for ρ . At this stage, the argument of [62] consists in assuming that the coefficient D_r , D_t and U_0 not only depends explicitly on x but rather explicitly on ρ itself. With a small notational

abuse, we replace $\rho \rightarrow \rho_i$ to deal with the density of a single particle and define the total density $\rho = \sum \rho_i = \sum \delta(\mathbf{x} - \mathbf{x}_i)$. Then, we suppose that the coefficients depends on ρ instead of ρ_i . Following standard procedures, rather technical, such as Ito rule, integrations by parts and the general identity $\dot{f}(\mathbf{x}_i) = \int d\mathbf{x}_i \rho_i(\mathbf{x}_i) f(\mathbf{x}_i)$, Eq.(6.15) can be recast into:

$$\dot{\rho}_i = -\nabla_i \cdot \left(\frac{U_0 \nabla_i U_0}{2D_r} \rho_i + \frac{U_0^2}{2D_r} \nabla_i \rho_i + \left(2 \frac{U_0^2}{2D_r} \rho_i \right)^{1/2} \lambda_i \right), \quad (6.16)$$

where λ_i is a white noise with unitary variance and zero average. We have also assumed $D_t = 0$, for the sake of simplicity (an assumption which is not required for the derivation). Summing over i , we obtain an equation for ρ :

$$\dot{\rho} = -\nabla \cdot \left(\mathbf{V}[\rho] \rho + \mathcal{D}[\rho] \nabla \rho + (2\mathcal{D}[\rho] \rho)^{1/2} \Lambda \right), \quad (6.17)$$

where Λ is a white noise vector and the two effective density-dependent coefficients read:

$$\mathbf{V} = \frac{U_0 \nabla_i U_0}{2D_r}, \quad \mathcal{D} = \frac{U_0^2}{2D_r}. \quad (6.18)$$

The expressions for \mathbf{V} and \mathcal{D} could be easily generalized to the case $D_t > 0$ and to the Run&Tumble dynamics. We point out that, even if the coarsening procedure is quite reasonable, this is not a derivation for ABP dynamics, for which even the assumptions of non-constant U_0 and D_r does not hold.

Eq.(6.17) is the main result of [62]. To predict MIPS further microscopic details are needed, i.e. the explicit dependence of \mathbf{V} and \mathcal{D} on ρ . Anyway, supposing that these coefficients decrease as ρ grows, is necessary to expect clustering or even phase separation. This requirement means that particles slow down when they are close.

6.3.1 Binodal decomposition: effective equilibrium approach

Following [62, 68, 287], Eq.(6.17) can be used as the starting point to build an equilibrium-like theory to “explain” the MIPS transition in terms of binodal decomposition. The many-body probability, $\mathcal{P}[\rho]$, associated to the dynamics (6.17), follows:

$$\frac{\partial \mathcal{P}}{\partial t} = \int d\mathbf{x} \frac{\delta}{\delta \rho} \nabla \cdot \left[\rho \mathbf{V} - \mathcal{D} \nabla \rho - \mathcal{D} \rho \nabla \frac{\delta}{\delta \rho} \right] \mathcal{P}, \quad (6.19)$$

where \mathbf{V} and \mathcal{D} are given by Eqs.(6.18) and, thus, are functional of ρ through the parameters of the self-propulsion. Assuming vanishing currents, i.e. the detailed balance condition, the steady-state distribution reads:

$$\mathcal{P} \propto e^{-\mathcal{F}[\rho]}, \quad (6.20)$$

where $\mathcal{F}[\rho]$ is a free-energy functional (and $f[\rho]$ its space density). In analogy with an equilibrium-like picture, these functionals are given by:

$$\mathcal{F}[\rho] = \int d\mathbf{x} \{ [\rho] = \mathcal{F}_{ex} + \int d\mathbf{x} \rho (\log \rho - 1) \}. \quad (6.21)$$

where the excess free-energy, \mathcal{F}_{ex} , satisfies the general relation:

$$\frac{\mathbf{V}[\rho]}{\mathcal{D}[\rho]} = -\nabla \frac{\mathcal{F}_{ex}[\rho]}{\delta \rho}. \quad (6.22)$$

Using the coefficients, \mathcal{D} and \mathbf{V} , we get:

$$\mathcal{F}_{ex} = \int d\mathbf{x} f_{ex}, \quad f_{ex} = \int_0^\rho ds \log U_0[s]. \quad (6.23)$$

upon assuming that $U_0[\rho, \mathbf{x}] = U_0[\rho]$. We obtain binodal conditions for phase coexistence by means of the usual tangent construction on the effective free-energy functional:

$$\frac{\delta^2 \mathcal{F}}{\delta^2 \rho} < 0. \quad (6.24)$$

Considering the shape of \mathcal{F} and differentiating two times respect to ρ , we get:

$$\frac{d^2 f}{d\rho^2} = \frac{1}{\rho} + \frac{d}{d\rho} \log U_0[\rho]. \quad (6.25)$$

Thus, the final condition for phase-separation in self-propelled systems is:

$$\frac{dU_0[\rho]}{d\rho} < -\frac{U_0[\rho]}{\rho}. \quad (6.26)$$

when $U_0[\rho]$ is the effective speed, coming from a coarsening. We remark that $U_0[\rho]$ is not the constant parameter of the ABP model, despite the abuse of notation. Even if such a theory has been revealed to be fairly in agreement with simulations, at least for moderate regimes of the active force parameters, the leading assumption behind such an approximation is the detailed balance which justifies the use of Eq.(6.22). This assumption is rather questionable for ABP or far-equilibrium systems in general.

For ABP particles, the dependence on ρ of the effective speed has been numerically calculated in [69], where a decreasing linear shape has been measured, at least, in the regime of parameters of their study. Such a profile satisfies the condition (6.26), and so, agrees with the occurrence of phase-separation. The functional form of the effective speed has been derived starting from the microscopic dynamics (from the Smoluchowski equation) upon some questionable assumptions[309]: for instance, that the system is homogeneous. The derivation is reported in Appendix 6.A and is the only existing connection between microscopic and coarse-grained approaches.

Effective interactions

In the framework of effective equilibrium theories, the authors of [90] approximate a system of self-propelled particles as a passive system with effective interactions. In particular, authors use the so-called Fox approximation [90], a phenomenological approximation which is connected (but not completely equivalent) to the UCNA [74]. Both approximations assume the validity of the detailed balance and embody the non-equilibrium feature of active systems into effective interactions. In the interacting case, such effective inter-particles forces have attractive components: the authors of [90] claim to explain MIPS, simply by performing such a mapping, since they can reproduce the internal structure of self-propelled particles, at least in the regime of parameters explored in their study.

6.3.2 Cahn-Hilliard equation

Recently, the key role of non-equilibrium in MIPS has been addressed by several authors [101, 328]. Even if effective-equilibrium theories are able to predict some aspects of MIPS (for instance the internal structure in the cluster phase, reproduced by the shape of the $g(r)$ [90]), the qualitative picture of equilibrium mapping is rather questionable and several aspects of the MIPS phenomenology cannot be reproduced.

Another approach, is represented by a coarse-grained theory which breaks “by hands” the Detailed Balance adding extra terms. Following [317, 286], Eq.(6.17), can be written formally as a Cahn-Hilliard equation:

$$\partial_t \rho = -\nabla \cdot \left[-\mathcal{M}[\rho] \nabla \mu_c + \sqrt{2\mathcal{M}[\rho]} \Lambda \right] \quad (6.27)$$

where $\mathcal{M}[\rho]$ is an effective mobility which is proportional to ρ and μ_c is the chemical potential which can be obtained from the functional differentiation of effective free-energy, \mathcal{F} . Λ is a noise vector such that its components satisfy $\langle \Lambda_i \mathbf{x}, t \Lambda_j(\mathbf{x}', t') \rangle = \delta_{ij} \delta(\mathbf{x} - \mathbf{x}') \delta(t - t')$, which is added to account for fluctuations.

Phase separation kinetics requires the presence of interface-like terms to stabilize the two phases. In analogy with the previous analysis, this is achieved assuming that U_0 is a function of $\tilde{\rho} = \rho + \gamma^2[\rho] \nabla^2 \rho$, where $\gamma[\rho] \propto U_0[\rho]$. Even if several arguments suggest that such a hypothesis is reasonable, the introduction of this term is quite ad hoc. The chemical potential, μ_c , reads:

$$\mu_c = \log \rho + \log U_0[\rho] - k[\rho] \nabla^2 \rho + O(\nabla^4 \rho), \quad (6.28)$$

where $k[\rho] \propto -v[\rho] \frac{dU_0}{d\rho}$. The interfacial term breaks the mapping to the “standard” Cahn-Hilliard equation since μ_c cannot be derived as a functional derivative of a free-energy functional. At variance with the effective free-energy approach, now, the detailed balance is broken by hands and the

non-equilibrium feature of such systems is included in the theory. Even if this approach explains MIPS, this coarse-grained phenomenological theory may appear quite artificial.

6.4 MIPS in the large persistence regime

In the existing literature [251, 329], several authors introduce the so-called Peclet number, Pe , to quantify the relevance of the active force and, thus, the non-equilibrium feature of the system. This dimensionless number is a combination of the active force parameters, thermal diffusion, and size of the particles. In particular, Pe is proportional to the persistence length U_0/D_r . With this prescription, it is possible to build a two-dimensional phase diagram in terms of Peclet number and packing fraction to detect the occurrence of MIPS. This assumes a U-shape [251, 286]. This analysis is performed in analogy with the well-know passive Brownian scenario, where, in the overdamped regime, temperature and packing fraction are the two leading parameters. Nevertheless, Eq.(6.6) shows that self-propelled suspensions are mapped into underdamped non-equilibrium dynamics, both for ABP and AOUP. Thus, the phase diagram of interacting self-propelled particles should involve three parameters: the persistence time, $1/D_r$, the strength of the self-propulsion, U_0 , and the packing fraction, ϕ . Such an observation is confirmed by a recent study in the framework of active glasses, at very high densities, where the phase diagram in term of τ and U_0 reveals the occurrence of very intriguing phases, for instance, the emergence of plastic turbulence, plastic yielding, an “intermittent” phase and even jamming, before the dynamically arrested phase [258]. This is a shred of evidence that two-dimensional space of the active parameters (U_0 and τ) cannot be reduced to a single one, $Pe \propto \sqrt{D_a \tau}$. The MIPS transition at moderate τ is well-studied, as described in Sec.6.2: a large fraction of particles, depending on ϕ and on τ , form a stable large cluster with a slow dynamics, while the remaining particles swim in the dilute phase, sometimes joining the cluster. The cluster boundary deforms even if its changes are very slow as slow is the particles’ motion inside the cluster.

In what follows, we study the motility Induced Phase Separation assuming the conditions of Sec.6.2 (we fix $U_0 = 50$ and $\phi = 0.65$ in the simulations) and increasing the persistence time, τ , until to reach a very large persistence regime to explore deep non-equilibrium dynamics. The consequences of the increase of τ are schematically illustrated in Fig.6.3, where five snapshot configurations are reported. In particular, under these conditions, MIPS occurs for $\tau \gtrsim 0.3$ and the increase of τ produces larger clusters up to $\tau \approx 5$. For larger τ , our numerical exploration reveals a new scenario in the current picture of MIPS: the cluster dynamics becomes faster and deeper deformations start to occur in its shape, as illustrated in the right panels of Fig.6.3. In this regime of τ , the cluster boundary deforms continuously

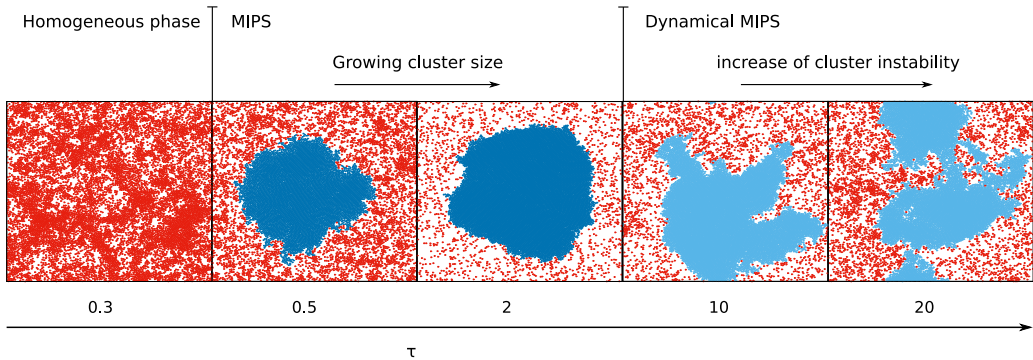


Figure 6.3: Snapshot configurations in the plane of motion for different values of $\tau = 0.3, 0.5, 2, 10, 20$ from the left to the right panel. Simulations are realized with $U_0 = 50$, $\phi = 0.65$ and the interacting potential described in the text.

in time, often producing a dynamical instability in its structure: during the perpetual deformations, the cluster could become non-convex and even separate in two (or more) small parts, which, successively could gather together to rejoin. Macroscopically, the cluster behaves as if was divided into several domains, whose average size roughly depends on τ . They move collectively and rearrange, producing deformations and reshapings.

Such a deep non-equilibrium regime suggests a scenario different from any equilibrium-like phase separation. Besides, in these regimes, even talking about “phase separation” is questionable. We propose to rename such a pure non-equilibrium state as “Dynamical MIPS”. The characterization of this phase, introducing a suitable order parameter, and its relation with U_0 and ϕ is a great deal, which will be further investigated in the future. The reason for which such a non-equilibrium phase has not observed or characterized, up to now, may have its origin in the protocol adopted to numerically explore MIPS, i.e. in the introduction of the Peclet number - i.e. in the projection of a two-dimensional space of parameters onto the curve $U_0/D_r = \text{const.}$

Besides, the whole equilibrium-like theoretical explanations, the binodal decomposition, for instance, is insufficient to fully understand the Dynamical MIPS presented here, where large currents are supposed to deform the main cluster. The presence of currents invalidates the detailed balance assumption preventing the possibility of introducing an equilibrium-like free-energy functional, as in the theoretical analysis reported in Sec.6.3.

We, also, mention recent studies performed at a higher coarse-grained level of description, in the framework of field theories for scalar active matter. An intriguing phase with several small clusters and a “bubbly phase”, i.e. a large cluster with moving empty regions, have been revealed [315, 318] using the Model B, for instance.

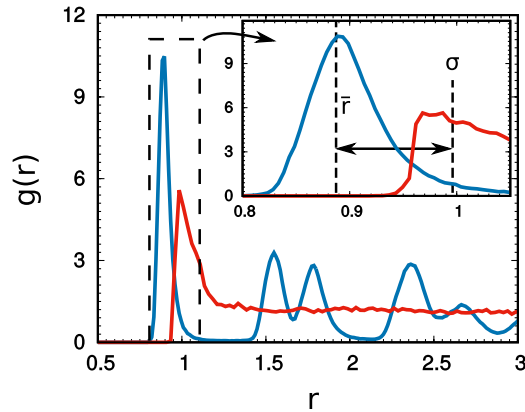


Figure 6.4: Pair correlation function, $g(r)$, inside (blue curve) and outside (red curve) the cluster for a system with $U_0 = 50$, $D_r = 0.4$ and the interaction potential defined along the text. The inset enlarges the region near the first peak to illustrate that $\bar{r} < \sigma$. Simulations are performed employing the ABP model.

6.4.1 Pair correlation function for self-propelled particles displaying MIPS

The pair correlation function, introduced in Appendix 5.A of Chapter 5, can be used to detect the internal structure of the system for different configurations of the control parameters and, in particular, the persistence time, $1/D_r = \tau$. In the homogenous phase, before MIPS occurs, the $g(r)$ can be evaluated within the whole box since the system is roughly translationally invariant. Instead, for D_r larger than the bifurcation point, it is convenient to evaluate separately the $g(r)$ inside and outside the cluster. As shown in Fig. 6.4, the $g(r)$ within the cluster displays the typical shape of a frozen configuration, with a split second peak - for more details and a discussion about the $g(r)$ of equilibrium systems see the Appendix 5.A. As usual, particles are placed onto a hexagonal lattice with a random orientation, as confirmed by the peak positions of the $g(r)$. Anyway, it is worthy to note that the position of the first peak occurs at distance $\bar{r} < \sigma$, meaning that the target particle climbs on the potential due to the surrounding particles and, in principle, has a larger potential energy than an equilibrium-like system. Instead, the shape of the $g(r)$ resembles the one of an equilibrium-gas outside the cluster: a low initial peak is placed at position $\bar{r} \approx \sigma$ and then the $g(r)$ rapidly goes towards one. Nevertheless, important differences appear from equilibrium: indeed, assuming the same packing fraction of our study in passive Brownian simulations, we cannot obtain a first peak independently on the temperature value considered. The occurrence of an anomalous first peak means that, even outside the cluster, active particles prefer to attain a non-homogenous configuration, forming small couples or small groups of particles involving the first neighbors. This observation coincides with the one obtained in

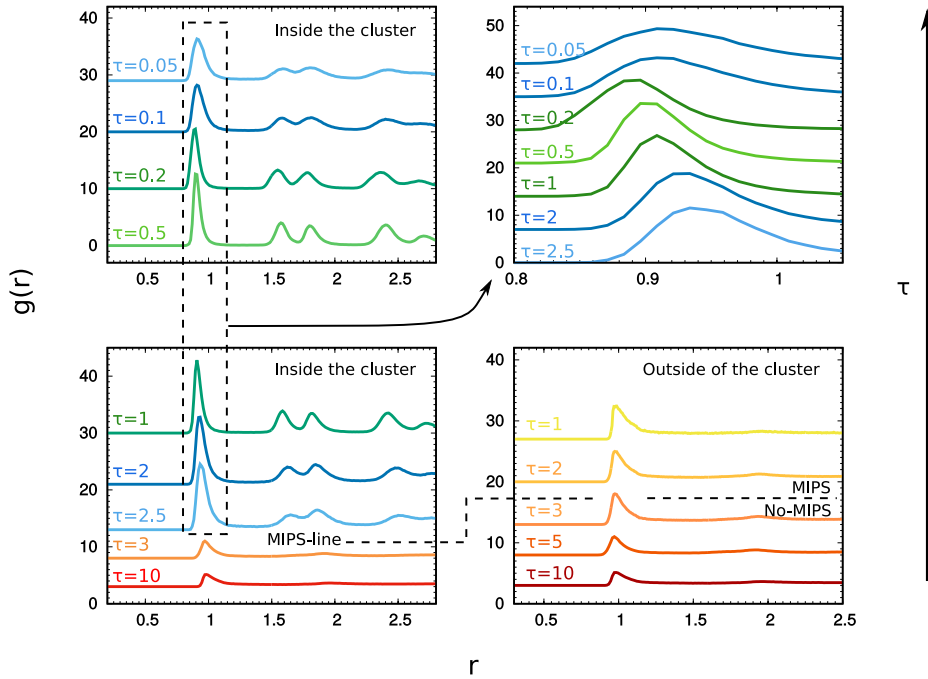


Figure 6.5: Pair correlation function, $g(r)$, for a system of self-propelled particles with $U_0 = 50$ with the inter-particle interactions described along with the text. Panels (a) and (b) show the $g(r)$ within the cluster (when MIPS occurs) and of the whole system (before the MIPS transition) in function of $\tau = 1/D_r$, whose values are reported in correspondence of each curve. Panel (c) enlarges the main peak of several configurations of panel (a) and (b) showing how the distance between neighboring particles changes with this parameter. Finally, in panel (d), the $g(r)$ outside the cluster are plotted for different $1/D_r$. We remark that in each panel, the $g(r)$ are shifted along the y axis for presentation reasons. The colors of the $g(r)$ are chosen to facilitate the identification of the different aggregation phases corresponding to the shape of $g(r)$: scales of red/orange, blue and green for gas-like, liquid-like and solid-like phases. Simulations are performed employing the ABP model.

Sec.5.5 of Chapter 5 for a low-density system of self-propelled particles in non-harmonic confinements. Thus, particles outside the cluster do not form an equilibrium-like phase.

In Fig.6.5, we study the $g(r)$ for different values of the persistence time $1/D_r = \tau$, exploring both the regime before the MIPS transition and the phase-separated regime. In this figure, we report only the $g(r)$ of a suspension of ABP particles, for the sake of simplicity, but it is worthy to mention that the same results are obtained with the AOUP model. In particular, panel (a) shows the $g(r)$ before the MIPS where the anomalous-gas-like phase takes place. The increasing of τ increases the height of the main peak: even before MIPS, such a parameter induces an apparent cooling of

the structure since a larger value of τ stabilizes couples or small clusters for a longer time. From the critical $1/D_r$ at which the MIPS transition occurs, the $g(r)$ inside the cluster shows a solid-like shape. Increasing τ , the peaks become more pronounced meaning that the structure becomes more frozen reaching a maximum around $D_r \approx 0.4$. In panel (b) we explore a further regime of $1/D_r$. The peaks of the $g(r)$ become less pronounced until the solid-like structure disappears and assumes a shape similar to the one of an equilibrium liquid. This non-monotonic behavior of the $g(r)$ is new and confirms the dynamical MIPS observed in this Section: the continuum and incoherent movement of the cluster favors a more fluid configuration instead of a solid-like one.

In panel (c) of Fig.6.5, we enlarge the main peak of the $g(r)$. At first, the increasing of τ leads to a more aggregated cluster since the position of the initial peak is shifted towards smaller distances. Then, from $D_r \approx 0.4$, the non-monotonicity takes place and such a position is shifted again towards larger r . Finally, in panel (d), we illustrate the τ -dependence of the $g(r)$ outside the cluster. As expected, the height of the anomalous peak increases as $1/D_r$ grows since the couples or the small clusters of particles are stable for a longer time, roughly $\propto \tau$.

6.4.2 The single-particle velocity distribution

It is worthy to study the single-particle distribution of the velocity modulus, $p(|\mathbf{v}|)$, varying the control parameters. In analogy with the $g(r)$ study, we calculate the $p(|\mathbf{v}|)$ in the whole system before the occurrence of the MIPS transition, while, when the system is phase-separated, the $p(|\mathbf{v}|)$ inside and outside the cluster are evaluated separately.

In Fig.6.6, we show a typical $p(|\mathbf{v}|)$ obtained in the MIPS configuration, inside and outside the cluster. In the former case, the distribution is very similar to a Gaussian with vanishing average velocity, while, in the latter case, the distribution is largely peaked at $U_0 = 50$, corresponding to the potential-free velocity value. The contribution to such narrow peak comes from the fraction of particles which are not interacting with any neighbor, i.e. are potential-free. In addition, a long high velocity tail occurs in the shape of $p(|v|)$ for smaller values of $|\mathbf{v}|$, which is due to the fraction of interacting particles, forming couples or small clusters. The shape of the matrix Γ is in agreement with such a result: the interaction causes larger effective Stokes forces which slow down the velocity dynamics. Nevertheless, it is interesting to note that $p(|\mathbf{v}|)$ displays a tail even for $|\mathbf{v}| > U_0$. Particles can explore velocities larger than the potential-free one, meaning that interactions can induce an acceleration. Such a picture resembles the occurrence of super-speeds already found in Sec.2.6 of Chapter2. In that case, the effect is produced by a negative curvature of the potential. Here, an analog mechanism takes place as we show later, in Sec.6.6. We stress that the narrow shape of $p(|\mathbf{v}|)$ (the δ -function shape) is typical of ABP particles since, in

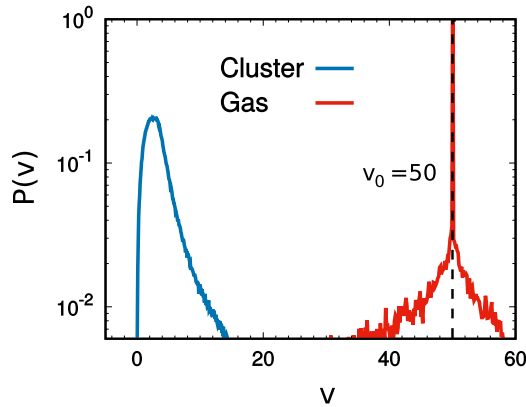


Figure 6.6: Probability distribution of the velocity modulus, $p(|\mathbf{v}|)$, inside (blue curve) and outside (red curve) the cluster for a configuration with $U_0 = 50$, $D_r = 0.4$ and the interaction potential used in the numerical study of this Chapter. Simulations are performed employing the ABP model.

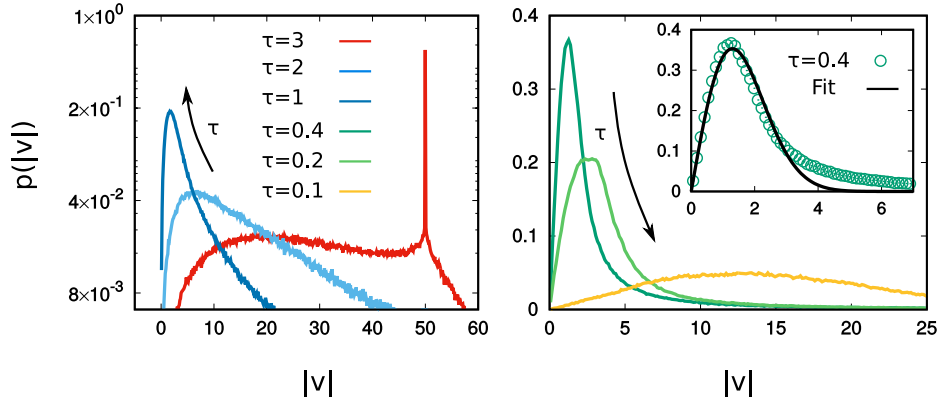


Figure 6.7: Probability distribution of the velocity modulus, $p(|\mathbf{v}|)$, varying D_r . $p(|\mathbf{v}|)$ is calculated in the whole space before that MIPS occurs (i.e. for $D_r = 3$) and in the main cluster when the system is phase-separated. The inset shows the comparison between the $p(|\mathbf{v}|)$ for $D_r = 0.4$ and $U_0 = 50$ and a Gaussian fit. Simulations are performed employing the ABP model.

the AOUP case, the peak of $p(|\mathbf{v}|)$ broadens even for potential-free particles. Instead, the distribution inside the cluster has a Gaussian-like shape, centered at $\mathbf{v} = 0$ in Cartesian coordinates (not shown). Even in this case, two symmetric higher and long tails occur, mostly due to the particles placed at the boundaries of the clusters which are typically faster. In the inset of panel (b) of Fig.6.7, we show the comparison between the numerical $p(|\mathbf{v}|)$ and the Gaussian prediction, showing a fair agreement, except for the long tail occurring for large $|\mathbf{v}|$. We note that the comparison of the distributions in the two different phases, reveals that particles inside the cluster are slower than particles outside it.

In panels (a) and (b) of Fig.6.7, we plot the $p(|\mathbf{v}|)$ varying the persistence

time $1/D_r$, showing the distribution of the whole system in the homogenous phase and the $p(|\mathbf{v}|)$ of the main cluster when MIPS occurs. Similarly to the distribution outside the cluster, the $p(|\mathbf{v}|)$ before the phase separation displays a pronounced and narrow peak at $U_0 = 50$ and two longer tails both for $|\mathbf{v}| > U_0$ and $|\mathbf{v}| = U_0$. This distribution shows the appearance of bimodality for small $|\mathbf{v}|$. After the MIPS-transition point for $D_r < 3$, the increasing of $1/D_r$ induces changes in the shape of $p(|\mathbf{v}|)$: the main peak is shifted towards smaller $|\mathbf{v}|$ and the tail becomes lower and shorter. This means that the increase of the persistence time leads particles to become slower with small velocity fluctuations. This is in agreement with the effect of τ in Eq.(6.6), where its growth induces the increase of the effective Stokes force in the \mathbf{v} -dynamics. This trend is stopped at $1/D_r = 0.4$, when the standard MIPS is replaced by clusters with very fast shape changes. For larger values of $1/D_r$, the main peak of $p(|\mathbf{v}|)$ shifts again towards larger values and the distribution broadens, as shown in panel (b) of Fig.6.7. As in the $g(r)$ study, this behavior is fully consistent with the dynamical MIPS introduced in the previous Section: when the cluster moves faster and changes shape continuously in time, also particles inside the cluster swim with increasing velocity.

6.5 Alignment velocity order and phase separation

In Sec.5.3 of Chapter 5, we have shown the emergence of a new long-range order in the alignment of the velocities for dense suspensions of self-propelled particles. This order is ruled by the persistence of the active force as confirmed by analytical arguments able to capture such intriguing phenomenology. In what follows, we repeat the same numerical study of Sec.5.3 in a system displaying MIPS, i.e. in a regime of smaller packing fraction, $\phi = 0.65$. We evaluate separately the dense and the dilute phases.

Inside the cluster, velocities spontaneously form oriented structures, arranging in aligned domains, as shown in panel (b) of Fig.6.8 or vortex-like domains, as illustrated in panel (c) of Fig.6.8. These structures are more pronounced in the bulk of the cluster, while they are not so evident at its boundary. Besides, such domains are not stable but change continuously in time: sometimes oriented domains collapse into vortex-structure and vice-versa. Their sizes increase with the growth of both the active force parameters, τ and U_0 , in analogy with the phenomenology of dense suspensions of self-propelled particles. In the present Section, we do not vary ϕ and U_0 whose variations are left to future investigations.

As already mentioned, the increasing of τ at fixed $U_0 = 50$ induces the formation of a stable cluster, approximatively at $D_r \lesssim 3$ for $\phi = 0.65$. Following the standard procedure of Sec.6.2, we monitor the MIPS transition using the distribution of the effective packing fraction. In panel (a) of

Cluster Formation & Velocity Alignment

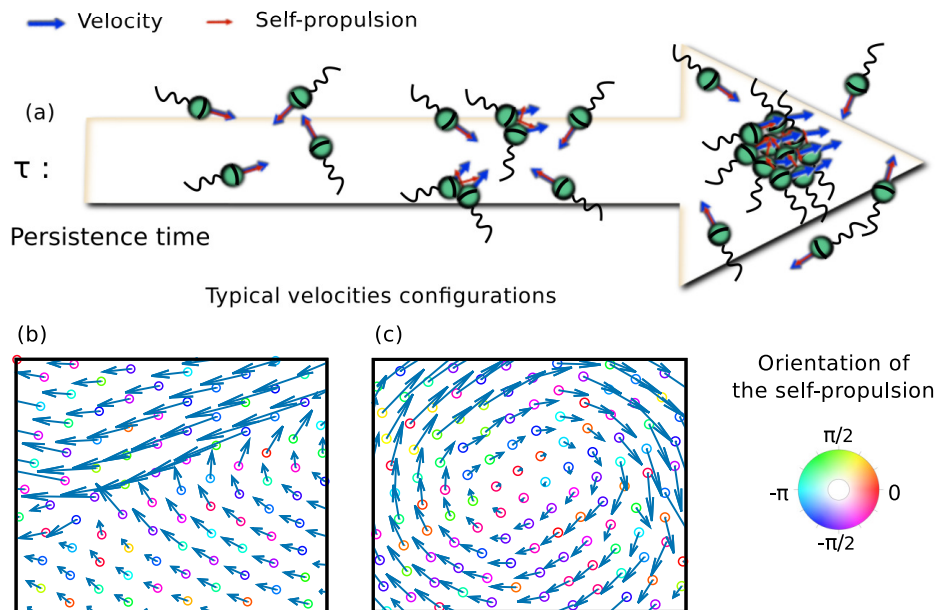


Figure 6.8: In the cartoon (a), we roughly show the main novel of the present Chapter: microswimmers moves with aligned velocity even if their self-propulsions are randomly distributed. Panel (b) and (c) display two snapshot configurations in the motion plane, obtained enlarging two small squares inside the main cluster of a simulation where the MIPS transition occurs. Such a simulation is realized in the same condition as Fig.6.4. Colors encode the orientations of self-propulsions while the blue arrows represent particles' velocities.

Fig.6.9, we report the curve of ϕ_g , i.e. the effective packing fraction in the homogenous phase, and ϕ_c , the one in the denser phase. In agreement with [288], at this density value, ϕ_g is a continuous function for the whole range of $1/D_r$ explored in our numerical study: ϕ_g returns $\phi = N/L^2\pi\sigma^2/4$ before the phase separation and decreases from $1/D_r \approx 0.33$ until to reach a plateau. From $1/D_r \approx 0.33$, ϕ_c starts to grow until to reach a saturation value in correspondence of the plateau of ϕ_g . Our study is stopped at $D_r = 0.2$, before the occurrence of the cluster dynamical changes. The extension of the present analysis to these regimes will be a matter of future investigations.

As addressed in Sec.5.3, the absence of an explicit polarization - no alignment interactions in the dynamics of the self-propulsions - does not allow to the use of $\langle\theta\rangle$ as a suitable order parameter and even $\langle\psi\rangle$, where ψ is the angle formed by the particle velocity respect to the x -axis, cannot account for the local polarization: in the cluster, we can distinguish several domains with different orientations, as shown in panels (c), (d) and (e) of Fig.6.9. Thus, $\langle\psi\rangle \approx 0$ eventually with large fluctuations. Employing the same strategy of Sec.5.3, we introduce the spatial correlation of the velocity direction,

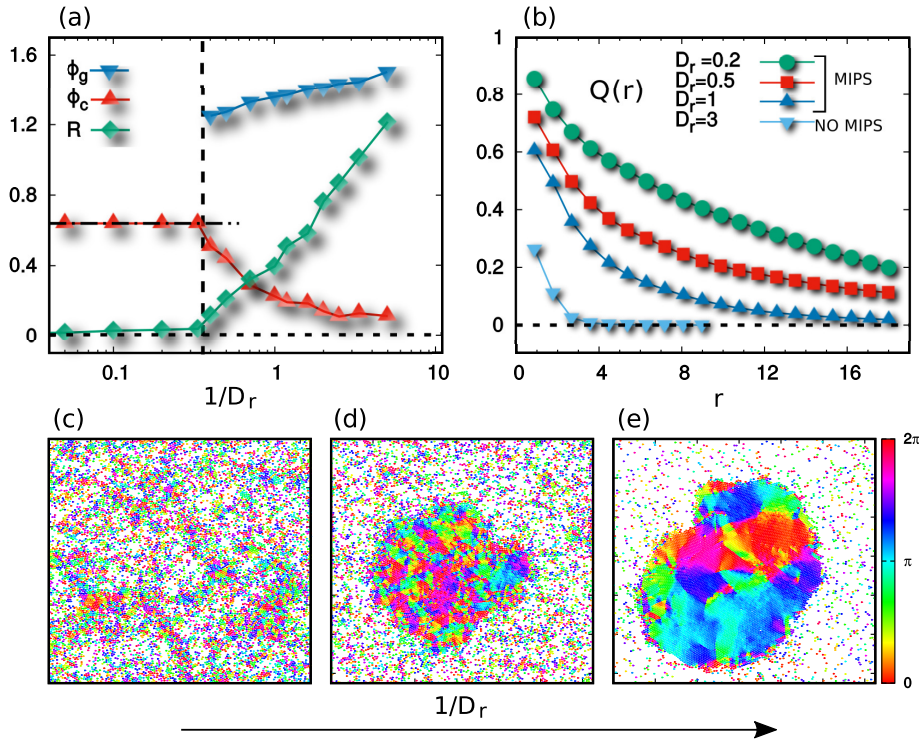


Figure 6.9: Panel (a) shows densities ϕ_g and ϕ_c in the dilute and in the cluster phase, respectively, and alignment velocity order parameter R in function of the persistence time $1/D_r$. The curves of ϕ_g and ϕ_c are obtained studying the distribution of the packing fraction, while R comes from the integration of $Q(r)$ along with the typical cluster size. Panel (b) shows several $Q(r)$ for different values of D_r as shown in the legend, where the presence MIPS or not is indicated. Finally, panels (c), (d) and (e) display different snapshot configurations in the motion plane for different values of $D_r = 3, 1, 0.5$, respectively.

$Q(r) = \sum_k Q_k(r)$, where $Q_k(r)$ reads:

$$Q_i(r) = 1 - 2 \sum_j \frac{d_{ij}}{\mathcal{N}_k \pi} \quad (6.29)$$

and $d_{ij} = \min[|\psi_i - \psi_k|, 2\pi - |\psi_i - \psi_k|]$. Integrating $Q(r)$, we extract a suitable order parameter, R , which is roughly the correlation length of $Q(r)$. At variance with the infinite system, $Q(r)$ is integrated along with the typical size of the cluster since exploring larger distances is meaningless. As a consequence, we cannot evaluate finite-size effects, since the size of the cluster is only fixed by the control parameters. Thus, $Q(r)$, in principle, does not approach to zero if the size of the domains is large enough with respect to the cluster size. We remark that this is not an unphysical effect, at variance with the denser systems discussed in Sec.5.3. A detailed discussion about Q and R is reported in Sec.5.3 of Chapter 5.

In panel (b) of Fig.6.9, we report the function $Q(r)$ for several values of D_r . As in the infinite system, its increasing produces both the growth of the first value of $Q(r)$ - neighboring particles are more aligned - both the slowing down of the relaxation. Roughly, starting from $D_r = 0.5$, the shape of $Q(r)$ does not approach to zero but apparently saturates to a larger value. This phenomenology resembles the one shown in Fig.5.3(a) of Sec.5.3 where finite-size effects occur, even if, now, this shape has physical origins.

In panel (a) of Fig.6.9, the shape of R is reported. As expected, R is an increasing function of $1/D_r$. In particular, its shape resembles the one of a continuous transition occurring at $1/D_r \approx 0.33$, i.e. in correspondence of the MIPS transition as shown emerged in Fig.6.9(a). Two regimes clearly emerge: a first slow monotonic growth is followed by a rapid increase. This shape resembles the one obtained In Sec.5.3, where the increase of $1/D_r$ leads to non-homogeneous dense phases.

6.5.1 Effective Vicsek interactions inside the cluster

As already shown in Sec.5.4 of Chapter5, the velocity dynamics of interacting self-propelled particles can be simplified taking advantage of the hexagonal spatial order of the internal structure. In this way, a Vicsek-like interaction takes place in the \mathbf{v}_i dynamics, i.e. a force which pushes the velocity of the tagged particle towards the average value of neighbors' velocities. The dynamics of a particle inside the cluster specifically reads:

$$\dot{\mathbf{v}} = -\frac{1}{\gamma} \hat{J} \cdot (\mathbf{v} - \mathbf{v}^*) - D_r \mathbf{v} + \mathbf{k}, \quad (6.30)$$

where the diagonal matrix \hat{J} is defined as:

$$\hat{J} = 3 \left[U''(\bar{r}) + \frac{U'(\bar{r})}{|\bar{r}|} \right] \mathcal{I} > 0, \quad (6.31)$$

being \mathcal{I} the identity matrix. Eq.(6.30) is derived in Appendix5.C and is largely discussed in Sec.5.4.

In a homogeneous system, the hexagonal spatial order assumption was confirmed by the study of the pair correlation function and, in that case, \bar{r} is fixed by the numerical density. Eq.(6.30) can be also used to describe the bulk of the cluster since, also in this case, the shape of the $g(r)$ reveals a clear hexagonal spatial order. Here, \bar{r} is a complex function of the active force parameters. Nevertheless, the assumptions behind Eq.(6.30) are broken at the cluster boundary - where a particle has fewer neighbors and even the contributions of the forces are not balanced - and, mostly, in the dilute phase outside the cluster.

6.6 The dilute phase: unstable pairs outside the cluster

The studies of the $g(r)$ and the $p(|\mathbf{v}|)$ has revealed some anomalies - compared to equilibrium diluted suspensions of particles at the same packing fraction - in the non-equilibrium dilute regime, i.e. when the inter-particles interactions are rare. Even if the study of this Section has been performed for suspensions of self-propelled particles outside the cluster (where the phase separation occurs), the current theoretical analysis is valid for any self-propelled systems at small densities in the regime of large persistence. Even in the presence of a confining mechanism - see Sec.5.5 of Chapter 5 - the dilute phase has been denoted as “anomalous-gas” because of the presence of the unexpected initial peak in the shape of $g(r)$. Instead of being homogeneously distributed, particles prefer to form couples or even clusters formed by few particles. These structures cannot be stable, otherwise, the formation of a large cluster, i.e. a phase separation, cannot be arrested. Such an argument implies that these small clusters have a finite lifetime.

In what follows, we develop a theoretical description of the dilute phase, assuming that only couples could form, for the sake of simplicity. In other words, we assume that the force contributions involve only two particles in Eq.(6.2) or equivalently in Eq.(6.6). This implies that $U_{tot} = U$ where U is given by Eq.(6.1). With these simplifications, it is convenient to perform a change of variables to reduce the two-body problem to a single-body problem in the presence of an external potential, taking advantage from the form of the interaction which depends only on the inter-particle distance, r . Denoting with $\mathbf{x}_{1,2}$ and $\mathbf{v}_{1,2}$ the positions and the velocities of the particles 1 and 2, respectively, we introduce the relative position, $\mathbf{r} = \mathbf{x}_2 - \mathbf{x}_1$, and the position of the center of mass, $\mathbf{R} = \frac{\mathbf{x}_2 + \mathbf{x}_1}{2}$, in Eq.(6.6). In the same way, we call $\mathbf{v} = \mathbf{v}_2 - \mathbf{v}_1$ the relative velocity and $\mathbf{V} = \frac{\mathbf{v}_2 + \mathbf{v}_1}{2}$ the velocity of the center of mass. The spherical shape of the interactions suggests to evaluate the relative position in polar coordinates, r and α , and to project the relative velocity over the radial and the tangential axes, v_r and v_t , respectively. In this way, the center of mass evolves as a potential-free overdamped active particle - i.e. an equilibrium underdamped passive particle - while the dynamics of the relative coordinate reads:

$$\dot{v}_r = -\frac{D_r}{\gamma}U'(r) + \frac{v_t^2}{r} - D_r \left(1 + \frac{U''(r)}{D_r\gamma}\right) v_r + k_r, \quad (6.32a)$$

$$\dot{v}_t = -\frac{v_r v_t}{r} - D_r \left(1 + \frac{U'(r)}{rD_r\gamma}\right) v_t + k_t, \quad (6.32b)$$

where $v_r = \dot{r}$ and $v_t = \dot{\alpha} r$, being α the polar angle. The vectors k_r and k_t are the projections of the noise contributions on the radial and the tangential axis and depend on the dynamics of the active force. In the AOUP case, they are simply two Gaussian white noises with variance $2D_a/\tau^2$ and independent

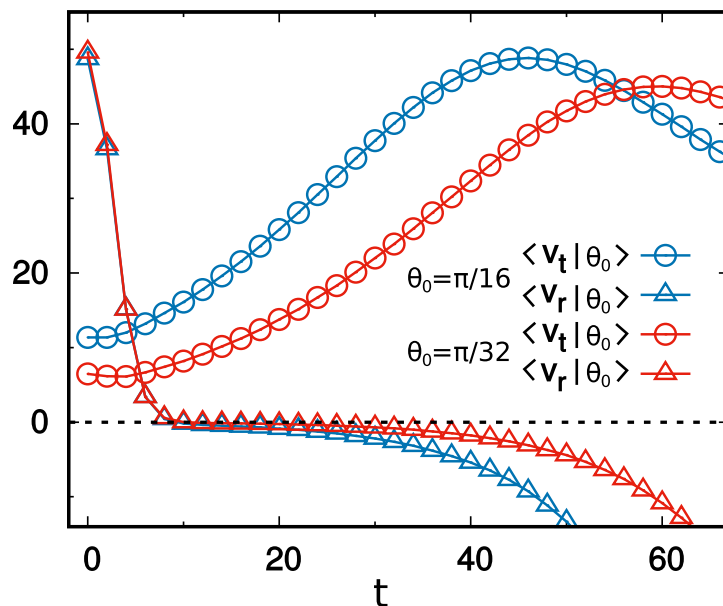


Figure 6.10: Average tangential and radial velocities in function of time, $\langle v_t | \theta_0 \rangle(t)$ and $-\langle v_r | \theta_0 \rangle(t)$, respectively. The notation $\langle \cdot | \theta_0 \rangle$, means that the initial angle of the collision is fixed, as described in the text. We start the collision from $r = \sigma$, showing the results for two different values of θ_0 .

components, while, in the ABP, we have:

$$k_r = v_t \sqrt{2D_r} \xi, \quad (6.33)$$

$$k_t = \left(v_r + \frac{U'(r)}{\gamma} \right) \sqrt{2D_r} \xi, \quad (6.34)$$

where ξ is a white noise with unitary variance and zero average. Even in this case, the difference between AOUP and ABP dynamics occurs only at the noise level and disappears in the large persistence regime $D_r \rightarrow 0$ ($\tau \rightarrow \infty$). This explains why AOUP and ABP models give rise to the same phenomenology, also in the dilute regime.

It is worthy to note that the dynamics of v_t and v_r are strictly correlated. Since the reference frame adopted in Eqs.(6.32a) and (6.32b) is non-inertial, apparent forces take place in the dynamics: specifically, the second addend of the right-hand side of Eq.(6.32a) and the first addend of the right-hand side of Eq.(6.32b). While the radial friction is always positive, being $U''(r) > 0$, and, thus, behaves as a space-dependent Stokes force as in the case of convex potentials (see Sec.2.4 of Chapter2), this is no longer true for v_t . Indeed, being $U'(r) < 0$ for all values of r , the tangential friction could become negative in the large persistence regime when the interaction takes place. Such an effect disappears in the limit of large D_r (small τ) and becomes relevant for small D_r , when $|U'(r)| > rD_r\gamma$. As shown in Sec.2.5 of Chapter 2 - see also [104] for a reference -, the occurrence of a negative friction produces a very peculiar dynamics: we expect that v_t increases exponentially in time,

as in the case of non-convex potentials. In Fig.6.10, we compare the average radial velocity, $\langle v_r|\theta_0\rangle(t)$ and the average tangential velocity $\langle v_t|\theta_0\rangle(t)$ as a function of time, t . Data are obtained from colliding pairs of particles. Since a collision only occurs when $v_r < 0$ and $r \leq \sigma$ (which are necessary conditions), the average is computed by fixing the initial conditions and averaging over different trajectories. In particular, we choose the following collision protocol: $r(0) = \sigma$ and $v_r(0) = -\sqrt{v_0^2 - v_t(0)^2}$, being $v_t(0)$ the initial tangential velocity. Since the interactions vanish at $r = \sigma$, at time zero the self-propulsion coincides with the velocity. Thus, in the ABP case, the modulus of the velocity is fixed and the only degree of freedom is given by the polar angle, θ_0 . Instead, in the AOUP case, we need to fix also the modulus of $\mathbf{v}_r = \mathbf{f}_r^a$ at the initial time, which can be chosen as U_0 , for consistency with the ABP system. Averaging also over the initial conditions of the modulus does not change consistently the average values of v_t and v_r because U_0 is the most probable value of $|\mathbf{v}_r|$, in the potential-free case. We start the simulations always from the same initial polar angle, α_0 , even if, for radial symmetry, such a prescription is irrelevant.

In Fig.6.10, we plot $-\langle v_r|\theta_0\rangle(t)$ and $\langle v_t|\theta_0\rangle(t)$ for two different values of θ_0 , showing the exponential growth of $v_t(t)$, in both cases. As expected, $-\langle v_r|\theta_0\rangle(t)$, fastly decreases towards zero from the initial condition and remains almost constant. Finally, becomes negative for a typical time, t_e , which depends on θ_0 . Instead, $\langle v_t|\theta_0\rangle(t)$ increases exponentially until t_e . The choice of θ_0 determines the shape of the increase: larger is θ_0 , faster will be the growth of $\langle v_t|\theta_0\rangle(t)$. This phenomenology suggests that a colliding event between two particles - which in relative coordinates is characterized by an initial radial velocity $v_r < 0$ - follows the steps illustrated below:

- i) In the early stage of the collision process v_r increases from $v_r(0) < 0$ towards zero, i.e. its absolute value is decreased. Indeed, in the large persistence regime, the dynamics of v_r depends solely on the positive friction term $D_r(1 + \frac{\tau}{\gamma}V''(r))v_r$, since the term $\frac{v_t^2}{r}$ is small at this stage (otherwise the particles do not collide). The distance from the origin is roughly kept fixed from the balance between the force term and the self-propulsion. Thus, it is a function of the active force parameters such that $\bar{r} < \sigma$. At this stage, the couple is formed.
- ii) In a second stage, v_t evolves with a negative friction term $D_r(1 + \frac{\tau V'(r)}{\gamma r})v_t$ (since $\bar{r} < \sigma$), while the first addend is roughly zero. Thus v_t increases its absolute value exponentially, while v_r is small and nearly constant, being approximatively $v_r \approx 0$. In particular if the initial condition $v_t(0)$, is negative v_t decreases. Instead, when $v_t(0) > 0$, v_t increases. Along with this stage, the two particles are close to each other and rotate with increasing angular velocity. This means that the couple is stable. This non-equilibrium effect has not a Brownian counterpart.

- iii) The term $\frac{v_t^2}{r}$ in the equation for \dot{v}_r increases as v_t grows, becoming relevant in the dynamics of v_r and acting as a strong centrifugal force. Such a mechanism induces the growth of $|v_r|$, which becomes negative - at a typical time, t_e , which depends on θ_0 and from the active force parameters. This means that particles are moving going far from each other: the radial coordinate $r(t)$ increases until to $r \geq \sigma$, i.e. until the colliding pair breaks apart.
- iv) Finally, the particles are well separated and the dynamics is that of two free particles, without interaction and friction D_r . This explains why v_t now decreases monotonically towards zero - due to the potential-free Stokes force - and we observe a maximum in the shape of $\langle v_t | \theta_0 \rangle(t)$.

The overall description explains the formation and instability of a couple of two self-propelled particles: two colliding particles form a bound pair for a time, t_e , whose duration depends on the balance between v_t^2/r and $\frac{1}{\gamma}V''(r)v_r$. After t_e , the pair breaks apart, showing the instability of such a bond. The formation and instability of clusters formed by few particles could be, in principle, understood with similar arguments. Nevertheless, adopting the above strategy not only requires a larger technical effort but also the introduction of suitable coordinates to simplify the many-body problem.

The above analysis suggests that Vicsek-like interactions does not occur only in the dense phase but occur also in the dilute phase. Indeed, until to the breaking time, t_e , the relative radial velocity of the couple is almost zero, $v_r \approx 0$. Thus, the two particles move together with the same velocity, i.e. the speed of the center of mass which evolves as a potential-free particle. It is not so surprising that, in the dilute regime, this effect is marginal. The same occurs in the Vicsek model, where a first-order transition occurs with the packing fraction as the order parameter.

This analysis unveils the deep non-equilibrium nature of the dilute phases and enforces the idea that equilibrium-like theories cannot explain the phase behavior of active matter and, specifically, its aggregation states. Even the rare interactions of the dilute regime have dramatic consequences.

6.7 Conclusion

In this Chapter, at first, we have reviewed experimental evidence of clustering and phase-separation, and some existing coarse-grained theories to explain Motility Induced Phase Separation for models of interacting self-propelled particles. We extend the study of MIPS to large persistence regimes, which differ from the ordinary MIPS and cannot be predicted with the current equilibrium-like theories, described in Sec.6.3. In large persistence regimes, clusters are non-static, deforming and reshaping continuously in time, splitting and reforming perpetually. We denote such a state as “dynamical MIPS” to be distinguished by the usual MIPS. Then, our second

result concerns the existence of an additional new long-range order occurring in concomitance with the phase-separation: velocities align each other, forming patterns with oriented domains or vortex-like structures. The new order phenomenon is ruled by the persistence time and resembles a continuous transition. In analogy with the study of Chapter 5, we explain such a phenomenology, occurring in the absence of explicit alignment interactions, in terms of effective Vicsek-like forces presenting analytical arguments. Similar strategies show that the velocity alignment takes place also in the dilute regime outside the cluster, even if it is quite “macroscopically” irrelevant: it leads to the formation of bound pairs with a finite lifetime. Besides, we present theoretical arguments showing the agreement between ABP and AOUP dynamics even in the large persistence regimes. As a confirmation, the MIPS transition is insensible to the choice of the model.

Recently, a large amount of numerical studies has focused on ABP-like dynamics (or similar) with the addition of hydrodynamic interactions, chiralities, shapes or deformability of the particles, explicit alignment forces, etc. Nevertheless, even the simpler case - spherical athermal ABP - was not fully theoretically understood. Both the phenomenologies, reported in this Chapter, cannot be explained in terms of the existing equilibrium-like theories, which are based on the mapping of self-propelled particles onto passive suspensions with attractive interactions (or equivalently with effective free-energy functionals). This enforces the idea that MIPS is a pure non-equilibrium transition. Also, other studies confirm this idea, where a large number of anomalies was found: negative surface tension between the two phases[312, 313], anomalous pressures [107] or different temperatures between the two coexisting phases [290], to make some examples. A more complex theory to explain this intriguing phenomenology is needed and even the current models, in the framework of field theories, should be expanded to account for the velocity order. We call our new and intriguing phenomenology predicted by ABP particles for experimental verifications, for instance, with apolar microswimmers such as Janus particles or photo-activated colloids.

From an experimental perspective, the agreement between ABP or AOUP dynamics with Janus particles is yet poor. Indeed, clustering in experiments occurs at lower packing fraction with respect to the ABP model. Hindered mechanisms - for instance, specific of Janus particles - should be included in the model to cover quantitatively the gap between models and experiments. This is an open problem which requires the adaption of ABP (or AOUP) to the specific properties of active colloidal systems, whose interest is mostly related to the design of new materials.

An interesting perspective for our study regards the generalization to more complex dynamics, to explain, for instance, the occurrence of polar order in the rod-like microswimmers, in the absence of explicit alignment interactions, as observed in [299]. In general, it is also very interesting to evaluate how the alignment velocity order is modified in a broad class of

ABP variants, observing what happens in the presence of hydrodynamics, quorum sensing[321] or visual perception interactions[330], for instance.

Appendices

6.A From the Smoluchowski equation to the coarse-grained theory for Active Brownian Particles

Here, a formal derivation of the linear dependence of effective speed on ρ is derived, starting from the microscopic dynamics. Below, we follow [309].

Let us start from the Smoluchowski equation governing the time evolution of the normalized joint probability, $\Psi_N(\{\mathbf{x}_k, \theta_k\}, t)$, depending on the whole set of coordinates of the system:

$$\partial_t \Psi_N = \sum_k \nabla_k \cdot [\nabla_k U_{tot} - U_0 \mathbf{n}_k + D_t \nabla_k] \Psi_N + D_r \sum_k \frac{\partial^2 \Psi_N}{\partial \theta_k^2}, \quad (6.35)$$

assuming $\gamma = 1$, for the sake of simplicity. We denote as $\nabla_k \equiv \nabla_{\mathbf{x}_k}$, for notational convenience, while the derivatives with respect to θ are explicitly indicated. Introducing the single-body probability, $\Psi_1(\mathbf{x}, \theta, t)$, as:

$$\Psi_1(\mathbf{x}, \theta, t) = N \int d\mathbf{x}_2 \dots d\mathbf{x}_N \int d\theta_2 \dots \theta_N \Psi_N, \quad (6.36)$$

where we have dropped the index of the tagged particle (namely particle 1). We can find an equation for Ψ_1 involving Ψ_2 , i.e. the first equation of the so-called BBGKY hierarchy for self-propelled particles:

$$\partial_t \Psi_1 = -\nabla \cdot [\mathcal{F} + U_0 \mathbf{n} \Psi_1 - D_t \nabla \Psi_1] + D_r \partial_\theta^2 \Psi_1, \quad (6.37)$$

where \mathcal{F} is a mean force which reads:

$$\begin{aligned} \mathcal{F} &= \int d\mathbf{x}_2 \dots d\mathbf{x}_N \int d\theta_2 \dots \theta_N (\nabla_1 U) \\ &= - \int d\mathbf{x}' U(|\mathbf{x} - \mathbf{x}'|) \frac{\mathbf{x} - \mathbf{x}'}{|\mathbf{x} - \mathbf{x}'|} \psi_2(\mathbf{x}, \theta, \mathbf{x}', t), \end{aligned} \quad (6.38)$$

where $\psi_2(\mathbf{x}, \theta, \mathbf{x}', t)$ is the two-body density distribution function to find another particle at \mathbf{x}' and the tagged particle at \mathbf{x} with orientation θ , and $U_{tot} = \sum_{i < j} U$. To proceed further, we project \mathcal{F} onto the orientation, assume that the system is homogeneous and neglect any time dependence. Then, upon decomposing the force onto a non-orthogonal basis spanned by the orientation and density gradient, $\nabla \Psi_1$, we expand to linear order in $|\nabla \Psi_1|$, we obtain a closed equation for Ψ_1 , which is:

$$\partial_t \Psi_1 = -\nabla \cdot [\mathcal{V} \mathbf{n} - \mathcal{D} \nabla] \Psi_1 + D_r \partial_\theta^2 \Psi_1, \quad (6.39)$$

where \mathcal{D} and \mathcal{V} are defined as:

$$\mathcal{D} = D_t - \mathcal{F} \cdot \frac{[\nabla\Psi_1 - \mathbf{n}(\mathbf{n} \cdot \nabla\Psi_1)]}{|\nabla\Psi_1|} \quad (6.40)$$

$$\mathcal{V} = U_0 - \rho\zeta. \quad (6.41)$$

ζ is a constant, which depends on the detail of the interaction, as a result of the homogeneous approximation adopted and ρ is the density of the system. Further details about the derivation of such a result are contained in [309]. Such a result connects the microscopic stochastic dynamics to a hydrodynamic-like equation for Ψ_1 : and it is the only existing argument which justifies an effective swimming velocity depending on the density. We remark that such a result is consistent with the passive case: when $U_0 = 0$, then $\zeta = 0$, as expected.

Conclusions and Perspectives

In this thesis, we presented a series of results about non-equilibrium systems in the framework of active matter. Several microorganisms, at different length scales, convert energy into direct motion, showing a very peculiar and general phenomenology which differs for several aspects from the phenomenology of passive colloids. In particular, we consider models for suspensions of self-propelled particles, representing apolar and spherical units which describe the behavior of both biological and artificial microswimmers. Our numerical and theoretical study focused both on dilute and dense suspensions, modeled in the framework of non-equilibrium stochastic processes to account for their persistence motion. We show the almost-equivalence between two models of self-propelled particles, namely the Active Brownian Particles and Active Ornstein-Uhlenbeck particles, both reproducing the leading phenomenology experimentally experienced by these systems.

The first part of the thesis is devoted to the dynamics of a single microswimmer confined by external traps - such as acoustic traps or optical tweezers - or in channels with different shapes. General approaches of non-equilibrium Statistical Mechanics, such linear response theory and stochastic thermodynamics are applied to self-propelled particles. We numerically explore the phenomenology of the accumulation near the walls, unveiling the effect of the solvent, chirality and first passage-properties even for complex geometries. Our theoretical approach is related to effective hydrodynamic-like methods, agrees with previous theories and, is able to explain interesting effects. Nevertheless, the interplay between external and self-propulsive forces produces strong non-equilibrium effects which are reflected in non-Boltzmann-like distributions, showing the accumulation far from the minima of potentials. Even if effective-equilibrium approximations are able to partially reproduce this phenomenology, self-propulsion pushes particles far from equilibrium. This is confirmed from an energetic perspective, developed in the framework of stochastic thermodynamics and linear response theory.

In the second part of this thesis, we focus on interacting systems of self-propelled particles at low, moderate and large densities. In all these cases, the deep non-equilibrium nature of active particles emerges in the peculiarities of active matter aggregation phases which are fairly different from their passive Brownian counterparts. Numerical investigations show

the occurrence of a new long-range order in the orientations of the velocities, which in the dilute phase implies the formation of moving pairs with a finite lifetime while at very large density leads to the intriguing patterns of alternating aligned domains and vortex-like configurations of velocities. The emergence of this phenomenology is accompanied by the well-known phase-separation occurring even in the absence of attracting interactions, which is reviewed, for completeness. In particular, its deep non-equilibrium nature is unveiled, as also the nature of dense phases with liquid-like structure featuring in unexpected spatial non-homogeneities. In all these cases, a mapping onto passive-like aggregation phases cannot be addressed. Besides, our theoretical study reveals a hindered connection between self-propelled and Vicsek-like models, showing that explicit alignment interactions are not needed to reproduce the phenomenon of flocking.

The new phenomenology explored in the second part of this thesis calls for experimental verifications, for instance, employing suspensions of artificial microswimmers, such as Janus particles or photo-activated colloids. The experimental detection of the new long-range velocity order, reported here, is a new intriguing phenomenon which may lead to interesting applications.

Our study offers interesting numerical and theoretical perspectives which will be surely addressed in future works. From one hand, the first part can be generalized to a system of interacting self-propelled particles, i.e. evaluating the effects of the excluded volume on the confined dynamics or the accumulation near the walls. Despite some numerical works have already been focused on such a generalization, we expect to discover, also in these cases, the velocity alignment order, which has not been yet observed. From the other hand, our theoretical methods could be extended to systems with more complex interactions, such as visual perception, quorum sensing mechanisms, non-spherical shapes, and shape-deformations. In all these cases - interacting or not - the dynamics of the particles' velocities will be affected by these new ingredients since they are usually embodied in the shape of the deterministic forces. We expect that we may be able to predict the emergence of polar orders in rod-shaped particles or the increase of the cluster cohesion in the presence of visual perception interactions.

Papers

Works discussed in this thesis

- 1) L. Caprini, U. Marini Bettolo Marconi, A. Puglisi and A. Vulpiani. Journal of Statistical Mechanics: Theory and Experiment, Volume 2019, 2019. *The entropy production of OrnsteinUhlenbeck active particles: a path integral method for correlations.*
- 2) L. Caprini, F. Cecconi, U. Marini Bettolo Marconi. The Journal of Chemical Physics 150, 144903, 2019. *Transport of an active particle in an open-wedge channel.*
- 3) L. Caprini, U. Marini Bettolo Marconi. Soft matter 15 (12), 2627-2637, 2019. *Active chiral particles under confinement: surface currents and bulk accumulation phenomena.*
- 4) L. Caprini, U. Marini Bettolo Marconi, A. Puglisi, A. Vulpiani. The Journal of Chemical Physics 150 (2), 024902, 2019. *Active escape dynamics: The effect of persistence on barrier crossing.*
- 5) L. Caprini, U. Marini Bettolo Marconi, A. Puglisi. Scientific Reports 9 (1), 1386, 2019. *Activity induced delocalization and freezing in self-propelled systems.*
- 6) L. Caprini a and U. Marini Bettolo Marconi. Soft matter 14 (44), 9044-9054, 2018. *Active particles under confinement and effective force generation among surfaces.*
- 7) L. Caprini, U. Marconi, A Puglisi, A Vulpiani. Physical Review Letters 121 (13), 139801, 2018. *Comment on “Entropy Production and Fluctuation Theorems for Active Matter”.*
- 8) L. Caprini, U. Marini Bettolo Marconi, A. Vulpiani. Journal of Statistical Mechanics: Theory and Experiment 2018 (3), 033203, 2018. *Linear response and correlation of a self-propelled particle in the presence of external fields.*

Other works

- L. Caprini, E. Hernandez-Garcia, C. Lopez and U. Marini Bettolo Marconi. ArXiv:1906.03016v1, June 2019. *A comparative study between two models of active cluster-crystals.*
- M. Baldovin, L. Caprini, A. Vulpiani. Physica A: Statistical Mechanics and its Applications, 2019. *Irreversibility and typicality: A simple analytical result for the Ehrenfest model.*
- L. Caprini, E. Hernandez-Garcia, C. Lopez. Physical Review E 98 (5), 052607, 2018. *Cluster crystals for Brownian particles with combined soft and hard-core repulsive interactions*
- L. Caprini, L. Cerino, A. Sarracino, A. Vulpiani. Entropy 19 (7), 350, 2017. *Fouriers Law in a Generalized Piston Model.*

Bibliography

- [1] A. Einstein, “On the movement of small particles suspended in a stationary liquid demanded by the molecular-kinetic theory of heat,” *Annalen der Physik*, vol. 17, no. 549.
- [2] A. Einstein, “On the theory of the brownian movement,” *Annalen der Physik*, vol. 19, no. 371.
- [3] D. S. Lemons and A. Gythiel, “Paul langevins 1908 paper on the theory of brownian motion[sur la théorie du mouvement brownien, cr acad. sci.(paris) 146, 530–533 (1908)],” *American Journal of Physics*, vol. 65, no. 11, pp. 1079–1081, 1997.
- [4] R. Brown, “Xxvii. a brief account of microscopical observations made in the months of june, july and august 1827, on the particles contained in the pollen of plants; and on the general existence of active molecules in organic and inorganic bodies,” *The Philosophical Magazine*, vol. 4, no. 21, pp. 161–173, 1828.
- [5] J. Ingen-Housz, “Bemerkungen über den gebrauch des vergrößerungsglases,” *Vermischte Schriften physisch-medicinischen Inhalts. Christian Friderich Wappler, Wien*, 1784.
- [6] C. Wiener, “Erklärung des atomistischen wesens des tropfbar-flüssigen körperzustandes, und bestätigung desselben durch die sogenannten molecularbewegungen,” *Annalen der Physik*, vol. 194, no. 1, pp. 79–94, 1863.
- [7] M. Von Smoluchowski, “Zur kinetischen theorie der brownschen molekularbewegung und der suspensionen,” *Annalen der Physik*, vol. 326, no. 14, pp. 756–780, 1906.
- [8] J. Perrin, *Brownian movement and molecular reality*. Courier Corporation, 2013.
- [9] K. Przibram, “Über die ungeordnete bewegung niederer tiere,” *Pflügers Archiv European Journal of Physiology*, vol. 153, no. 8, pp. 401–405, 1913.

- [10] K. Prziбраm, “Über die ungeordnete bewegung niederer tier. ii,” *Development Genes and Evolution*, vol. 43, no. 1, pp. 20–27, 1917.
- [11] R. Fürth, “Die brownsche bewegung bei berücksichtigung einer persistenz der bewegungsrichtung. mit anwendungen auf die bewegung lebender infusorien,” *Zeitschrift für Physik A Hadrons and Nuclei*, vol. 2, no. 3, pp. 244–256, 1920.
- [12] G. E. Uhlenbeck and L. S. Ornstein, “On the theory of the brownian motion,” *Physical Review*, vol. 36, no. 5, p. 823, 1930.
- [13] H. C. Berg, *Random walks in biology*. Princeton University Press, 1993.
- [14] H. C. Berg, “Bacterial behaviour,” *Nature*, vol. 254, no. 5499, p. 389, 1975.
- [15] H. C. Berg, “Symmetries in bacterial motility,” *Proceedings of the National Academy of Sciences*, vol. 93, no. 25, pp. 14225–14228, 1996.
- [16] H. Berg, *E. Coli in Motion*. Springer Science & Business Media, 2008.
- [17] S. Ramaswamy, “The mechanics and statistics of active matter,” *Annual Review of Condensed Matter Physics*, vol. 1, pp. 323–345, 2010.
- [18] P. Romanczuk, M. Bär, W. Ebeling, B. Lindner, and L. Schimansky-Geier, “Active Brownian particles,” *The European Physical Journal Special Topics*, vol. 202, no. 1, pp. 1–162, 2012.
- [19] M. Marchetti, J. Joanny, S. Ramaswamy, T. Liverpool, J. Prost, M. Rao, and R. A. Simha, “Hydrodynamics of soft active matter,” *Reviews of Modern Physics*, vol. 85, pp. 1143–1189, 2013.
- [20] C. Bechinger, R. Di Leonardo, H. Löwen, C. Reichhardt, G. Volpe, and G. Volpe, “Active particles in complex and crowded environments,” *Reviews of Modern Physics*, vol. 88, no. 4, p. 045006, 2016.
- [21] T. Vicsek and A. Zafeiris, “Collective motion,” *Physics Reports*, vol. 517, no. 3-4, pp. 71–140, 2012.
- [22] D. Needleman and Z. Dogic, “Active matter at the interface between materials science and cell biology,” *Nature Reviews Materials*, vol. 2, no. 9, p. 17048, 2017.
- [23] J. Elgeti, R. G. Winkler, and G. Gompper, “Physics of microswimmersingle particle motion and collective behavior: a review,” *Reports on Progress in Physics*, vol. 78, no. 5, p. 056601, 2015.
- [24] G. Popkin, “The physics of life,” *Nature News*, vol. 529, no. 7584, p. 16, 2016.

- [25] É. Fodor and M. C. Marchetti, “The statistical physics of active matter: From self-catalytic colloids to living cells,” *Physica A: Statistical Mechanics and its Applications*, vol. 504, pp. 106–120, 2018.
- [26] A. Najafi and R. Golestanian, “Simple swimmer at low reynolds number: Three linked spheres,” *Physical Review E*, vol. 69, no. 6, p. 062901, 2004.
- [27] K. Son, J. S. Guasto, and R. Stocker, “Bacteria can exploit a flagellar buckling instability to change direction,” *Nature Physics*, vol. 9, no. 8, p. 494, 2013.
- [28] H. Machemer, “Ciliary activity and the origin of metachrony in paramecium: effects of increased viscosity,” *Journal of Experimental Biology*, vol. 57, no. 1, pp. 239–259, 1972.
- [29] D. Woolley, “Motility of spermatozoa at surfaces,” *REPRODUCTION-CAMBRIDGE-*, vol. 126, no. 2, pp. 259–270, 2003.
- [30] B. M. Friedrich, I. H. Riedel-Kruse, J. Howard, and F. Jülicher, “High-precision tracking of sperm swimming fine structure provides strong test of resistive force theory,” *Journal of Experimental Biology*, vol. 213, no. 8, pp. 1226–1234, 2010.
- [31] K. Drescher, R. E. Goldstein, N. Michel, M. Polin, and I. Tuval, “Direct measurement of the flow field around swimming microorganisms,” *Physical Review Letters*, vol. 105, no. 16, p. 168101, 2010.
- [32] K.-I. Okamoto and Y. Nakaoka, “Reconstitution of metachronal waves in ciliated cortical sheets of paramecium-asymmetry of the ciliary movements,” *Journal of Experimental Biology*, vol. 192, no. 1, pp. 73–81, 1994.
- [33] C. A. Solari, K. Drescher, and R. E. Goldstein, “The flagellar photoreponse in volvox species (volvocaceae, chlorophyceae) 1,” *Journal of Phycology*, vol. 47, no. 3, pp. 580–583, 2011.
- [34] C. W. Harvey, F. Morcos, C. R. Sweet, D. Kaiser, S. Chatterjee, X. Liu, D. Z. Chen, and M. Alber, “Study of elastic collisions of myxococcus xanthus in swarms,” *Physical Biology*, vol. 8, no. 2, p. 026016, 2011.
- [35] R. D. Vale, “The molecular motor toolbox for intracellular transport,” *Cell*, vol. 112, no. 4, pp. 467–480, 2003.
- [36] F. Jülicher, A. Ajdari, and J. Prost, “Modeling molecular motors,” *Reviews of Modern Physics*, vol. 69, no. 4, p. 1269, 1997.

- [37] R. Bruinsma, A. Y. Grosberg, Y. Rabin, and A. Zidovska, “Chromatin hydrodynamics,” *Biophysical journal*, vol. 106, no. 9, pp. 1871–1881, 2014.
- [38] L. Angelani, R. Di Leonardo, and G. Ruocco, “Self-starting micromotors in a bacterial bath,” *Physical review letters*, vol. 102, no. 4, p. 048104, 2009.
- [39] R. Di Leonardo, L. Angelani, D. DellArciprete, G. Ruocco, V. Iebba, S. Schippa, M. Conte, F. Mecarini, F. De Angelis, and E. Di Fabrizio, “Bacterial ratchet motors,” *Proceedings of the National Academy of Sciences*, vol. 107, no. 21, pp. 9541–9545, 2010.
- [40] G. Vizsnyiczai, G. Frangipane, C. Maggi, F. Saglimbeni, S. Bianchi, and R. Di Leonardo, “Light controlled 3d micromotors powered by bacteria,” *Nature Communications*, vol. 8, p. 15974, 2017.
- [41] G. Frangipane, D. Dell’Arciprete, S. Petracchini, C. Maggi, F. Saglimbeni, S. Bianchi, G. Vizsnyiczai, M. L. Bernardini, and R. Di Leonardo, “Dynamic density shaping of photokinetic e. coli,” *Elife*, vol. 7, p. e36608, 2018.
- [42] N. Koumakis, A. Lepore, C. Maggi, and R. Di Leonardo, “Targeted delivery of colloids by swimming bacteria,” *Nature Communications*, vol. 4, p. 2588, 2013.
- [43] S. Rode, J. Elgeti, and G. Gompper, “Sperm motility in modulated microchannels,” *New Journal of Physics*, 2018.
- [44] W. F. Paxton, K. C. Kistler, C. C. Olmeda, A. Sen, S. K. St. Angelo, Y. Cao, T. E. Mallouk, P. E. Lammert, and V. H. Crespi, “Catalytic nanomotors: autonomous movement of striped nanorods,” *Journal of the American Chemical Society*, vol. 126, no. 41, pp. 13424–13431, 2004.
- [45] S. Fournier-Bidoz, A. C. Arsenault, I. Manners, and G. A. Ozin, “Synthetic self-propelled nanorotors,” *Chemical Communications*, no. 4, pp. 441–443, 2005.
- [46] R. Golestanian, T. B. Liverpool, and A. Ajdari, “Propulsion of a molecular machine by asymmetric distribution of reaction products,” *Physical Review Letters*, vol. 94, no. 22, p. 220801, 2005.
- [47] J. R. Howse, R. A. Jones, A. J. Ryan, T. Gough, R. Vafabakhsh, and R. Golestanian, “Self-motile colloidal particles: from directed propulsion to random walk,” *Physical Review Letters*, vol. 99, no. 4, p. 048102, 2007.

- [48] J. Palacci, S. Sacanna, A. P. Steinberg, D. J. Pine, and P. M. Chaikin, “Living crystals of light-activated colloidal surfers,” *Science*, vol. 339, no. 6122, pp. 936–940, 2013.
- [49] H.-R. Jiang, H. Wada, N. Yoshinaga, and M. Sano, “Manipulation of colloids by a nonequilibrium depletion force in a temperature gradient,” *Physical Review Letters*, vol. 102, no. 20, p. 208301, 2009.
- [50] H.-R. Jiang, N. Yoshinaga, and M. Sano, “Active motion of a janus particle by self-thermophoresis in a defocused laser beam,” *Physical Review Letters*, vol. 105, no. 26, p. 268302, 2010.
- [51] G. Volpe, I. Buttinoni, D. Vogt, H.-J. Kümmerer, and C. Bechinger, “Microswimmers in patterned environments,” *Soft Matter*, vol. 7, no. 19, pp. 8810–8815, 2011.
- [52] A. Snezhko, M. Belkin, I. Aranson, and W.-K. Kwok, “Self-assembled magnetic surface swimmers,” *Physical Review Letters*, vol. 102, no. 11, p. 118103, 2009.
- [53] A. Ghosh and P. Fischer, “Controlled propulsion of artificial magnetic nanostructured propellers,” *Nano Letters*, vol. 9, no. 6, pp. 2243–2245, 2009.
- [54] R. Dreyfus, J. Baudry, M. L. Roper, M. Fermigier, H. A. Stone, and J. Bibette, “Microscopic artificial swimmers,” *Nature*, vol. 437, no. 7060, p. 862, 2005.
- [55] S. Thutupalli, R. Seemann, and S. Herminghaus, “Swarming behavior of simple model squirmers,” *New Journal of Physics*, vol. 13, no. 7, p. 073021, 2011.
- [56] Z. Izri, M. N. Van Der Linden, S. Michelin, and O. Dauchot, “Self-propulsion of pure water droplets by spontaneous marangoni-stress-driven motion,” *Physical Review Letters*, vol. 113, no. 24, p. 248302, 2014.
- [57] D. Patra, S. Sengupta, W. Duan, H. Zhang, R. Pavlick, and A. Sen, “Intelligent, self-powered, drug delivery systems,” *Nanoscale*, vol. 5, no. 4, pp. 1273–1283, 2013.
- [58] B. J. Nelson, I. K. Kaliakatsos, and J. J. Abbott, “Microrobots for minimally invasive medicine,” *Annual Review of Biomedical Engineering*, vol. 12, pp. 55–85, 2010.
- [59] J. Wang and W. Gao, “Nano/microscale motors: biomedical opportunities and challenges,” *ACS nano*, vol. 6, no. 7, pp. 5745–5751, 2012.

- [60] L. K. Abdelmohsen, F. Peng, Y. Tu, and D. A. Wilson, “Micro-and nano-motors for biomedical applications,” *Journal of Materials Chemistry B*, vol. 2, no. 17, pp. 2395–2408, 2014.
- [61] M. J. Schnitzer, “Theory of continuum random walks and application to chemotaxis,” *Physical Review E*, vol. 48, no. 4, p. 2553, 1993.
- [62] J. Tailleur and M. Cates, “Statistical mechanics of interacting run-and-tumble bacteria,” *Physical Review Letters*, vol. 100, no. 21, p. 218103, 2008.
- [63] K. Martens, L. Angelani, R. Di Leonardo, and L. Bocquet, “Probability distributions for the run-and-tumble bacterial dynamics: An analogy to the lorentz model,” *The European Physical Journal E*, vol. 35, no. 9, p. 84, 2012.
- [64] L. Angelani, R. Di Leonardo, and M. Paoluzzi, “First-passage time of run-and-tumble particles,” *The European Physical Journal E*, vol. 37, p. 59, 2014.
- [65] C. Gardiner, *Handbook of Stochastic: For the Natural and Social Sciences*, vol. 4. Springer, Berlin, 2009.
- [66] B. ten Hagen, S. van Teeffelen, and H. Löwen, “Brownian motion of a self-propelled particle,” *Journal of Physics: Condensed Matter*, vol. 23, p. 194119, 2011.
- [67] R. Zwanzig, *Nonequilibrium statistical mechanics*. Oxford University Press, 2001.
- [68] M. E. Cates and J. Tailleur, “When are active brownian particles and run-and-tumble particles equivalent? consequences for motility-induced phase separation,” *EPL (Europhysics Letters)*, vol. 101, no. 2, p. 20010, 2013.
- [69] Y. Fily and M. C. Marchetti, “Athermal phase separation of self-propelled particles with no alignment,” *Physical Review Letters*, vol. 108, no. 23, p. 235702, 2012.
- [70] C. Maggi, M. Paoluzzi, N. Pellicciotta, A. Lepore, L. Angelani, and R. Di Leonardo, “Generalized energy equipartition in harmonic oscillators driven by active baths,” *Physical Review Letters*, vol. 113, no. 23, p. 238303, 2014.
- [71] C. Maggi, M. Paoluzzi, L. Angelani, and R. Di Leonardo, “Memoryless response and violation of the fluctuation-dissipation theorem in colloids suspended in an active bath,” *Scientific Reports*, vol. 7, no. 1, p. 17588, 2017.

- [72] S. Steffenoni, K. Kroy, and G. Falasco, “Interacting Brownian dynamics in a nonequilibrium particle bath,” *Physical Review E*, vol. 94, no. 6, p. 062139, 2016.
- [73] G. Szamel, “Self-propelled particle in an external potential: Existence of an effective temperature,” *Physical Review E*, vol. 90, no. 1, p. 012111, 2014.
- [74] U. M. B. Marconi and C. Maggi, “Towards a statistical mechanical theory of active fluids,” *Soft Matter*, vol. 11, no. 45, pp. 8768–8781, 2015.
- [75] C. Maggi, U. M. B. Marconi, N. Gnan, and R. Di Leonardo, “Multi-dimensional stationary probability distribution for interacting active particles,” *Scientific Reports*, vol. 5, p. 10742, 2015.
- [76] S. Das, G. Gompper, and R. G. Winkler, “Confined active brownian particles: theoretical description of propulsion-induced accumulation,” *New Journal of Physics*, vol. 20, no. 1, p. 015001, 2018.
- [77] L. Caprini, U. M. B. Marconi, and A. Puglisi, “Activity induced delocalization and freezing in self-propelled systems,” *Scientific Reports*, vol. 9, no. 1, p. 1386, 2019.
- [78] L. Caprini, E. Hernández-García, C. Lòpez, and U. M. B. Marconi, “A comparative study between two models of active cluster-crystals,” *arXiv preprint arXiv:1906.03016*, 2019.
- [79] E. Lauga, W. R. DiLuzio, G. M. Whitesides, and H. A. Stone, “Swimming in circles: motion of bacteria near solid boundaries,” *Biophysical Journal*, vol. 90, no. 2, pp. 400–412, 2006.
- [80] B. Friedrich and F. Jülicher, “The stochastic dance of circling sperm cells: sperm chemotaxis in the plane,” *New Journal of Physics*, vol. 10, no. 12, p. 123025, 2008.
- [81] W. R. DiLuzio, L. Turner, M. Mayer, P. Garstecki, D. B. Weibel, H. C. Berg, and G. M. Whitesides, “Escherichia coli swim on the right-hand side,” *Nature*, vol. 435, no. 7046, p. 1271, 2005.
- [82] M. Loose and T. J. Mitchison, “The bacterial cell division proteins ftsa and ftsz self-organize into dynamic cytoskeletal patterns,” *Nature Cell Biology*, vol. 16, no. 1, p. 38, 2014.
- [83] F. Kümmel, B. ten Hagen, R. Wittkowski, I. Buttinoni, R. Eichhorn, G. Volpe, H. Löwen, and C. Bechinger, “Circular motion of asymmetric self-propelling particles,” *Physical Review Letters*, vol. 110, no. 19, p. 198302, 2013.

- [84] H. Löwen, “Chirality in microswimmer motion: From circle swimmers to active turbulence,” *The European Physical Journal Special Topics*, vol. 225, no. 11-12, pp. 2319–2331, 2016.
- [85] S. van Teeffelen and H. Löwen, “Dynamics of a brownian circle swimmer,” *Physical Review E*, vol. 78, no. 2, p. 020101, 2008.
- [86] M. Mijalkov and G. Volpe, “Sorting of chiral microswimmers,” *Soft Matter*, vol. 9, no. 28, pp. 6376–6381, 2013.
- [87] B.-q. Ai, Y.-f. He, and W.-r. Zhong, “Chirality separation of mixed chiral microswimmers in a periodic channel,” *Soft Matter*, vol. 11, no. 19, pp. 3852–3859, 2015.
- [88] S. Meinhardt, J. Smiatek, R. Eichhorn, and F. Schmid, “Separation of chiral particles in micro-or nanofluidic channels,” *Physical Review Letters*, vol. 108, no. 21, p. 214504, 2012.
- [89] L. Caprini and U. M. B. Marconi, “Active chiral particles under confinement: surface currents and bulk accumulation phenomena,” *Soft Matter*, vol. 15, no. 12, pp. 2627–2637, 2019.
- [90] T. F. Farage, P. Krinninger, and J. M. Brader, “Effective interactions in active brownian suspensions,” *Physical Review E*, vol. 91, no. 4, p. 042310, 2015.
- [91] A. Zöttl and H. Stark, “Hydrodynamics determines collective motion and phase behavior of active colloids in quasi-two-dimensional confinement,” *Physical Review Letters*, vol. 112, no. 11, p. 118101, 2014.
- [92] R. Matas-Navarro, R. Golestanian, T. B. Liverpool, and S. M. Fielding, “Hydrodynamic suppression of phase separation in active suspensions,” *Physical Review E*, vol. 90, no. 3, p. 032304, 2014.
- [93] G. Pessot, H. Löwen, and A. M. Menzel, “Binary pusher–puller mixtures of active microswimmers and their collective behaviour,” *Molecular Physics*, vol. 116, no. 21-22, pp. 3401–3408, 2018.
- [94] E. Lauga and T. R. Powers, “The hydrodynamics of swimming microorganisms,” *Reports on Progress in Physics*, vol. 72, no. 9, p. 096601, 2009.
- [95] E. M. Purcell, “Life at low reynolds number,” *American Journal of Physics*, vol. 45, no. 1, pp. 3–11, 1977.
- [96] T. Eisenstecken, G. Gompper, and R. Winkler, “Conformational properties of active semiflexible polymers,” *Polymers*, vol. 8, no. 8, p. 304, 2016.

- [97] A. Kaiser, S. Babel, B. ten Hagen, C. von Ferber, and H. Löwen, “How does a flexible chain of active particles swell?,” *The Journal of Chemical Physics*, vol. 142, no. 12, p. 124905, 2015.
- [98] R. G. Winkler, A. Wysocki, and G. Gompper, “Virial pressure in systems of spherical active brownian particles,” *Soft Matter*, vol. 11, no. 33, pp. 6680–6691, 2015.
- [99] C. Kurzthaler, S. Leitmann, and T. Franosch, “Intermediate scattering function of an anisotropic active Brownian particle,” *Scientific Reports*, vol. 6, p. 36702, 2016.
- [100] H. Risken, *Fokker-Planck Equation*. Springer, 1984.
- [101] É. Fodor, C. Nardini, M. E. Cates, J. Tailleur, P. Visco, and F. van Wijland, “How far from equilibrium is active matter?,” *Physical Review Letters*, vol. 117, no. 3, p. 038103, 2016.
- [102] U. M. B. Marconi, A. Puglisi, and C. Maggi, “Heat, temperature and clausius inequality in a model for active brownian particles,” *Scientific Reports*, vol. 7, p. 46496, 2017.
- [103] L. Caprini, U. M. B. Marconi, A. Puglisi, and A. Vulpiani, “The entropy production of ornstein–uhlenbeck active particles: a path integral method for correlations,” *Journal of Statistical Mechanics: Theory and Experiment*, vol. 2019, no. 5, p. 053203, 2019.
- [104] L. Caprini, U. Marini Bettolo Marconi, A. Puglisi, and A. Vulpiani, “Active escape dynamics: The effect of persistence on barrier crossing,” *The Journal of Chemical Physics*, vol. 150, p. 024902, 2019.
- [105] G. Junot, G. Briand, R. Ledesma-Alonso, and O. Dauchot, “Active versus passive hard disks against a membrane: mechanical pressure and instability,” *Physical Review Letters*, vol. 119, no. 2, p. 028002, 2017.
- [106] A. P. Solon, J. Stenhammar, R. Wittkowski, M. Kardar, Y. Kafri, M. E. Cates, and J. Tailleur, “Pressure and phase equilibria in interacting active brownian spheres,” *Physical Review Letters*, vol. 114, no. 19, p. 198301, 2015.
- [107] A. P. Solon, Y. Fily, A. Baskaran, M. E. Cates, Y. Kafri, M. Kardar, and J. Tailleur, “Pressure is not a state function for generic active fluids,” *Nature Physics*, vol. 11, no. 8, p. 673, 2015.
- [108] N. Nikola, A. P. Solon, Y. Kafri, M. Kardar, J. Tailleur, and R. Voituriez, “Active particles with soft and curved walls: Equation of state, ratchets, and instabilities,” *Physical Review Letters*, vol. 117, no. 9, p. 098001, 2016.

- [109] A. Ivlev, L. Hartmut, G. Morfill, C. P. Royall, *et al.*, *Complex plasmas and colloidal dispersions: particle-resolved studies of classical liquids and solids*, vol. 5. World Scientific Publishing Company, 2012.
- [110] S. C. Takatori, R. De Dier, J. Vermant, and J. F. Brady, “Acoustic trapping of active matter,” *Nature Communications*, vol. 7, p. 10694, 2016.
- [111] J. Liu and Z. Li, “Controlled mechanical motions of microparticles in optical tweezers,” *Micromachines*, vol. 9, no. 5, p. 232, 2018.
- [112] S. Gutiérrez-Ramos, M. Hoyos, and J. Ruiz-Suárez, “Induced clustering of escherichia coli by acoustic fields,” *Scientific Reports*, vol. 8, no. 1, p. 4668, 2018.
- [113] U. M. B. Marconi, N. Gnan, M. Paoluzzi, C. Maggi, and R. Di Leonardo, “Velocity distribution in active particles systems,” *Scientific Reports*, vol. 6, p. 23297, 2016.
- [114] A. Puglisi, A. Sarracino, and A. Vulpiani, “Temperature in and out of equilibrium: A review of concepts, tools and attempts,” *Physics Reports*, vol. 709, pp. 1–60, 2017.
- [115] L. F. Cugliandolo, “The effective temperature,” *Journal of Physics A: Mathematical and Theoretical*, vol. 44, no. 48, p. 483001, 2011.
- [116] L. Caprini and U. M. B. Marconi, “Active particles under confinement and effective force generation among surfaces,” *Soft Matter*, vol. 14, no. 44, pp. 9044–9054, 2018.
- [117] P. Hänggi and P. Jung, “Colored noise in dynamical systems,” *Advances in Chemical Physics*, vol. 89, pp. 239–326, 1995.
- [118] P. Jung and P. Hänggi, “Dynamical systems: a unified colored-noise approximation,” *Physical Review A*, vol. 35, no. 10, p. 4464, 1987.
- [119] M. Hennes, K. Wolff, and H. Stark, “Self-induced polar order of active brownian particles in a harmonic trap,” *Physical Review Letters*, vol. 112, no. 23, p. 238104, 2014.
- [120] S. Rana, M. Samsuzzaman, and A. Saha, “Tuning self organization of confined active particles by steepness of the trap,” *arXiv preprint arXiv:1903.12241*, 2019.
- [121] A. Pototsky and H. Stark, “Active Brownian particles in two-dimensional traps,” *EPL (Europhysics Letters)*, vol. 98, no. 5, p. 50004, 2012.

- [122] O. Dauchot and V. Démery, “Dynamics of a self-propelled particle in a harmonic trap,” *Physical Review Letters*, vol. 122, no. 6, p. 068002, 2019.
- [123] K. Malakar, A. Das, A. Kundu, K. V. Kumar, and A. Dhar, “Exact Steady State of Active Brownian particles in a 2d harmonic trap,” *arXiv preprint arXiv:1902.04171*, 2019.
- [124] U. Basu, S. N. Majumdar, A. Rosso, and G. Schehr, “Long time position distribution of an active brownian particle in two dimensions,” *arXiv preprint arXiv:1908.10624*, 2019.
- [125] C. Bechinger, F. Sciortino, and P. Zihlerl, *Physics of complex colloids*, vol. 184. IOS Press, 2013.
- [126] Y. Fily, “Self-propelled particle in a nonconvex external potential: Persistent limit in one dimension,” *The Journal of Chemical Physics*, vol. 150, no. 17, p. 174906, 2019.
- [127] E. Woillez, Y. Zhao, Y. Kafri, V. Lecomte, and J. Tailleur, “Activated escape of a self-propelled particle from a metastable state,” *arXiv preprint arXiv:1904.00599*, 2019.
- [128] V. I. Mel’nikov, “The kramers problem: Fifty years of development,” *Physics Reports*, vol. 209, no. 1-2, pp. 1–71, 1991.
- [129] H. A. Kramers, “Brownian motion in a field of force and the diffusion model of chemical reactions,” *Physica*, vol. 7, no. 4, pp. 284–304, 1940.
- [130] N. G. Van Kampen, *Stochastic processes in physics and chemistry*, vol. 1. Elsevier, 1992.
- [131] A. Sharma, R. Wittmann, and J. Brader, “Escape rate of active particles in the effective equilibrium approach,” *Physical Review E*, vol. 95, p. 012115, 2017.
- [132] L. Cerino, A. Puglisi, and A. Vulpiani, “A consistent description of fluctuations requires negative temperatures,” *Journal of Statistical Mechanics: Theory and Experiment*, vol. 2015, no. 12, p. P12002, 2015.
- [133] M. Baldovin, A. Puglisi, and A. Vulpiani, “Langevin equation in systems with also negative temperatures,” *Journal of Statistical Mechanics: Theory and Experiment*, vol. 2018, no. 4, p. 043207, 2018.
- [134] D. B. Brückner, A. Fink, C. Schreiber, P. J. Röttgermann, J. O. Rädler, and C. P. Broedersz, “Stochastic nonlinear dynamics of confined cell migration in two-state systems,” *Nature Physics*, vol. 15, no. 6, p. 595, 2019.

- [135] R. Eichhorn, P. Reimann, and P. Hänggi, “Brownian motion exhibiting absolute negative mobility,” *Physical Review Letters*, vol. 88, no. 19, p. 190601, 2002.
- [136] Y. Fily, A. Baskaran, and M. F. Hagan, “Equilibrium mappings in polar-isotropic confined active particles,” *The European Physical Journal E*, vol. 40, no. 6, p. 61, 2017.
- [137] D. Ribet and P. Cossart, “How bacterial pathogens colonize their hosts and invade deeper tissues,” *Microbes and Infection*, vol. 17, no. 3, pp. 173–183, 2015.
- [138] M. T. Barry, R. Rusconi, J. S. Guasto, and R. Stocker, “Shear-induced orientational dynamics and spatial heterogeneity in suspensions of motile phytoplankton,” *Journal of The Royal Society Interface*, vol. 12, no. 112, p. 20150791, 2015.
- [139] K. Nelson, A. Massoudieh, and T. Ginn, “E. coli fate and transport in the happel sphere-in-cell model,” *Advances in Water Resources*, vol. 30, no. 6-7, pp. 1492–1504, 2007.
- [140] G. Li and J. X. Tang, “Accumulation of microswimmers near a surface mediated by collision and rotational Brownian motion,” *Physical Review Letters*, vol. 103, no. 7, p. 078101, 2009.
- [141] G. Miño, M. Baabour, R. Chertcoff, G. Gutkind, E. Clément, H. Auradou, and I. Ippolito, “E coli accumulation behind an obstacle,” *Advances in Microbiology*, vol. 8, pp. 451–464, 2018.
- [142] E. Altshuler, G. Mino, C. Pérez-Penichet, L. del Río, A. Lindner, A. Rousselet, and E. Clément, “Flow-controlled densification and anomalous dispersion of e. coli through a constriction,” *Soft Matter*, vol. 9, no. 6, pp. 1864–1870, 2013.
- [143] R. Nosrati, P. J. Graham, Q. Liu, and D. Sinton, “Predominance of sperm motion in corners,” *Scientific Reports*, vol. 6, p. 26669, 2016.
- [144] W. Uspal, M. N. Popescu, S. Dietrich, and M. Tasinkevych, “Self-propulsion of a catalytically active particle near a planar wall: from reflection to sliding and hovering,” *Soft Matter*, vol. 11, no. 3, pp. 434–438, 2015.
- [145] C. F. Lee, “Active particles under confinement: aggregation at the wall and gradient formation inside a channel,” *New Journal of Physics*, vol. 15, no. 5, p. 055007, 2013.
- [146] P. Margaretti and H. Stark, “Model microswimmers in channels with varying cross section,” *The Journal of Chemical Physics*, vol. 146, no. 17, p. 174901, 2017.

- [147] C. Maggi, J. Simmchen, F. Saglimbeni, J. Katuri, M. Dipalo, F. De Angelis, S. Sanchez, and R. Di Leonardo, “Self-assembly of micromachining systems powered by janus micromotors,” *Small*, vol. 12, no. 4, pp. 446–451, 2016.
- [148] L. Caprini, F. Cecconi, and U. Marini Bettolo Marconi, “Transport of active particles in an open-wedge channel,” *The Journal of chemical physics*, vol. 150, no. 14, p. 144903, 2019.
- [149] R. Wittmann, F. Smalenburg, and J. M. Brader, “Pressure, surface tension, and curvature in active systems: A touch of equilibrium,” *The Journal of Chemical Physics*, vol. 150, no. 17, p. 174908, 2019.
- [150] H. Wensink and H. Löwen, “Aggregation of self-propelled colloidal rods near confining walls,” *Physical Review E*, vol. 78, no. 3, p. 031409, 2008.
- [151] A. Kaiser, H. Wensink, and H. Löwen, “How to capture active particles,” *Physical Review Letters*, vol. 108, p. 268307, 2012.
- [152] Y. Fily, A. Baskaran, and M. Hagan, “Dynamics of self-propelled particles under strong confinement,” *Soft Matter*, vol. 10, pp. 5609–5617, 2014.
- [153] C. G. Wagner, M. F. Hagan, and A. Baskaran, “Steady-state distributions of ideal active Brownian particles under confinement and forcing,” *Journal of Statistical Mechanics: Theory and Experiment*, vol. 2017, no. 4, p. 043203, 2017.
- [154] R. Wittmann and J. M. Brader, “Active Brownian particles at interfaces: An effective equilibrium approach,” *EPL (Europhysics Letters)*, vol. 114, no. 6, p. 68004, 2016.
- [155] W. Yan and J. F. Brady, “The force on a boundary in active matter,” *Journal of Fluid Mechanics*, vol. 785, 2015.
- [156] W. Yan and J. F. Brady, “The curved kinetic boundary layer of active matter,” *Soft Matter*, vol. 14, no. 2, pp. 279–290, 2018.
- [157] M. Widder and U. M. Titulaer, “The moment method for boundary layer problems in brownian motion theory,” *Journal of Statistical Physics*, vol. 56, pp. 471–498, 1989.
- [158] K. Huang, *Introduction to statistical physics*. Chapman and Hall/CRC, 2009.
- [159] T. Speck and R. L. Jack, “Ideal bulk pressure of active brownian particles,” *Physical Review E*, vol. 93, no. 6, p. 062605, 2016.

- [160] R. Ni, M. A. C. Stuart, and P. G. Bolhuis, “Tunable long range forces mediated by self-propelled colloidal hard spheres,” *Physical Review Letters*, vol. 114, no. 1, p. 018302, 2015.
- [161] D. Vella, J. S. Wettlaufer, *et al.*, “Fluctuation spectra and force generation in nonequilibrium systems,” *Proceedings of the National Academy of Sciences*, vol. 114, no. 35, pp. 9255–9260, 2017.
- [162] J. Elgeti and G. Gompper, “Wall accumulation of self-propelled spheres,” *EPL (Europhysics Letters)*, vol. 101, no. 4, p. 48003, 2013.
- [163] S. K. Anand and S. P. Singh, “Behavior of active filaments near solid-boundary under linear shear flow,” *Soft Matter*, vol. 15, no. 19, pp. 4008–4018, 2019.
- [164] K. Malakar, V. Jemseena, A. Kundu, K. Kumar, S. Sabhapandit, S. Majumdar, S. Redner, and A. Dhar, “Steady state, relaxation and first-passage properties of a run-and-tumble particle in one-dimension,” *Journal of Statistical Mechanics: Theory and Experiment*, vol. 2018, no. 4, p. 043215, 2018.
- [165] G. H. Weiss, “Some applications of persistent random walks and the telegrapher’s equation,” *Physica A*, vol. 311, no. 3-4, pp. 381–410, 2002.
- [166] A. Scacchi and A. Sharma, “Mean first passage time of active brownian particle in one dimension,” *Molecular Physics*, vol. 116, no. 4, pp. 460–464, 2018.
- [167] P. Margaretti and H. Stark, “Model microswimmers in channels with varying cross section,” *The Journal of Chemical Physics*, vol. 146, p. 174901, 2017.
- [168] J. chun Wu, Q. Chen, and B. quan Ai, “Entropic transport of active particles driven by a transverse ac force,” *Physics Letters A*, vol. 379, no. 47, pp. 3025 – 3028, 2015.
- [169] M. H. Jacobs, *Diffusion processes*. Springer, 1935.
- [170] R. Zwanzig, “Diffusion past an entropy barrier,” *The Journal of Physical Chemistry*, vol. 96, pp. 3926–3930, 1992.
- [171] D. Reguera and J. M. Rubí, “Kinetic equations for diffusion in the presence of entropic barriers,” *Physical Review E*, vol. 64, p. 061106, Nov 2001.
- [172] P. Burada, P. Hnggi, F. Marchesoni, G. Schmid, and P. Talkner, “Diffusion in confined geometries,” *ChemPhysChem*, vol. 10, pp. 45–54.

- [173] M. Sandoval and L. Dagdug, “Effective diffusion of confined active brownian swimmers,” *Physical Review E*, vol. 90, p. 062711, 2014.
- [174] F. J. Sevilla, A. V. Arzola, and E. P. Cital, “Stationary superstatistics distributions of trapped run-and-tumble particles,” *Physical Review E*, vol. 99, p. 012145, 2019.
- [175] Y. Fily, “Self-propelled particle in a nonconvex external potential: Persistent limit in one dimension,” *arXiv preprint arXiv:1812.05698*, 2018.
- [176] P. S. Burada, G. Schmid, D. Reguera, J. M. Rubí, and P. Hänggi, “Biased diffusion in confined media: Test of the fick-jacobs approximation and validity criteria,” *Physical Review E*, vol. 75, p. 051111(8), 2007.
- [177] G. Forte, F. Cecconi, and A. Vulpiani, “Transport and fluctuation-dissipation relations in asymptotic and preasymptotic diffusion across channels with variable section,” *Physical Review E*, vol. 90, p. 062110(10), 2014.
- [178] G. Arfken and H. Weber, “Mathematical methods for physicists,” 2001.
- [179] P. K. Ghosh, V. R. Misko, F. Marchesoni, and F. Nori, “Self-propelled janus particles in a ratchet: Numerical simulations,” *Physical Review Letters*, vol. 110, p. 268301(5), 2013.
- [180] B. Rogers, J. Adams, and S. Pennathur, *Nanotechnology: understanding small systems*. Crc Press, 2014.
- [181] A. Puglisi, A. Sarracino, and A. Vulpiani, “Thermodynamics and statistical mechanics of small systems,” 2018.
- [182] G. Gallavotti and E. G. D. Cohen, “Dynamical ensembles in nonequilibrium statistical mechanics,” *Physical Review Letters*, vol. 74, no. 14, p. 2694, 1995.
- [183] J. L. Lebowitz and H. Spohn, “A gallavotti–cohen-type symmetry in the large deviation functional for stochastic dynamics,” *Journal of Statistical Physics*, vol. 95, no. 1-2, pp. 333–365, 1999.
- [184] U. Seifert, “Stochastic thermodynamics, fluctuation theorems and molecular machines,” *Reports on Progress in Physics*, vol. 75, no. 12, p. 126001, 2012.
- [185] U. Seifert, “Entropy production along a stochastic trajectory and an integral fluctuation theorem,” *Physical Review Letters*, vol. 95, no. 4, p. 040602, 2005.

- [186] T. Speck, V. Blickle, C. Bechinger, and U. Seifert, “Distribution of entropy production for a colloidal particle in a nonequilibrium steady state,” *EPL (Europhysics Letters)*, vol. 79, no. 3, p. 30002, 2007.
- [187] F. Zamponi, F. Bonetto, L. F. Cugliandolo, and J. Kurchan, “A fluctuation theorem for non-equilibrium relaxational systems driven by external forces,” *Journal of Statistical Mechanics: Theory and Experiment*, vol. 2005, no. 09, p. P09013, 2005.
- [188] T. Speck, “Driven soft matter: entropy production and the fluctuation-dissipation theorem,” *Progress of Theoretical Physics Supplement*, vol. 184, pp. 248–261, 2010.
- [189] T. Speck and U. Seifert, “Restoring a fluctuation-dissipation theorem in a nonequilibrium steady state,” *EPL (Europhysics Letters)*, vol. 74, no. 3, p. 391, 2006.
- [190] H. Kleinert and A. Chervyakov, “Perturbation theory for path integrals of stiff polymers,” *Journal of Physics A: Mathematical and General*, vol. 39, no. 26, p. 8231, 2006.
- [191] D. Mandal, K. Klymko, and M. R. DeWeese, “Entropy production and fluctuation theorems for active matter,” *Physical Review Letters*, vol. 119, no. 25, p. 258001, 2017.
- [192] L. Caprini, U. M. B. Marconi, A. Puglisi, and A. Vulpiani, “Comment on entropy production and fluctuation theorems for active matter,” *Physical Review Letters*, vol. 121, no. 13, p. 139801, 2018.
- [193] L. Bonilla, “Active ornstein-uhlenbeck particles,” *Physical Review E*, vol. 100, no. 2, p. 022601, 2019.
- [194] A. Puglisi and U. Marini Bettolo Marconi, “Clausius relation for active particles: what can we learn from fluctuations,” *Entropy*, vol. 19, no. 7, p. 356, 2017.
- [195] L. Onsager, “Reciprocal relations in irreversible processes. i.,” *Physical Review*, vol. 37, no. 4, p. 405, 1931.
- [196] L. Onsager, “Reciprocal relations in irreversible processes. ii.,” *Physical Review*, vol. 38, no. 12, p. 2265, 1931.
- [197] S. R. De Groot and P. Mazur, *Non-equilibrium thermodynamics*. Courier Corporation, 2013.
- [198] H. B. Callen and T. A. Welton, “Irreversibility and generalized noise,” *Physical Review*, vol. 83, no. 1, p. 34, 1951.

- [199] R. Kubo, “The fluctuation-dissipation theorem,” *Reports on Progress in Physics*, vol. 29, no. 1, p. 255, 1966.
- [200] P. Hänggi and H. Thomas, “Stochastic processes: Time evolution, symmetries and linear response,” *Physics Reports*, vol. 88, no. 4, pp. 207–319, 1982.
- [201] M. Falcioni, S. Isola, and A. Vulpiani, “Correlation functions and relaxation properties in chaotic dynamics and statistical mechanics,” *Physics Letters A*, vol. 144, no. 6-7, pp. 341–346, 1990.
- [202] G. Agarwal, “Fluctuation-dissipation theorems for systems in non-thermal equilibrium and applications,” *Zeitschrift für Physik A Hadrons and nuclei*, vol. 252, no. 1, pp. 25–38, 1972.
- [203] D. J. Evans and G. Morriss, *Statistical mechanics of nonequilibrium liquids*. Cambridge University Press, 2008.
- [204] D. J. Evans, E. G. Cohen, and G. P. Morriss, “Probability of second law violations in shearing steady states,” *Physical Review Letters*, vol. 71, no. 15, p. 2401, 1993.
- [205] G. E. Crooks, “Entropy production fluctuation theorem and the nonequilibrium work relation for free energy differences,” *Physical Review E*, vol. 60, no. 3, p. 2721, 1999.
- [206] C. Jarzynski, “Nonequilibrium equality for free energy differences,” *Physical Review Letters*, vol. 78, no. 14, p. 2690, 1997.
- [207] R. E. Spinney and I. J. Ford, “Nonequilibrium thermodynamics of stochastic systems with odd and even variables,” *Physical Review Letters*, vol. 108, no. 17, p. 170603, 2012.
- [208] R. E. Spinney and I. J. Ford, “Entropy production in full phase space for continuous stochastic dynamics,” *Physical Review E*, vol. 85, no. 5, p. 051113, 2012.
- [209] D. Chaudhuri, “Entropy production by active particles: Coupling of odd and even functions of velocity,” *Physical Review E*, vol. 94, no. 3, p. 032603, 2016.
- [210] K. Sekimoto and S.-i. Sasa, “Complementarity relation for irreversible process derived from stochastic energetics,” *Journal of the Physical Society of Japan*, vol. 66, no. 11, pp. 3326–3328, 1997.
- [211] K. Sekimoto, “Kinetic characterization of heat bath and the energetics of thermal ratchet models,” *Journal of the Physical Society of Japan*, vol. 66, no. 5, pp. 1234–1237, 1997.

- [212] É. Fodor, W. W. Ahmed, M. Almonacid, M. Bussonnier, N. S. Gov, M.-H. Verlhac, T. Betz, P. Visco, and F. van Wijland, “Nonequilibrium dissipation in living oocytes,” *EPL (Europhysics Letters)*, vol. 116, no. 3, p. 30008, 2016.
- [213] É. Fodor, K. Kanazawa, H. Hayakawa, P. Visco, and F. Van Wijland, “Energetics of active fluctuations in living cells,” *Physical Review E*, vol. 90, no. 4, p. 042724, 2014.
- [214] E. Ben-Isaac, É. Fodor, P. Visco, F. van Wijland, and N. S. Gov, “Modeling the dynamics of a tracer particle in an elastic active gel,” *Physical Review E*, vol. 92, no. 1, p. 012716, 2015.
- [215] É. Fodor, M. Guo, N. Gov, P. Visco, D. Weitz, and F. van Wijland, “Activity-driven fluctuations in living cells,” *EPL (Europhysics Letters)*, vol. 110, no. 4, p. 48005, 2015.
- [216] S. Chaki and R. Chakrabarti, “Entropy production and work fluctuation relations for a single particle in active bath,” *Physica A: Statistical Mechanics and its Applications*, vol. 511, pp. 302–315, 2018.
- [217] M. S. e Silva, B. Stuhmann, T. Betz, and G. H. Koenderink, “Time-resolved microrheology of actively remodeling actomyosin networks,” *New Journal of Physics*, vol. 16, no. 7, p. 075010, 2014.
- [218] L. Dabelow, S. Bo, and R. Eichhorn, “Irreversibility in active matter systems: Fluctuation theorem and mutual information,” *Physical Review X*, vol. 9, no. 2, p. 021009, 2019.
- [219] P. Pradhan and U. Seifert, “Nonexistence of classical diamagnetism and nonequilibrium fluctuation theorems for charged particles on a curved surface,” *EPL (Europhysics Letters)*, vol. 89, no. 3, p. 37001, 2010.
- [220] D. Andrieux and P. Gaspard, “Quantum work relations and response theory,” *Physical Review Letters*, vol. 100, no. 23, p. 230404, 2008.
- [221] H.-M. Chun and J. D. Noh, “Microscopic theory for the time irreversibility and the entropy production,” *Journal of Statistical Mechanics: Theory and Experiment*, vol. 2018, no. 2, p. 023208, 2018.
- [222] C. Kwon, J. Yeo, H. K. Lee, and H. Park, “Unconventional entropy production in the presence of momentum-dependent forces,” *Journal of the Korean Physical Society*, vol. 68, no. 5, pp. 633–638, 2016.
- [223] L. Cerino and A. Puglisi, “Entropy production for velocity-dependent macroscopic forces: The problem of dissipation without fluctuations,” *EPL (Europhysics Letters)*, vol. 111, no. 4, p. 40012, 2015.

- [224] U. M. B. Marconi, A. Puglisi, L. Rondoni, and A. Vulpiani, “Fluctuation–dissipation: response theory in statistical physics,” *Physics Reports*, vol. 461, no. 4-6, pp. 111–195, 2008.
- [225] L. Caprini, U. M. B. Marconi, and A. Vulpiani, “Linear response and correlation of a self-propelled particle in the presence of external fields,” *Journal of Statistical Mechanics: Theory and Experiment*, vol. 2018, no. 3, p. 033203, 2018.
- [226] K. Asheichyk, A. P. Solon, C. M. Rohwer, and M. Krüger, “Response of active brownian particles to shear flow,” *The Journal of Chemical Physics*, vol. 150, no. 14, p. 144111, 2019.
- [227] S. Shankar and M. C. Marchetti, “Hidden entropy production and work fluctuations in an active gas,” *arXiv preprint arXiv:1804.03099*, 2018.
- [228] S. Bandopadhyay, D. Chaudhuri, and A. Jayannavar, “Rotational brownian motion: Trajectory, reversibility and stochastic entropy,” *Journal of Statistical Physics*, vol. 168, no. 3, pp. 549–560, 2017.
- [229] T. Speck, “Stochastic thermodynamics for active matter,” *EPL (Europhysics Letters)*, vol. 114, no. 3, p. 30006, 2016.
- [230] D. Chaudhuri, “Active brownian particles: Entropy production and fluctuation response,” *Physical Review E*, vol. 90, no. 2, p. 022131, 2014.
- [231] S. Pigolotti, I. Neri, É. Roldán, and F. Jülicher, “Generic properties of stochastic entropy production,” *Physical Review Letters*, vol. 119, no. 14, p. 140604, 2017.
- [232] U. Seifert, “From stochastic thermodynamics to thermodynamic inference,” *Annual Review of Condensed Matter Physics*, 2018.
- [233] L. P. Dadhichi, A. Maitra, and S. Ramaswamy, “Origins and diagnostics of the nonequilibrium character of active systems,” *Journal of Statistical Mechanics: Theory and Experiment*, vol. 2018, no. 12, p. 123201, 2018.
- [234] T. Speck, “Active brownian particles driven by constant affinity,” *EPL (Europhysics Letters)*, vol. 123, no. 2, p. 20007, 2018.
- [235] H. Löwen, “Melting, freezing and colloidal suspensions,” *Physics Reports*, vol. 237, no. 5, pp. 249–324, 1994.
- [236] N. D. Mermin and H. Wagner, “Absence of ferromagnetism or antiferromagnetism in one-or two-dimensional isotropic heisenberg models,” *Physical Review Letters*, vol. 17, no. 22, p. 1133, 1966.

- [237] N. D. Mermin, “Crystalline order in two dimensions,” *Physical Review*, vol. 176, no. 1, p. 250, 1968.
- [238] K. Zahn, R. Lenke, and G. Maret, “Two-stage melting of paramagnetic colloidal crystals in two dimensions,” *Physical Review Letters*, vol. 82, no. 13, p. 2721, 1999.
- [239] R. Dullens, A. Thorneywork, J. Abbott, and D. Aarts, “Two-dimensional melting of colloidal hard spheres,” *Physical Review Letters*, vol. 118, no. 15, 2017.
- [240] N. Klongvessa, F. Ginot, C. Ybert, C. Cottin-Bizonne, and M. Leocmach, “Relaxation of weakly self-propelled particles dramatically changes at glass transition,” *arXiv preprint arXiv:1902.01746*, 2019.
- [241] J. Deseigne, O. Dauchot, and H. Chaté, “Collective motion of vibrated polar disks,” *Physical Review Letters*, vol. 105, no. 9, p. 098001, 2010.
- [242] G. Briand and O. Dauchot, “Crystallization of self-propelled hard discs,” *Physical Review Letters*, vol. 117, no. 9, p. 098004, 2016.
- [243] T. E. Angelini, E. Hannezo, X. Trepât, M. Marquez, J. J. Fredberg, and D. A. Weitz, “Glass-like dynamics of collective cell migration,” *Proceedings of the National Academy of Sciences*, vol. 108, no. 12, pp. 4714–4719, 2011.
- [244] S. Garcia, E. Hannezo, J. Elgeti, J.-F. Joanny, P. Silberzan, and N. S. Gov, “Physics of active jamming during collective cellular motion in a monolayer,” *Proceedings of the National Academy of Sciences*, vol. 112, no. 50, pp. 15314–15319, 2015.
- [245] A. Mongera, P. Rowghanian, H. J. Gustafson, E. Shelton, D. A. Kealhofer, E. K. Carn, F. Serwane, A. A. Lucio, J. Giammona, and O. Campàs, “A fluid-to-solid jamming transition underlies vertebrate body axis elongation,” *Nature*, vol. 561, no. 7723, p. 401, 2018.
- [246] D. Bi, X. Yang, M. C. Marchetti, and M. L. Manning, “Motility-driven glass and jamming transitions in biological tissues,” *Physical Review X*, vol. 6, no. 2, p. 021011, 2016.
- [247] J. Bialké, T. Speck, and H. Löwen, “Crystallization in a dense suspension of self-propelled particles,” *Physical Review Letters*, vol. 108, no. 16, p. 168301, 2012.
- [248] A. M. Menzel and H. Löwen, “Traveling and resting crystals in active systems,” *Physical Review Letters*, vol. 110, no. 5, p. 055702, 2013.
- [249] A. M. Menzel, T. Ohta, and H. Löwen, “Active crystals and their stability,” *Physical Review E*, vol. 89, no. 2, p. 022301, 2014.

- [250] G. Briand, M. Schindler, and O. Dauchot, “Spontaneously flowing crystal of self-propelled particles,” *Physical Review Letters*, vol. 120, no. 20, p. 208001, 2018.
- [251] P. Digregorio, D. Levis, A. Suma, L. F. Cugliandolo, G. Gonnella, and I. Pagonabarraga, “Full phase diagram of active brownian disks: From melting to motility-induced phase separation,” *Physical Review Letters*, vol. 121, no. 9, p. 098003, 2018.
- [252] L. F. Cugliandolo, P. Digregorio, G. Gonnella, and A. Suma, “Phase coexistence in two-dimensional passive and active dumbbell systems,” *Physical Review Letters*, vol. 119, no. 26, p. 268002, 2017.
- [253] J. Stenhammar, D. Marenduzzo, R. J. Allen, and M. E. Cates, “Phase behaviour of active brownian particles: the role of dimensionality,” *Soft Matter*, vol. 10, no. 10, pp. 1489–1499, 2014.
- [254] J. U. Klamser, S. C. Kapfer, and W. Krauth, “Thermodynamic phases in two-dimensional active matter,” *Nature Communications*, vol. 9, no. 1, p. 5045, 2018.
- [255] J. Toner and Y. Tu, “Long-range order in a two-dimensional dynamical xy model: how birds fly together,” *Physical Review Letters*, vol. 75, no. 23, p. 4326, 1995.
- [256] G. Grégoire and H. Chaté, “Onset of collective and cohesive motion,” *Physical Review Letters*, vol. 92, no. 2, p. 025702, 2004.
- [257] T. Vicsek, A. Czirók, E. Ben-Jacob, I. Cohen, and O. Shochet, “Novel type of phase transition in a system of self-driven particles,” *Physical Review Letters*, vol. 75, no. 6, p. 1226, 1995.
- [258] R. Mandal, P. J. Bhuyan, P. Chaudhuri, C. Dasgupta, and M. Rao, “Extreme active matter at high densities,” *arXiv preprint arXiv:1902.05484*, 2019.
- [259] H. Chaté, F. Ginelli, G. Grégoire, and F. Raynaud, “Collective motion of self-propelled particles interacting without cohesion,” *Physical Review E*, vol. 77, no. 4, p. 046113, 2008.
- [260] S. Mishra, A. Baskaran, and M. C. Marchetti, “Fluctuations and pattern formation in self-propelled particles,” *Physical Review E*, vol. 81, no. 6, p. 061916, 2010.
- [261] A. M. Menzel, “Collective motion of binary self-propelled particle mixtures,” *Physical Review E*, vol. 85, no. 2, p. 021912, 2012.

- [262] L. Berthier and G. Biroli, “Theoretical perspective on the glass transition and amorphous materials,” *Reviews of Modern Physics*, vol. 83, no. 2, p. 587, 2011.
- [263] L. Berthier, E. Flenner, and G. Szamel, “Glassy dynamics in dense systems of active particles,” *The Journal of Chemical Physics*, vol. 150, no. 20, p. 200901, 2019.
- [264] L. Janssen, “Active glasses,” *arXiv preprint arXiv:1906.03678*, 2019.
- [265] G. Szamel, E. Flenner, and L. Berthier, “Glassy dynamics of athermal self-propelled particles: Computer simulations and a nonequilibrium microscopic theory,” *Physical Review E*, vol. 91, no. 6, p. 062304, 2015.
- [266] L. Berthier, E. Flenner, and G. Szamel, “How active forces influence nonequilibrium glass transitions,” *New Journal of Physics*, vol. 19, no. 12, p. 125006, 2017.
- [267] R. Ni, M. A. C. Stuart, and M. Dijkstra, “Pushing the glass transition towards random close packing using self-propelled hard spheres,” *Nature Communications*, vol. 4, p. 2704, 2013.
- [268] R. Mandal, P. J. Bhuyan, M. Rao, and C. Dasgupta, “Active fluidization in dense glassy systems,” *Soft Matter*, vol. 12, no. 29, pp. 6268–6276, 2016.
- [269] S. K. Nandi, R. Mandal, P. J. Bhuyan, C. Dasgupta, M. Rao, and N. S. Gov, “A random first-order transition theory for an active glass,” *Proceedings of the National Academy of Sciences*, vol. 115, no. 30, pp. 7688–7693, 2018.
- [270] A. J. Ward, D. J. Sumpter, I. D. Couzin, P. J. Hart, and J. Krause, “Quorum decision-making facilitates information transfer in fish shoals,” *Proceedings of the National Academy of Sciences*, vol. 105, no. 19, pp. 6948–6953, 2008.
- [271] M. Ballerini, N. Cabibbo, R. Candelier, A. Cavagna, E. Cisbani, I. Giardina, V. Lecomte, A. Orlandi, G. Parisi, A. Procaccini, *et al.*, “Interaction ruling animal collective behavior depends on topological rather than metric distance: Evidence from a field study,” *Proceedings of the National Academy of Sciences*, vol. 105, no. 4, pp. 1232–1237, 2008.
- [272] A. Attanasi, A. Cavagna, L. Del Castello, I. Giardina, S. Melillo, L. Parisi, O. Pohl, B. Rossaro, E. Shen, E. Silvestri, *et al.*, “Finite-size scaling as a way to probe near-criticality in natural swarms,” *Physical Review Letters*, vol. 113, no. 23, p. 238102, 2014.

- [273] T. Mora, A. M. Walczak, L. Del Castello, F. Ginelli, S. Melillo, L. Parisi, M. Viale, A. Cavagna, and I. Giardina, “Local equilibrium in bird flocks,” *Nature Physics*, vol. 12, no. 12, p. 1153, 2016.
- [274] A. Cavagna, D. Conti, C. Creato, L. Del Castello, I. Giardina, T. S. Grigera, S. Melillo, L. Parisi, and M. Viale, “Dynamic scaling in natural swarms,” *Nature Physics*, vol. 13, no. 9, p. 914, 2017.
- [275] A. P. Solon, H. Chat e, and J. Tailleur, “From phase to microphase separation in flocking models: The essential role of nonequilibrium fluctuations,” *Physical Review Letters*, vol. 114, no. 6, p. 068101, 2015.
- [276] A. Cavagna, L. Del Castello, I. Giardina, T. Grigera, A. Jelic, S. Melillo, T. Mora, L. Parisi, E. Silvestri, M. Viale, *et al.*, “Flocking and turning: a new model for self-organized collective motion,” *Journal of Statistical Physics*, vol. 158, no. 3, pp. 601–627, 2015.
- [277] A. Cavagna, I. Giardina, and T. S. Grigera, “The physics of flocking: Correlation as a compass from experiments to theory,” *Physics Reports*, vol. 728, pp. 1–62, 2018.
- [278] A. Attanasi, A. Cavagna, L. Del Castello, I. Giardina, T. S. Grigera, A. Jeli c, S. Melillo, L. Parisi, O. Pohl, E. Shen, *et al.*, “Information transfer and behavioural inertia in starling flocks,” *Nature Physics*, vol. 10, no. 9, p. 691, 2014.
- [279] D. DellArciprete, M. Blow, A. Brown, F. Farrell, J. S. Lintuvuori, A. McVey, D. Marenduzzo, and W. C. Poon, “A growing bacterial colony in two dimensions as an active nematic,” *Nature Communications*, vol. 9, no. 1, p. 4190, 2018.
- [280] F. Peruani, J. Starru , V. Jakovljevic, L. S gaard-Andersen, A. Deutsch, and M. B r, “Collective motion and nonequilibrium cluster formation in colonies of gliding bacteria,” *Physical Review Letters*, vol. 108, no. 9, p. 098102, 2012.
- [281] A. P. Petroff, X.-L. Wu, and A. Libchaber, “Fast-moving bacteria self-organize into active two-dimensional crystals of rotating cells,” *Physical Review Letters*, vol. 114, no. 15, p. 158102, 2015.
- [282] J. Bialk , T. Speck, and H. L wen, “Active colloidal suspensions: Clustering and phase behavior,” *Journal of Non-Crystalline Solids*, vol. 407, pp. 367–375, 2015.
- [283] I. Buttinoni, J. Bialk , F. K mmel, H. L wen, C. Bechinger, and T. Speck, “Dynamical clustering and phase separation in suspensions of self-propelled colloidal particles,” *Physical Review Letters*, vol. 110, no. 23, p. 238301, 2013.

- [284] F. Ginot, I. Theurkauff, F. Detcheverry, C. Ybert, and C. Cottin-Bizonne, “Aggregation-fragmentation and individual dynamics of active clusters,” *Nature Communications*, vol. 9, no. 1, p. 696, 2018.
- [285] J. Yan, M. Han, J. Zhang, C. Xu, E. Luijten, and S. Granick, “Reconfiguring active particles by electrostatic imbalance,” *Nature Materials*, vol. 15, no. 10, p. 1095, 2016.
- [286] G. Gonnella, D. Marenduzzo, A. Suma, and A. Tiribocchi, “Motility-induced phase separation and coarsening in active matter,” *Comptes Rendus Physique*, vol. 16, no. 3, pp. 316–331, 2015.
- [287] M. E. Cates and J. Tailleur, “Motility-induced phase separation,” *Annual Review of Condensed Matter Physics*, vol. 6, no. 1, pp. 219–244, 2015.
- [288] G. S. Redner, M. F. Hagan, and A. Baskaran, “Structure and dynamics of a phase-separating active colloidal fluid,” *Physical Review Letters*, vol. 110, no. 5, p. 055701, 2013.
- [289] G. Redner, A. Baskaran, and M. Hagan, “Reentrant phase behavior in active colloids with attraction,” *Physical Review E*, vol. 88, no. 1, p. 012305, 2013.
- [290] S. Mandal, B. Liebchen, and H. Löwen, “Motility-induced temperature difference in coexisting phases,” *arXiv preprint arXiv:1902.06116*, 2019.
- [291] G.-J. Liao and S. H. Klapp, “Clustering and phase separation of circle swimmers dispersed in a monolayer,” *Soft Matter*, vol. 14, no. 38, pp. 7873–7882, 2018.
- [292] C. Reichhardt and C. O. Reichhardt, “Reversibility, pattern formation, and edge transport in active chiral and passive disk mixtures,” *The Journal of Chemical Physics*, vol. 150, no. 6, p. 064905, 2019.
- [293] M. Theers, E. Westphal, K. Qi, R. G. Winkler, and G. Gompper, “Clustering of microswimmers: interplay of shape and hydrodynamics,” *Soft Matter*, vol. 14, no. 42, pp. 8590–8603, 2018.
- [294] R. van Damme, J. Rodenburg, R. van Roij, and M. Dijkstra, “Interparticle torques suppress motility-induced phase separation for rod-like particles,” *The Journal of Chemical Physics*, vol. 150, no. 16, p. 164501, 2019.
- [295] E. Sese-Sansa, I. Pagonabarraga, and D. Levis, “Velocity alignment promotes motility-induced phase separation,” *EPL (Europhysics Letters)*, vol. 124, no. 3, p. 30004, 2018.

- [296] J. Barré, R. Chétrite, M. Muratori, and F. Peruani, “Motility-induced phase separation of active particles in the presence of velocity alignment,” *Journal of Statistical Physics*, vol. 158, no. 3, pp. 589–600, 2015.
- [297] M. N. van der Linden, L. C. Alexander, D. G. Aarts, and O. Dauchot, “Interrupted motility induced phase separation in aligning active colloids,” *arXiv preprint arXiv:1902.08094*, 2019.
- [298] G. Delphine, M. David, T. Julien, and D. Bartolo, “Freezing a flock: Motility-induced phase separation in polar active liquids,” *arXiv preprint arXiv:1903.01134*, 2019.
- [299] R. Großmann, I. S. Aranson, and F. Peruani, “A particle-field representation unifies paradigms in active matter,” *arXiv preprint arXiv:1906.00277*, 2019.
- [300] F. Schmidt, B. Liebchen, H. Löwen, and G. Volpe, “Light-controlled assembly of active colloidal molecules,” *The Journal of Chemical Physics*, vol. 150, no. 9, p. 094905, 2019.
- [301] I. Petrelli, P. Digregorio, L. F. Cugliandolo, G. Gonnella, and A. Suma, “Active dumbbells: Dynamics and morphology in the coexisting region,” *The European Physical Journal E*, vol. 41, no. 10, p. 128, 2018.
- [302] Ö. Duman, R. E. Isele-Holder, J. Elgeti, and G. Gompper, “Collective dynamics of self-propelled semiflexible filaments,” *Soft Matter*, vol. 14, no. 22, pp. 4483–4494, 2018.
- [303] A. Pandey, P. S. Kumar, and R. Adhikari, “Flow-induced nonequilibrium self-assembly in suspensions of stiff, apolar, active filaments,” *Soft Matter*, vol. 12, no. 44, pp. 9068–9076, 2016.
- [304] R. K. Manna and P. S. Kumar, “Emergent topological phenomena in active polymeric fluids,” *Soft Matter*, vol. 15, no. 3, pp. 477–486, 2019.
- [305] J. Denk, L. Huber, E. Reithmann, and E. Frey, “Active curved polymers form vortex patterns on membranes,” *Physical Review Letters*, vol. 116, no. 17, p. 178301, 2016.
- [306] V. Schaller, C. Weber, C. Semmrich, E. Frey, and A. R. Bausch, “Polar patterns of driven filaments,” *Nature*, vol. 467, no. 7311, p. 73, 2010.
- [307] Y. Sumino, K. H. Nagai, Y. Shitaka, D. Tanaka, K. Yoshikawa, H. Chaté, and K. Oiwa, “Large-scale vortex lattice emerging from collectively moving microtubules,” *Nature*, vol. 483, no. 7390, p. 448, 2012.

- [308] M. Rein and T. Speck, “Applicability of effective pair potentials for active brownian particles,” *The European Physical Journal E*, vol. 39, no. 9, p. 84, 2016.
- [309] T. Speck, “Collective behavior of active brownian particles: From microscopic clustering to macroscopic phase separation,” *The European Physical Journal Special Topics*, vol. 225, no. 11-12, pp. 2287–2299, 2016.
- [310] J. Bialké, H. Löwen, and T. Speck, “Microscopic theory for the phase separation of self-propelled repulsive disks,” *EPL (Europhysics Letters)*, vol. 103, no. 3, p. 30008, 2013.
- [311] T. Speck, J. Bialké, A. M. Menzel, and H. Löwen, “Effective cahn-hilliard equation for the phase separation of active brownian particles,” *Physical Review Letters*, vol. 112, no. 21, p. 218304, 2014.
- [312] J. Bialké, J. T. Siebert, H. Löwen, and T. Speck, “Negative interfacial tension in phase-separated active brownian particles,” *Physical Review Letters*, vol. 115, no. 9, p. 098301, 2015.
- [313] A. Patch, D. M. Sussman, D. Yllanes, and M. C. Marchetti, “Curvature-dependent tension and tangential flows at the interface of motility-induced phases,” *Soft Matter*, vol. 14, no. 36, pp. 7435–7445, 2018.
- [314] R. Wittkowski, A. Tiribocchi, J. Stenhammar, R. J. Allen, D. Marenduzzo, and M. E. Cates, “Scalar φ^4 field theory for active-particle phase separation,” *Nature Communications*, vol. 5, p. 4351, 2014.
- [315] E. Tjhung, C. Nardini, and M. Cates, “Cluster phases and bubbly phase separation in active fluids: reversal of the ostwald process,” *Physical Review X*, vol. 8, no. 3, p. 031080, 2018.
- [316] A. P. Solon, J. Stenhammar, M. E. Cates, Y. Kafri, and J. Tailleur, “Generalized thermodynamics of phase equilibria in scalar active matter,” *Physical Review E*, vol. 97, no. 2, p. 020602, 2018.
- [317] J. Stenhammar, A. Tiribocchi, R. J. Allen, D. Marenduzzo, and M. E. Cates, “Continuum theory of phase separation kinetics for active brownian particles,” *Physical Review Letters*, vol. 111, no. 14, p. 145702, 2013.
- [318] F. Caballero, C. Nardini, and M. Cates, “From bulk to microphase separation in scalar active matter: A perturbative renormalization group analysis,” *Journal of Statistical Mechanics: Theory and Experiment*, vol. 2018, p. 123208, 2018.

- [319] I. Theurkauff, C. Cottin-Bizonne, J. Palacci, C. Ybert, and L. Bocquet, “Dynamic clustering in active colloidal suspensions with chemical signaling,” *Physical Review Letters*, vol. 108, no. 26, p. 268303, 2012.
- [320] F. Ginot, I. Theurkauff, D. Levis, C. Ybert, L. Bocquet, L. Berthier, and C. Cottin-Bizonne, “Nonequilibrium equation of state in suspensions of active colloids,” *Physical Review X*, vol. 5, no. 1, p. 011004, 2015.
- [321] T. Bäuerle, A. Fischer, T. Speck, and C. Bechinger, “Self-organization of active particles by quorum sensing rules,” *Nature Communications*, vol. 9, 2018.
- [322] X. Chen, X. Yang, M. Yang, and H. Zhang, “Dynamic clustering in suspension of motile bacteria,” *EPL (Europhysics Letters)*, vol. 111, no. 5, p. 54002, 2015.
- [323] H.-P. Zhang, A. Beer, E.-L. Florin, and H. L. Swinney, “Collective motion and density fluctuations in bacterial colonies,” *Proceedings of the National Academy of Sciences*, vol. 107, no. 31, pp. 13626–13630, 2010.
- [324] X. Chen, X. Dong, A. Beer, H. L. Swinney, and H. Zhang, “Scale-invariant correlations in dynamic bacterial clusters,” *Physical Review Letters*, vol. 108, no. 14, p. 148101, 2012.
- [325] R. Nash, R. Adhikari, J. Tailleur, and M. Cates, “Run-and-tumble particles with hydrodynamics: sedimentation, trapping, and upstream swimming,” *Physical Review Letters*, vol. 104, no. 25, p. 258101, 2010.
- [326] M. Paoluzzi, R. Di Leonardo, and L. Angelani, “Effective run-and-tumble dynamics of bacteria baths,” *Journal of Physics: Condensed Matter*, vol. 25, no. 41, p. 415102, 2013.
- [327] E. Mani and H. Löwen, “Effect of self-propulsion on equilibrium clustering,” *Physical Review E*, vol. 92, no. 3, p. 032301, 2015.
- [328] C. Nardini, É. Fodor, E. Tjhung, F. Van Wijland, J. Tailleur, and M. E. Cates, “Entropy production in field theories without time-reversal symmetry: Quantifying the non-equilibrium character of active matter,” *Physical Review X*, vol. 7, no. 2, p. 021007, 2017.
- [329] L. F. Cugliandolo and G. Gonnella, “Phases of active matter in two dimensions,” *arXiv preprint arXiv:1810.11833*, 2018.
- [330] F. A. Lavergne, H. Wendehenne, T. Bäuerle, and C. Bechinger, “Group formation and cohesion of active particles with visual perception-dependent motility,” *Science*, vol. 364, no. 6435, pp. 70–74, 2019.